5-2019

Microstructural-Based Modeling Framework for High Temperature Behavior of Ferritic-Martensitic Steels Using Crystal Plasticity and Grain Boundary Finite Element Approaches

Omar Mohd Nassif
University of Tennessee, onassif@vols.utk.edu

To the Graduate Council:

I am submitting herewith a dissertation written by Omar Mohd Nassif entitled "Microstructural-Based Modeling Framework for High Temperature Behavior of Ferritic-Martensitic Steels Using Crystal Plasticity and Grain Boundary Finite Element Approaches." I have examined the final electronic copy of this dissertation for form and content and recommend that it be accepted in partial fulfillment of the requirements for the degree of Doctor of Philosophy, with a major in Civil Engineering.

Timothy J. Truster, Major Professor

We have read this dissertation and recommend its acceptance:

Dayakar Penumadu, Yanfei Gao, Reza Abedi

Accepted for the Council:

Dixie L. Thompson

Vice Provost and Dean of the Graduate School

(Original signatures are on file with official student records.)

Microstructural-Based Modeling Framework for High Temperature Behavior of Ferritic-Martensitic Steels Using Crystal Plasticity and Grain Boundary Finite Element Approaches

A Dissertation Presented for the
Doctor of Philosophy
Degree
The University of Tennessee, Knoxville

Omar Mohd Maher Nassif
May 2019

ACKNOWLEDGEMENTS

The completion of this work may never be possible without the participation and assistance of many people whose names could not all be enumerated. The contributions of those people are sincerely and gratefully appreciated and acknowledged. However, I would like to express my deep appreciation and indebtedness particularly to my supervisors in my M.Sc. and Ph.D. degrees: Prof. Samer Barakat and Dr. Timothy Truster.

I would also like to thank my brother, Saad Nassif and hope him all the best in his future endeavors.

I am also thankful for my neighbor, Mr. Steve Genard, for his generousity and hospitality. He made me welcome as if I'm home whenever I paid him a visit.

I would also like to thank my colleagues for their kindly help, Dr. Ran Ma, and Mr. Sunday Aduloju.

Additionally, I would like to thank my coworkers in Room 324: Mr. Ammar Elhassan, Mr. Usama Al-Saffar, Mr. Abdollah Javidialesaadi, Mr. Amir, Dr. Mohamed Eid and the rest of my colleagues who I forgot to mention their name.

And last but not least, I am deeply grateful to my mom, Mrs. Fatin Samoor, for all her love and support.

ABSTRACT

Ferritic/martensitic 9-12Cr steel alloys, have had widespread use as structural materials in power plants. Among this family of alloys, Grade 91 (Gr91) steel was a landmark in the development of 9-12Cr alloys. However, the unique microstructure complexity of the alloy has raised doubt regarding the techniques of data extrapolation in estimating its service-life for operation in next-generation power plants at higher temperatures and presssures. Conservatism becomes essential when the alloy is to be used in components lasting the life-cycle of power plants without replacement.

This dissertation develops a physically-based microstructural model for creep rupture at 600 degrees Celsius for Gr91 steel as well as fundamental modeling tools that apply more broadly to microstructural modeling in metals. Key features of the Gr91 modeling framework capture the mechanical behavior of its prior austenite grains (PAG) and grain boundaries. Ultimately, a constitutive expression was adopted that captured the response from experiments conducted in the creep strain rate regime.

An initial model intended to simulate low-cycle fatigue was first developed using the idea of geometrically necessary dislocations (GNDs) in crystal plasticity (CP) framework. That necessitated evaluating strain gradients and a patch-recovery method was implemented to recover a linear elastic deformation gradient field across the domain in linear elements. A Lie-group to Lie-algebra mapping was used to preserve orthogonality when projecting the rotation tensor from the elements' Gauss points to the nodes.

A statistically-stored dislocation density model was investigated to span the regimes of moderate strain rates (tension tests) to low strain rates (creep tests). Calibration of this model was possible against tension tests, but its application to creept tests suggested that other dislocation mechanisms were present during the primary creep regime of Gr91. Therefore, the CP model in the PAGs was changed to represent dislocation climb-glide motion and recovery along with linear viscous diffusional creep for point defect diffusion. This revised model more closely captured the measurements of creep response.

Lastly, a robust Discontinuous Galerkin method is proposed to model the grain boundary interface elements to address traction oscillations observed for cohesive models. Stability and convergence are assessed along with non-conforming meshes.

TABLE OF CONTENTS

LIST OF TABLES

LIST OF FIGURES

Chapter 1

INTRODUCTION AND GENERAL INFORMATION

1.1 Motivation

The class of high-temperature structural materials broadly termed 9-12Cr ferritic/martensitic steels has been under development and investigation, and in service for multiple decades, and on the basis of this broad array of results and experience, there remains considerable interest in further elevated service temperature applications for these and related materials in advanced power plant designs [1]. Important among the many performance criteria for such applications are the mechanical requirements of providing sufficient margins of structural reliability with respect to limits on accumulated creep deformation and creep rupture life, including interactions with thermal-transient-induced low cycle fatigue, over the course of projected service lives which extend to 500,000 hours, for some advanced high temperature reactor concepts.

Engineering decisions concerning material composition and processing, and both design and service conditions must necessarily be made on the basis of incomplete knowledge and understanding of long-term mechanical response. The long-term creep deformation and creep fracture are of particular importance, and experience to date with these alloys has demonstrated and documented a number of trends which motivate further study.

The 9-12Cr ferritic/martensitic steels have a complex microstructure comprising prior austenite grains, of representative diameter 30 μm, which transform to lath martensite during normalizing. The martensite formed within a prior austenite grain is hierarchically

organized into progressively smaller units including packets, blocks, and laths having respective representative scales of order 10 μm, 1 μm, and 0.2 μm. A subsequent tempering leaves "initial" (or "as-received") microstructure consisting of packet and block boundaries within prior austenite grains, and populations of $M_{23}C_6$ and MX precipitates, where the M denotes one of the metal alloying species present, often Nb or V, and X denotes C or N. The Cr-rich $M_{23}C_6$ carbides, of representative initial diameter 120 nm, have typical volume fraction of order 2%, and are preferentially located along high-angle internal interfaces including prior austenite grain boundaries (PABG) as well as packet and block boundaries. The interface-bound $M_{23}C_6$ carbides are much larger than the finer MX particles, of order 30 nm, which tend to be more homogeneously distributed throughout the matrix at a total volume fraction of order 0.2%. A high initial dislocation density, of order $10^{14}/m^2$, is partitioned among lath boundaries and lower-angle, partially-recovered (polygonized, but elongated) subgrain boundaries, of initial width scale of order 0.2 μm, along with dislocation density dispersed within the lath and subgrain structures. Higher tempering temperatures lead to lower dislocation density than is obtained from lower tempering temperatures. These are the major metallurgical features that evolve, as a complex and coupled dynamical system, in response to histories of exposure to elevated temperature and stress; macroscopically, the collective response of the system both defines the resulting deformation and sets the stage for ultimate fracture/failure.

The key metallurgical details outlined above are quite different from corresponding features in other classes of high-temperature materials, including austenitic alloys, and several aspects of the resulting macroscopic creep responses differ as well. For example, over a 550-650°C target range of service temperatures, the 9-12 Cr ferritic/martensitic steels exhibit pronounced primary creep, with a creep-rate only modestly sensitive to stress that diminishes logarithmically over decades of time before reaching a stress-and-temperature-dependent minimum creep rate. Lower values of applied stress level lead to

lower minimum creep rates, which are reached after increasing primary creep times. Once the minimum creep rate is established, progressively-accelerating tertiary creep leads to fracture within an additional time interval that often scales with the time to minimum creep rate. There is no prolonged period of "steady state," or secondary, creep. Under dead-load tensile creep, the final creep fracture tends to exhibit high levels of creep ductility, manifested in large values, of order several tens of percent, for the fractional reduction of area at failure, %RA, especially for tests involving "higher" stress levels and "shorter" resulting creep lives (say, 20,000 hours or less).

However, experience has also shown that at "lower" applied stress levels leading to "longer" creep lives, these alloys have exhibited dramatic reductions in %RA to values as small as only a few per cent, a cause of concern for many applications. In addition, intermittent low-cycle fatigue loadings have led to strong creep-fatigue coupling, with major accompanying reductions in performance windows. The microstructural mechanisms responsible for such ductility transitions are complex, but extensive metallurgical investigation has identified major features of a suite of inter-related processes of deformation and microstructural evolution which take place in these alloys, and many aspects have been quantified through mechanism-based modeling at the scale of dislocations and precipitates.

Briefly, the $M_{23}C_6$ particles on PAGBs and packet boundaries coarsen during extended elevated temperature exposure, and intermetallic Laves phase nucleation and rapid growth likewise occurs, often in close proximity to interface $M_{23}C_6$ particles. (The fine MX particles distributed more homogeneously through the matrix are much more resistant to coarsening in this temperature regime, although in Grade 91 steel (Gr91) at long exposure times at 600°C and 70 MPa, a loss in MX number density and size with increasing boundary precipitation of modified Z-phase, {Cr(V,Nb)N} has been correlated [2].) The

interface-situated arrays of coarsened particles (both Laves and $M_{23}C_6$) have been shown to provide nucleation sites for creep cavities that subsequently grow by coupled mechanisms of interface sliding, diffusion, and deformation. Such mechanisms of creep cavity nucleation, growth, and coalescence have previously been extensively studied and modeled [3-7].

A related class of microstructural coarsening mechanisms takes place in the recovery of dislocation density and the growth of subgrain domains through processes of dislocation climb and glide. While such mechanisms operate at temperature in the absence of stress, the kinetics of dislocation recovery is significantly accelerated under stress by deformation-producing dislocation fluxes [8, 9]. Climb and glide permit mobile dislocation motion toward sites both within and at the boundaries of subgrain structures, where dipole-coalescence-based dislocation recovery mechanisms take place. The kinetics of the boundary mobility is accelerated by the reduction in Zener pinning effectiveness that accompanies the coarsening of interface $M_{23}C_6$ particles (and, perhaps, to a lesser extent, to exchange of distributed MX for Z-phase precipitates). The scale of low-angle subgrain structures also coarsens as the dislocations comprising their boundaries are mobilized by climb and glide, often doubling (or more) from initial as-tempered dimensions. The extent of microstructural recovery grows with the scale of inelastic strain that is accommodated by dislocation climb and glide. As a result of these and related dislocation and microstructural recovery and particle coarsening processes, macroscopic measures of deformation resistance decrease over time.

Indeed, the gradual monotonic decrease in deformation resistance, as parameterized mainly through dislocation interactions with glide barriers including precipitates, solid solution species, and microstructural interfaces, is in large part responsible for the observed acceleration of strain rate during tertiary creep. The nucleation and growth of

Laves precipitates, intermetallics of composition Fe_2(Mo,W), removes solid solution Mo from the lath and subgrain structures, contributing to a decrease in the relatively small contribution of solid solution lattice strengthening. Although the precipitated Laves particles resulting from this process can (and do) serve a countering role in strengthening, the relevance of such processes is, at best, limited to shorter-life applications that necessarily limit the extent of Laves particle growth. At longer exposure times, coarsening of the Laves phases to large diameters and spacings obviates any potential strengthening contributions from this phase, leaving only its deleterious role in cavity nucleation.

A mechanistically similar loss of strength is associated with the coarsening of the $M_{23}C_6$ particles on PAGB, packet, and block boundaries: in addition to the potential for cavity nucleation at the coarsened particles, there is a reduced resistance to interface sliding, compared to that of the initial distribution of $M_{23}C_6$. The coarsening of pinning particles also facilitates subgrain mobility toward larger scales that offer lowered interface/boundary resistance to dislocation flux.

The relative stability of macroscopic flow under such conditions of deformation-induced "softening" is tied to the strong rate-sensitivity of the thermally-activated climb mechanism. Other manifestations of rate-dependent deformation softening in these materials include pronounced softening regimes during high-temperature constant strain rate tensile testing, and the softening associated with cyclic plastic deformation. The evolution of progressive softening is also evident in ambient temperature hardness measurements made on interrupted creep tests.

Because the time-and-deformation-induced reduction in deformation resistance is gradual, the deformation driving the softening mechanisms leads to relatively large values for creep ductility and the creep life-fraction spent in the tertiary regime. Both of these features are characteristic of the creep behavior of 9-12Cr ferritic/martensitic steels at

"higher" stress and temperature levels and "lower" creep lives. If the final failure under such conditions can be considered as being effectively determined by the deformation kinetics of the continuously-accelerating softening processes, it is possible to view the "other" damage mechanisms of creep cavity nucleation and growth as assuming a minor, or at least, operationally less significant role in characterizing the final creep failure.

The scenario outlined above summarizes many aspects of the creep resistance of 9-12 Cr ferritic/martensitic steels, and, to the extent that it is broadly applicable for relevant service conditions, one might minimize the need for more detailed assessments of the processes of creep cavity nucleation and growth in these alloys. However, as noted above, under the lower stress levels typical of service lives well in excess of 100,000 hours, the creep ductility often drops dramatically. Under such circumstances, the stability of deformation-induced softening that worked to provide large creep ductility at shorter lives is evidently no longer as effective: the continuation of creep deformation to large ductility at low stress does not take place.

The reduction in creep ductility raises questions on what microstructural developments might account for such behavior. Recalling the prominent roles of grain boundary creep cavitation in limiting creep life and in leading to typically small values of creep ductility in a broad range of other metals and alloys, as well as evidence documenting the evolution of creep cavity nucleation and growth in the 9-12 Cr ferritic/martensitic steels themselves [10, 11] we are motivated to focus attention on the operation of creep cavitation processes, bearing in mind particular and somewhat unique details of their microstructure and deformation mechanisms, and the joint evolution of these fields under histories of elevated temperature and stress.

Although there is much less data and consensus on operative mechanisms leading to low ductility at low stress and long creep life in 9-12 Cr ferritic/martensitic steels, there

are strong reasons to focus on grain boundary cavitation in these materials. Collectively, the proposed scenario suggests that key features of our modeling capabilities, namely, 3D grain boundary sliding and diffusionally-accommodated interface cavitation, along with crystal plasticity (CP) treatments of dislocation flow and microstructural evolution, perhaps augmented by a diffusional creep mechanism like Nabarro-Herring, offer promise of predictive utility.

Major features potentially associated with low creep ductility:

- At applied low stress, the dislocation climb and glide creep in the grains is strongly diminished compared with higher stress value. Even though the time available for microstructural recovery of dislocation structures increases, because the stress is so low, the inelastic dislocation climb-and-glide strain (which accelerates the softening through dislocation and microstructural recovery; see above) is strongly reduced. This tends to "slow down" the deformation-induced softening (per unit deformation). But the extra time at temperature does lead to enhanced coarsening of $M_{23}C_6$ and the nucleation and growth of Laves particles on boundaries, both of which can serve as potent sites for creep cavity nucleation and growth.

- At the lowest applied stress levels, the grain strain-rates arising from dislocation climb and glide might become so small that the dominant creep mechanism switches to one based on a diffusional creep mechanism. Earlier work on Gr91 [12] has shown a transition in the (raw) stress-dependence of minimum creep rate from a creep exponent, n, of the form

$$\left(\dot{\varepsilon}^{C}\right)_{\min} \sim \sigma^{n} \tag{1.1}$$

with $n \sim 10+$ or so, (as is typical of creep-strengthened alloys resisting deformation by dislocation climb and glide), to linear viscous behavior, with $n=1$, at the very

low stress levels that might be typical of those used in very long life power plant and reactor plant applications. The "standard" climb and glide creep stress exponent of $n=5$ that is often observed in pure metals is typically not seen in particle-strengthened materials, with $n\sim 10$ (or greater, depending on temperature) as typical. However, it is possible to reinterpret the Norton creep driving stress as an "effective" measure, the difference between macroscopically applied stress and a "back stress" due to dislocation interactions with particles and the dislocation resistances embedded in high angle boundaries that themselves resist coarsening through particle pinning:

$$\left(\dot{\varepsilon}^{C}\right)_{(\min)} \sim \left(\sigma - \sigma_{\text{back}}\right)^{5} \tag{1.2}$$

In this view the softening is due to on-going time- temperature-, and deformation-dependent reductions in σ_{back}.

- There is some uncertainty as to whether or not the $n=1$ mechanism is Nabarro-Herring (bulk diffusion), or perhaps Harper-Dorn, or Coble in nature. The CP constitutive formulations discussed here, focus on mechanisms of dislocation climb and glide, and microstructural recovery and particle coarsening, enriched by incorporating bulk diffusion in the Ashby map sense of superposing an additional creep strain rate based on diffusion in the grains. At stress and microstructural state levels where power-law climb and glide dominates, the added linear viscous strain rate is negligible, and, conversely, if stress and microstructural state results in dislocation-based strain rates that are sufficiently low, the climb/glide contribution to strain-rate will be swamped by the linear viscous contribution.

- Returning to the low stress/long creep life microstructural evolution: because of the kinematically-required grain boundary sliding on high-angle boundaries like

PABG and packet boundaries, there will always remain stress concentration at/near triple points and sliding interface boundaries. The elevated stress in the vicinity of such concentrations might well be large enough to (locally) activate the dislocation climb/glide deformation that leads to dislocation recovery and softening, even though the stress in more remote portions of the grains is still small enough that only diffusional creep and thermally-driven ageing are taking place. Such a scenario could lead to a situation in which the strong crystallographic softening associated with dislocation flux around particles and through coarsening subgrain boundaries would be preferentially confined (spatially) to the vicinity of the sliding boundaries. Indeed, instances of strongly localized subgrain coarsening recovery along PAGB interface segments have been associated with low values of long-life creep ductility [13, 14].

- If the non-negligible climb/glide deformation and softening is highly-localized along interface boundaries, it would nonetheless lead to only a modest increase in the macroscopic creep deformation (beyond the background deformation contributed by all other operative mechanisms), but locally the softening effect would be large, and confined to the immediate vicinity of sliding boundaries that are in the process of growing creep cavities.

Based on the scenario outlined above, among others, we believe that the combination of high-performance continuum mechanics simulation tools incorporating mechanism-based constitutive models of deformation and microstructural evolution that is being developed and applied in this dissertation have great potential in elucidating and understanding important features of the high-temperature mechanical behavior of 9-12 Cr ferritic/martensitic steels in power plant and reactor plant applications.

1.2 Crystal Plasticity

A physically-based microstructure model for creep simulation necessitates using a robust crystal-plasticity finite element (CPFE) framework to capture much of the anisotropic behavior due to mesoscale slip activity in the alloy's crystal in a continuum fashion. This involves modeling the evolution of grains inside the material. The CPFE framework from [15] is adopted throughout this work. Fundamentally, this finite-strains CPFE model involves a flow rule relating the slip rate along slip systems to the special velocity gradient. The special velocity gradient is then used in a hypo-elastic formulation to compute the green-naghdi objective stress rate and the algorithmic tangent as described in the following section.

1.2.1 Kinematics and the stress rate description

Let $\Omega_0 \subset \mathbb{R}^3$ be an open bounded reference configuration and with boundary Γ_0 and let $\Omega \subset \mathbb{R}^3$ be its corresponding current (deformed) configuration with boundary Γ. The $\boldsymbol{\phi}(\boldsymbol{X},t)$ is one-to-one mapping between two particles $\boldsymbol{X} \in \Omega_0$ and $\boldsymbol{x} \in \Omega$:

$$\boldsymbol{x} = \boldsymbol{\phi}(\boldsymbol{X},t) \tag{1.3}$$

The deformation gradient $\boldsymbol{F}$ associated with mapping $\boldsymbol{\phi}$ is then defined as the partial derivative of this mapping with respect to the reference coordinates:

$$\boldsymbol{F}(\boldsymbol{X},t) = \frac{\partial \boldsymbol{\phi}(\boldsymbol{X},t)}{\partial \boldsymbol{X}} = \frac{\partial \boldsymbol{x}}{\partial \boldsymbol{X}} = \boldsymbol{I} + \mathrm{GRAD}\ \boldsymbol{u} \tag{1.4}$$

where $\boldsymbol{I}$ is the unit (identity) tensor and $\boldsymbol{u}$ is the displacement field describing the motion. The deformation gradient $\boldsymbol{F}$ can be multiplicatively split into a rotation and a stretch tensor:

$$\boldsymbol{F} = \boldsymbol{R}\boldsymbol{U} = \boldsymbol{V}\boldsymbol{R} \tag{1.5}$$

where $\boldsymbol{R}$ is the rotational tensor, $\boldsymbol{U}$ is the right stretch tensor and $\boldsymbol{V}$ is the left stretch tensor. The deformation gradient $\boldsymbol{F}$ can then also be decomposed multiplicatively into plastic and elastic parts:

$$\boldsymbol{F} = \boldsymbol{F}^e\boldsymbol{F}^p = \boldsymbol{V}^e\boldsymbol{R}^e\boldsymbol{R}^p\boldsymbol{U}^p \tag{1.6}$$

Now applying the assumption of small elastic strains $\boldsymbol{V}^e \approx (\boldsymbol{I} + \boldsymbol{\varepsilon})$, (1.6) becomes:

$$\boldsymbol{F} \approx (\boldsymbol{I} + \boldsymbol{\varepsilon})\boldsymbol{R}^e\boldsymbol{R}^p\boldsymbol{U}^p \tag{1.7}$$

Then the velocity gradient $\boldsymbol{L} = \dot{\boldsymbol{F}}\boldsymbol{F}^{-1}$ can be written as:

$$\boldsymbol{L} = \dot{\boldsymbol{F}}\boldsymbol{F}^{-1} \approx \left(\dot{\boldsymbol{R}}\boldsymbol{U}^p + \boldsymbol{R}\dot{\boldsymbol{U}}^p + \dot{\boldsymbol{\varepsilon}}\boldsymbol{R}\boldsymbol{U}^p + \boldsymbol{\varepsilon}\dot{\boldsymbol{R}}\boldsymbol{U}^p + \boldsymbol{\varepsilon}\boldsymbol{R}\dot{\boldsymbol{U}}^p\right)\cdot\left(\boldsymbol{U}^{p-1}\boldsymbol{R}^T - \boldsymbol{U}^{p-1}\boldsymbol{R}^T\boldsymbol{\varepsilon}\right) \tag{1.8}$$

Removing the quadratic terms from the above equation, it can then be simplified as:

$$\boldsymbol{L} = \dot{\boldsymbol{\varepsilon}} + \boldsymbol{\varepsilon}\boldsymbol{\omega} - \boldsymbol{\omega}\boldsymbol{\varepsilon} + \boldsymbol{\omega} + \boldsymbol{\varepsilon}\boldsymbol{l}^p - \boldsymbol{l}^p\boldsymbol{\varepsilon} + \boldsymbol{l}^p \tag{1.9}$$

where $\boldsymbol{\omega} = \dot{\boldsymbol{R}}\boldsymbol{R}^T$ is the rate of change of the rotation tensor and $\boldsymbol{l}^p = \dot{\boldsymbol{F}}^p\boldsymbol{F}^{p-1}$ is the plastic part of the velocity gradient. Following [16], $\boldsymbol{l}^p$ in a crystal plasticity framework can be defined as:

$$\boldsymbol{l}^p = \sum_{\alpha}^{n_{slip}} \dot{\gamma}^{\alpha}\ \boldsymbol{m}^{\alpha} \otimes \boldsymbol{s}^{\alpha} \tag{1.10}$$

where $\dot{\gamma}^{\alpha}$ is the slip rate along individual crystallographic slip systems, $\boldsymbol{m}^{\alpha}$ and $\boldsymbol{s}^{\alpha}$ are the slip system's directions and normal and n_{slip} is the number of slip systems of the material's lattice configuration. The symmetric and skew-symmetric parts of the plastic velocity gradient can then be defined as:

$$\boldsymbol{D}^p = \sum_{\alpha}^{n_{slip}} \dot{\gamma}^{\alpha}\ \text{symm}\ (\boldsymbol{m}^{\alpha} \otimes \boldsymbol{s}^{\alpha}) \tag{1.11}$$

$$\boldsymbol{W}^p = \sum_{\alpha}^{n_{slip}} \dot{\gamma}^{\alpha}\ \text{skew}\ (\boldsymbol{m}^{\alpha} \otimes \boldsymbol{s}^{\alpha}) \tag{1.12}$$

The spatial rate of deformation tensor is the symmetric part of the velocity gradient, the symmetric part of Eq. (1.9) becomes:

$$\boldsymbol{D} = \frac{1}{2}(\boldsymbol{L} + \boldsymbol{L}^T) = \dot{\boldsymbol{\varepsilon}} + \boldsymbol{\varepsilon\omega} - \boldsymbol{\omega\varepsilon} + \boldsymbol{\varepsilon W}^p - \boldsymbol{W}^p\boldsymbol{\varepsilon} + \boldsymbol{D}^p \tag{1.13}$$

The Cauchy stress rate equation can then be obtained by multiplying the above equation by the elasticity tensor $\boldsymbol{C}_0$ such that $\boldsymbol{\sigma} = \boldsymbol{C}_0\boldsymbol{\varepsilon}$:

$$\dot{\boldsymbol{\sigma}} = \mathbf{C}_0 : \dot{\boldsymbol{\varepsilon}} = \mathbf{C}_0 : \left(\boldsymbol{D} - \boldsymbol{D}^p\right) - \boldsymbol{\sigma\omega} + \boldsymbol{\omega\sigma} - \boldsymbol{\sigma W}^p + \boldsymbol{W}^p\boldsymbol{\sigma} \tag{1.14}$$

Adopting the Green-Naghdi objective stress rate [17] $\overset{\square}{\boldsymbol{\sigma}} = \dot{\boldsymbol{\sigma}} + \boldsymbol{\sigma\omega} - \boldsymbol{\omega\sigma}$, Eq. (1.14) becomes :

$$\overset{\square}{\boldsymbol{\sigma}} = \mathbf{C}_0 : \left(\boldsymbol{D} - \boldsymbol{D}^p\right) - \boldsymbol{\sigma W}^p + \boldsymbol{W}^p\boldsymbol{\sigma} \tag{1.15}$$

Using the definition of the corotational Cauchy stress, the stress and its corresponding stress rate becomes $\boldsymbol{t} = \boldsymbol{R}^T\boldsymbol{\sigma R}$ and $\dot{\boldsymbol{t}} = \boldsymbol{R}^T\overset{\square}{\boldsymbol{\sigma}}\boldsymbol{R}$, respectively. Eq.(1.15) then becomes:

$$\dot{\boldsymbol{t}} = \mathbf{C}_0 : \left(\boldsymbol{d} - \boldsymbol{d}^p\right) - \boldsymbol{t W}^p + \boldsymbol{W}^p\boldsymbol{t} \tag{1.16}$$

where $\boldsymbol{d} = \boldsymbol{R}^T\boldsymbol{DR}$ and $\boldsymbol{d}^p = \boldsymbol{R}^T\boldsymbol{D}^p\boldsymbol{R}$. Similar to [18], we approximate the plastic rotation evolution using the plastic vorticity tensor as follows:

$$\dot{\boldsymbol{R}}^p = \bar{\boldsymbol{w}}^p \cdot \boldsymbol{R}^p \tag{1.17}$$

where $\bar{\boldsymbol{w}}^p = \boldsymbol{R}^e \cdot \boldsymbol{W}^p \cdot \boldsymbol{R}^{eT}$. Effectually, the plastic rotation is defined at the micro-constitutive level, which is valid up to modest plastic strains and when the plastic strains weakly affect the elastic response [19]. The time discretization of the above equation then becomes:

$$\Delta\boldsymbol{t}_{n+1} = \left[\mathbf{C}_0 : \left(\Delta\boldsymbol{d}_{n+1} - \Delta\boldsymbol{d}^p_{n+1}\right) - \boldsymbol{t}_{n+1}\Delta\boldsymbol{W}^p_{n+1} + \Delta\boldsymbol{W}^p_{n+1}\boldsymbol{t}_{n+1}\right] \cdot \Delta t \tag{1.18}$$

1.3 Summary

This dissertation develops a physically-based microstructural model of creep deformation in Ferretic-Martensitic steels, suitable for temperatures in the $550^\circ - 600^\circ$ range and

loading stresses less than 200 MPa. The purpose of this modeling is to have a conservative estimate of the life-expectancy of such alloys in stress and temperature conditions typical in nuclear reactors. The model is incorporated into a finite element modeling framework whose constitutive equations describe observed phenomena in that family of alloys. Various techniques of the microstructural modeling are investigated, generally divided into two parallel parts. The first part simulates the Prior Austenite Grains (PAG) and the other one simulates the Prior Austenite Grain Boundaries (PAGB). The PAGs are represented by solid finite elements in a Crystal Plasticity (CP) framework that utilizes a hypoelastic finite-displacement formulation. Meanwhile, the PAGB are represented by interface elements that are intended to simulate various mechanisms comprised of grain boundary sliding and cavity nucleation and growth along the PAGB. Those various developed techniques are then tested against published experimental creep data for the 9Cr-1Mo-V alloy [20], with the goal of matching secondary and tertiary creep, as well as the minimum creep rate achieved for various stress rates.

This work is organized as follows:

To model low-cyclic fatigue in the alloy, a strain-gradient method was proposed. Chapter 2 develops a method to project a smooth global strain-related field across the model's nodes. This was done to avoid the use of higher-order elements or solving for fields other than the displacement (mixed methods). The strain-related field in question is the elastic rotation tensor $\boldsymbol{R}^e$ and the global smoothing method uses a patch-recovery technique similar to [21]. Since the aforementioned method involves extrapolating $\boldsymbol{R}^e$ from gauss points onto element nodes, a Lie-group to Lie-algebra mapping was implemented to preserve the orthogonality of the rotation tensor [22]. Additionally, an implicit update scheme was developed for the internal variables used in the crystal plasticity formulations. Numerical tests were perfomed to test stability, robustness and accuracy of the method.

A surrogate Mechanical Threshold Stress (MTS) hardening model was used for the tests as it was already verified for aluminum alloys (FCC) simulations [15], hence reducing any uncertainty arising from the type of hardening model used.

Chapter 3 describes the initially proposed anisotropic dislocation-based modeling of the PAGs. The model, based on the works of [23, 24], relates the state of dislocation substructure to the evolution creep resistense in PAGs in the Ferritic-Martensitic alloys. The parameters used in the model were calibrated against the experimental data of [25]. Since the calibration involves more than 20 parameters, the curve fiiting was done using a Genetic-Algorithm technique developed by [26]. To further cut the run time of all simulations needed, an isostrain approximation was employed into a single element with 100 crystals (each crystal has a different orientation but is subjected to the same amount of incremental strain). After the best-fit parameters were obtained, they were plugged into a 100-grain cell model (10402 and 3922 solid and interface elements, respectively). This cell model was then simulated to failure (around 20,000 hrs) and compared to experimental data [20].

Due to the inaccuracies exhibited by the dislocation-based model in capturing the creep response, a new model was introduced in Chapter 4. The solid element part of the model includes deformation mechanisms from dislocation and diffusional motion within the prior austenite grains (PAG) while the interface part includes viscous sliding and cavity growth and nucleation along grain boundaries, the latter considered to be the material's primary deformations modes. The cavity growth model builds upon the smeared cavity population model of [11, 27, 28] by including the effect of creep strain and stress triaxiality from material points in the grains next to the grain boundary. Several simulations were conducted to understand the features of each deformation mode. First, a study on a polycrystalline microstructure with compliant elastic grain boundaries revealed a sensitivity of the finite element method to stress concentrations at triple points. This

study influenced the calibration process of the material parameters for each component mechanism, targeted at 600 °C response against Grade 91 creep data from [29]. A post-process decomposition approach provided an analysis of the complete cell model response. Each mechanism plays a role at different stages of the creep response, including the effect of grain diffusional creep on the minimum strain rate.

Chapter 5 continues the work of Chapter 4 by examining the effect of stress level, stress triaxiality, and temperature on the engineering and microscale response of Grade 91 under elevated temperature service. Stress levels ranging from 140 MPa to 60 MPa were simulated. The chapter elucidates this mechanism shift with a simple micromechanical model that reproduces and explains the results of the full CPFEM simulations described here.

Due to the oscillations of the traction field present on the interface elements simulating the PAGBs, Chapter 6 develops a Discontinuous Galerkin (DG) method with evolving stability parameters based on the shape and material of the elements facing each other. This was done by utilizing the Variational Multiscale concepts and weakly enforcing the displacement and traction continuity along such interfaces. A number of numerical tests were performed to investigate the stability and robustness of the method.

Finally, Chapter 7 abridges the conclusions of this dissertation and presents subjects of future research. These subjects include extending the Lie Group/Algebra method of Chapter 2 to GND model of Bailey and Geers, comparing uniform and preferential texture effects in RVE of Grade 91 crystal plasticity creep model, extending the stabilized DG crystal plasticity method in Chapter 6 to include grain boundary sliding effects, and applying machine learning method (e.g. Neural networks) to improve the fit of model parameters to experimental data and quantify sensitivities.

Chapter 2

VARIATIONAL PROJECTION METHODS FOR GRADIENT CRYSTAL PLASTICITY USING LIE ALGEBRAS[1]

2.1 Introduction

The development of constitutive models incorporating strain gradient effects have become particularly important for the design of metallic components with dimensions on the order of microns. Polycrystalline materials have been observed to exhibit a size-dependent effect [30, 31] whereby experiments conducted on specimens with smaller grain sizes have exhibited higher flow stress [32]. These effects are also manifested through Stage IV hardening, exhibiting linear hardening rather than saturation at large strains [33]. Recent contributions from continuum dislocation mechanics theories have provided further rational basis to these mechanisms. For example, Scardia et al. [34] describes a rigorous upscaling theory for quantifying strengthening effects from dislocation pile ups. Also, Wulfinghoff and Böhlke [35] modeled dislocation pile-ups using a continuum dislocation formulation that includes curvature field variables and dislocation transport.

For models focused on the component scale (mesoscale), size effects have often been incorporated into continuum formulations through strain gradient terms [22, 36, 37] based on elastic incompatibilities generated from geometrically necessary dislocations (GND) [38]. Other size-dependent formulations have been devised through micro-forces conjugated to strain gradients [39, 40], micromorphic continua [41], and micropolar single crystal plasticity [42]. However, in these theories, the additional constitutive terms take

[1] This Chapter has been adapted from "Truster, T.J., Nassif, O., 2017. Variational projection methods for gradient crystal plasticity using Lie algebras. International Journal for Numerical Methods in Engineering, 110, pp.303-332".

the form of partial differential equations rather than ordinary differential equations. Hence, the additional field usually must be treated as an internal degree of freedom (DOF) rather than an internal variable. The most rigorous numerical formulations treat either the dislocation density [43] or the plastic strain field [44, 45] as nodal DOF and solve the resulting mixed field problem. Alternative variational approaches can be formulated as dual problems for determining the nodal forces conjugate to the gradient terms [46]. However, both classes of methods are computationally expensive when solved in a monolithic fashion due to the expanded matrix equations. Also, these gradient terms may not be the primary source of hardening within the material system. Thus, we will consider simplified numerical approaches for evaluating the strain gradient that involve projections of an internal variable onto an internal degree of freedom field.

A simple numerical approximation of the strain gradients is to perform projections onto discontinuous fields that are defined over each finite element. In an early approach, Dia [47] proposed a model for GND within face-centered cubic (FCC) materials to capture the grain size effect. Extensions of this method to three dimensions include Meissonnier et al. [36] for modeling effects of precipitates in a two phase nickel superalloy and Messner [15] for modeling aluminum-lithium alloys. While the elemental methods are simple to implement, the projected strain gradient is closely tied to the finite element length scale, and issues with mesh dependency have been observed by Cheong et al. [48]. Also, linear triangular and tetrahedral elements are not compatible with this technique.

As an alternative to the elemental projection, the internal variables can be projected onto a globally smooth field defined from the nodal shape functions of the domain mesh. An early example of these nodal methods is the super element technique proposed by Abu Al-Rub and Voyiadjis [49], accomplished by a local least squares fit over patches of elements. While this method applied only to structured meshes, a similar technique allowing unstructured meshes was developed by Han et al. [22] using the patch recovery

technique from Zienkiewicz and Zhu [21], a classical technique employed for stress post-processing, error estimation, and mesh adaptivity. The patch recovery approach determines each projected nodal value by solving a local problems posed over the elements surrounding that node. Later developments were conducted by Gan and Akin [50, 51] to evaluate second derivatives within phenomenological plasticity models for modeling shear bands. Due to increased zone of support, the nodal projection is not tied as closely to the mesh size as is the case for the elemental projection, lessening the possibility for mesh sensitivity issues.

One subtle point overlooked by several of these methods is the preservation of tensorial properties during the projection operation and subsequent interpolation. For example, Dia [47] suggests an ad hoc scaling to ensure that the determinant of the plastic deformation tensor remains equal to unity. Also, approximations to the Nye tensor involving elastic rotations may fail to account for the orthogonality of the tensors [15]. Recently, a framework was proposed by Mota et al. [52] for projections that preserve tensorial properties by invoking the exponential and logarithmic mapping of tensors. Their method represents an enhancement to classical L^2 projection techniques for transferring state variables at integration points between adaptively refined meshes; see e.g. the work of Ortiz and Quigley [53] for strain localization modeling. However, these approaches have primarily been considered only for transferring state variables without subsequently differentiating the field. Also, because the formulation is posed over the entire domain, the method's computational expense is directly tied to the treatment of the resulting matrix equation.

In the present work, we develop and compare several projection methods for computing the gradient terms within a geometrically necessary dislocation based crystal plasticity model. We select the mechanical threshold stress based model [33, 54, 55] for FCC materials as a prototypical constitutive model, which includes temperature and strain rate

dependence in the plastic slip equations. Since small elastic strains are assumed within a hypoelastic kinematic formulation, the Nye tensor is expressed in terms of gradients of the elastic rotation tensor. Two projection methods are compared: an elemental method [15] and a recently proposed nodal method [56]. The nodal method incorporates the Lie group – Lie algebra relations from [52] to ensure that the projected elastic rotation tensor remains orthogonal. A lumped approximation of the global projection matrix is utilized such that the method is computationally more economical than a mixed formulation. We also investigate the impact of explicit and implicit time integration for the plastic rotation tensor upon numerical stability and computational cost. The implicit scheme is accomplished using a staggered approach within each iteration of the Newton-Raphson method for the equilibrium equation. Previous studies have typically pursued only a single spatial and temporal discretization scheme in isolation. Therefore, a distinct contribution of the present work is the systematic comparison of these approaches within a unified framework. The various methods are assessed through a series of numerical problems involving several element types both in two and three dimensions. Problems involving multi-axial loading and several grains within the domain are considered. The performance of the methods are quantified in terms of accuracy, stability, and computational cost through such measures as the number of Newton iterations.

A discussion of the elemental and nodal projection methods along with the Lie group and Lie algebra relations is contained in Section 2.3. Section 2.4 presents the explicit and implicit time integration algorithms for the plastic rotation tensor. Numerical studies for these methods are conducted in Section 2.5. Finally, conclusions are drawn in Section 2.6.

2.2 Gradient-based Crystal Plasticity Finite Element Method

2.2.1 Constitutive model and effects of geometrically necessary dislocations

As a means to relate the plastic slip rates $\dot{\gamma}^{(s)}$ to the current applied stress $\boldsymbol{\sigma}$ and other factors, we adopt the mechanical threshold stress (MTS) based model proposed by Koks et al. [54], which accurately captures stage II and stage III hardening in FCC metals [57, 58] . Additionally, the model is extended to stage IV hardening by including effects from geometrically necessary dislocations (GND), which renders the model as nonlocal and necessitates particular algorithmic treatment [33, 55]. The pertinent equations are summarized herein to provide context for the projection method.

A power law expression is taken to relate the slip rate $\dot{\gamma}^{(s)}$ to the resolved shear stress $\tau^{(s)}$ on slip system (s) through the macroscopic strain rate $\dot{\varepsilon}$ and threshold stress $\tilde{\tau}$ as follows:

$$\dot{\gamma}^{(s)} = \frac{\dot{\varepsilon}}{\tilde{\tau}}\left|\frac{\tau^{(s)}}{\tilde{\tau}}\right|^{n-1}\tau^{(s)} \tag{2.1}$$

$$\tau^{(s)} = \tilde{\boldsymbol{b}}^{(s)} \cdot \left[\boldsymbol{R}^{p}\boldsymbol{t}\boldsymbol{R}^{pT}\right] \cdot \tilde{\boldsymbol{n}}^{(s)} \tag{2.2}$$

$$\dot{\varepsilon} = \sqrt{\tfrac{2}{3}\boldsymbol{d}:\boldsymbol{d}} \tag{2.3}$$

Note that the reference shear rate $\dot{\varepsilon}$ is evaluated through the unrotated deformation rate tensor $\boldsymbol{d}$ applied to the material point in the crystal, which isolates the treatment of rate effects into the threshold stress $\tilde{\tau}$ [54].

Three terms contribute to the threshold stress $\tilde{\tau}$: an athermal term τ_a and strain-rate and temperature sensitive intrinsic stress τ_y and work hardening stress τ_w:

$$\tilde{\tau} = \tau_a + \tau_y\left(\frac{\mu}{\mu_0}\right) + \tau_w\left(\frac{\mu}{\mu_0}\right) \tag{2.4}$$

where μ and μ_0 are the shear moduli at current temperature and reference temperature

(0 Kelvin), respectively. The hardening stress τ_w is approximated by a Voce-type hardening law:

$$\frac{\partial \tau_w}{\partial t} = \sum_{s=1}^{n_{slip}} \theta_0 \left[1 + \frac{\tau_w}{\tau_v} + \frac{\tau_\lambda^{(s)}}{\tau_w} \right]^{\kappa} \left| \dot{\gamma}^{(s)} \right| \tag{2.5}$$

where θ_0 is an initial hardening rate, κ controls the shape of the hardening curve between the initial flow point ($\tau_w = 0$) and the saturation stress τ_v, and $\tau_\lambda^{(s)}$ is a modification for geometric hardening described momentarily. Both the intrinsic stress τ_y and the saturation stress τ_v are related to their reference state values $\hat{\tau}_y$ and $\hat{\tau}_v$ at a zero temperature and reference strain rate through an Arrhenius relation:

$$\tau_* \left(T, \dot{\varepsilon} \right) = \hat{\tau}_* \left\{ 1 - \left[\frac{k_B T}{\mu b^3 g_{0,*}} \ln \left(\frac{\dot{\varepsilon}_{0,*}}{\dot{\varepsilon}} \right) \right]^{\frac{1}{q_*}} \right\}^{\frac{1}{p_*}} \tag{2.6}$$

where the subscript * takes the value y and v and T denotes the absolute temperature. The other parameters are defined as follows: normalized activation energy $g_{0,*}$, reference strain rate $\dot{\varepsilon}_{0,*}$, shape-fitting constants p_* and q_*, magnitude of Burgers vector b, and Boltzmann constant k_B.

The hardening stress $\tau_\lambda^{(s)}$ is the distinguishing feature of the model, which represents the additional resistance to dislocation slip on system (s) due to GND. This term is related to the linear GND density $\lambda^{(s)}/b$ impeding slip on a particular system according to the expression given by [33, 55]:

$$\tau_\lambda^{(s)} = k_0 \frac{\eta^2 \mu^2 b}{2\theta_0} \lambda^{(s)} \tag{2.7}$$

where $\eta = \frac{1}{3}$ and k_0 is a material parameter controlling the hardening from geometrical contributions. The linear dislocation density $\lambda^{(s)}/b$ for each system is determined from the current deformation state through the Nye tensor $\boldsymbol{\alpha}$ as follows:

$$\lambda^{(s)} = \sqrt{\left(\boldsymbol{\alpha}\boldsymbol{n}^{(s)}\right):\left(\boldsymbol{\alpha}\boldsymbol{n}^{(s)}\right)} \tag{2.8}$$

$$\boldsymbol{\alpha} = -\nabla \times \boldsymbol{F}^{e-1} = \epsilon_{ijk} \frac{\partial F^{e-1}_{mj}}{\partial X_i} \boldsymbol{e}_k \otimes \boldsymbol{e}_m \tag{2.9}$$

where ϵ_{ijk} is the permutation symbol and $\boldsymbol{n}^{(s)} = \boldsymbol{R}\boldsymbol{R}^{pT}\tilde{\boldsymbol{n}}^{(s)}$. Nye [38] was the first to relate the elastic incompatibility $\boldsymbol{\alpha}$ at a continuum point to the presence of geometrically arranged dislocations in a small neighborhood.

For small elastic strains (1.7), the inverse of the elastic deformation gradient simplifies to:

$$\boldsymbol{F}^{e-1} = \left(\boldsymbol{V}^e\boldsymbol{R}^e\right)^{-1} \approx \left(\boldsymbol{I}\boldsymbol{R}\boldsymbol{R}^{p-1}\right)^{-1} = \boldsymbol{R}^p\boldsymbol{R}^{-1} = \boldsymbol{R}^p\boldsymbol{R}^T = \boldsymbol{R}^{eT} \tag{2.10}$$

Nonetheless, including the effects of GND on the work hardening stress τ_w (2.5) induces a nonlocal character to the constitutive model. The higher order derivatives of strain (2.9) – (2.10) require special treatment which is addressed by the numerical methods discussed in Section 0.

2.2.2 Finite element approximation: spatial and temporal discretization

These constitutive equations are now employed to pose a boundary value problem over domain $\Omega \subset \mathbb{R}^{n_{sd}}$ during a time interval of interest $\mathbb{I} = [0,T]$. The time-dependent field $\boldsymbol{\phi}(\boldsymbol{X},t) = \boldsymbol{x} \in \mathbb{R}^{n_{sd}}$ characterizes the deformation of body Ω and yields the deformation gradient $\boldsymbol{F} = \partial\boldsymbol{\phi}/\partial\boldsymbol{X}$ appearing in the elastoplastic decomposition (1.7). The equilibrium equation defined on the current configuration $\boldsymbol{\phi}(\Omega,t)$ is stated as follows:

$$\text{div}\,\boldsymbol{\sigma} + \boldsymbol{b} = \boldsymbol{0} \quad \text{in} \quad \boldsymbol{\phi}(\Omega,t) \tag{2.11}$$

$$\boldsymbol{\phi}(\boldsymbol{X},t) = \bar{\boldsymbol{\phi}} \quad \text{on} \quad \boldsymbol{\phi}(\Gamma_u,t) \tag{2.12}$$

$$\boldsymbol{\sigma}\cdot\boldsymbol{n} = \bar{\boldsymbol{t}} \quad \text{on} \quad \boldsymbol{\phi}(\Gamma_\sigma,t) \tag{2.13}$$

where $\mathrm{div}(\bullet)$ is the divergence operator with respect to $\boldsymbol{x}$, $\boldsymbol{b}$ is the external body force vector, $\overline{\boldsymbol{\phi}}$ is the prescribed deformation on the Dirichlet boundary Γ_u, $\overline{\boldsymbol{t}}$ is the prescribed traction on the Neumann boundary Γ_σ, and $\boldsymbol{n}$ is the outward unit normal vector in the current configuration on the domain boundary $\Gamma = \Gamma_u \cup \Gamma_\sigma$.

Using standard arguments from continuum mechanics, the strong form (2.11) - (2.13) can be converted to an equivalent weak form, which is nonlinear due to the kinematics and constitutive model discussed previously. This time-dependent weak form will be solved approximately by employing standard Lagrange finite elements in space and backward Euler integration in time. Hence, we adopt the representation $\boldsymbol{\phi}^h = \mathbf{N}(\boldsymbol{X})\left[\mathbf{X} + \mathbf{d}(t_{n+1})\right]$ for the deformation field, where $\mathbf{N}$ denotes the matrix of global shape functions defined over a set of finite elements $\Omega^e \subseteq \Omega$, $\mathbf{X}$ is the vector of nodal coordinates, and $\mathbf{d}$ is the nodal displacement vector. Also, the time interval $\mathbb{I}$ is divided into a series of time steps $[0, t_1, ..., t_N]$ with (possibly variable) time increment $\Delta t = t_{n+1} - t_n$. Sparing the details (see e.g. [59]), the resulting nonlinear system of equations for the deformation field $\boldsymbol{\phi}^h_{n+1} = \boldsymbol{\phi}^h(\boldsymbol{X}, t_{n+1})$ at a given time step $t_{n+1} \in \mathbb{I}$ is stated as:

$$\mathbf{F}^{\mathrm{ext}}_{n+1} = \mathbf{F}^{\mathrm{int}}_{n+1}, \qquad \mathbf{F}^{\mathrm{ext}}_{n+1} = \int_{\phi(\Omega)} \mathbf{N}^T \mathbf{b}\, \mathrm{d}v + \int_{\phi(\Gamma_\sigma)} \mathbf{N}^T \overline{\mathbf{t}}\, \mathrm{d}a, \qquad \mathbf{F}^{\mathrm{int}}_{n+1} = \int_{\phi(\Omega)} \mathbf{B}^T \boldsymbol{\sigma}_{n+1}\, \mathrm{d}v \tag{2.14}$$

where $\mathbf{B}$ is the matrix of global shape function derivatives in the current configuration, and the external loads $\mathbf{b}$ and $\overline{\mathbf{t}}$ as well as the Cauchy stress $\boldsymbol{\sigma}$ have been converted to column vectors.

In the usual finite element setting, each of the integrals in the nonlinear system (2.14) would be approximated using numerical integration. As such, the internal variables that characterize the material state would be tracked at each Gauss quadrature point within an element Ω^e for evaluating the Cauchy stress $\boldsymbol{\sigma}_{n+1}$ via the time-discrete form of (1.15). However, the dependence of the stress on the Nye tensor $\boldsymbol{\alpha}$ according to (2.7) - (2.9)

induces a nonlocal character and necessitates defining the gradient of the internal variable field $\boldsymbol{R}^e$. Also, either explicit or implicit approximations could be considered for connecting the temporal evolution of these gradient-based terms to the Cauchy stress. Therefore, in the following sections, we will review and propose several numerical treatments for these gradient-based terms within (2.14) both in space and in time.

2.3 Spatial Approaches for Evaluating the Nye Tensor

As mentioned in the previous section, the curl operator appearing in the definition of the Nye tensor (2.9) - (2.10) requires the spatial variation of the elastic rotation tensor $\boldsymbol{R}^e$ across the domain. Therefore, a field approximation is needed for this tensor quantity rather than an internal variable representation. The most mathematically rigorous approach is to employ mixed methods whereby $\boldsymbol{R}^e$ is interpolated as an independent field along with the displacement field. A related method for interpolating the dislocation density of each slip system was proposed by Bayley et al. [43]. However, such mixed methods are very computationally expensive when solved in a monolithic fashion. Also, the GND term involving the Nye tensor within (2.7) is not expected to be the predominant component of the plastic response but rather to contribute primarily to later hardening stages. Therefore, less rigorous numerical approximations are justified, in particular those employing projections of the elastic rotation from discrete integration point values onto a nonlocal field. We consider two classes of methods herein: projections onto elemental fields and projections onto nodal fields.

To simply the notation, we will use the variable $\boldsymbol{Z}$ in place of $\boldsymbol{R}^{eT}$ to denote the transpose of the elastic rotation tensor, which is the field required for evaluating the Nye tensor (2.9). Subscripts will denote the spatial components of the tensor, e.g. Z_{32}. Superscripts will denote the restriction of the quantity to an integration point by using a lower case

letter (e.g. Z_{ij}^{a}), to an element using the letter e, and to a node using an upper case letter (e.g. Z_{ij}^{A}).

2.3.1 Elemental projection of elastic rotation

A simple numerical approximation of the derivative in (2.9) is to perform calculations within individual elements. Namely, the integration point values Z_{ij}^{a} are projected onto discontinuous fields that are defined over each finite element. This class of approaches are historically the first methods applied to gradient plasticity. Examples of elemental projection methods using extrapolation with finite element shape functions include [36, 47, 48, 60].

For the studies herein, we adopt the elemental projection method employed by Messner [15] as a reference for comparing with the nodal methods in the following sections. This method involves a least squares fit of the Gauss point values Z_{ij}^{a} to a linear field within each element, applied separately for each component, as summarized in Box 1. Let Z^{a} denote the value of a particular component (i, j) at Gauss point a, and let ξ^{a} and η^{a} denote the isoparametric coordinates of the Gauss point. The elemental projected field $\bar{Z}(\xi,\eta)$ is represented in terms of three constants to be determined:

$$\bar{Z}(\xi,\eta) = Z^{c} + Z^{\xi}\xi + Z^{\eta}\eta \tag{2.15}$$

These constants are determined through a least-squares fit, such that $\bar{Z}(\xi^{a},\eta^{a}) \approx Z^{a}$ for each Gauss point. Then, the partial derivatives of the elemental projected field are constant over the element: $\partial\bar{Z}/\partial\xi = Z^{\xi}$ and $\partial\bar{Z}/\partial\eta = Z^{\eta}$. These partial derivatives are mapped from the isoparametric space to the physical space using the element Jacobian matrix at each integration point, $\boldsymbol{J}^{a} = \partial\boldsymbol{X}/\partial\boldsymbol{\xi}(\xi^{a},\eta^{a})$. Repeating this process for each

component yields the elemental projected field $\bar{\boldsymbol{Z}}$ and its gradient $\partial\bar{\boldsymbol{Z}}/\partial\boldsymbol{X}$ evaluated at each Gauss point. An example of the projected field for a four-node bilinear element is shown in Figure 2-1.

Box 1. Algorithm for elemental projection

For each tensor component Z_{ij}:

1. Solve for coefficients: $\begin{bmatrix}\mathbf{1} & \boldsymbol{\xi} & \boldsymbol{\eta}\end{bmatrix}^T \begin{bmatrix}\mathbf{1} & \boldsymbol{\xi} & \boldsymbol{\eta}\end{bmatrix}\begin{bmatrix}Z_{ij}^c & Z_{ij}^{\xi} & Z_{ij}^{\eta}\end{bmatrix}^T = \begin{bmatrix}\mathbf{1} & \boldsymbol{\xi} & \boldsymbol{\eta}\end{bmatrix}^T \begin{bmatrix}\mathbf{Z}_{ij}\end{bmatrix}$

2. Compute constant gradients: $Z_{ij,X} = Z_{ij}^{\xi}\xi_{,X} + Z_{ij}^{\eta}\eta_{,X}$ and $Z_{ij,Y} = Z_{ij}^{\xi}\xi_{,Y} + Z_{ij}^{\eta}\eta_{,Y}$

The primary advantage of the elemental projection is its simplicity. Algorithmically, the calculations remain local to each finite element, which means that the method is usually easy to implement within element-based finite element codes. This simple approximation to the contribution of GND has captured the grain size dependent features exhibited in experiments [15, 36, 47, 48].

However, the linear field $\bar{\boldsymbol{Z}}$ possesses only a nonzero first derivative and therefore cannot be applied to higher-order gradient theories, such as the dislocation-based back-stress formulation of [43] for fatigue modeling. The method also does not apply to linear triangular and tetrahedral elements since the stress field and therefore quadrature values Z_{ij}^a are constant. Note that linear triangular elements typically exhibit volumetric locking when modeling incompressible plastic flow. Such locking may be alleviated by utilizing mixed methods or patch-based enhanced strain methods; see [61, 62] and references therein.

Additionally, studies for a polycrystalline specimen under tension by Cheong et al. [48] have indicated mesh sensitivity with respect to the grain size. Those authors suggest that

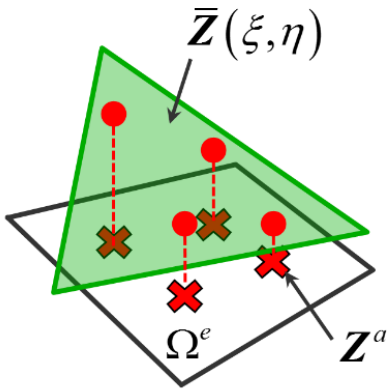

Figure 2-1. Elemental projection of elastic rotation $\boldsymbol{Z}$

the sensitivity arises because the element diameter provides the length scale within this projection method. However, the results from Dia [47] for 2D examples do not indicate a sensitivity between mesh size and grain size. Other studies have shown [63] that substantial numbers of finite elements per grain may be required to resolve heterogeneous deformation and reorientation, irrespective of the contributions from GND. To analyze these sensitivity issues, we conduct a convergence rate study for the elemental projection method in Section 5.1.

2.3.2 Nodal projection of elastic rotation

As an alternative to the elemental projection, the integration point values Z_{ij}^a can be projected onto a globally smooth field defined from the nodal shape functions of the domain mesh. Then to evaluate the Nye tensor (2.9), the Lagrange shape functions are differentiated to obtain directly the field's derivative within each element. Examples of nodal projections include the patch recovery methods [22, 49, 64] [50, 51] and the global L^2 methods of Ortiz and Quigley [53] and Mota et al. [52].

Our proposed nodal projection method [56] builds upon the work by Mota et al. [52], but the distinguishing feature is that a lumped approximation of the projection matrix is utilized in order to minimize the cost of the calculations. Let the globally smooth field for the rotation tensor $\tilde{\boldsymbol{Z}}$ be interpolated using the same Lagrange shape functions as used for the deformation field $\boldsymbol{\phi}^h$:

$$\tilde{Z}_{ij}\left(\boldsymbol{X}\right) = \sum_{A=1}^{n_{umnp}} N^A\left(\boldsymbol{X}\right)\tilde{Z}_{ij}^A \tag{2.16}$$

where n_{umnp} is the number of nodes in the mesh and N^A are the shape functions appearing in the matrix $\mathbf{N}$ within the discrete form (2.14). Then the L^2 projection of the integration point values $\boldsymbol{Z}^a$ onto the field $\tilde{\boldsymbol{Z}}$ is expressed through the following integral equation (posed in the reference configuration) [52, 53]: find $\tilde{\boldsymbol{Z}} \in \mathcal{V}^h$ such that for all $\boldsymbol{\zeta} \in \mathcal{V}^h$:

$$\int_\Omega \boldsymbol{\zeta} : \left(\tilde{\boldsymbol{Z}} - \boldsymbol{Z}\right) \mathrm{d}V = 0 \tag{2.17}$$

with the discrete functional space $\mathcal{V}^h \subset \mathcal{V}$ defined in terms of the Sobolev space $H^1\left(\Omega\right)$ of functions with square-integrable derivatives:

$$\mathcal{V}^h \subset \mathcal{V} = \left[H^1\left(\Omega\right)\right]^{n_{sd1}\times n_{sd1}} \tag{2.18}$$

A representation of the tensor quantities $\boldsymbol{Z}$ and $\tilde{\boldsymbol{Z}}$ is shown in Figure 2-2 on a small mesh. Fortunately, the integral (2.17) can be evaluated directly using the same quadrature points as for the internal force vector in (2.14), which are exactly the locations where $\boldsymbol{Z}^a$ is defined. Substituting the quadrature formulas yields the following expression:

$$\sum_{B=1}^{n_{unmp}} \sum_{A=1}^{n_{unmp}} \boldsymbol{\zeta}^B : M^{AB}\tilde{\boldsymbol{Z}}^A = \sum_{B=1}^{n_{unmp}} \boldsymbol{\zeta}^B : \boldsymbol{F}^B \tag{2.19}$$

$$M^{BA} = \sum_{e=1}^{n_{el}} \sum_{a=1}^{n_{\mathrm{int}}} N^B\left(\boldsymbol{X}^{ea}\right) N^A\left(\boldsymbol{X}^{ea}\right) j^{ea} w^{ea} \tag{2.20}$$

$$\boldsymbol{F}^B = \sum_{e=1}^{n_{el}} \sum_{a=1}^{n_{\mathrm{int}}} N^B\left(\boldsymbol{X}^{ea}\right) j^{ea} w^{ea} \boldsymbol{Z}^{ea} \tag{2.21}$$

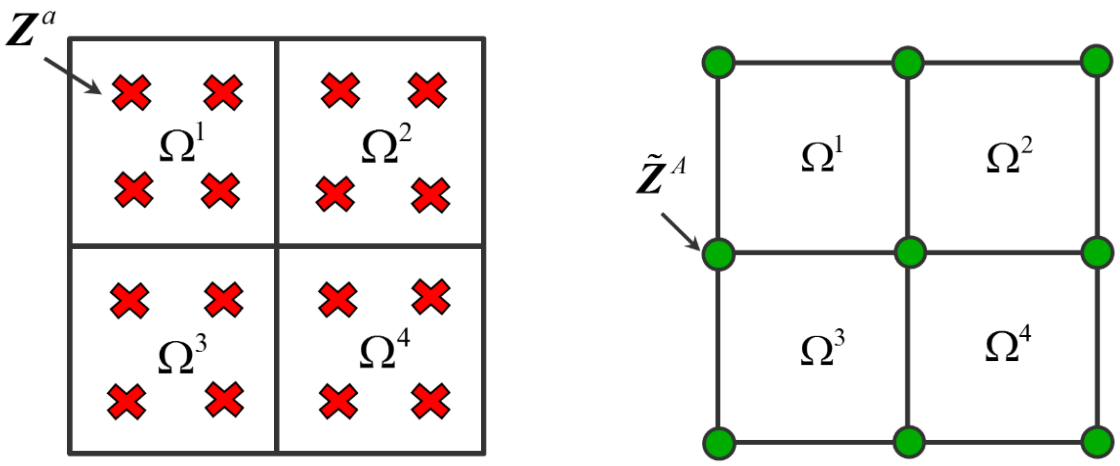

(a) (b)

Figure 2-2. Nodal projection of elastic rotation: (a) initial values $\boldsymbol{Z}^a$ at Gauss points; (b) projected field $\tilde{\boldsymbol{Z}}^A$ at nodes

where the test function $\boldsymbol{\zeta} \in \mathcal{V}^h$ has been represented using the same shape functions as in (2.16). The matrices in (2.20) and (2.21) are evaluated using the typical assembly operation over elements and integration points, where $j^{ea} = \det\left(\boldsymbol{J}\left(\boldsymbol{X}^{ea}\right)\right)$ denotes the determinant of the Jacobian matrix and w^{ea} denotes the quadrature weight at the integration point. In particular, the matrix M^{BA} has the same form as the consistent mass matrix in elastodynamics problems, and it is usually non-diagonal because of the product $N^B N^A$ between different shape functions. Thus, the solution of (2.19) involves the factorization of M^{BA}, which greatly increases the cost of the method compared to the elemental projection in Section 2.3.1. Therefore, we adopt a lumped approximation of the mass matrix M^{BA} to simplify the calculation of the nodal projection. The HRZ lumping method [65] is chosen such that the lumped mass matrix contains all positive terms even for higher order finite elements. This method involves computing the element mass matrix, dropping the off-diagonal terms, and scaling the diagonal terms such that mass of the element is maintained. The lumped approximation of (2.20) is then given by:

$$m_e^{BA} = \sum_{a=1}^{n_{\text{int}}} N^B\left(\boldsymbol{X}^{ea}\right) N^A\left(\boldsymbol{X}^{ea}\right) j^{ea} w^{ea} \tag{2.22}$$

$$M_e = \sum_{B=1}^{n_{unmp}} \sum_{A=1}^{n_{unmp}} m_e^{BA}\ ,\ \tilde{M}_e = \sum_{A=1}^{n_{unmp}} m_e^{AA} \tag{2.23}$$

$$\tilde{m}_e^{BA} = \begin{cases} 0 & A \neq B \\ m_e^{AA}\left(M_e / \tilde{M}_e\right) & A = B \end{cases},\ \tilde{M}^{BA} = \sum_{e=1}^{n_{el}} \tilde{m}_e^{BA} \tag{2.24}$$

Due to the diagonal form of $\tilde{M}^{BA}$, the solution of (2.19) takes a simplified form:

$$\tilde{\boldsymbol{Z}}^A = \boldsymbol{F}^A / \tilde{M}^{AA} \qquad \text{for each } A = 1,...,n_{umnp} \tag{2.25}$$

These nodal coefficient tensors $\tilde{\boldsymbol{Z}}^A$ are substituted into (2.16) to provide the definition of the nodal projection field, which can be differentiated to yield the components for evaluating the Nye tensor (2.9):

$$\frac{\partial \tilde{\boldsymbol{Z}}}{\partial \boldsymbol{X}}\left(\boldsymbol{X}\right) = \sum_{A=1}^{n_{umnp}} \frac{\partial N^A}{\partial \boldsymbol{X}}\left(\boldsymbol{X}\right) \otimes \tilde{\boldsymbol{Z}}^A \tag{2.26}$$

Since the definition of the mass matrix is time-independent, the values from (2.22) –(2.24) may be precomputed at the start of an analysis and recalled from memory for use in evaluating the nodal projection at each time step. Thus, the evaluation of the Nye tensor from the nodal projection involves a classical gather-scatter operation: a loop over all elements to gather the nodal values $\tilde{\boldsymbol{Z}}^A$ using (2.25), and a second loop over all elements to evaluate the derivatives at the integration point locations $\boldsymbol{X}^{ea}$ using (2.26). The impact on solution accuracy by using a consistent or lumped form of the projection matrix is assessed numerically in Section 2.5.3.

Remark: *When the crystallographic orientation is different between two elements (such as along a grain boundary), the elastic rotation field is not necessarily expected to be continuous in the physical specimen. The elemental projection naturally accommodates such discontinuities. However, the nodal projection or patch recovery techniques will result in a continuous field unless special care is taken. In the present studies, we allow*

independent nodal values for the rotation field along grain boundaries by assembling the mass matrix contributions to separate degrees of freedom for elements along grain boundaries.

2.3.3 Preserving rotation tensor orthogonality using Lie group-algebra relations

Although the projection methods in the preceding sections are conceptually straightforward, an important issue has been ignored regarding a property of the elastic rotation tensor $\boldsymbol{R}^e$. Recall that rotation tensors are members of the space of orthonormal tensors $SO(3)$:

$$SO(3) = \left\{ \boldsymbol{A} \middle| \boldsymbol{A}\boldsymbol{A}^T = \boldsymbol{I},\ \det \boldsymbol{A} = 1 \right\} \tag{2.27}$$

As observed by Mota et al. [52], this space of tensors is not closed under addition, meaning that the sum of two orthonormal tensors is not necessarily orthonormal. Rather, $SO(3)$ is closed under multiplication and therefore can be characterized as a Lie group.

The implication is that the interpolation formulas (2.15) and (2.16) will produce tensor fields that are not orthonormal everywhere. For example, the values $\tilde{\boldsymbol{Z}}^A$ produced by the linear combination as well as their interpolation back to the integration points (2.16) may not be orthonormal tensors. This loss of orthogonality does not invalidate the numerical method because we do not employ the projected field $\bar{\boldsymbol{Z}}$ or $\tilde{\boldsymbol{Z}}$ within the constitutive equations such as the rotation update formula (1.17); rather, the integration point values $\boldsymbol{Z}^a$ are retained for all computations requiring the rotation. Nonetheless, this issue may upset the accuracy of the Nye tensor $\boldsymbol{\alpha}$ computed from the projected field and subsequently bias the evolution of the geometric hardening contribution from the GND term (2.7).

A resolution to this interpolation issue is proposed by Mota et al. [52], who recognized that each Lie group has an associated Lie algebra which is closed under the operation of addition. In the case of orthonormal tensors, the associated Lie algebra is the space of skew tensors $so(3)$:

$$so(3) = \left\{ \boldsymbol{A} \middle| \boldsymbol{A}^T = \boldsymbol{A} \right\} \tag{2.28}$$

Observe that the sum of any two skew tensors $\boldsymbol{A}, \boldsymbol{B} \in so(3)$ results in a skew tensor $\boldsymbol{C} = \boldsymbol{A} + \boldsymbol{B} \in so(3)$. Therefore, the interpolation operations (2.15) and (2.16) apply naturally to skew tensors. With these motivations, we adopt a modified procedure for evaluating the Nye tensor field $\boldsymbol{\alpha}$.

First, the values for the elastic rotation tensor $\boldsymbol{Z}^a$ are mapped from the Lie group $SO(3)$ into the Lie algebra $so(3)$ by applying the tensor logarithm:

$$\boldsymbol{z}^a = \ln\left(\boldsymbol{Z}^a\right) \tag{2.29}$$

The resulting skew tensors $\boldsymbol{z}^a$ at each integration point are then carried through the remainder of the nodal projection method described in Section 3.2, arriving at a nodal field $\tilde{\boldsymbol{z}}(\boldsymbol{X})$ according to (2.16) and (2.25). Finally, the value of the smoothed elastic rotation tensor field $\tilde{\boldsymbol{Z}}(\boldsymbol{X})$ at any point is obtained by applying the tensor exponential to the skew tensor field $\tilde{\boldsymbol{z}}(\boldsymbol{X})$:

$$\tilde{\boldsymbol{Z}}(\boldsymbol{X}) = \exp\left(\tilde{\boldsymbol{z}}(\boldsymbol{X})\right) \tag{2.30}$$

since the exponential operator is the inverse map from the Lie algebra $so(3)$ to the Lie group $SO(3)$.

However, the gradient of the elastic rotation is required for evaluating the Nye tensor $\boldsymbol{\alpha}$ according to (2.9). Therefore, we proceed one step further than the procedure in [52] and directly differentiate the mapped-projected field expressed in (2.30):

$$\nabla\tilde{\boldsymbol{Z}}\left(\boldsymbol{X}\right)=\nabla\left[\exp\left(\tilde{\boldsymbol{z}}\left(\boldsymbol{X}\right)\right)\right]=\frac{\partial\exp\tilde{\boldsymbol{z}}}{\partial\tilde{\boldsymbol{z}}}:\frac{\partial\tilde{\boldsymbol{z}}}{\partial\boldsymbol{X}} \tag{2.31}$$

The value of the tensor exponential derivative $\partial\exp\tilde{\boldsymbol{z}}/\partial\tilde{\boldsymbol{z}}$ can be evaluated by several numerical schemes, see e.g. [52, 66]. Applying (2.31) at each integration point $\boldsymbol{X}_a$ in element Ω^e provides the approximation for the Nye tensor $\boldsymbol{\alpha}$ and the linear dislocation density $\lambda^{(s)}$, completing the constitutive description. The complete procedure combined with the steps in Section 3.2 are summarized in Box 2.

Compared to the elemental projection, the advantage of the nodal approach lies in the rigor of the numerical approximation. Namely, the entire rotation tensor $\boldsymbol{R}^e$ is interpolated as a single entity with the orthonormal property preserved. The component-wise calculations of the elemental projection method can never be expected to preserve such properties of the entire tensor. Also, the zone of support for the nodal projection spans many elements, so the numerical approximation of the GND term (2.7) is not tied as closely to the mesh size as is the case for the elemental projection method, lessening the possibility for mesh sensitivity issues. Also, the nodal projection method accommodates higher-order interpolation functions, which can be useful for evaluating higher-order derivatives as needed for extended constitutive models such as [43].

Remark: *According to Mota et al.* [52]*, this algorithm is capable of representing spatially uniform fields exactly and also yields stable interpolations without spurious oscillations.*

2.4 Temporal Representation of Rate-Dependent Terms

With the spatial discretization of the strain gradient GND terms from Section 0 in hand, we now turn to the temporal discretization of the constitutive rate equations. Both explicit and implicit time integration may be considered for the various material and kinematic quantities in the MTS model, and this choice affects the accuracy, robustness, and

Box 2. Algorithm for nodal projection

1. Logarithmic map using (2.29): $\boldsymbol{z}^a = \ln\left(\boldsymbol{Z}^a\right)$ for each $a = 1,\ldots, n_{\text{int}}$

2. Assembly using (2.21) – (2.24): $\tilde{M}^{AA} = \sum_{e=1}^{n_{el}} m_e^{AA}\left(M_e / \tilde{M}_e\right)$ and

$$\boldsymbol{f}^A = \sum_{e=1}^{n_{el}} \sum_{a=1}^{n_{\text{int}}} N^A\left(\boldsymbol{X}^{ea}\right) j^{ea} w^{ea} \boldsymbol{z}^{ea}$$

3. Compute nodal values using (2.25): $\tilde{\boldsymbol{z}}^A = \boldsymbol{f}^A / \tilde{M}^{AA}$ for each $A = 1,\ldots, n_{umnp}$

4. Evaluate derivative using (2.26): $\tilde{z}^a_{ij,k} = \sum_{A=1}^{n_{umnp}} \tilde{z}^A_{ij} N^A_{,k}\left(\boldsymbol{X}^a\right)$ for each $a = 1,\ldots, n_{\text{int}}$

5. Differentiate exponential map: $H^a_{ijkl} = \left[\partial \exp \tilde{\boldsymbol{z}} / \partial \tilde{\boldsymbol{z}}\right]_{ijkl}$ at $\tilde{z}_{ij}\left(\boldsymbol{X}^a\right) = \sum_{A=1}^{n_{umnp}} \tilde{z}^A_{ij} N^A\left(\boldsymbol{X}^a\right)$

6. Compute rotation gradient using (2.31): $\tilde{Z}^a_{ij,k} = H^a_{ijmn} \tilde{z}^a_{mn,k}$ for each $a = 1,\ldots, n_{\text{int}}$

stability properties of the resulting numerical model. Examples of formulations using explicit integration for both the stress and internal variable fields are the works of Lee et al. [67] and Bittencourt [68], which are suitable for dynamic applications with higher strain rates. Herein, we follow [15, 18, 69, 70] and adopt a mid-point rule for evaluating the unrotated deformation rate $\boldsymbol{d}$ and a backward Euler scheme for evaluating the unrotated Cauchy stress $\boldsymbol{t}$ and threshold stress $\tilde{\tau}$. This implicit treatment yields improved stability and accuracy across larger time step sizes Δt compared to explicit methods. However, the plastic rotation $\boldsymbol{R}^p$ and Nye tensors $\boldsymbol{\alpha}$ may be treated in an explicit or implicit fashion. Thus, the time-discrete counterparts of the objective stress rate (1.16), hardening relation (2.5), and plastic rotation evolution (1.17) can be expressed in a generic sense as follows:

$$\boldsymbol{t}_{n+1} = \boldsymbol{t}_n + \Delta\boldsymbol{t}_n, \;\; \Delta\boldsymbol{t}_n^i = f\left(\Delta\boldsymbol{d}_{n+1/2}, \boldsymbol{t}_{n+1}, \tilde{\tau}_{n+1}, \boldsymbol{R}^p_{n+\beta}, \boldsymbol{\alpha}_{n+\beta}\right) \tag{2.32}$$

$$\tilde{\tau}_{n+1} = \tilde{\tau}_n + \Delta\tilde{\tau}_n, \qquad \Delta\tilde{\tau}_n = g\left(\Delta\boldsymbol{d}_{n+1/2}, \boldsymbol{t}_{n+1}, \tilde{\tau}_{n+1}, \boldsymbol{R}^p_{n+\beta}, \boldsymbol{\alpha}_{n+\beta}\right) \tag{2.33}$$

$$\boldsymbol{R}^p_{n+1} = \exp\left(\Delta\overline{\boldsymbol{w}}^p_{n+\beta}\right)\cdot\boldsymbol{R}^p_n, \qquad \Delta\overline{\boldsymbol{w}}^p_{n+\beta} = h\left(\Delta\boldsymbol{d}_{n+1/2}, \boldsymbol{t}_{n+1}, \tilde{\tau}_{n+1}, \boldsymbol{R}^p_{n+\beta}, \boldsymbol{\alpha}_{n+\beta}\right) \tag{2.34}$$

$$\boldsymbol{\alpha}_{n+1} = \left[-\nabla\times\boldsymbol{R}^{e-1}_{n+1}\right] = \left[-\nabla\times\left(\boldsymbol{R}^T_{n+1}\boldsymbol{R}^p_{n+1}\right)\right] \tag{2.35}$$

where the functions f, g, h denote the rate terms from the aforementioned equations, and β is a parameter denoting the explicit $(\beta = 0)$ or implicit $(\beta = 1)$ treatment of $\boldsymbol{R}^p$. The unrotated deformation increment $\Delta\boldsymbol{d}_{n+1/2}$ at the intermediate time $t_{n+1/2}$ is defined in terms of the spatial strain increment associated with the nodal displacement $\mathbf{d}_{n+1}$ and $\mathbf{d}_n$ and the rotation tensor $\boldsymbol{R}_{n+1/2}$; see [69, 70] for more details. All other quantities, such as the internal force vector $\mathbf{F}^{\text{int}}_{n+1}$, are evaluated at time level t_{n+1}. This mid-point rule enables the stress update (2.32) to be performed exactly as in the small strain context, with the slip rates $\dot{\gamma}^{(s)}$ evaluated through (1.12) using $\Delta\boldsymbol{d}_{n+1/2}$ in place of $\boldsymbol{d}$. The square brackets in (2.35) symbolize the use of either the elemental projection or nodal projection to obtain a nonlocal representation of the elastic rotation field $\boldsymbol{R}^e$ for evaluating the curl operator.

Note that the elastic rotation $\boldsymbol{R}^e$ is obtained at each Gauss point from the product of the polar decomposition rotation tensor $\boldsymbol{R}$ and the plastic rotation $\boldsymbol{R}^p$ as shown in (2.10) prior to applying the algorithms from Section 0.

The explicit and implicit algorithms for $\boldsymbol{R}^p$ are described in the following sections, and their implications on accuracy will be assessed in Section 2.5.

2.4.1 Explicit integration through post process procedure

Previous numerical implementations of the MTS model [15, 18] have adopted explicit treatment for $\boldsymbol{R}^p$ and $\boldsymbol{\alpha}$, which was justified for modeling problems where the evolution of GND during Stage IV hardening has slower time scales compared to the primary hardening in Stages I-III.

A schematic of the algorithmic solution procedure combining (2.32) – (2.35) with the global equilibrium equation (2.14) is presented in Box 3 for proceeding from step n to $n+1$. The nonlinear equilibrium equation is solved iteratively using the Newton-Raphson algorithm, where the single iteration counter is denoted by i. Crucially, the plastic rotation $\boldsymbol{R}_n^p$ and Nye tensor $\boldsymbol{\alpha}_n$ are held frozen at their values from the previous time step n during all iterations. The other arguments, summarized by the variable $\boldsymbol{\chi}_{n+1}^i = \left\{\Delta \boldsymbol{d}_{n+1/2}^i, \boldsymbol{t}_{n+1}^i, \tilde{\tau}_{n+1}^i\right\}$, are updated within the equilibrium iteration loop. The computation of the internal force vector $\mathbf{F}_{n+1}^{\text{int},i}$ occurs in the usual manner by a loop over all Gauss points in the mesh. The stress update (2.32) and hardening update (2.33) are a coupled set of nonlinear equations which are solved by a local Newton algorithm at each Gauss point; see [18] for details on these local solvers and the expression for the tangent moduli required for the global stiffness matrix $\mathbf{K}_{n+1}^i$.

Box 3. Explicit material update procedure

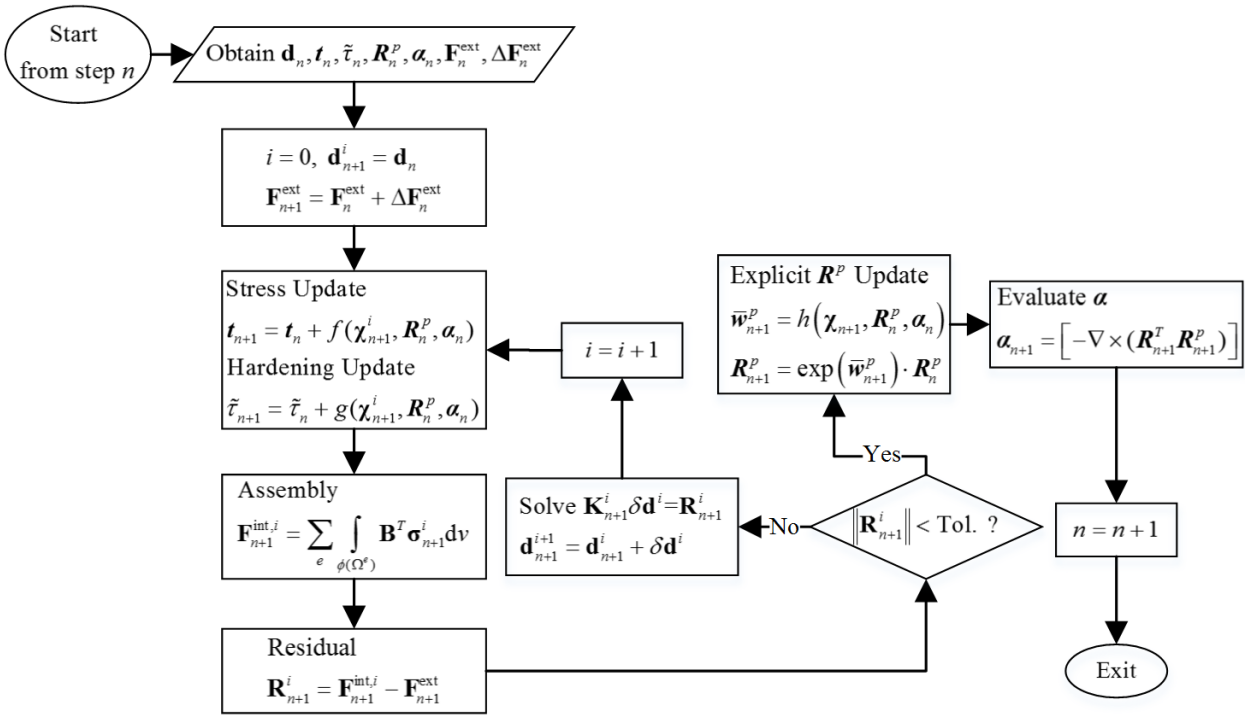

Once the balance of external and internal forces is achieved within a specified tolerance, the equilibrium iteration loop is terminated. Then, a post-process procedure is invoked to compute the plastic rotation $\boldsymbol{R}^p$ and Nye tensor $\boldsymbol{\alpha}$ using the converged displacements and stresses, amounting to an explicit computation. First, the plastic rotation tensor is evaluated at each Gauss point using (2.34). Then, either the elemental or nodal projection method can be employed to compute the $\boldsymbol{\alpha}$ field, which is interpolated back to the Gauss points. These values are then retained for use in the following load step.

Clearly, the benefit of explicit integration is that the number of self-consistent equations is limited to the displacement and stress fields, thereby speeding up the calculations. Because the update of rotations is performed outside of the Newton loop, this method fits naturally within the standard implementation of nonlinear finite element codes. Also, the definition of the tangent stiffness matrix $\mathbf{K}^i_{n+1}$ is simplified since the linearization does not need to take account of variations in the elastic rotation and Nye tensors. However, this post-processing procedure results in a hybrid explicit/implicit approach with certain kinematic quantities lagging behind by one-time step. Also, the assumption of slowly varying rotations places a restriction on the size of the loading increment to maintain stability and accuracy of the computed response. Addressing this issue by reducing the load step size can increase the overall computational cost across the greater number of load steps.

2.4.2 Implicit integration through staggered procedure

To obtain a fully implicit algorithm, we can transfer the computation stage for the plastic rotation and Nye tensors inside of the equilibrium Newton-Raphson loop. As shown in Box 4, this amounts to an expanded material update phase during which the stress $\boldsymbol{t}_{n+1}$,

Box 4. Staggered implicit material update through subcycling

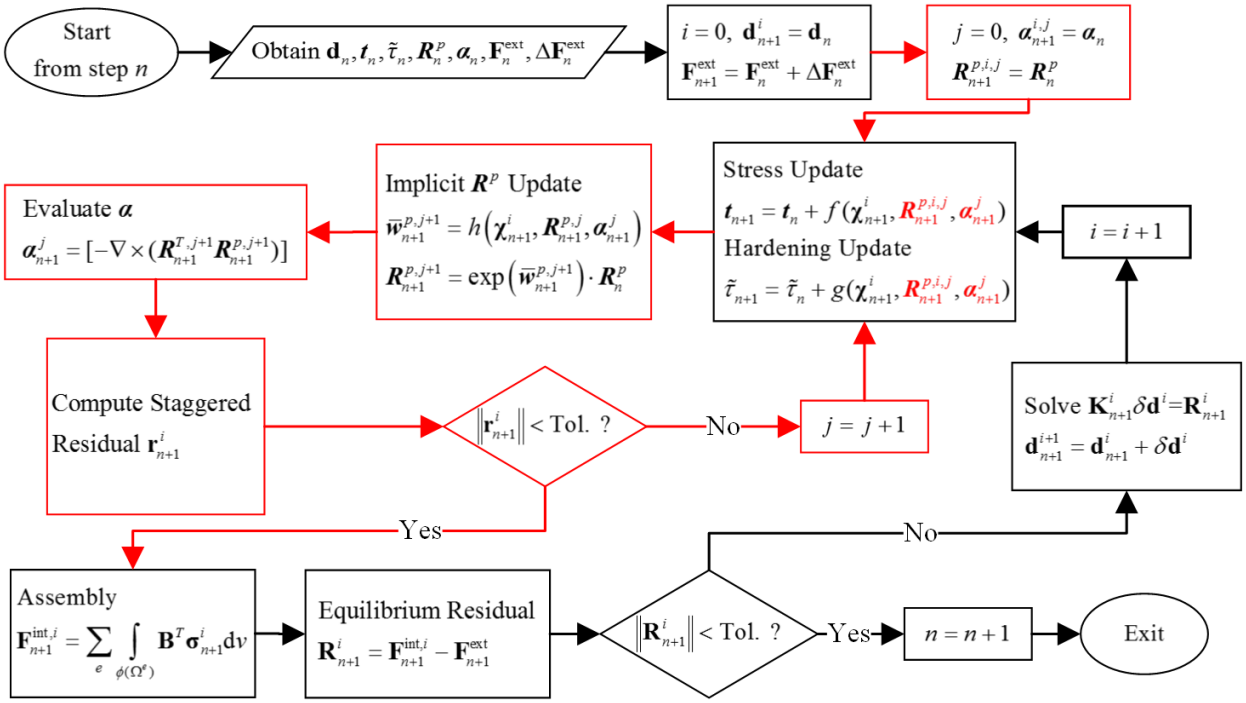

hardening $\tilde{\tau}_{n+1}$, rotation $\boldsymbol{R}^{p}_{n+1}$, and Nye tensor $\boldsymbol{\alpha}_{n+1}$ are made self-consistent with the current nodal displacement increment $\Delta\mathbf{d}^{i}_{n+1}$. However, solving the four equations (2.32) – (2.35) concurrently would require major revisions to the stress/hardening update framework at the Gauss point level. Therefore, this set of equations is solved in a staggered fashion using a fixed point algorithm.

The fixed point material update procedure contained within the red outlined steps within Box 4 essentially alternates between the Gauss point stress update and the Nye tensor methods from Section 2.2. Each pass through the alternation is termed herein as a "subcycle" and is denoted by a counter j. We discuss the procedure within the context of the nodal projection method from Section 2.3.2; the steps are simplified for the elemental projection. First, the stress update is performed to obtain $\boldsymbol{\chi}^{j+1}_{n+1}$ at each Gauss point using frozen values for $\boldsymbol{R}^{p,j}_{n+1}$ and $\boldsymbol{\alpha}^{j}_{n+1}$, which is identical to the process in Section 2.4.1. Then, we perform a second pass through the Gauss points to evaluate (2.34) to obtain $\boldsymbol{R}^{p,j+1}_{n+1}$ for use in the projection (2.35). Here, the values of $\boldsymbol{t}^{j+1}_{n+1}$ and $\tilde{\tau}^{j+1}_{n+1}$ are kept frozen. Also, since the plastic vorticity $\boldsymbol{W}^{p}$ (1.12) depends on the slip rates $\dot{\gamma}^{(s)}$ (2.1) and thus upon the resolved shear stress $\tau^{(s)}$ (2.2) in the current configuration, expression (2.34) is nonlinear in terms of $\boldsymbol{R}^{p,j+1}_{n+1}$, which can be solved locally via fixed point or Newton's method. Finally, the nodal projection method is applied to the elastic rotation tensor $\boldsymbol{R}^{eT,j+1}_{n+1} = \boldsymbol{R}^{T}_{n+1}\boldsymbol{R}^{p,j+1}_{n+1}$ to compute the Nye tensor $\boldsymbol{\alpha}^{j+1}_{n+1}$ as discussed in Section 2.3.2. Note that the polar decomposition rotation $\boldsymbol{R}_{n+1}$ is fixed during each of the subcycles since the unrotated deformation increment $\Delta\boldsymbol{d}^{i}_{n+1/2}$ is also fixed (the superscript i has been suppressed for clarity).

After the subcycle is completed, the values of the Cauchy stress, hardening parameter, and elastic rotation are compared with those from the previous subcycle. If the computed difference is above a specified tolerance, then a new subcycle is performed, first using

$\boldsymbol{R}_{n+1}^{p,j+1}$ and $\boldsymbol{\alpha}_{n+1}^{j+1}$ within the stress update followed by $\boldsymbol{t}_{n+1}^{j+1}$ and $\tilde{\tau}_{n+1}^{j+1}$ within the rotation update. We have adopted the following three quantities within the convergence criteria (denoted by $\left\|\mathbf{r}_{n+1}^{j}\right\|$) for the fixed point material update, where the tolerance is set to $\varepsilon = 10^{-7}$ and $\|\bullet\|_{l^2}$ denotes the Euclidean norm:

1. Nodal values of elastic rotation $\tilde{\boldsymbol{r}}_A$: $\sum_A \left\|\tilde{\boldsymbol{r}}_A^{e,j+1} - \tilde{\boldsymbol{r}}_A^{e,j}\right\|_{l^2}^2 \le \varepsilon^2 \sum_A \left\|\tilde{\boldsymbol{r}}_A^{e,0}\right\|_{l^2}^2$
2. Gauss point values of stress $\boldsymbol{\sigma}$: $\sum_a \left\|\boldsymbol{\sigma}_a^{j+1} - \boldsymbol{\sigma}_a^{j}\right\|_{l^2}^2 \le \varepsilon^2 \sum_a \left\|\boldsymbol{\sigma}_a^{0}\right\|_{l^2}^2$
3. Gauss point values of hardening $\tilde{\tau}$: $\sum_a \left|\tilde{\tau}_a^{j+1} - \tilde{\tau}_a^{j}\right|^2 \le \varepsilon^2 \sum_a \left|\tilde{\tau}_a^{0}\right|^2$

When these convergence criteria are met, then the values $\boldsymbol{t}_{n+1}$, $\tilde{\tau}_{n+1}$, $\boldsymbol{R}_{n+1}^{p}$, $\boldsymbol{\alpha}_{n+1}$ have simultaneously solved the implicit rate equations (2.32) – (2.35) and thus are self-consistent. The value of the Cauchy stress $\boldsymbol{\sigma}_{n+1}$ is then available for assembly of the internal force vector, and the remaining portion of the Newton-Raphson equilibrium iteration proceeds unchanged with respect to Box 3 and Box 4.

The aforementioned staggered procedure has several advantages over other possible implicit schemes. First, the Gauss point stress update and nodal projection method have remained isolated, which minimizes the burden to implement the method in existing codes. Also, the size of the global stiffness matrix has not expanded, which would be necessary for monolithic solution of mixed formulations such as those advocated in [43]. Rather, the self-consistent field values are obtained through sequential passes through the material update algorithm. Also, the stress update phase as well as the nodal projection method are highly parallelizable, making the staggered algorithm suitable for high performance computing platforms. Finally, if the number of equilibrium iterations does not increase (e.g. if the effects of the Nye tensor on the linearization are neglected in the calculation of the stiffness matrix $\mathbf{K}_{n+1}^{i}$), then the overall cost of the method is comparable with the

hybrid explicit method presented in Section 2.4.1. The only additional runtime would come from the multiple passes through the stress update phase per Newton iteration.

The main disadvantage of the staggered procedure as presented is that the convergence rate of the subcycles is limited by the use of the fixed point algorithm. Therefore, we investigate the robustness of the fixed point algorithm in Section 2.5 for several numerical tests. The Newton algorithm could possibly be used to improve the stability of the staggered procedure; however, the linearization of the nodal projection method is not straightforward. From the numerical studies that follow, the typical number subcycles required for convergence is 5 to 6. This higher computational time during the material update is likely overshadowed by the factorization of the stiffness matrix for large-scale problems.

Remark: *Observe that a shuffling of the steps for the explicit algorithm in* Box 3 *would unify the implementation of both algorithms. Namely, if the rotation tensor update and evaluation of the Nye tensor are performed at the end of the stress update during each iteration, then these quantities would be prepared for use in the subsequent time step. This minimizes the revisions to the program architecture and enables a switch between the explicit and implicit algorithms simply by limiting the number of subcycles to 1. The tradeoff is that the calculated values are simply overwritten during Newton iterations prior to equilibrium convergence.*

Remark: *At the start of the staggered material update during each equilibrium iteration, the initial values of the plastic rotation* $\boldsymbol{R}_{n+1}^{p,0}$ *and Nye tensor* $\boldsymbol{\alpha}_{n+1}^{0}$ *are assigned from the previous time step,* $\boldsymbol{R}_{n}^{p}$ *and* $\boldsymbol{\alpha}_{n}$*. Alternatively, the values could be initialized from the values obtained at the end of the material update during the previous equilibrium iteration, e.g.* $\boldsymbol{R}_{n+1}^{p,i-1}$ *and* $\boldsymbol{\alpha}_{n+1}^{i-1}$*. However, the physical domain is not necessarily equilibrated during the previous iteration, and thus each of the field quantities likely contains errors. These errors could bias the staggered material update to converge to a nonphysical branch of the*

material response. Similar arguments also justify retaining the Cauchy stress and hardening variables from the previous step to initialize the stress update procedure [59].

2.5 Numerical Results

In this section, we investigate the accuracy, robustness and stability of each aspect of the proposed nodal projection formulation with Lie algebra mapping against the baseline elemental projection method [15] for three test cases. The first two problems simulate a single crystal using linear shape functions: the first employs a two-dimensional mesh of rectangular elements whilst the second employs a three-dimensional mesh of hexahedral elements. The third problem simulates the behavior of a polycrystalline material using quadratic triangular elements. All elements are fully integrated using Gauss quadrature. Different features of the methods are investigated for each problem. The convergence of the elemental projection method versus the nodal projection is investigated in the first problem through a mesh refinement study. The second problem tests the robustness and stability of the explicit and implicit integration strategies by subjecting a specimen to multi-directional loading and unloading with large load increments and reporting the required number of Newton-Raphson iterations. Lastly, the third problem illustrates the behavior of the formulations for a polycrystalline domain modeled with quadratic finite elements while comparing the lumped approximation of the projection matrix to the one with full information. Numerical simulations were conducted using a Matlab finite element code with the refined solutions computed using research code WARP3D [71].

2.5.1 Flexure loading and size effect

For this problem, the bending of a single crystal strip subjected to monotonically increasing rotations is investigated. A schematic of the beam is shown in Figure 2-3. The

bending of single-crystal aluminum specimens was studied experimentally by [72] and has been computationally modeled using a discrete dislocation dynamics approach [73] and a continuum crystal plasticity model [74]. In particular, the beam bending induces non-zero strain gradients that give rise to higher yield stress or strain hardening. Presently, our objective is to quantify the domain size effect produced by the GND term in equation (2.7) as well as to test the numerical convergence of the nodal projection method compared to the elemental one as discussed in 2.3.1.

Two domain sizes are considered: a smaller beam with $L = 12$ μm and $h = 4$ μm and a larger beam with $L = 48$ μm and $h = 16$ μm. In both cases, different levels of refinement for the FE meshes are employed, with the coarsest mesh containing 12×4 trilinear hexahedral elements and another three levels of refined meshes are obtained by uniform bisection, with one element through the thickness $t = 1$ μm. The solution obtained on a refined 384×128 elements mesh is taken as the reference solution for evaluating the norms of displacement error and considered to be fine enough such that the dominant elasto-plastic response of the beam is accurately captured. The twelve FCC slip systems $\{111\}\langle 110\rangle$ are assigned to the elements of the single crystal, and the orientation of the lattice is specified through the Kock's Euler angles as $\Psi = 69.2^{\circ}$, $\Theta = 65.9^{\circ}$ and $\phi = 26.6^{\circ}$. The material properties for the beam specimen are listed in Table 2-1 and correspond to the Aluminum alloy AL5182, as adopted from [54]. Note that an approximate value of order unity is assigned to k_0 as suggested in [33]; in practice, this parameter would also be calibrated against experimental data. The shear modulus μ is modeled by [54] as

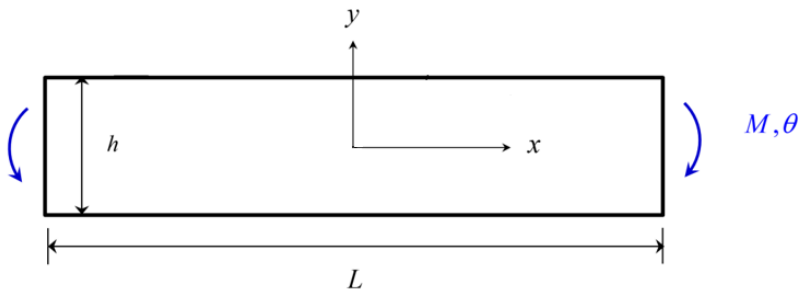

Figure 2-3. Single-crystal bending schematic

Table 2-1. Material properties for beam bending model

Property	Value	Property	Value
E	78,811 MPa	n	20
ν	0.33	$\dot{\varepsilon}_{0,y}$	10^7 s^{-1}
μ_0	28815 MPa	$\hat{\tau}_v$	59 MPa
D_0	3440 MPa	$g_{0,v}$	1.6
T_0	215 K	q_v	1.0
b	2.86×10^{-7} mm	p_v	0.66667
τ_a	3.333 MPa	$\dot{\varepsilon}_{0,v}$	10^7 s^{-1}
$\hat{\tau}_y$	99 MPa	θ_0	800 MPa
$g_{0,y}$	1.196	k_0	2.0
q_y	1.5	κ	1.0
p_y	0.5		

$$\mu = \mu_0 - D_0 \cdot \left[\exp\left(\frac{T_0}{T} \right) - 1 \right]^{-1} \tag{2.36}$$

where μ_0 is a reference value of the shear modulus and D_0 and T_0 are empirical constants. The beam is modeled in plane strain by imposing the z displacement to be zero at all nodes in the mesh. Additionally, the top and bottom surfaces are treated as traction-free, and shear stress on the left and right faces is prescribed to be zero. The horizontal displacement of the left and right faces is evaluated in terms of the applied rotation θ as follows:

$$u_x\left(x = -L/2, y\right) = -\theta y, \qquad u_x\left(x = L/2, y\right) = \theta y \tag{2.37}$$

In the following simulations, the rotation θ is incremented during 80 load steps at a rate of $\dot{\theta} = 5 \times 10^{-14}$ rad/s up to a maximum value $\theta = 0.04$ radians. The small deformations generated by this applied rotation ensure that the beam response is dominated by pure bending. The resultant moment M is computed by integrating the moments of the axial stresses at the end faces about the centerline of the beam:

$$M = \int_{-h/2}^{h/2} y \sigma_{xx}\left(L/2, y\right) dy \tag{2.38}$$

This resultant moment is normalized against the elastic moment at the proportional limit, the point where the slope of the stress-strain curve ceases to be constant. Accordingly, the response loses proportionality approximately at the load level $M/M_{ref} = 1.$

The simulations are performed at temperature $T = 300$ K. The response of the two beam specimens 12×4 μm and 48×16 μm under the applied flexural loading is obtained using both the elemental and nodal projection methods and explicit integration of the rotation tensor. First, the convergence of the method is assessed qualitatively by plotting the relative moment M/M_{ref} versus the applied angle θ in Figure 2-4 for increasing levels of mesh refinement using the nodal projection method which yielded same graphs as the

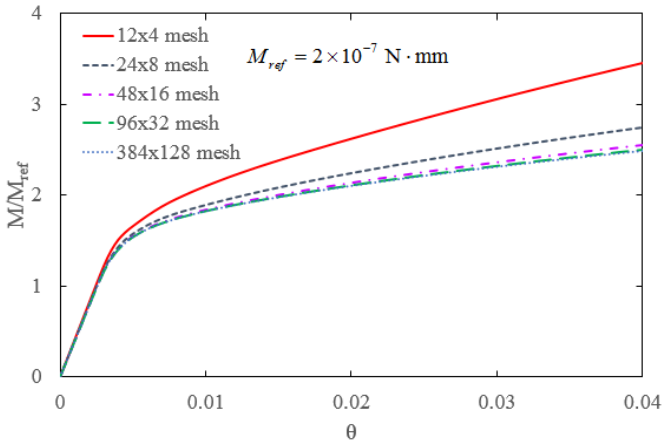

Figure 2-4. Comparison of normalized moment versus applied rotation for beam of size 12×4 μm using nodal projection method

element projection one. Only the results for the 12×4 μm beam are shown; the values of M_{ref} are listed in the figure. The figure indicates that the computed strain hardening decreases with mesh refinement. The moment-rotation curve appears to converge from above to the solution of the refined mesh.

Next, the moment-rotation curves are compared in Figure 2-5 for each beam size as obtained on the 96×32 element meshes. Note that the curves have been normalized by $M_{ref} = 2\times10^{-7}$ N·mm in order to highlight the common response within the elastic regime. Again, the results of the nodal projection simulation are qualitatively identical to the elemental one. A size effect is clearly present in the response of the beams in Figure 2-5 upon the onset of plastic flow. While lower strength is observed at higher temperature, increased hardening is apparent for the smaller beam compared to the larger one, with an increase in the moment M/M_{ref} by about 20% at $\theta = 0.04$. Recall that the only difference between the simulations is the dimensions of the beam; the number of elements, applied rotation, and all material properties are kept constant. For classical continuum plasticity models, the normalized moment curves for two specimen sizes would be identical both in

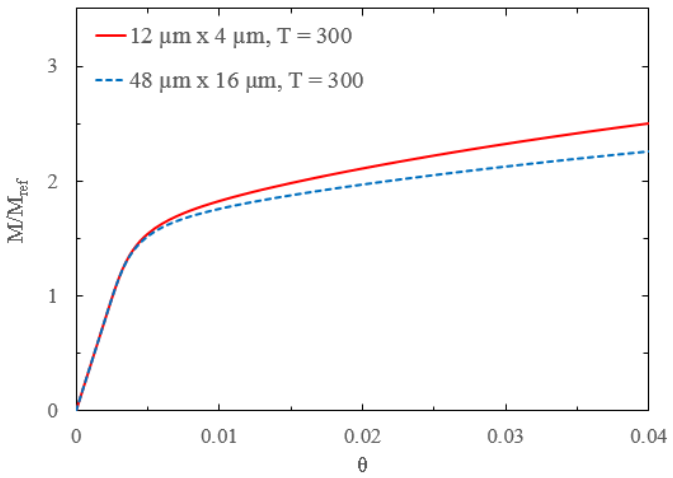

Figure 2-5. Comparison of normalized moment versus applied rotation using nodal projection for both beam sizes 12×4 µm and 48×16 µm and 96×32 mesh.

the elastic and plastic regimes. Such models are based on flow rules that are entirely local in nature. In contrast, the GND term within the MTS model, given by (2.7), incorporates the effect of strain gradients into the constitutive response. The increased hardening for the smaller beam can be explained as follows. For an equal level of applied end rotations θ, the curvature κ of the 12×4 µm beam will be larger than the 48×16 µm beam. For small elastic deformations, the strain at any fiber parallel to the x-axis is $\varepsilon_{xx}=\kappa y$. Therefore, a non-zero strain gradient $\varepsilon_{xx,y}=\kappa$ exists, which contributes to the GND hardening term. For larger curvatures, the effect of the GND term increases, leading to greater hardening in the post-elastic regime of Figure 2-5.

Figure 2-6 presents the relative L^2 norm and H^1 semi-norm for the displacement error obtained for each test case using the following equations:

$$e_{L^2}(\boldsymbol{u}^h)=\frac{\left\|\boldsymbol{u}^h-\boldsymbol{u}^{ref}\right\|_{L^2}}{\left\|\boldsymbol{u}^{ref}\right\|_{L^2}}=\left(\int_\Omega\left(\boldsymbol{u}^h-\boldsymbol{u}^{ref}\right)\cdot\left(\boldsymbol{u}^h-\boldsymbol{u}^{ref}\right)d\Omega\right)^{\frac{1}{2}}\cdot\left(\int_\Omega\left(\boldsymbol{u}^{ref}\right)\cdot\left(\boldsymbol{u}^{ref}\right)d\Omega\right)^{\frac{-1}{2}} \tag{2.39}$$

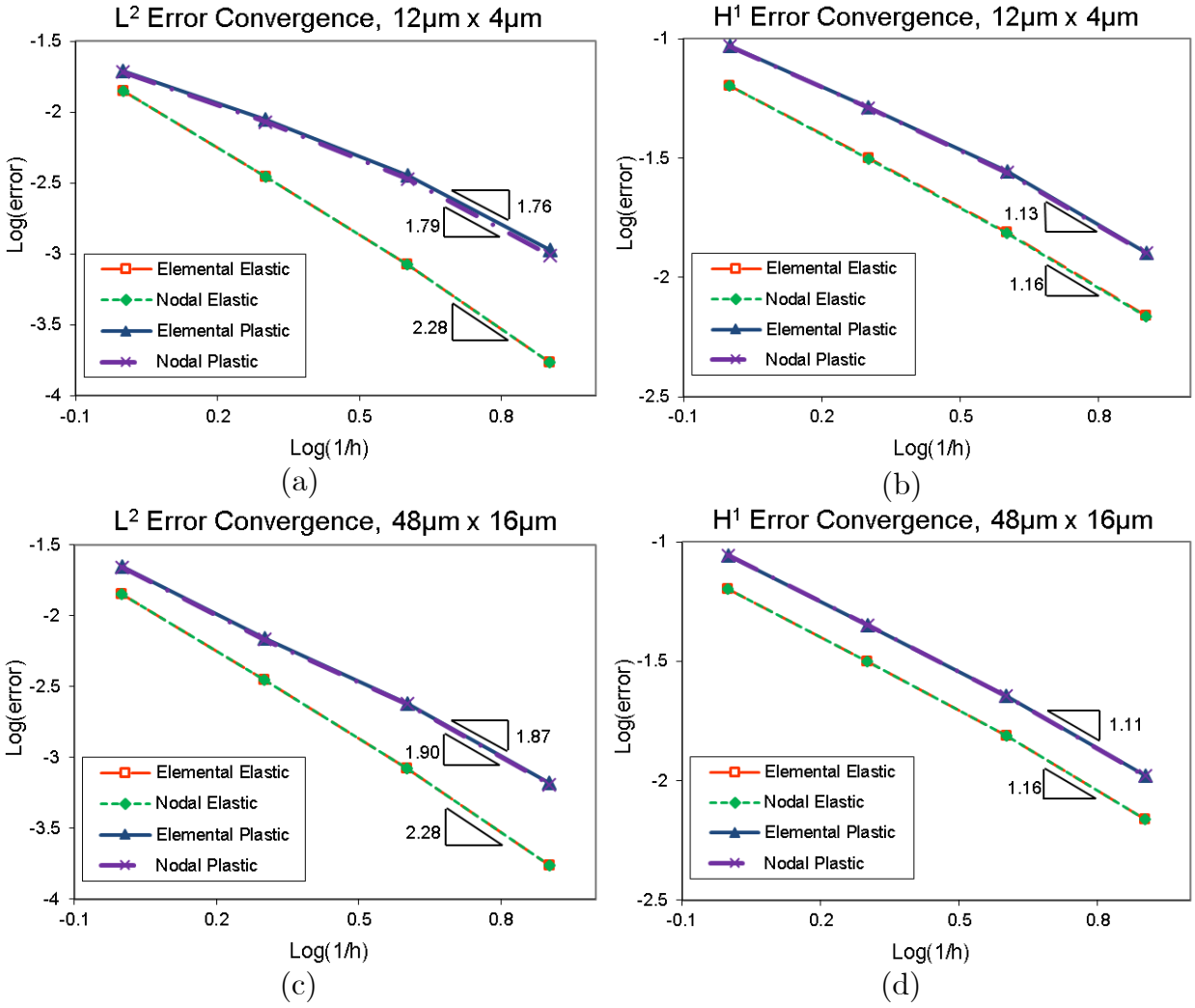

Figure 2-6. Displacement error norms for the explicit elemental and nodal projection methods for (a) L^2 error for the *12×4* μm beam, (b) H^1 error for the *12×4* μm beam, (c) L^2 error for the *48×16* μm beam and (d) H^1 error for the *48×16* μm beam.

$$e_{H^1}(\boldsymbol{u}^h) = \frac{\left(\int_\Omega \nabla\left(\boldsymbol{u}^h - \boldsymbol{u}^{ref}\right) : \nabla\left(\boldsymbol{u}^h - \boldsymbol{u}^{ref}\right) d\Omega \right)^{\frac{1}{2}}}{\left(\int_\Omega \left(\nabla \boldsymbol{u}^{ref}\right) : \left(\nabla \boldsymbol{u}^{ref}\right) d\Omega \right)^{\frac{1}{2}}} \tag{2.40}$$

where $\boldsymbol{u}^h$ is the displacement field for one of the four levels of refinement and $\boldsymbol{u}^{ref}$ is the displacement field for the reference solution computed on a very fine mesh (384×128). The error norms are evaluated at two applied rotations $\theta_1 = 0.0005$ and $\theta_2 = 0.04$ to investigate the accuracy of the elastic and plastic response, respectively. Clearly, all simulations exhibit nearly constant slopes or rates of convergence, which is a strong indication of the stability of the element projection method. The elastic response of the beams for each size and temperature gave the close to optimal rates of about 2.0 for the L^2 norm and 1.0 for the H^1 semi-norm for linear polynomial shape functions. At the plastic load level, when the Nye tensor term is active, the convergence rates do drop somewhat below the optimal values. The elemental and nodal projection methods gave similar convergence rates with the nodal one having a slightly better L^2 norm, meaning that no degradation of accuracy happens when using the nodal method. These stable results are in agreement with the performance observed by [47] and do not show the mesh sensitivity found by [48].

As an additional result, contour plots on the deformed configuration of the flexural stress σ_{xx} for $T = 300$ K at the load levels $\theta = 0.0015$ and $\theta = 0.04$ are provided in Figure 2-7 and Figure 2-8, respectively. For the smaller load level in Figure 2-7, the variation of the stress field is linear through the depth of the beam, as expected. At the higher level of rotation, the stress profile is more uniform in the upper and lower regions of the beam, indicating that plasticity is dominant throughout the cross-section. Stress concentrations are observed at the ends of the beam and are more pronounced for the larger beam.

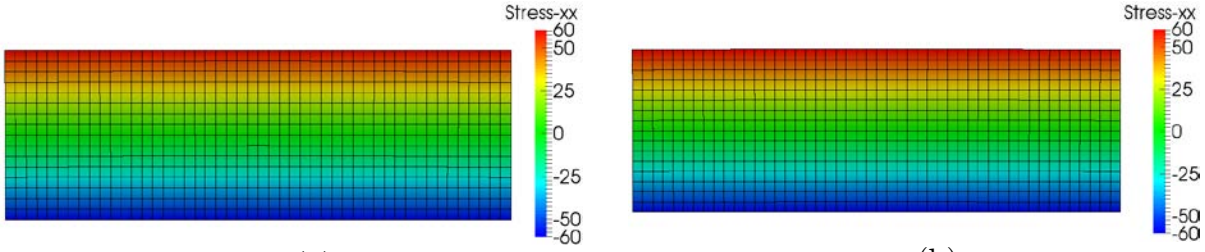

(a) (b)

Figure 2-7. Flexural stress σ_{xx} (MPa) at elastic load level $\theta = 0.0015$ radians for (a) beam size 12×4 µm and (b) beam size 48×16 µm

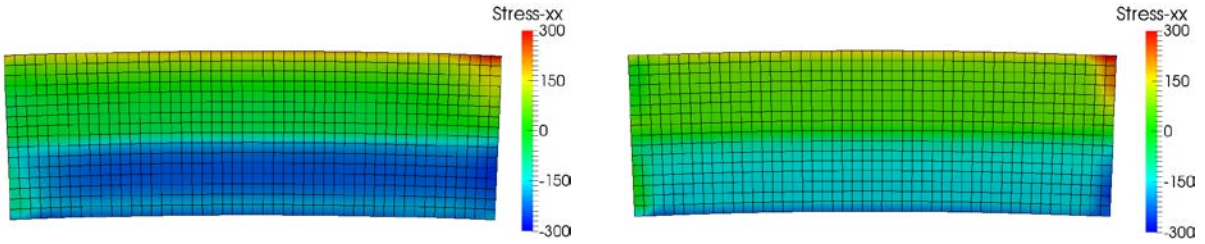

(a) (b)

Figure 2-8. Flexural stress σ_{xx} (MPa) at plastic load level $\theta = 0.04$ radians for (a) beam size 12×4 µm and (b) beam size 48×16 µm

2.5.2 Three-dimensional multipath loading

The objective of this problem is to investigate the accuracy, robustness and stability of the implicit time integration of $\boldsymbol{R}^p$ for a three-dimensional domain subjected to large displacements applied in multiple directions. The problem was designed to be a challenging test for the numerical formulation. However, such deformations can be experienced during complex forging or thermo-mechanical treatment and as such do have physical significance. The model as shown in Figure 2-9 consists of two material regions: a single crystal cube with side length $L = 1$ μm denoted by white elements and elastic regions on both ends of the cube with length $L_b = 0.6667$ μm denoted by shaded elements.

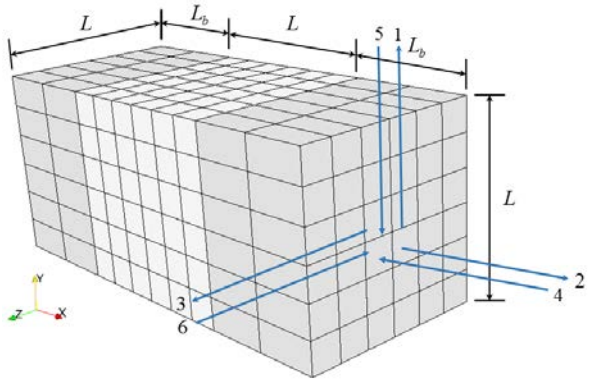

Figure 2-9. 3D Multipath loading schematic

The elastic (buffer) regions provide a transition between the boundary conditions on the faces of the domain and the single crystal region in order to lessen the stress concentrations at the corners of the central cube. The surface $x = 0.0$ is fully fixed with $\boldsymbol{u} = \boldsymbol{0}$, and prescribed time-varying displacement are applied uniformly across the $x = 2.333$ μm surface. These displacements are first increased (termed as loading) and subsequently returned to zero (termed as unloading) as shown by arrows in Figure 2-9. The loading

and unloading direction sequences are ordered differently to induce a heterogeneous stress state and therefore harsh conditions for the algorithmic stress update. Each loading or unloading phase consists of a displacement $u_i = 0.4$ μm applied to the surface mentioned above in $t = 400$ s. The material parameters for the single crystal are maintained as the Aluminum-5182 alloy from Table 2-1, with temperature $T = 300$ K and the Kocks Euler angles $\Psi = 45.0^\circ$, $\Theta = 0.0^\circ$, $\phi = 30.0^\circ$. The buffer regions are treated as a hypoelastic material with modulus $E = 19{,}700$ MPa and $\nu = 0.33$.

The problem was solved by all three proposed gradient-based methods: explicit time integration of $\boldsymbol{R}^p$ with elemental projection and nodal projection as well as implicit time integration of $\boldsymbol{R}^p$. A coarse mesh is employed as shown in Figure 2-9; the center cube contains $6 \times 6 \times 6$ elements while each buffer region contains $6 \times 6 \times 2$ elements. All elements are fully integrated eight-node linear hexahedral. The results from this coarse mesh are compared to those obtained on finer meshes solved through the explicit method: one medium mesh with $12 \times 12 \times 12$ elements for the center cube, and a fine mesh with $24 \times 24 \times 24$ elements for the center cube. Two time discretizations are considered: the first with one hundred increments per phase and the other with fifty increments per phase.

To assess the accuracy of the solution techniques and highlight the response, we report the shear stress component σ_{xy}, as it is representative of the level of heterogeneity observed in the solution. Contour plots are provided only for the elemental projection, explicit integration case with 100 load increments per phase. Figure 2-10 presents the deformed configuration of the specimen at the end of each of the six phases. The stress field in the crystal plasticity region appears to be homogenous for the first two phases (shown in Figure 2-10 (a) and (b)); stress concentrations appear only within the buffer region. Heterogeneities begin to appear in the central stress field during phase three as observed in Figure 2-10(c). Also, the crystal plasticity elements near the buffer region exhibit a distorted or kinked shape. Those kinks persist during the subsequent unloading

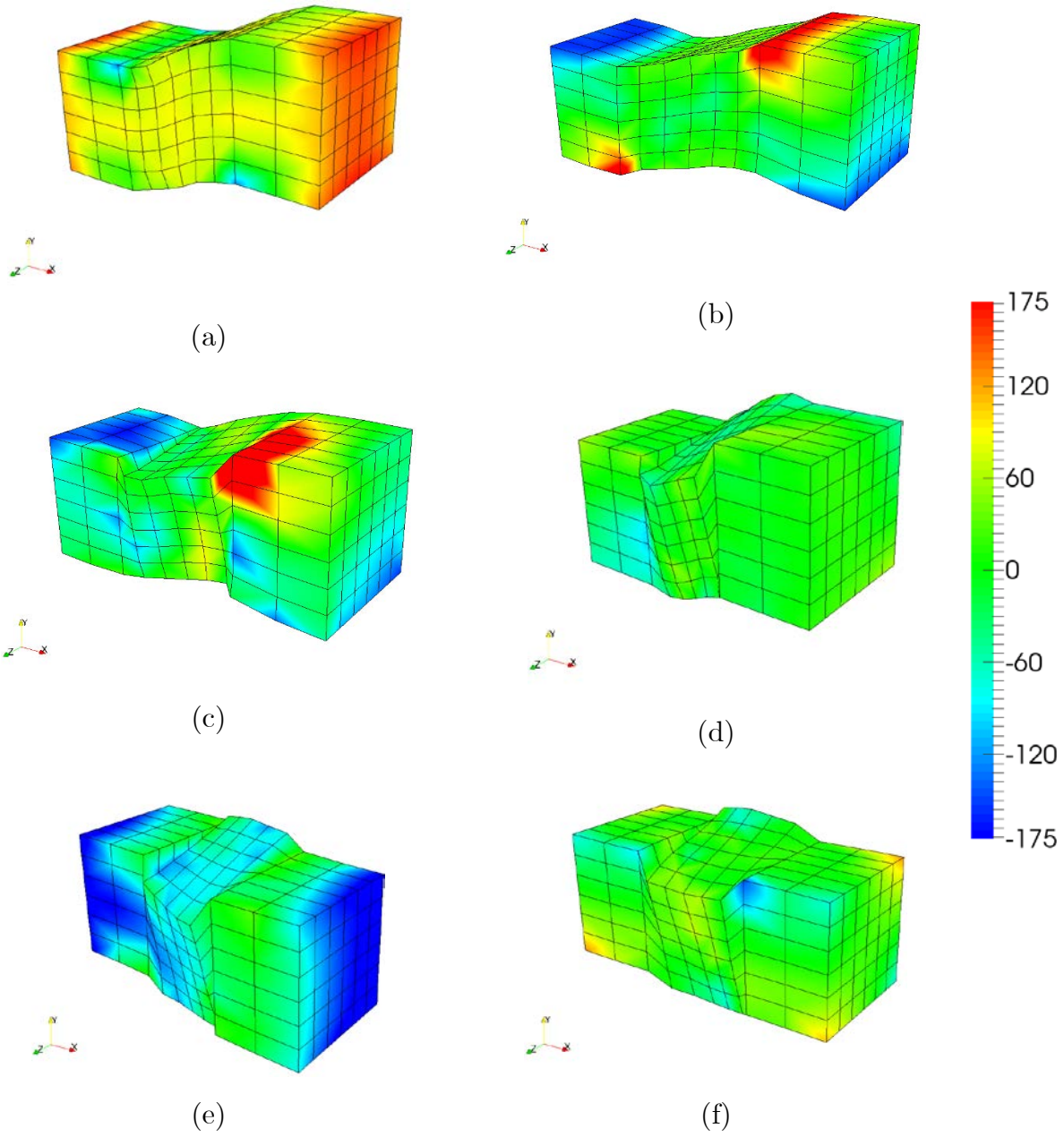

Figure 2-10: Shearing stress σ_{xy} (MPa) for the explicit time integration of $\boldsymbol{R}^p$ at the end of each phase: (a) phase 1; (b) phase 2; (c) phase 3; (d) phase 4; (e) phase 5; (f) phase 6

phases, indicating the development of localized permanent plastic deformation. These distortions do not prevent the nonlinear equation solver from converging even for the large time step size for the 50 increment case.

The localized features of the solution are not completely captured by the coarse mesh due to kinematically limited linear hexahedral elements. For comparison, the σ_{xy} fields at selected phases are provided in Figure 2-11 for the finer meshes. There, the localized features appear to be smoother in Figure 2-11 (a) and (b) and the magnitude of the stresses has reduced somewhat compared to the coarse mesh in Figure 2-10 (c). Taken together, the trend of contour fields upon mesh refinement indicates that the numerical solution is converging. Additional refinement would be needed to fully resolve the internal heterogeneities. Nonetheless, the gradient crystal plasticity method considered herein does exhibit robust numerical performance for this problem.

We also provide a qualitative comparison in Figure 2-12 of the three numerical treatments of $\boldsymbol{R}^p$ at the end of phase 3 (full loading of the specimen). The shear stress contour and deformed shape produced by the three methods is nearly identical. While the accuracy of the elemental and nodal methods is similar, we are more interested in assessing the relative computational cost of each method. Therefore, the number of the Newton iterations required for the numerical convergence at each step is shown in Figure 2-13 and Figure 2-14. A common convergence criterion of six orders of magnitude reduction of the norm of the out-of-balance force vector was applied for each case. For all three stress updating techniques, convergence did not change significantly for either 50 or 100 increments per loading phase. The average number of Newton iterations per step for each method was about 4.7, except in the second unloading phase when more iterations were needed. Overall, the algorithm required more iterations during the first load step of a new load direction phase. This behavior is attributed to the global solution strategy of the finite element code, which uses displacement extrapolation to initialize the Newton method for

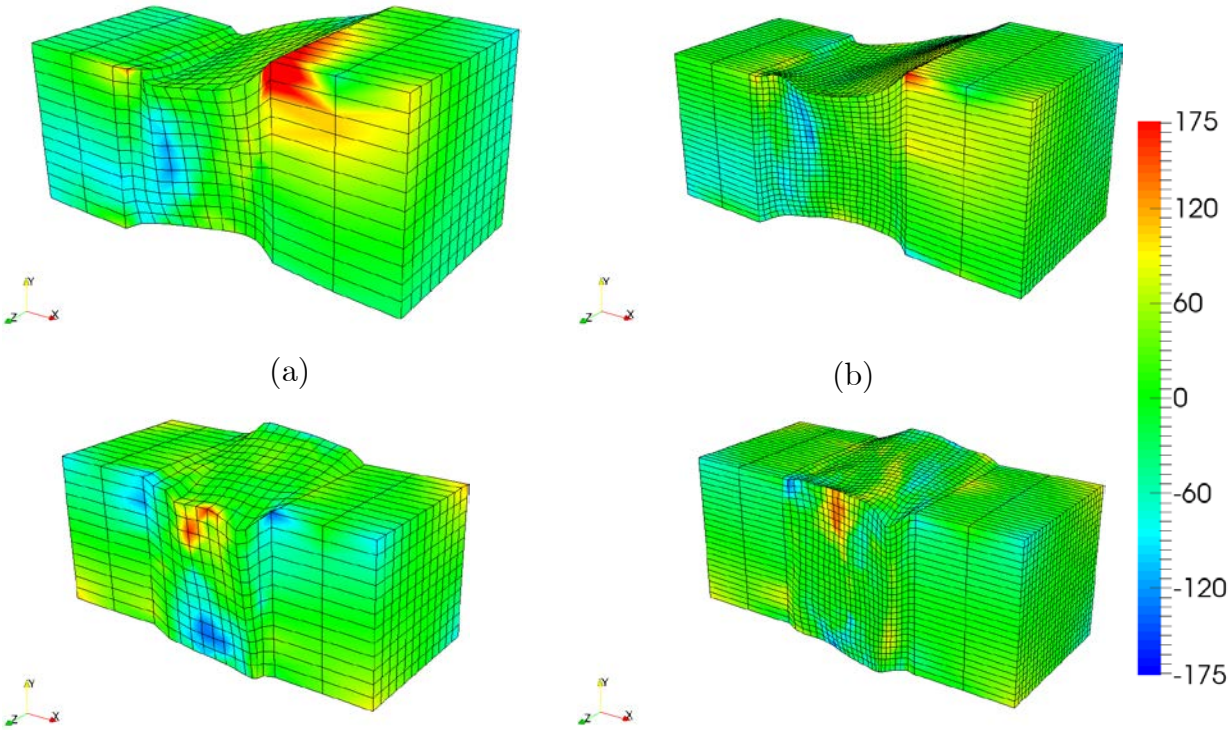

(a) (b)

(c) (d)

Figure 2-11: Shearing stress σ_{xy} (MPa) for the explicit time integration of $\boldsymbol{R}^p$: (a) $12\times12\times12$ mesh at the end of phase 3; (b) $24\times24\times24$ mesh at the end of phase 3; (c) $12\times12\times12$ mesh at the end of phase 6; (d) $24\times24\times24$ mesh at the end of phase 6

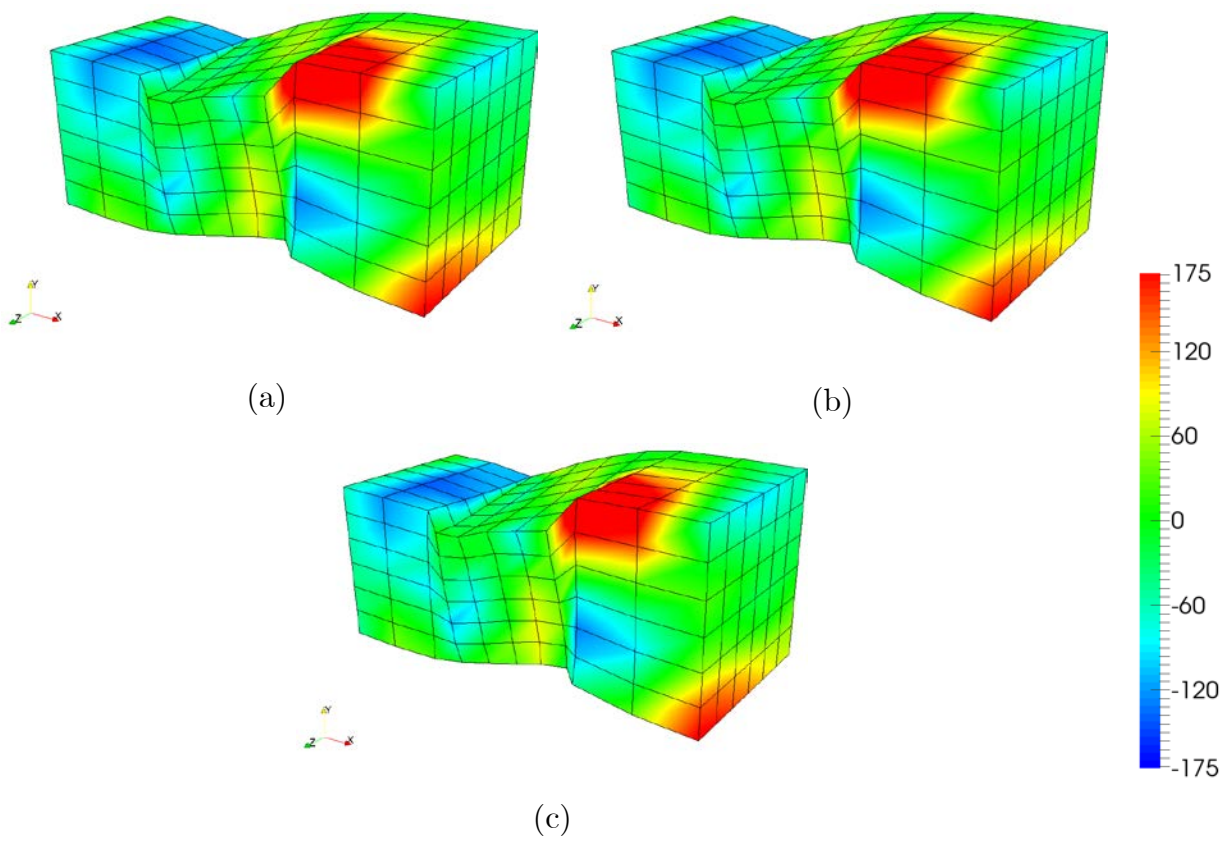

Figure 2-12. Shearing stress σ_{xy} (MPa) for the three methods: (a) explicit time integration with elemental projection; (b) explicit time integration with nodal projection; (c) implicit time integration

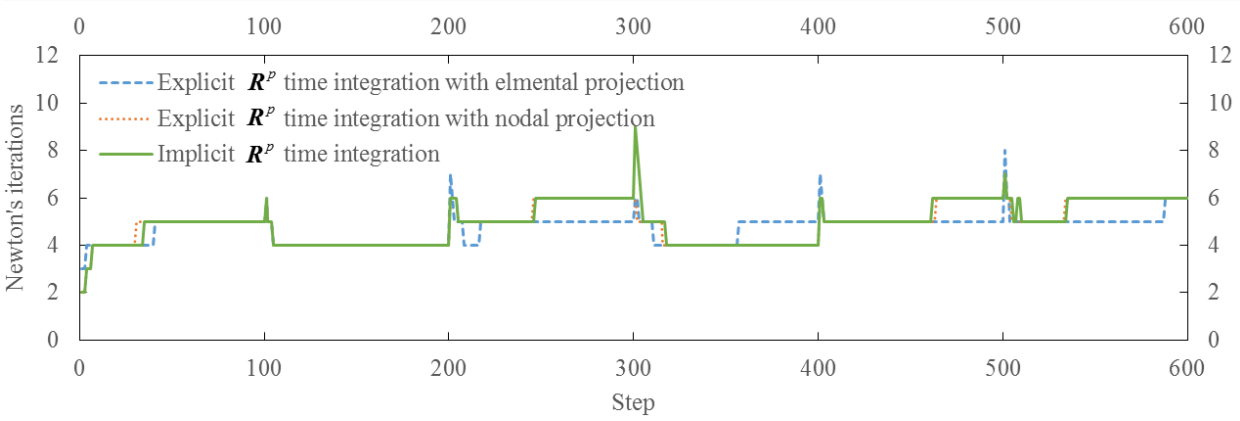

Figure 2-13. Newton's iterations for each loading step, 100 steps per phase

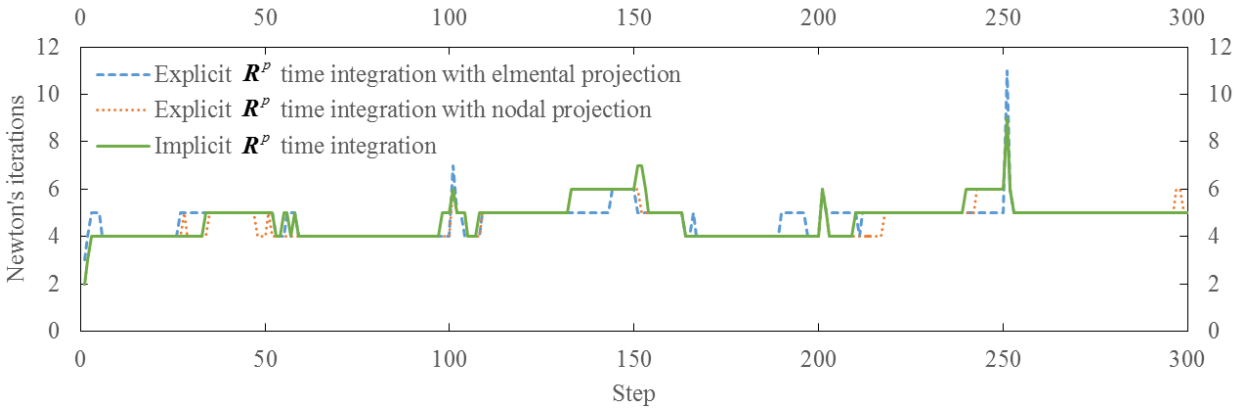

Figure 2-14. Newton's iterations for each loading step, 50 steps per phase

each load step. Extrapolation produces inaccurate initial guesses for non-proportional load paths. In general, all three methods required similar numbers of iterations. Therefore, the computational cost of each method is almost identical. For large-scale problems, the computing time to factorize the global stiffness matrix overwhelms the time for the stress update or $\boldsymbol{R}^p$ calculation. Note that simulations with 25 increments per phase were also attempted. However, the accuracy of the solution fields was significantly degraded due to the discretization error in the backward Euler equations; further increase of the step size led to divergence of the equation solver.

Finally, we investigate the computational cost of the implicit $\boldsymbol{R}^p$ integration method by showing in Figure 2-15 the number of subcycles for the fixed-point algorithm per load step. Recall that the fixed point algorithm to obtain self-consistent values of stress and $\boldsymbol{R}^p$ is performed during each global Newton iteration. As long as the number of subcycles does not increase during the simulation, then the overall computational time for the algorithm is still controlled by factorization time. Indeed, this number remains constant throughout the simulation for Figure 2-15 (a) except during the start of unloading. However, the average number increases to 6.5 per iteration during the unloading phases of the 50 increment case. This behavior indicates a certain sensitivity of the fixed point

algorithm to the level of plastic heterogeneity in the solution. Overall, the implicit method appears to be robust with respect to the evolving nonlinearity of the problem.

Remark: *While the nodal projection method yields similar results to the elemental projection counterpart, the nodal projection could be used for higher-order gradient constitutive models where second derivatives of the rotation tensor are needed. Similarly,*

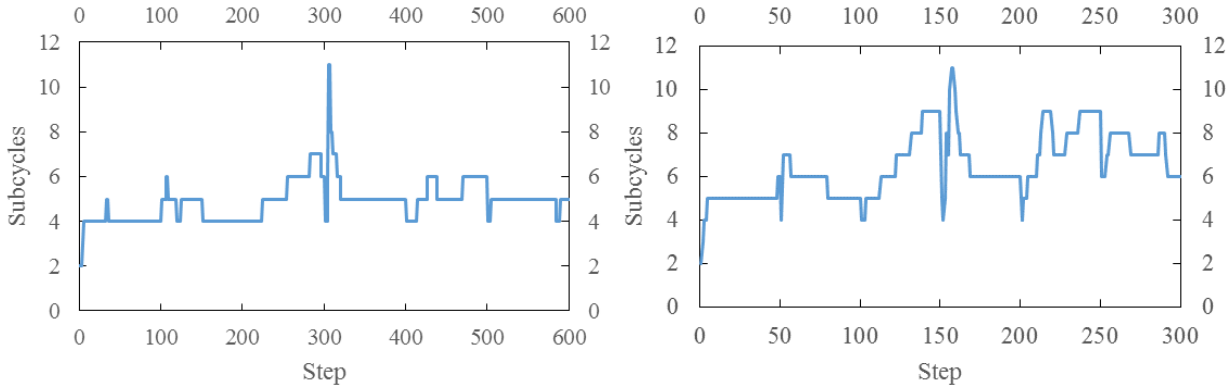

Figure 2-15. Fixed-point subcycles for each loading step, (a) 100 steps per phase (b) 50 steps per phase

the Lie mapping step in the projection would enable a fully implicit method whereby the nodally projected rotation tensor field can be used with the stress update rather than the original values at the Gauss points. The tensors obtained from linear interpolation alone may not be orthonormal and thus would generate errors within the constitutive equations.

2.5.3 Two-dimensional polycrystalline domain under compression

The objective of this problem is to investigate the behavior of the crystal plasticity model for a specimen with multiple crystallographic orientations under a large compressive

strain, with features characteristic of metallic microstructures with multiple grains. Also, the accuracy of the lumping scheme for the nodal projection discussed in Section 3.2 is investigated by comparing it to the consistent variational projection without lumping. The specimen as shown in Figure 2-16 is 1.0×1.0 μm containing twenty grains of the same material but different crystallographic orientations. In contrast to previous cases, the finite element mesh for this model consists of quadratic triangular elements generated from a Voronoi tessellation. Thus, this problem provides a testbed for evaluating higher-order polynomial elements within the projection formulations.

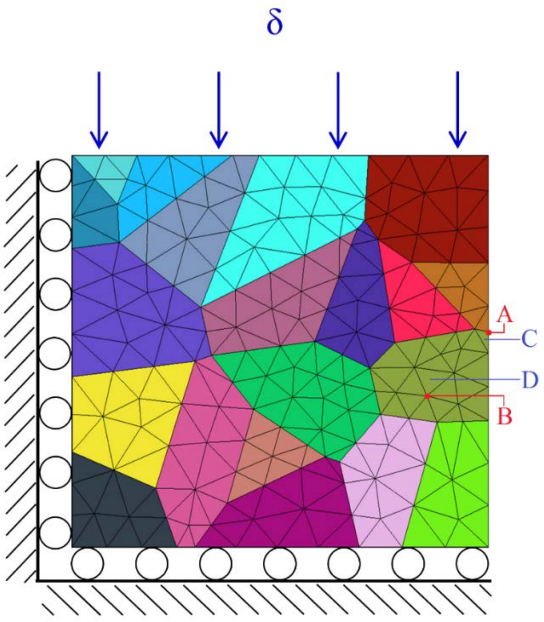

Figure 2-16. Problem description

The specimen is constrained by symmetry conditions on the bottom and left faces. A uniform prescribed displacement was applied to the surface to achieve a constant true strain rate of $\dot{\varepsilon} = 10^{-4}$; the final true strain is $\varepsilon = 50\%$ after 100 increments. The right face of the specimen is taken as traction-free to accommodate the large deformations. Plane strain conditions are assumed. For simplicity, the Euler angles representing the

grains orientation were taken in such a way that the grains under loading will rotate only about the z-axis. Thus, the orientation of the crystal lattice with respect to the xy-plane can be specified through a single angle measured counterclockwise from the positive x-axis. Twenty uniformly-spaced orientations were generated between 0° and 171°. To further investigate the behavior of the multi-grain problem, these orientations were assigned to the grains in the microstructure in two different patterns, denoted Set (1) and Set (2), as shown in Figure 2-17. The crystal plasticity material parameters are again taken from Table 2-1 with $k_0 = 1.0$ and the temperature set to $T = 300$ K.

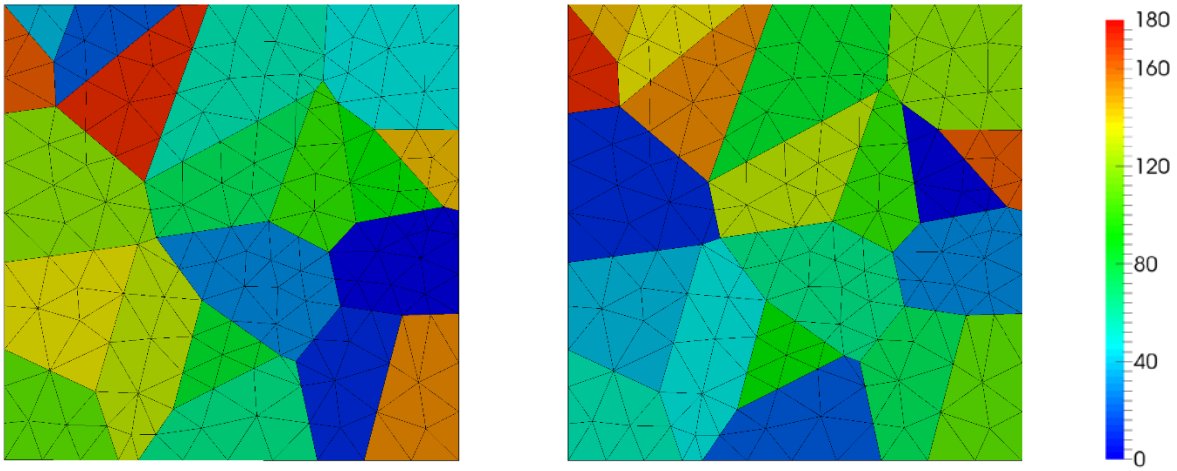

(a) (b)

Figure 2-17. Initial lattice orientations with respect to the horizontal axis: (a) Set (1); (b) Set (2)

This problem is modeled using both the explicit (elemental and nodal projections) and the implicit methods. The 50% applied strain leads to a deformation and rotation of the lattice for several grains. The final lattice orientations in the deformed configuration are shown in Figure 2-18 for each set. Comparing these orientations with Figure 2-17, we observe that the amount of rotation is not constant between all grains, and some grains

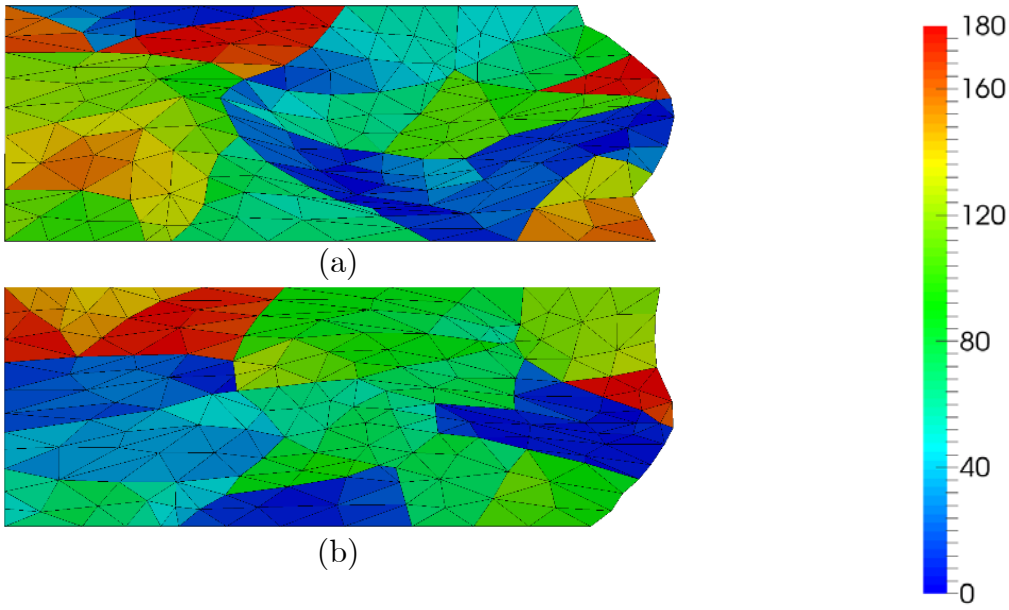

Figure 2-18. Final lattice orientations: (a) Set (1); (b) Set (2)

develop internal heterogeneity of orientation. The largest measured misorientations between the initial and final configuration are 50^{o} for Set (1) and 41^{o} for Set (2). We also notice a tendency for grains with neighbors of similar orientation to deform together and reach a state with nearly equal lattice orientation, having the appearance of a larger grain. However, these simulations involve only a small population of 20 grains with plane strain confinement, so these observations may not translate to three-dimensional, larger specimens; see e.g. [75]. The von Mises stress field obtained from each microstructure is provided in Figure 2-19(a) and (c). Figure 2-19 (b) and (d) illustrates the absolute difference in the Von Mises stress field between using the lumped and the consistent projection matrices. The maximum error is about 5% for a few nodes, and the remaining nodal values typically have closer agreement. Given the reduced cost, one would argue that lumping the projection matrix gives good approximation. By comparing the stresses with the grain rotations in Figure 2-18, we observe that grains which experience larger rotation also tend to carry higher stresses. The highest stresses for both microstructures

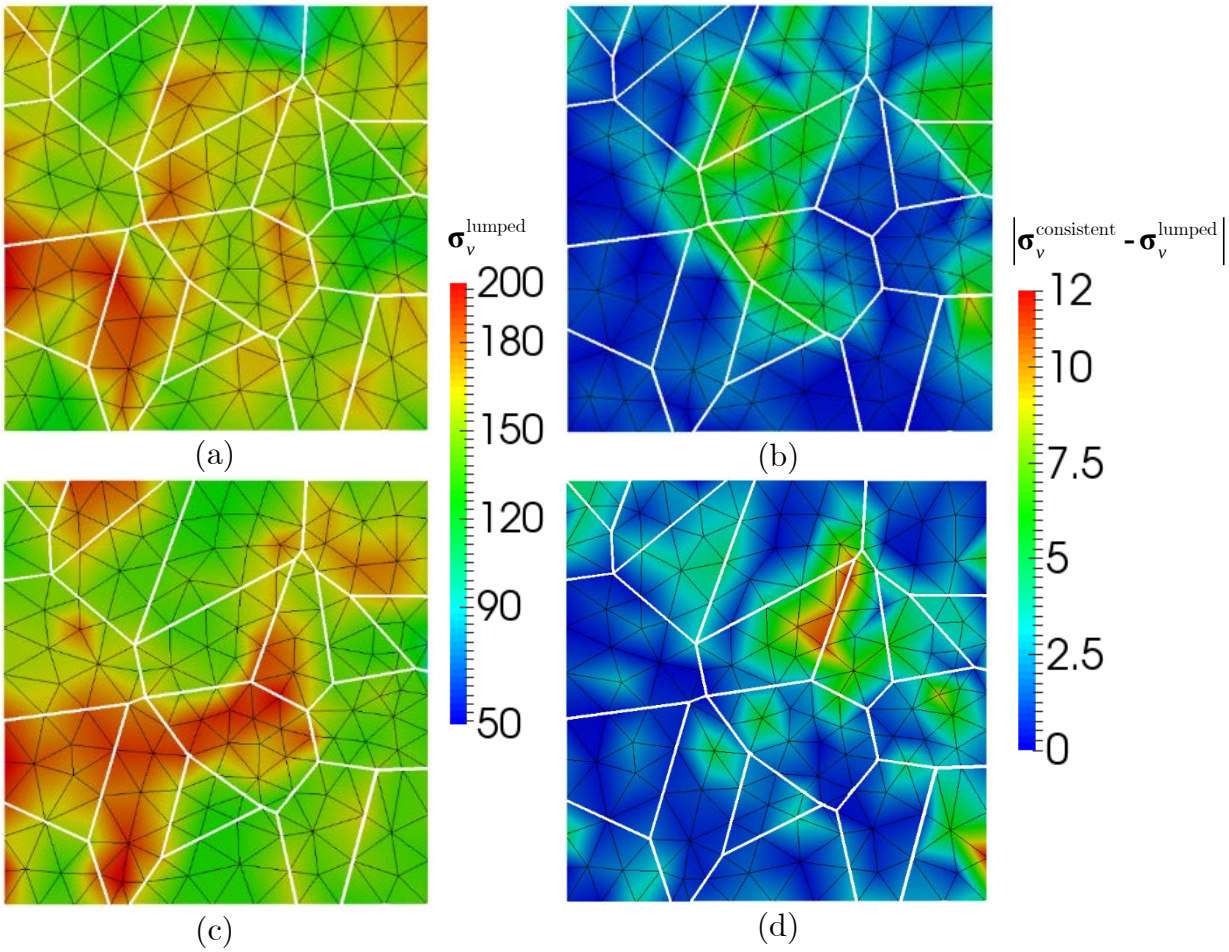

Figure 2-19. Von Mises stress (MPa) at the end of 50% true strain loading for the lumped nodal projection for (a) set 1; (c) set 2 as well as the absolute difference of the stress field between the consistent and lumped nodal projection for (b) set 1; (d) set 2

are also found near the left half of the domain closer to the confinement or symmetry boundary conditions. The traction-free right surface of the domain deforms differently based on the set of initial Euler angles. Also, the mesh lines from Set (1) and (2) trace out the different deformations undergone by each domain. Some of the elements exhibit a distorted shape; the use of quadratic interpolations helps to minimize the effect of distortion on the computed solution.

Qualitatively, the stress field for the different solving methods and projection techniques are quite similar to those reported in Figure 2-18 and Figure 2-19. Therefore, the values of particular field quantities are provided in a series of tables, all at the level of 50% strain. The overall computational effort of each method was also similar, requiring an average of about 5 Newton-Raphson iterations for convergence during each time step.

This polycrystalline numerical test also enables the investigation of the effect of assumed level of continuity in the elastic rotation field $\boldsymbol{R}^{eT}$ for the nodal projection method. Recall from Figure 2-18 that grains having different initial orientations also tended to exhibit different amounts of relative rotation between the initial and final configuration. Therefore, the projection of the elastic rotation onto a globally continuous field for the calculation of the Nye tensor may not be an appropriate representation of the physical response. Thus, simulations are performed with the nodal projection method where the rotation tensor is projected on a grain-by-grain basis (termed as grain-local). Note that nodes along the grain boundaries may thus have distinct values of the rotation tensor for each element in different grains, which requires additional bookkeeping. As a simplified approach, results are also provided for the implicit nodal method with projection carried out across the entire domain (termed as domain-global), yielding a continuous field for $\boldsymbol{R}^{eT}$ and a single value at each node. Recall that the projected fields are used solely for computing the Nye tensor and do not enter into the lattice orientation used for the crystal plasticity kinetics.

Two representative points are selected for comparing the method results, as shown in Figure 2-16: point A near a grain boundary and point B from an element in the interior of a grain. All methods produce similar values for the von Mises stress as given in Table 2-2. The solutions differ in the 3rd significant digit. This level of agreement is less that what was found for the problem in Section 2.5.2, mainly due to the heterogeneity of the grains.

Remark: *Notice that the results of the lumping scheme differ in about only 1% - 2% from those of the consistent counterpart. Therefore, even considering the large deformations and heterogeneous stresses encountered in this test, the nodal projection using the lumped matrix provides an accurate approximation with less computational cost compared to the consistent matrix.*

Next, we report the l^2 norm of the Nye tensor $\|\boldsymbol{\alpha}\|_2$ for elements C and D in Table 2-3. Due to the plane strain nature of the problem, only the components α_{zx} and α_{zy} are non-zero; see (2.9). For element D on the grain interior, the variation in the values of the Nye tensor were within 20% of each other, with the largest difference exhibited by the consistent nodal projection ones. However, element C near a grain boundary has a larger discrepancy between each method, with the largest norm reported for the elemental projection method. Generally, the elemental projection method has the largest discrepancy compared to the other methods. However, the lumped nodal projection values also differ significantly from the consistent projection ones. Note that the mechanical fields in polycrystals typically exhibit large gradients near the grain boundaries that lead to reduced accuracy in the finite element results. According to the convergence properties seen in Section 5.2, the differences between the Nye tensor values of each method are expected to decrease with higher mesh refinement. Also, these noticeable variations in the Nye tensor reflect a significantly smaller variation in the stress field due to it having a higher order of accuracy.

Table 2-2. Nodal value of von Mises stress (MPa) for Set (1) at two locations

Node	Explicit elemental projection	Explicit lumped nodal projection, grain-local	Implicit lumped nodal projection, grain-local	Explicit consistent nodal projection, grain-local	Implicit consistent nodal projection, grain-local	Implicit lumped nodal projection, domain-global
A	134.70	133.87	133.99	131.20	131.35	135.53
B	122.76	123.90	123.94	122.47	122.49	123.83

Table 2-3. Nye tensor l^2 norm for Set (1) at two locations

Element	Explicit elemental projection	Explicit lumped nodal projection, grain-local	Implicit lumped nodal projection, grain-local	Explicit consistent nodal projection, grain-local	Implicit consistent nodal projection, grain-local	Implicit lumped nodal projection, domain-global
C	17.040	6.082	6.086	8.685	8.686	7.568
D	1.293	1.338	1.337	1.975	1.975	1.338

To more closely examine the effect of assumed continuity for $\boldsymbol{R}^{eT}$ on the solution, contour plots for the l^2 norm of the Nye tensor are shown in Figure 2-20 for both microstructures. In general, the trend across Sets (1) and (2) is that the computed Nye tensor is very similar for elements that are located within the grains (do not have any nodes which are attached to a grain boundary). Otherwise, elements that share an edge with a grain boundary differ in their Nye tensor values. Thus, the effect of the discontinuous interpolation of the $\boldsymbol{R}^{eT}$ field is localized to the layer of elements near grain boundaries that are directly aware of the discontinuity. For this benchmark problem, the choice of the grain-local or domain global projection for the nodal method does not affect the computed stress field or deformed shape of the microstructure. This behavior is reasonable since the contribution of the GND hardening term has a second order effect on the solution physics compared to the other first order hardening terms. Thus, either projection field

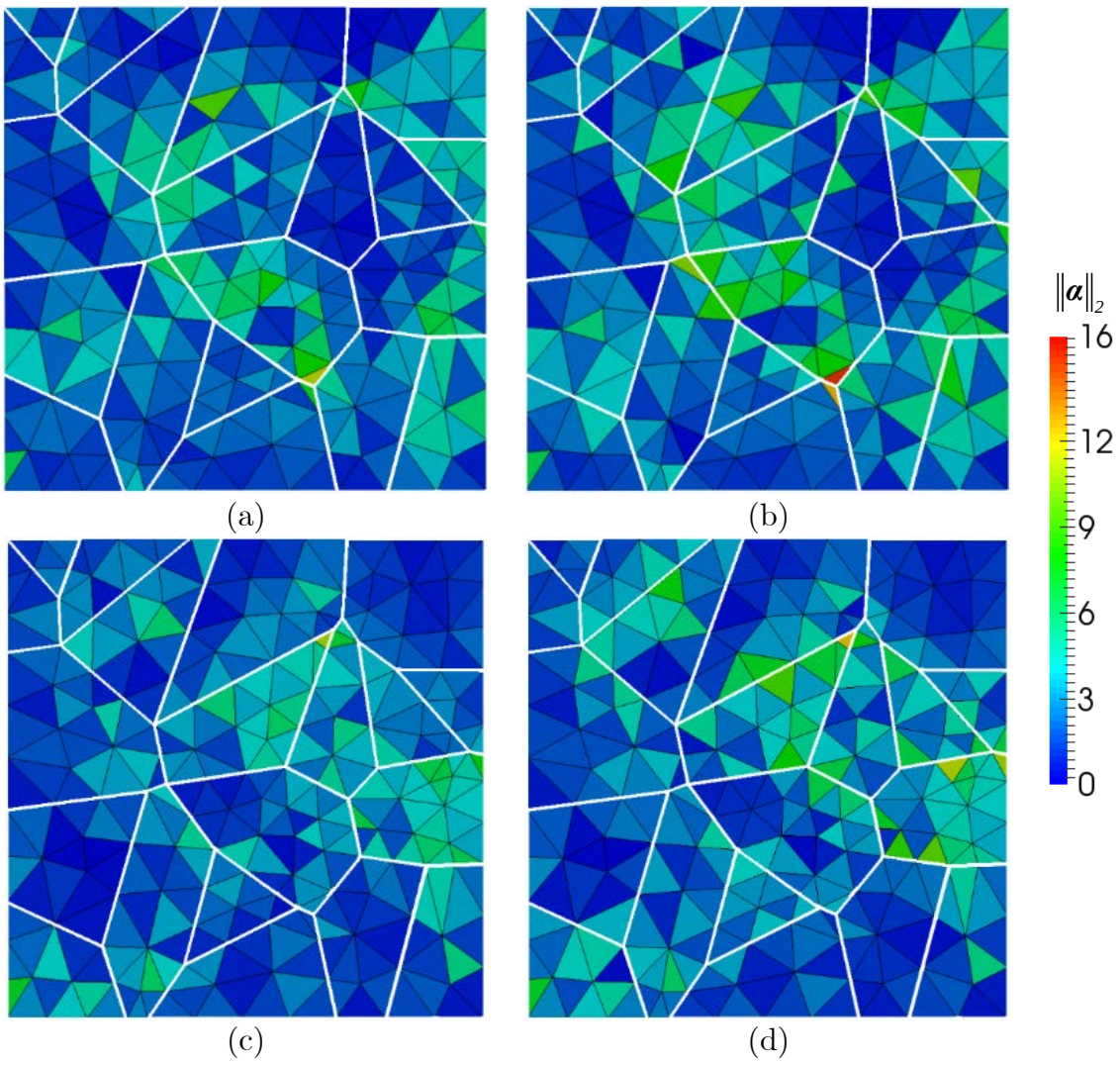

Figure 2-20. Nye tensor l^2 norm for implicit integration of $\boldsymbol{R}^p$: (a) Set (1) with grain-local projection; (b) Set (1) with domain-global projection; (c) Set (2) with grain-local projection; (d) Set (2) with domain-global projection

may be appropriately used unless the accuracy of the Nye tensor field along grain boundaries is of significant importance of the particular application.

2.6 Conclusion

We have presented and compared several numerical methods for evaluating the plastic strain gradient within a geometrically necessary dislocation (GND) crystal plasticity formulation. The GND density is expressed through the Nye tensor, which is represented in terms of the gradient of the elastic rotation tensor in the context of small elastic strains. Herein, the elastic rotation tensor is variationally projected from discrete quadrature points onto smooth fields defined either within individual elements or across the nodal shape functions of the spatial mesh. These projections are simplified by utilizing lumped approximations of the global projection matrix, thereby avoiding the significant cost of mixed methods for displacement and dislocation density fields. A distinguishing feature of the method is the use of tensorial mappings between Lie groups and algebras to preserve the orthogonality of the rotation tensors. Also, within the stress update procedure for crystal plasticity, the differential equation for evolution of the elastic rotation and Nye tensors can be treated either in explicitly or implicitly, with the latter solved in a staggered fashion using a fixed-point algorithm.

Numerical studies were conducted for three benchmark problems to compare the algorithmic performance of the three proposed methods: explicit elemental projection, implicit nodal projection, and implicit nodal projection, as well as testing the accuracy of the lumped projection matrix approximation compared to the consistent matrix. For the bending of a single crystal beam, the explicit elemental method reproduces the size effect whereby the normalized moment versus rotation curve exhibits greater hardening for beams with smaller dimensions. Convergence of the displacement and strain fields is

achieved at nearly optimal rates for a mesh refinement study performed for linear quadrilateral elements, with no loss of accuracy when using the nodal projection over the elemental one. The second problem subjects a single crystal cube with linear hexahedral elements to harsh multi-directional loading. The displacement and stress results of all three methods were very similar. Also, the number of global Newton iterations per load step were comparable, meaning that each method requires similar computing time for large scale problems. The third problem consisted of a polycrystalline microstructure discretized into quadratic triangular elements. Two versions of the implicit method were tested: a domain-global projection of the elastic rotation and a grain-local projection. The resultant stress fields obtained from all methods were very similar, and convergence was achieved within a similar number of Newton iterations. The values of the Nye tensor exhibited larger differences especially when compared to values from the consistent projection matrix simulations in the vicinity of grain boundaries depending on the type of projection, but closer agreement was seen for elements located on grain interiors. These favorable results are strong indicators that the GND-based formulation can be extended to higher-order gradient crystal plasticity formulations.

Chapter 3

DISLOCATION DENSITY-BASED CRYSTAL PLASTICITY MODELING OF CREEP DEFORMATION IN GRADE 91

3.1 Introduction

This chapter discusses the development of the crystal plasticity (CP) finite element modeling framework with the goal of predicting the evolution of the dislocation substructure that is vital to characterizing the evolution of the creep resistance of Gr91 during service life [76]. In contrast to the Norton-Bailey isotropic creep model, the use of crystal plasticity to model the inelastic response within the grains of the microstructure accounts for crystalline anisotropy, which gives rise to preferential directions of plastic strain. Also, the use of dislocation mechanism-based flow rules provides a means to track the average internal state of the material within the grains in terms of quantities that can be experimentally measured, such as dislocation density and mean radius of precipitates. These factors provide additional means to validate the computational modeling framework but more importantly provide a window toward studying the local stress and strain states along with dislocation structure that promote the actual evolution of defects such as cavities along grain boundaries.

The goal of this modeling effort was to calibrate a dislocation density-based constitutive model from macroscopic stress-strain curves obtained under various temperatures and strain rates, which are easily measured in the lab. This model would then be employed to simulate the creep response of Gr91 and validated against creep curves in the literature at 550C temperature. However, as discussed Section 3.3, this validation was not entirely successful. Nonetheless, the novel numerical modeling

developments herein provide key benefits to the modeling of Gr91 and related polycrystalline metals as detailed below.

The following section describes the vision for the crystal plasticity framework for Gr91 steel in terms of mechanism-based constitutive relations, crystallographic relationships of prior austenite grains (PAG), and strain-gradient enhanced formulations to model Bauschinger effects produced by geometrically necessary dislocations. Then, Section 3.3 describes the somewhat reduced scope of the implemented CP constitutive relations for modeling plasticity and creep within PAG of Gr91, and the determination of material parameters within those relations by fitting stress-strain curves at different strain rates and temperatures to experimental tension tests using a genetic algorithm (GA). These constitutive relations and material parameters are employed to predict the creep response of fully-resolved microstructural models. Lastly, the remaining theoretical and computational developments required to realize the model vision outlined in Section 3.2 are discussed in Section 3.5.

3.2 Overview of crystal plasticity modeling in relation to microstructural features

As described in Chapter 1, the microstructure of Gr91 consists of a complex hierarchy of defect structures with increasingly finer spatial dimensions. During the normalizing process, the prior austenite grains (PAG) transform to lath martensite, and fractions of each grain interior experience different lattice transformations that are approximated by the Kurdjumov-Sachs misorientation relationship [77]. These regions of distinct martensite variants are referred to as packets, which have similar lath morphology but possibly high angle lattice mis-orientation. A substantial amount of dislocation density is also generated

during the normalizing process and self organizes into structures, the largest of which are called blocks. Within blocks, alternating patterns of densely packed and immobilized dislocations interspaced by relatively uninterrupted atomic lattice are observed and are termed as laths [76]. Due to their geometrical arrangement, the laths are often called dislocation cells, and the regions of high and low dislocation density are termed as cell walls and cell interiors, respectively. This hierarchical network of dislocations, packet boundaries, and PAG boundaries provides substantial barriers to motion of mobile dislocation density and thus high resistance to creep. Nonetheless, recovery of this network occurs at high temperatures and sustained mechanical stress, leading ultimately to creep rupture. Therefore, to develop capabilities for predicting the useful service life of Gr91, a crystal plasticity finite element modeling framework is developed to capture the recovery processes of these microstructural features.

The virtual laboratory for modeling this microstructural evolution consists of representative volume elements (RVE) containing many finite elements arranged in patterns to approximate the PAG. Similar microstructural models using both 2D (plane-strain) and 3D realizations were developed previously by Cochran et al. [78] with emphasis on the grain boundary deformation mechanisms. Due to the prohibitive expense of resolving length scales across several orders of magnitude, only the PAG and packets will be explicitly represented; the subgrain features (blocks and laths) will be modeled through the constitutive relations within the solid finite elements.

An example microstructure containing a few grains is shown in Figure 3-1 (a). The grains are outlined by solid black lines, while some of the packets within grains are shown with dashed lines. The lattice orientation of all finite elements within a single packet are assigned a common value at the start of numerical simulations. The orientation of packets is obtained as follows. The orientation of each grain is selected randomly from the texture

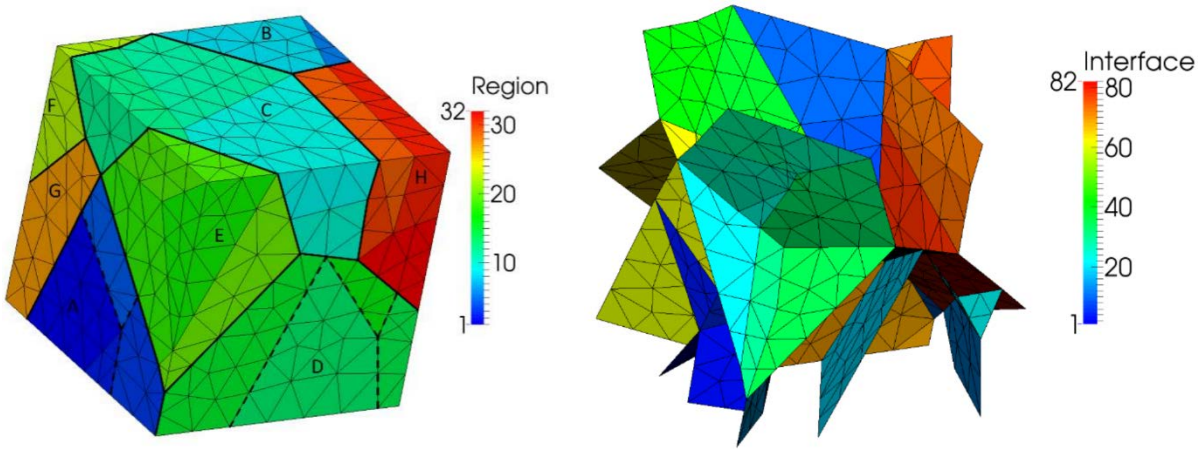

(a) (b)

Figure 3-1. Example representative volume element (RVE) of microstructure containing packets within prior austenite grains: (a) depiction of volume showing PAG boundaries with solid lines and packet boundaries as dashed lines; (b) interface finite elements along grain boundaries. Each of the grains and interfaces are numbered in order to easily assign material properties.

of the parent austenite material so that the RVE provides a statistical representation of that texture.

Then, the packet orientations are selected randomly from the 24 combinations of transformations expressed by the Kurdjumov-Sachs relationship. Denoting the austenite phase as γ and the martensite phase as α, this relationship is expressed through the Miller indices of the rolling direction and normal plane:

$$\{111\}_{\gamma} \parallel \{011\}_{\alpha} \tag{3.1}$$

$$\langle 10\bar{1}\rangle_{\gamma} \parallel \langle 11\bar{1}\rangle_{\alpha} \tag{3.2}$$

Typically, about 3 to 5 packets are modeled within a PAG. The crystal lattice also transforms from a face-centered cubic (FCC) crystal to a body-centered tetragonal (BCT) crystal, which will be approximated herein as a body-centered cubic (BCC) structure. The primary slip systems for BCC crystals are the 12 $\{1\bar{1}0\}\langle 111\rangle$ systems, 12 $\{11\bar{2}\}\langle 111\rangle$ systems, and 24 $\{12\bar{3}\}\langle 111\rangle$ systems, for a total of 48 systems. The motion of dislocations in directions specified by these slip systems leads to anisotropic response that is expected to affect the stress distribution within grains and along boundaries in contrast to the isotropic Norton-Bailey model commonly employed [79].

In the crystal plasticity finite element method, the plastic slip of dislocations is driven by the resolved shear stress $\tau^{(s)}$ on each slip system (s), as described in Chapter 2. This motion gives rise to the observed creeping deformation of the material during experiments. Dislocation slip is impeded by several barriers within the blocks and laths which must be accounted for in the constitutive model. The primary mechanism of dislocation motion at low stress and high temperature is considered as the alternating glide and climb of dislocations around pinning obstacles [80, 81]. Climb and glide permit mobile dislocation

motion toward sites both within and at the boundaries of subgrain structures, where dipole-coalescence-based dislocation recovery mechanisms take place. The kinetics of the boundary mobility is accelerated by the reduction in Zener pinning effectiveness that accompanies the coarsening of interface $M_{23}C_6$ particles (and, perhaps, to a lesser extent, to exchange of distributed MX for Z-phase precipitates). The scale of low-angle subgrain structures also coarsens as the dislocations comprising their boundaries are mobilized by climb and glide, often doubling from initial as-tempered dimensions. The extent of microstructural recovery grows with the scale of inelastic strain that is accommodated by dislocation climb and glide. As a result of these dislocation and microstructural recovery processes, macroscopic measures of deformation resistance decrease over time.

Ongoing efforts have been underway to realize these interacting mechanisms of dislocation mobility and substructure evolution within the crystal plasticity constitutive model for the PAG. The implemented version of the model described in Section 3.3 is based on tracking the evolution of the total dislocation density as partitioned to the individual slip systems within the body centered cubic (BCC) lattice. This model features several mechanisms for dislocation evolution, such as thermally-activated recovery by dislocation climb and dipole capture, and it also captures the crystallographic distribution of the dislocation network with high fidelity. However, this model treats the hierarchy of dislocation structures in a homogenized manner. Other researchers [23, 82, 83] have pursued composite dislocation density models in which the total density is decomposed into categories of mobile dislocations, immobile dislocations in cell insides, and immobile dislocations in cell walls. That decomposition appears to capture the variety of deformation rates evident in both monotonic creep tests and cyclic creep-fatigues tests with improved accuracy.

Therefore, a broader framework is envisioned for the CP constitutive model that contains as subsets the currently developed modeling features. The two primary components of the framework are (a) treatment of statistically-stored dislocations (SSD) through a mechanism-based composite model to capture subgrain evolution and (b) treatment of geometrically-necessary dislocations (GND) through a gradient-enhanced finite element method to capture back stresses observed during cyclic loading. This CP modeling framework provides enhanced capabilities compared to the isotropic Norton-Bailey model for resolving the distribution of stress within the prior austenite grains and other substructure features. Predicting the evolution of these driving stresses is crucial for capturing both the loss of creep resistance within the grains as well as the local stress state along grain boundaries that influences the rates of cavity nucleation and growth.

3.2.1 Constitutive model for statistically-stored dislocation density evolution

The CP constitutive model proposed in Table 3-1 is developed by combining the crystallographic model of Busso and McClintock [24] with the physically based isotropic model of Barrett et al. [23] The realization of this model described in Section 3.3 has a crystallographic distribution of the total SSD density among the 48 slip systems of BCC crystals. While a higher fidelity model would capture the anisotropic hardening of these slip systems, a composite model with 3 fractions of dislocation density per slip system would be prohibitively expensive. Thus, only the isotropic density is tracked in this proposed constitutive model. Several physically-based mechanisms are accounted for within the dislocation evolution equations. These include precipitate hardening (3.5), subgrain strengthening (3.9), motion of mobile dislocations between pinning obstacles (3.11), immobilization of dislocations within cell interiors (3.13), coarsening of dislocation cell walls (3.15), and coarsening of $M_{23}C_6$ particles through Ostwald ripening (3.18). A subclass of these modeling features are included in the current CP model of Section 3.3,

Table 3-1. Flow rule and dislocation density evolution for Gr91 constitutive model

Equation	Number
$\dot{\gamma}^{(\alpha)} = \rho_m v_s \lambda^{(\alpha)} \times \exp\left[\frac{-F_o}{kT}\left(1-\left\langle\frac{\left\lvert\tau^{(\alpha)}-\tau_b^{(\alpha)}\right\rvert-\tau_{obs}}{\hat{\tau}_0\, G/G_0}\right\rangle^{p}\right)^{q}\right]\mathrm{sign}\left(\tau^{(\alpha)}-\tau_b^{(\alpha)}\right)$	(3.3) – Slip rate
$\tau_{obs} = \tau_p + \tau_d + \tau_\rho$	(3.4) – Obstacle stress
$\tau_p = \tau_0\left[1+\frac{18}{5}\left(\frac{CG}{\tau_0}\right) f_{\mathrm{M23C6}}^{3/2}\int\dot{\gamma}\,dt\right]$	(3.5) – Precipitate stress
$\dot{\gamma} = \sum_s\left\lvert\dot{\gamma}^{(s)}\right\rvert$	(3.6) – Total slip rate
$\tau_\rho = \alpha_1 Gb\sqrt{\rho}, \qquad \dot{\tau}_\rho = \frac{\alpha_1 Gb}{2\sqrt{\rho}}\dot{\rho}$	(3.7) – Dislocation substructure stress
$\tau_0 = \frac{Gb}{\lambda_{\mathrm{M23C6}}}, \qquad \lambda_{\mathrm{M23C6}} = \frac{r_{\mathrm{M23C6}}}{\sqrt{6\, f_{\mathrm{M23C6}}/\pi}} - 2r_{\mathrm{M23C6}}\sqrt{\frac{2}{3}}$	(3.8) – Orowan stress
$\tau_d = \alpha_1 Gb\sqrt{\rho_i} + \alpha_2 Gb\left(\frac{1}{\delta}\right), \qquad \dot{\tau}_d = Gb\left(\alpha_1\frac{\dot{\rho}_i}{\sqrt{\rho_i}} - \alpha_2\frac{\dot{\delta}}{\delta^2}\right)$	(3.9) – Subgrain stress
$\rho = \rho_m + (1-f_w)\rho_i + f_w\rho_w$	(3.10) – Total dislocation density
$\dot{\rho}_m = \frac{\dot{\gamma}}{bn_s}\left(\frac{1}{L_e} - \rho_m\left(2d_{dip} + 4d_{lock}(n_s-1) + d_e\right)\right)$	(3.11) – Mobile dislocation density
$L_e = \frac{\delta}{\kappa},\ n_s = 5$	(3.12) – Mean free path, number of active slip sys.
$\dot{\rho}_i = \frac{\dot{\gamma}}{bn_s} 4d_{lock}(n_s-1)\rho_m - m_{cl}Gb^2\rho_i^2$	(3.13) – Immobile dislocation density
$\rho_w = \left(\frac{\alpha_2}{\alpha_1}\frac{1}{\delta}\right)^2, \qquad \dot{\rho}_w = -2\left(\frac{\alpha_2}{\alpha_1}\right)^2\frac{\dot{\delta}}{\delta^3}$	(3.14) – Cell wall dislocation density
$\dot{\delta} = \left(\alpha_{\delta,0}\exp\left(\frac{-F_\delta}{RT}\right) + \beta_\delta\dot{\gamma}\right)\delta^{\gamma_\delta}$	(3.15) – Cell wall spacing
$f_w = \frac{3t_w}{\delta}$	(3.16) – Cell wall fraction
$m_{cl} = k_{sol}\frac{b}{kT}D_{\mathrm{Fe},0}\exp\left(\frac{-F_{cr}}{RT}\right)$	(3.17) – Climb coefficient
$\left(r_{\mathrm{M23C6}}(t,T)\right)^3 = r_{\mathrm{M23C6},0}^3 + k_{\mathrm{M23C6}}(T)\cdot t$	(3.18) – Ostwald ripening

Table 3-2. Nomenclature for Gr91 model and physical units employed

Parameter	Description	Units
v_s	Slip velocity	mm/s
F_0	Effective activation energy for dislocation slip	mJ
$D_{\mathrm{Fe},0}$	Diffusion coefficient for iron	mJ/mm
d_e	Critical distance for mobile dislocation annihilation	mm
δ_0	Initial cell wall dimension	mm
f_{M23C6}	Volume fraction of precipitate	dimensionless
k_{sol}	Solute atom parameter	dimensionless
α_1	Material parameter	dimensionless
α_2	Material parameter	dimensionless
r_{M23C6}	Mean precipitate radius	mm
t_w	Cell wall thickness	mm
d_{dip}	Critical distance for dipole formation	mm
d_{lock}	Critical distance for lock formation	mm
κ	Material parameter	dimensionless
ρ_0	Initial total dislocation density	mm^{-2}
$\rho_{i,0}$	Initial immobile dislocation density	mm^{-2}
$\rho_{w,0}$	Initial cell wall dislocation density	mm^{-2}
$\alpha_{\delta,0}$	Lath growth parameter	dimensionless
β_δ	Lath growth parameter	dimensionless
γ_δ	Lath growth parameter	dimensionless

such as the thermally-activated annihilation due to climb (3.17). However, the decomposition of SSD density is expected to enhance the predictive capabilities of the modeling framework in regards to cyclic softening. During repeated load reversal, the dislocations that are mobilized from pile-ups by reversal of local driving stress may travel across subgrains to be captured within the lath boundaries on the opposite side of the subgrain, leading to annihilations within the dense cell walls in the process. These modeling equations with separate measures of mobile and cell wall dislocation density have the capacity for capturing these physical phenomena.

3.2.2 Gradient-enhanced finite element method for geometrically-necessary dislocations

Gr91 steel is known to exhibit cyclic softening during fatigue tests [23, 84, 85], where the maximum flow stress decreases and the total deformation increases over several hundred cycles. To model these effects in the microstructure, the geometrically necessary dislocation (GND) density based model from Bayley and Geers will be employed [43]. In this model, the back stress is a function of the GND spatial gradient according to the following relation:

$$\tau_b^{(\alpha)} = \tilde{\boldsymbol{b}}^{(s)} \cdot \left(\boldsymbol{\sigma}_s^{\text{int}} + \boldsymbol{\sigma}_e^{\text{int}} \right) \cdot \tilde{\boldsymbol{n}}^{(s)} \tag{3.19}$$

This model is based on the mechanism of dislocation pile up against grain boundaries. When the dislocation density varies spatially, the elastic field produced by individual dislocation can be integrated within a small zone of influence to yield a resultant back stress. The derivations within [43] provide expressions for the back stress, which are highly dependent on the crystallographic orientation. Both edge and screw dislocations are

considered. These derivations were applied in general without restriction to particular crystallographic slip systems. Therefore, the present developments will extend the existing results for face-centered cubic (FCC) systems to body-centered cubic (BCC) systems, which is the crystal structure of martensite.

$$\boldsymbol{\sigma}_s^{\text{int}} = \frac{GbR^2}{4} \sum_{s,\text{screw}} \nabla_0 \rho_{GND}^{(s)} \cdot 2\left[\tilde{\boldsymbol{t}}^{(s)} \otimes \text{sym}\left(\tilde{\boldsymbol{n}}^{(s)} \otimes \tilde{\boldsymbol{b}}^{(s)} \right) - \tilde{\boldsymbol{n}}^{(s)} \otimes \text{sym}\left(\tilde{\boldsymbol{t}}^{(s)} \otimes \tilde{\boldsymbol{b}}^{(s)} \right) \right] \tag{3.20}$$

$$\boldsymbol{\sigma}_s^{\text{int}} = \frac{GbR^2}{8(1-\nu)} \sum_{s,\text{edge}} \nabla_0 \rho_{GND}^{(s)} \cdot \begin{bmatrix} \tilde{\boldsymbol{n}}^{(s)} \otimes \left(3\tilde{\boldsymbol{t}}^{(s)} \otimes \tilde{\boldsymbol{t}}^{(s)} + \tilde{\boldsymbol{n}}^{(s)} \otimes \tilde{\boldsymbol{n}}^{(s)} + 4\nu \tilde{\boldsymbol{b}}^{(s)} \otimes \tilde{\boldsymbol{b}}^{(s)} \right) \\ -2\tilde{\boldsymbol{b}}^{(s)} \otimes \text{sym}\left(\tilde{\boldsymbol{n}}^{(s)} \otimes \tilde{\boldsymbol{b}}^{(s)} \right) \end{bmatrix} \tag{3.21}$$

where $\tilde{\boldsymbol{b}}^{(s)}$ is the slip direction within a crystal plane s, $\tilde{\boldsymbol{t}}^{(s)}$ is the tangent vector, and $\tilde{\boldsymbol{n}}^{(s)}$ is the unit normal to the plane.

In order to calculate the GND density gradient, Bayley et al. employed a mixed formulation with dislocation density as nodal unknowns. However, that method is computationally expensive because each node in the mesh has 18 additional degrees of freedom (DOF) which must be included in the global system of equations. Currently, the architecture of WARP3D does not permit the addition of DOFs per node. Therefore, a simplified approximation is pursued in this work that is based only on displacement nodal unknowns and using projections of the elastic deformation gradient tensor to obtain the GND.

The measure of geometrically necessary dislocation density is obtained from the elastic incompatibility quantified by the Nye tensor $\boldsymbol{\alpha}$ (2.9) discussed in Chapter 2. The mapping of Nye tensor components into dislocation densities on slip systems is accomplished through an L^2 minimization process advocated by Arsenlis and Parks [86], leading to the following equation:

$$\boldsymbol{\rho}_{GND} = \left(\mathbf{A}^T\mathbf{A}\right)^{-1}\mathbf{A}^T\boldsymbol{\alpha} = \mathbf{B}\boldsymbol{\alpha}, \qquad A_{ij}^{(s)} = \tilde{\boldsymbol{b}}_i^{(s)} \otimes \tilde{\boldsymbol{t}}_j^{(s)} \tag{3.22}$$

As a candidate crystal plasticity model, the Mechanical Threshold Strength (MTS) model that is implemented in WARP3D was chosen.

Due to the assumption of small elastic strains (1.7), the quantity which we need to interpolate in order to compute the Nye tensor $\boldsymbol{\alpha} = \nabla \times \boldsymbol{F}^{e-1}$ is the elastic rotation tensor $\boldsymbol{R}^e$:

$$\boldsymbol{R}^e = \boldsymbol{R}\left[\boldsymbol{R}^p\right]^{-1}, \qquad \boldsymbol{R} = \boldsymbol{F}\boldsymbol{U}^{-1} \tag{3.23}$$

where $\boldsymbol{R}^p$ is the plastic rotation tensor evaluated through the constitutive model and $\boldsymbol{R}$ is the rotation tensor defined from the right polar decomposition of the deformation gradient $\boldsymbol{F}$. For the elemental projection, the values of $\boldsymbol{R}^e$ at the Gauss points in each element are employed to fit a linear function for each component, and this linear function is differentiated to obtain the curl $\nabla \times \boldsymbol{F}^{e-1}$. While the elemental projection was sufficient for conducting the simulations in Messner et al. [87], it is an ad hoc procedure. First, this element-based approach does not incorporate any communication of the field response between elements of the mesh, dampening the nonlocal contribution from the GND hardening term. Also, it is valid only for obtaining the first derivatives of the rotation tensor field. In contrast, crystal plasticity models involving a measure of the back-stress require the second derivative of the elastic rotation to be well-defined [88, 89].

In light of these motivations, a new numerical method is developed for extending the values of the plastic deformation gradient at the integration points into a non-locally defined field. The procedure is motivated by the developments of Mota et al. [52] on the projection of internal variables. First, the value of the plastic deformation gradient is obtained at each integration point by the usual loop over all the finite elements in the mesh during the stress-update process. These values are extrapolated to the nodes of the

mesh by using the bilinear finite element shape functions, in a process directly analogous to the post-processing of elemental stress fields for contour plots. The multiple values of the field at each node, which are generated by the various elements neighboring that node, are then averaged to a single value based on the tributary area of the adjoining elements. This unique nodal value then forms a field that can be interpolated using the Lagrangian finite element shape functions. The derivative of the field is then obtained by directly differentiating the Lagrangian shape functions, specifically at the integration points of the finite element mesh. This provides the value of the oriented GND density $\lambda^{(s)}$ that are needed within the evaluation of the material model listed above.

To allow for the higher order derivatives of strain required by the GND relation (3.22), quadratic hexahedral elements are employed to interpolate the finite element displacement field. The flow-chart of this algorithm as well as preliminary results for cyclic tension tests that exhibit the Bauschinger effect will be presented at the oral defense. Ongoing efforts are pursued to complete the verification of this alternative modeling approach with the benchmarks given in the work of Bayley and Geers [43].

3.3 Dislocation density based crystal plasticity model for Gr91

A dislocation density-based model was developed and implemented within the multi-variable crystal plasticity framework of WARP3D to capture the material response across a range of deformation modes including strain-driven tensile tests, creep-fatigue, and creep [90]. The constitutive model retains the dislocation geometrical interactions proposed in the Ma and Roters [91] model but accounts for other microstructurally relevant mechanisms for Grade 91 as described in Section 3.2. The slip systems for face-centered cubic (FCC) aluminum were replaced with the body-centered cubic (BCC) systems for

martensitic steel. While dislocations in BCC crystals slip along the $[111]$ direction, the relative slip resistance offered along the (110), (112), and (123) planes are nearly equal, particularly at high temperatures [92]. Therefore, all 48 of these slip systems are utilized in the model; each system is listed in Table 3-3. The interaction of dislocations across slip systems is calculated geometrically through sine and cosine functions of the slip planes, defining parallel and forest dislocation contributions. Only statistically stored edge dislocations were considered in the crystal plasticity model.

The relevant equations for the crystal plasticity model proposed for Grade 91 are listed in Table 3-4; details on the variable definitions and units are given in [90]. The flow rule has been modified from [91] to capture two key features of the material mechanisms. First, constitutive models for BCC materials [24] typically consider the lattice resistance or Peierls stress to be the most significant short-range obstacle to dislocation motion, which is taken as a constant stress $\hat{\tau}_0$ that does not depend on the dislocation network. Also, during creep at high temperatures under sustained lower stresses, the motion of dislocations may be described through a glide-climb mechanism [23, 93]. In this mechanism, the dislocations are pinned against precipitates or dense cell walls in the microstructure for extended periods. A distinguishing feature of the proposed model is that the mean free path actually evolves in time due to the coarsening of the $M_{23}C_6$ carbides and the spreading out of the subgrain cell walls. The coarsening rate for particles is modeled through the Ostwald ripening equation [82], which accounts for agglomeration together over time due to diffusion at high temperatures. However, the simulation results in [90] adopt a constant mean free path to focus the contribution to the creep rate acceleration to be the grain boundary cavitation alone.

The crystal plasticity model in Table 3-4 has 12 material parameters, several elastic moduli that are functions of temperature, and the initial dislocation density on each of

Table 3-3. Slip system Miller indices for slip plane and direction for BCC crystals

ID	Slip System	ID	Slip System	ID	Slip System
(1)	$(110)[\bar{1}11]$	(2)	$(110)[1\bar{1}1]$	(3)	$(1\bar{1}0)[111]$
(4)	$(1\bar{1}0)[11\bar{1}]$	(5)	$(101)[11\bar{1}]$	(6)	$(101)[\bar{1}11]$
(7)	$(10\bar{1})[111]$	(8)	$(10\bar{1})[1\bar{1}1]$	(9)	$(011)[11\bar{1}]$
(10)	$(011)[1\bar{1}1]$	(11)	$(01\bar{1})[111]$	(12)	$(01\bar{1})[\bar{1}11]$
(13)	$(112)[11\bar{1}]$	(14)	$(\bar{1}12)[1\bar{1}1]$	(15)	$(1\bar{1}2)[\bar{1}11]$
(16)	$(11\bar{2})[111]$	(17)	$(121)[1\bar{1}1]$	(18)	$(\bar{1}21)[11\bar{1}]$
(19)	$(1\bar{2}1)[111]$	(20)	$(12\bar{1})[\bar{1}11]$	(21)	$(211)[\bar{1}11]$
(22)	$(\bar{2}11)[111]$	(23)	$(2\bar{1}1)[11\bar{1}]$	(24)	$(21\bar{1})[1\bar{1}1]$
(25)	$(123)[11\bar{1}]$	(26)	$(123)[1\bar{1}1]$	(27)	$(1\bar{2}3)[\bar{1}11]$
(28)	$(12\bar{3})[111]$	(29)	$(132)[1\bar{1}1]$	(30)	$(\bar{1}32)[11\bar{1}]$
(31)	$(1\bar{3}2)[111]$	(32)	$(13\bar{2})[\bar{1}11]$	(33)	$(213)[11\bar{1}]$
(34)	$(\bar{2}13)[1\bar{1}1]$	(35)	$(2\bar{1}3)[\bar{1}11]$	(36)	$(21\bar{3})[111]$
(37)	$(231)[1\bar{1}1]$	(38)	$(\bar{2}31)[11\bar{1}]$	(39)	$(2\bar{3}1)[111]$
(40)	$(23\bar{1})[\bar{1}11]$	(41)	$(312)[\bar{1}11]$	(42)	$(\bar{3}12)[111]$
(43)	$(3\bar{1}2)[11\bar{1}]$	(44)	$(31\bar{2})[1\bar{1}1]$	(45)	$(321)[\bar{1}11]$
(46)	$(\bar{3}21)[111]$	(47)	$(3\bar{2}1)[11\bar{1}]$	(48)	$(32\bar{1})[1\bar{1}1]$

Table 3-4. Flow rule and dislocation density evolution for Grade 91 constitutive model

Equation	Eqn. Number
$\dot{\gamma}^{(\alpha)} = \left(f_{\mathrm{M}} \rho_{\mathrm{SSD}}^{(\alpha)} \right) v_s \lambda^{(\alpha)} \times \exp\left[\frac{-F_o}{kT} \left(1 - \left\langle \frac{\left\lvert \tau^{(\alpha)} \right\rvert - \tau_{\mathrm{pass}}^{(\alpha)}}{\hat{\tau}_0 \, G/G_0} \right\rangle^{p} \right)^{q} \right] \mathrm{sign}\left(\tau^{(\alpha)} \right)$	(3.24) – Slip rate
$\lambda^{(\alpha)} = c_\lambda b \eta_{\mathrm{part}}\left(t,T\right)$	(3.25) – Mean free path
$\tau_{\mathrm{pass}}^{(\alpha)} = c_\rho G b \sqrt{\rho_{\mathrm{P}}^{(\alpha)}}$	(3.26) – Passing stress
$\rho_{\mathrm{F}}^{(\alpha)} = \sum_{\beta=1}^{N} \rho_{\mathrm{SSD}}^{(\beta)} \left\lvert \cos\left(\tilde{\boldsymbol{m}}^{(\alpha)}, \tilde{\boldsymbol{t}}^{(\beta)} \right) \right\rvert$	(3.27) – Forest dislocations
$\rho_{\mathrm{P}}^{(\alpha)} = \sum_{\beta=1}^{N} \rho_{\mathrm{SSD}}^{(\beta)} \left\lvert \sin\left(\tilde{\boldsymbol{m}}^{(\alpha)}, \tilde{\boldsymbol{t}}^{(\beta)} \right) \right\rvert$	(3.28) – Parallel dislocations
$\dot{\rho}_{\mathrm{SSD}}^{(\alpha)} = \dot{\rho}_{\mathrm{Lock}}^{(\alpha)} - \dot{\rho}_{\mathrm{DR}}^{(\alpha)} - \dot{\rho}_{\mathrm{Climb}}^{(\alpha)}$	(3.29) – Dislocation evolution
$\dot{\rho}_{\mathrm{Lock}}^{(\alpha)} = \frac{c_{\mathrm{Lock}}}{b} \sqrt{\rho_{\mathrm{F}}^{(\alpha)}} \dot{\gamma}^{(\alpha)}$	(3.30) – Lock formation
$\dot{\rho}_{\mathrm{DR}}^{(\alpha)} = c_{\mathrm{DR}} \rho_{\mathrm{SSD}}^{(\alpha)} \dot{\gamma}^{(\alpha)}$	(3.31) – Dynamic recovery
$\dot{\rho}_{\mathrm{Climb}}^{(\alpha)} = c_{\mathrm{Climb}} \exp\left(-\frac{F_{\mathrm{Climb}}}{kT} \right) \frac{\left\lvert \tau^{(\alpha)} \right\rvert}{kT} \left(\rho_{\mathrm{SSD}}^{(\alpha)} \right)^2 \left(\dot{\gamma}^{(\alpha)} \right)^{m_{\mathrm{C}}}$	(3.32) – Climb annihilation
$\eta_{\mathrm{part}} = \frac{\lambda_p}{b} \approx 1.6 r_p \left[\sqrt{\frac{\pi}{4\phi_p}} - 1 \right]$	(3.33) – Relative particle spacing (not used)
$\left(r_p\left(t,T\right) \right)^3 = r_{p,o}^3 + k_p\left(T\right) t$	(3.34) – Particle radius (not used)
$\phi_p = 0.15$	(3.35) – Volume fraction
$G\left(T\right) = G_0 - \frac{D_0}{\exp\left(\frac{T_0}{T} \right) - 1}$	(3.36) – Temperature dependent shear modulus

the 48 slip systems. These parameters were estimated by fitting the results of finite element tensile simulations to the experimental tensile data from Swindeman [25] for Grade 91, which has stress-strain curves for several temperatures and strain rates. This dataset had been used by Mooseburger [94] to calibrate an isotropic plasticity model for Grade 91. Presently, the data for the temperature of 600°C is relevant for the fatigue and creep simulations conducted in subsequent sections of this work. The elastic material parameters E and ν are fixed to the values appropriate for 600°C as employed by the Norton-Bailey model. The temperature dependence of the shear modulus G is specified to agree with experimentally measured variations [76]. Initial ranges for some of the plasticity parameters were determined from explicit integration of the plastic slip rate equation and dislocation density equations in MATLAB. However, the interconnectedness of the parameters and their effects on the initial yield point and saturation stress suggested that additional help would be needed to isolate the values. With the goal of selecting material parameters that would match the response near the 600°C temperature, a modified version of the Genetic Algorithm (GA) was used since a brute force method would not be efficient enough when the values of several parameters must be obtained. This modified GA method was developed by [95] and adds a domain trimming functionality.

Due to the hundreds of generations and simulations performed during GADT, the computational model in WARP3D needed to be very simple and efficient. Therefore, the computational domain was chosen as a single trilinear hexahedral element with dimensions $5 \times 5 \times 5$ mm. The WARP3D crystal plasticity framework allows for multiple crystals to be modeled within a single element by using the Taylor (isostrain) assumption, where each crystal is assumed to experience the same applied incremental strain but responds with a different internal stress. The orientation of each crystal can be different, to approximate a polycrystal. Therefore, 100 orientations were sampled from a random

texture and applied to the integration points in the single element. The boundary conditions of the model were specified for uniaxial tension, and 30 load steps of prescribed strain increments are applied to reach a total true strain of $\varepsilon = 0.03$ at constant true strain rate, to approximate the experimental conditions.

The GADT targets the best fit of the stress-strain curves compared to the Swindeman tensile data for: $T = 500^{\circ}\mathrm{C}$ and $\dot{\varepsilon} = 6.7 \times 10^{-5}\ s^{-1}$, $T = 550^{\circ}\mathrm{C}$ and $\dot{\varepsilon} = 6.7 \times 10^{-5}\ s^{-1}$, $T = 600^{\circ}\mathrm{C}$ and $\dot{\varepsilon} = 6.7 \times 10^{-5}\ s^{-1}$, $T = 600^{\circ}\mathrm{C}$ and $\dot{\varepsilon} = 6.7 \times 10^{-5}\ s^{-1}$, and $T = 600^{\circ}\mathrm{C}$ and $\dot{\varepsilon} = 6.7 \times 10^{-5}\ s^{-1}$. The parameters obtained from the GADT are reported in Table 3-5. Most of the parameters are in acceptable ranges as described in [91]. However, the activation energy F_0 and attack velocity v_s were somewhat larger than expected. These larger values seemed to be necessary to fit the proper strain rate and temperature sensitivity observed in the experimental data.

Figure 3-2 shows the resulting stress-strain curves in tension corresponding to these material parameters obtained from the GA. The parameter set provides adequate results for the temperatures $T = 500^{\circ}\mathrm{C}$, $T = 550^{\circ}\mathrm{C}$ and $T = 600^{\circ}\mathrm{C}$ with higher strain rate. The simulated stresses are larger than the experimental data at lower strain rates. Also, the amount of straining to the saturation point appears to be under-predicted. However, these parameters were obtained when the GA had settled into a stagnant state after 3 days of iterations where the fitness function values were remaining constant between generations. Also, the initial dislocation density in total across the 48 slip systems is about $9 \times 10^{7}\ \mathrm{mm}^{-2}$ or $9 \times 10^{13}\ \mathrm{m}^{-2}$, which is a reasonable value for normalized and tempered martensitic steel [76]. Thus, the parameter values listed in Table 3-5 are employed within the crystal plasticity finite element simulations of the creep response of the 100 grain cell model reported in Section 3.2.6.

Table 3-5. Best fit material parameters obtained from GADT

Parameter	**Value**	**Units**
E	150,000	MPa
ν	0.285	dimensionless
D_0	. .	MPa
T_0	4,800	K
G_0	60,940	MPa
ρ_0	1.852×10^{6}	mm^{-2}
ν_s	2.72×10^{12}	s^{-1}
F_0	6.901×10^{-16}	mJ
$\hat{\tau}_0$	621.9	MPa
p	1.0	dimensionless
q	1.0	dimensionless
c_ρ	0.2495	dimensionless
$c_\lambda \eta_{\mathrm{part}}$	1,540	dimensionless
c_{Lock}	0.0058	dimensionless
c_{DR}	40.86	dimensionless
c_{Climb}	2.87×10^{-15}	$\mathrm{mm}^5\ \mathrm{s}^{m_C}$
m_{C}	0.3259	dimensionless
F_{climb}	3.457×10^{-16}	mJ

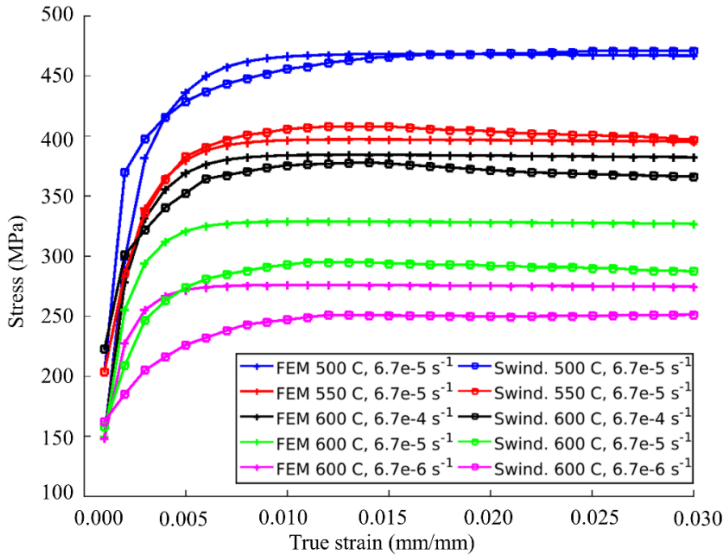

Figure 3-2. Stress-strain curves of the boundary value problem solved by GA vs. the experimental data by Swindeman.

3.4 Modeling creep response using 3D cell model and dislocation density-based model

The primary benchmark case for evaluating the performance of the crystal plasticity model for creep response is a 100-grains cell model discussed in [90] for the Norton-Bailey model. This model is also employed for the simulations with the multi-mechanism crystal plasticity model described in Chapter 5. Therefore, the description of the cell model is repeated below, with the few distinguishing features highlighted. Additionally, key results from the multi-dislocation model described in Section 3.2.4 are reproduced from [90] to highlight proficiencies and deficiencies in the model predictions that prompted the constitutive formulation revisions in Section 3.3.2.

The 3D cell model is a $(0.2\ \text{mm})^2$ cube-shaped domain containing 100 grains that is meshed with 10,402 quadratic tetrahedral finite elements. Figure 3-3 shows the

arrangement of the grains within the cell. For the CP model, the crystallographic orientation of each grain needs to be specified. The list of 100 orientations sampled from a uniform texture that is employed for the tension and fatigue simulations is also used for the cell model. As shown in Figure 3-3, all of the finite elements within the same geometric region corresponding to a grain are assigned the same Euler angles, according to the Kocks convention.

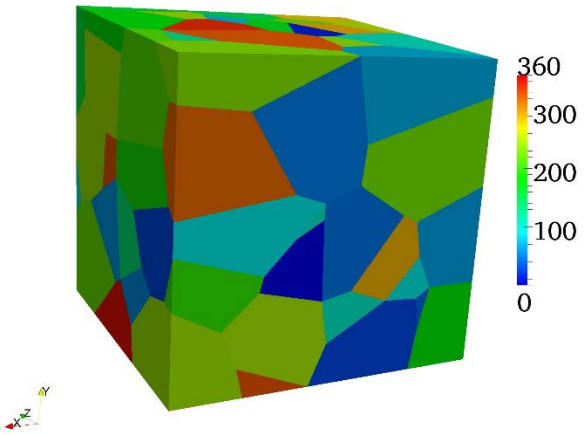

Figure 3-3. Representation of 3D cell model for CP model creep simulations: fringe plot of first Kocks Euler angle to indicate orientation of crystal lattice.

Two instances of the microstructure are considered. In the first, full continuity of the displacement field is enforced between grains in the model, to focus solely on the creep response predicted from the crystal plasticity model of dislocation climb-glide. This finite element mesh contains 15,761 nodes, which is fewer than the models in Chapter 2 because the nodes along grain boundaries have not been duplicated. In the second, 3,921 interface elements are inserted between the boundaries of the grains, leading to 25,299 nodes in the model identical to the finite element meshes analyzed in Chapter 2, and the grain

boundary behavior was specified as sliding plus cavity growth but nucleation was suppressed.

The boundary conditions on the cell consist of symmetry conditions on the faces $x = 0$, $y = 0$, and $z = 0$. The effectively incomplete periodic boundary conditions obtained through multi-point constraints (MPC) are applied on the other 3 faces of the cube. For the simulations herein, a uniform pressure is applied on the $z = 0.2$ mm face to represent the tensile creep loading. The stress is increased linearly during 100 steps at 3.6 seconds per step to reach maximum load at 0.1 hours. This stress increase period is subsequently referred to as the "load ramp period". The values of stress are set to 100, 120, and 140 MPa to correspond to the load levels investigated experimentally by Kimura et al. [96]. The temperature is set to 600°C. The evolution of the dislocation density state variables within the crystal plasticity model are expressed through stiff differential equations. Therefore, small time step sizes were required to achieve convergence of the nonlinear finite element equation solver. Table 3-6 lists the time steps for the simulations.

For the crystal plasticity (CP) model, material parameters identified through the genetic algorithm listed in Table 3-5 are used for the simulations of both grain deformation only and combined grain boundary deformation. The primary units are: stress, MPa; length, mm; time, seconds. The material parameters for the grain boundary cavitation model, listed in Table 3-7, were calibrated in [90] such the Norton-Bailey finite element simulation of the 3D cell model at 120 MPa and 600°C produces the same tertiary creep response as the experimental data reported by Kimura et al. [96].

These simulations are performed on a high-performance Linux cluster with compute nodes having 20 cores with 3.1 GHz clock speed. Each of the simulation cases requires different lengths of wall time for analysis completion. For the CP model simulation with cavity growth suppressed and sliding enabled, a typical simulation with 1300 load steps

Table 3-6: Description of time steps within CP finite element simulation of creep.

Ending step	**Number of steps**	**Time step (s)**	**Total model time (hr)**
100	100	3.6	0.1
160	60	36	0.7
200	40	360	4.7
400	200	720	44.7
600	200	1,440	124.7
800	200	2,880	284.7
1,000	200	5,760	604.7
1,200	200	11,520	1,244.7
1,400	200	23,040	2,524.7
1,600	200	46,080	5,084.7
1,800	200	92,160	10,204.7
4,000	2000	92,160	11,2604.7

Table 3-7. Material parameters for traction-separation rate equations and units

Property	**Value**	**Units**
η_b	3.6×10^{5}	$\mathrm{MPa\cdot s\cdot mm^{-1}}$
a_0	0.0005	mm
b_0	0.005	mm
D	4.444×10^{-19}	$\mathrm{MPa^{-1}\cdot s^{-1}\cdot mm^{3}}$
ψ	$15\pi/36\ \ (=75°)$	radians

required 13 hours to complete using eight cores. The statistics reported by the WARP3D output file indicate that 80% of the wall time is spent within stress updates for the crystal plasticity model. As shown in Section 3.4.1, changes to the low-level subroutines of the CP code within the past year have substantially decreased the run time.

First, three creep simulations are conducted at the applied stress levels of 100 MPa, 120 MPa, and 140 MPa for the CP only microstructural cell model. Similar to the studies for the Norton-Bailey model, the macroscopic average creep rate is computed using a finite difference calculation of the vertical nodal displacement of the top face of the cube from load step to load step. Figure 3-4 shows the variation of the creep rate during the simulation for each stress level. To more clearly interpret the response of the cell, the response of the cell model during the first 10 hours is plotted on a larger set of axes in Figure 3-4(a), and the response under the constant applied stress is shown in Figure 3-4(b).

During the load ramp period, the strains developed in the cell remain essentially elastic because the applied stress is below the yield stress of the material at this strain rate (approximately 1.0×10^{-2} hr^{-1} $\approx 2.8\times10^{-6}$ s^{-1}). Thus, the observed strain rate is the elastic strain rate, which is proportional to the applied stress. After the maximum remote stress is reached at 0.1 hour, the strain rate immediately drops to the viscoplastic strain rate level corresponding to the CP equations. These strain rates exhibit a variation with applied stress, due to the exponential nature of the flow rule. Also, the 140 MPa simulation reaches a minimum creep rate after about 20,000 hours, indicating that the CP model captures the effects of both transient and steady state creep. However, the contribution observed for grain boundary sliding is typically larger than the reduction in creep rate shown in Figure 3-4(b). Here, the creep rate drops by a factor of 10 over the duration from 10 hours to 10,000 hours. More importantly, the stress dependence of the

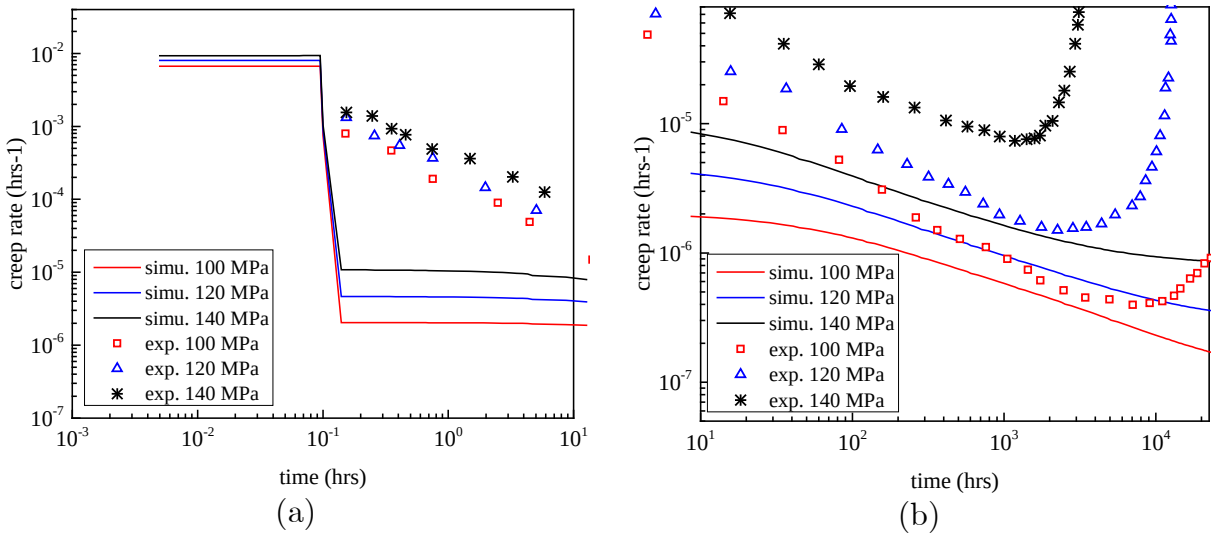

Figure 3-4. Macroscopic cell strain rate (/h) versus model time (h) for cell model without grain boundaries as a function of remote applied stress. (a) early portion of the creep response; (b) later portion of the creep response.

CP model under-predicts the variation in the experimental data [96]. This discrepancy may be due to missing features in the proposed model, such as the trapping of mobile or free dislocation density within subgrain structures that lead to slowly decreasing rates of plastic strain during transient creep.

The second set of creep simulations incorporates the grain boundary mechanisms of sliding and cavity growth. Figure 3-5 shows the results for creep strain rate as a function of time for the imposed stress levels of 100, 120, and 140 MPa. The accuracy of the crystal plasticity model is quite striking for the 120 MPa load level, for which the interface material parameters were calibrated. While the minimum creep rate is overpredicted by a factor of 5, the time to minimum creep rate is much closer, at about 1,000 hours compared to 2,000 hours in the experimental data. The computed solution is also reasonable for the 140 MPA stress level. However, the creep strain rate for 100 MPa is

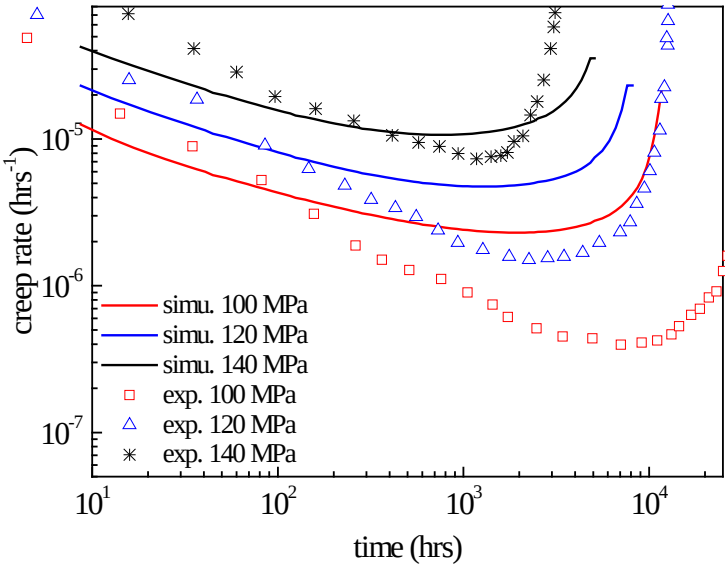

Figure 3-5. Macroscopic cell strain rate (/h) versus model time (h) for cell model with cavity growth and with sliding on grain boundaries as a function of remote applied stress.

overpredicted during much of the simulated creep lifespan, and the simulated strain rate variation is less compared to the experimental data. Each of the computed strain-rate curves appear flatter than the corresponding measured curves, meaning that less evolution of the microstructure is captured in the model during early creep life. As indicated by the results for the CP-only model, the characterized stress-dependent features of the crystal plasticity material flow rule require modification to capture this variation correctly.

The overall trends shown in Figure 3-5 indicate that the current CP model overpredicts the creep strain rates experienced within the 3D cell model. These preliminary results are impacted by several factors. First, the crystal plasticity material parameters are calibrated to match the stress-strain curves for older specimens of Grade 91 tested by Swindeman [25]. Second, the finite element models used for the calibration process contain only one solid element where the grains are approximated using the isostrain assumption. Third, the material parameters for the grain boundary constitutive models as well as the

NB model for the grains are calibrated together to match the minimum creep rate and tertiary response of the experimental data from Kimura et al. [96]. Nonetheless, an extensive study of different material parameter sets for the crystal plasticity and interface constitutive models did no produce an improved fit to the experimentally observed primary creep behavior while simultaneously matching the tensile stress-strain curves from Swindeman [25]. This discrepancy suggested that a different creep deformation mechanism is active at the lower stress levels that is not captured in the proposed model in Section 3.2, thereby prompting the investigation of the multi-mechanism model in Chapter 4.

3.5 Conclusions and recommendations for multi-mechanism model for creep deformation in prior austenite grains

A dislocation density-based model including effects from statistically stored and geometrically necessary dislocations was developed for modeling the creep and fatigue response of Grade 91 and partially implemented within a crystal plasticity framework. While some positive features were exhibited by the multi-dislocation density-based model in Section 3.3, several drawbacks of this model were also identified. First, the simulated creep curves did not capture the long duration of primary creep exhibited in the experimentally measured response, which could affect the history of stress concentrations at triple points and grain boundaries that lead to the eventual acceleration of creep strain rate. Second, the stress-sensitivity of the model was less than the measurements of Grade 91, so that the differences of minimum creep strain rate were not well approximated at load levels other than 120 MPa in Figure 3-5. Third, experimental data for minimum creep strain rate obtained by Kloc et al. [97] exhibit a change in deformation mechanism at applied stress below 100 MPa at 600 C. Figure 3-6 shows the variation of minimum

strain rate for different stresses from two Grade 91 creep test data sets; other sources show similar trends with power law relationship with $n=1$ below 100 MPa and $n>10$ above 100 MPa. Fourth, the previous model contained hardening variables representing the dislocation density on each of the 48 BCC slip systems. Several studies, such as Section 3.4.3, indicated that the local anisotropy of the crystal plasticity model did not have a significant effect on the bulk response of the cell model during creep simulations. Without local stress or strain measurements of crystal-scale deformation during creep tests, the added computational expense from tracking many state variables at each integration point was difficult to justify.

In pursuit of understanding the deformation mechanism transition in Grade 91 at lower operating stresses at temperatures at or below 600 C, a multi-mechanism crystal plasticity model is proposed in the following section that is a combination of dislocation creep and diffusional creep. These two mechanisms, described subsequently, are assumed to occur simultaneously through motion of different types of defects (dislocations and atoms/vacancies), and thus the strain rates from each are summed together. This CP modeling framework provides enhanced capabilities compared to the isotropic viscoplastic models for resolving the distribution of stress within the prior austenite grains and other substructure features. Predicting the evolution of these driving stresses is crucial for capturing both the loss of creep resistance within the grains as well as the local stress state along grain boundaries that influences the rates of cavity nucleation and growth.

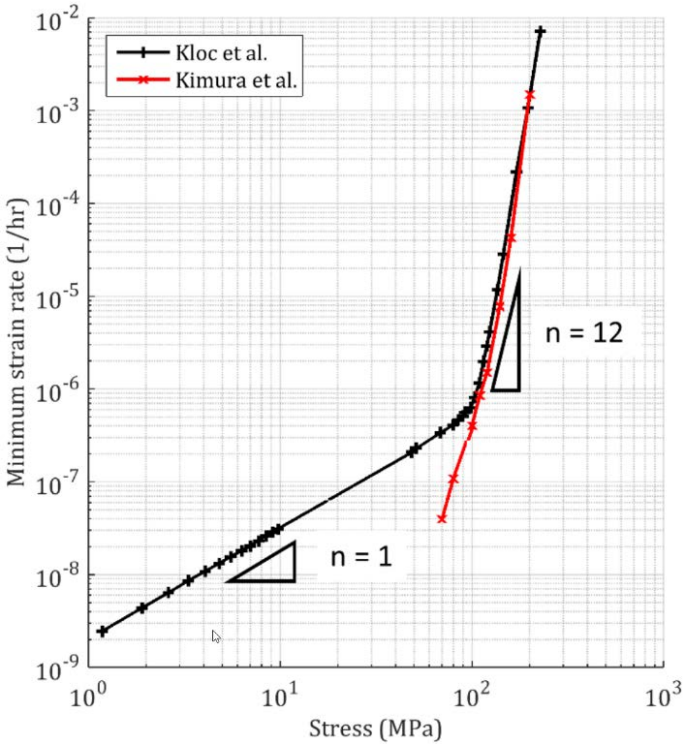

Figure 3-6. Experimental creep results from [98] and [29] for minimum creep rate of Grade 91 loaded in uniaxial tension at 600 °C

Chapter 4

COMBINED CRYSTAL PLASTICITY AND GRAIN BOUNDARY MODELING OF CREEP IN FERRITIC-MARTENSITIC STEELS: THEORY AND IMPLEMENTATION

4.1 Introduction

The modified 9Cr-1Mo-V alloy (Grade 91) was developed for good high temperature creep performance in Liquid Metal Reactors (LMRs) by Oak Ridge National Laboratory and Combustion Engineering [99, 100] and since then is commonly used as high temperature structural components in fossil and petrochemical plants. Section 2 below describes its grain structure, precipitates, and other major microstructural features. Next generation power reactor concepts are calling for higher operating temperatures to improve efficiency and economy while maintaining a long design lifespan [101]. However, test data or material response knowledge of creep deformation and rupture is required for maintaining adequate design margins. Since sixty-year creep experiments are not practical, designers typically extrapolate expected long-term properties from available relatively short-term experiments conducted at higher stresses [102]. These extrapolation methods may produce non-conservative predictions since the deformation and rupture mechanisms of Grade 91 are often observed to differ between low (service) and high (testing) stress regimes [98, 103, 104].

Physically-based microstructural modeling provides an alternative manner to quantify long-term creep response by incorporating the relevant deformation mechanisms at the microscale to simulate macroscale properties, providing a rational basis as opposed to empirical models to extrapolate away from the testing conditions used to calibrate the model. Early Grade 91 constitutive models such as [94] were developed from unified

phenomenological models [105, 106], and thus do not contain information about the microstructure evolution. Many experimental characterizations of Grade 91 during and after creep tests [80, 81, 103, 107, 108] reveal a coarsening of the dislocation-rich substructure and the appearance of coarsened precipitate phases such as Laves and Z-phases. This evidence has led to a series of physics-based macroscale models for creep based on the alternating climb and glide of dislocations [93] influenced by the coarsening of precipitates, although at lower stresses viscous diffusion of point defects is also present [104].

Basirat et al. [109] developed a dislocation creep model with mobile and immobile fractions united with a continuum damage mechanics treatment of void growth. Another model [110] emphasizes the coarsening of the smaller MX precipitates as a contributor to creep strain rate acceleration. Recent developments by [111, 112] have led to a dislocation density and precipitate evolution model that captures Grade 91 creep response across a range of applied stresses and temperatures. Fatigue and creep-fatigue in Grade 91, while not addressed by the model proposed herein, is also important to high temperature operations in fossil and nuclear plants, and several models exist [113, 114] that are physically based on dislocation mechanisms leading to cyclic softening.

A common aspect of the aforementioned continuum approaches is their limited ability to resolve the local distributions of stress and damage across the microstructure that drive the creep rupture process [115, 116], specifically in Grade 91 at the scale of crystalline grains. Crystal plasticity (CP) finite element modeling is targeted at this length scale to resolve the anisotropic motion of dislocations along slip systems at preferential orientations. Several phenomenological and dislocation density-based CP models exist for Grade 91 [117-122] but mainly target the response at higher strain rates associated with yielding, fatigue, and larger cracks. Crystal plasticity modeling of creep historically has been limited to single crystal simulations of Ni-based super alloys [123, 124]. Only in the

last couple years have polycrystalline models with dislocation climb mechanisms been developed for high temperature creep modeling [125], such as a model for Grade 91 including particle coarsening [126].

While Grade 91 microstructural evolution during creep is heavily influenced by dislocation mechanisms within the grains, an equally large body of experimental and modeling evidence exists for the role of cavity nucleation and growth on creep strain rate acceleration and creep rupture. Post-mortem and in-situ characterizations of creep specimens [127-131] reveal distributions of cavities of varying size both within grains and particularly along prior austenite grain boundaries. Research on ductile fracture by void growth in elastoplastic materials was initiated e.g. by [132, 133]. Subsequent models for cavity growth along grain boundaries, stemming from the plastic dilatation models of [134], were launched by [11, 28] from computational studies of viscoplastic materials containing individual spherical cavities. Later enhancements [6, 28, 104, 135-140] have produced constitutive equations for growth of continuously distributed cavity populations subjected to varying states of stress triaxiality. Other authors [141] propose formulations for individual cavity elements that are assembled into networks along grain boundaries. These distributed population cavity growth models have been applied, e.g. by [142, 143], to simulate growth of specimen-scale cracks via length scale transition methods. Kassner and Hayes [144] have reviewed the literature prior to 2003 on cavitation in metals mediated by diffusion and creep in the vicinity of grain boundaries; later works have included the extension to elliptical voids and further resolution of issues with triaxiality [145, 146]. Extensions to other materials such as ceramics [147, 148] have studied the transitions between creep-controlled vs diffusion-controlled regimes as well as solving coupled problems of mass diffusion by pressure gradients along grain boundaries [149].

Nonetheless, the aforementioned studies on cavity growth and nucleation along grain boundaries have almost exclusively been limited to two-dimensional analyses of idealized

or irregular grain shapes. Meanwhile, the limited available three-dimensional polycrystalline models of creep cavitation [150, 151] reveal a greater level of constraint against both boundary sliding and opening which dampen the overall creep strain rates. Additionally, the background material in neighboring grains is represented as an isotropic viscoplastic material via the Norton-Bailey model, thereby neglecting the additional stress field heterogeneity that develops from anisotropy as well as possible transitions in active dislocation mechanisms. Therefore, a need exists for combining crystal plasticity finite element modeling of grains with cavity growth and nucleation along grain boundaries within three-dimensional micromechanical models to understand the relative roles of these mechanisms throughout the creep life of a single specimen and at different load levels across multiple specimens.

The present two-part work aims to develop such a microstructural model for analyzing creep in Grade 91 ferritic-martensitic steel. The model includes deformation mechanisms from dislocation and diffusional motion within the prior austenite grains and viscous sliding and cavity growth and nucleation along grain boundaries, considered to be the material's primary deformations modes. The physically-based cavity growth model extends from the smeared cavity population model of [11, 27, 28] by including the effect of creep strain and stress triaxiality from material points in the grains next to the grain boundary. These models are implemented into a nonlinear finite element code using both solid and interface finite elements that explicitly capture these features in the geometry of a cell domain representative of a Grade 91 microstructure. The influence of grain boundaries is first studied within a linear elastic microstructural cell model to quantify the effect of stress concentrations and mesh resolution on interfacial tractions. Next, simulations of uniaxial creep under 100 MPa stress at 600 °C are conducted, and the relative role of each mechanism during the stages of primary, secondary, and tertiary creep is analyzed. The second part of this work further validates the cell model and its

various deformation mechanisms against other short-life creep tests, provides predictions of creep response at longer-life at lower stresses, and analyzes the effect of varying levels of stress triaxiality on the creep rupture time.

The remaining sections are organized as follows. Section 2 identifies the most prominent mechanisms of the microstructural response in Grade 91 in the creep regime. Section 3 provides the constitutive equations for the grain and grain boundary models. Section 4 lists key aspects of implementing these models. Section 5 describes a study on traction oscillations, the calibration of the model parameters, and a mechanism decomposition study at 100 MPa loading during creep simulations. Conclusions are drawn in Section 6.

4.2 Material and Physical Mechanisms Modeled

Grade 91 has a hierarchical microstructure [6, 137] within the prior austenite grains (PAG) depicted in Figure 4-1. Several martensitic blocks form during normalizing and represent different austenite to martensite lattice transformation variants. Each PAG typically contains several parallel groups of blocks called packets. Subsequent tempering leads to the formation of parallel laths within each block [138]. These features' typical length scales range from about 30 μm diameter for the approximately equiaxed PAGs down to the laminar lath structures with internal layer width of 0.2 μm.

The initial dislocation density in Grade 91 is a high value, typically around 10^{+13} m^{-2} [6], and the local density within the dense networks of lath boundaries is even greater. A large fraction of the dislocation density within lath interiors is lightly trapped and thus easily mobilized during creep loading. The Grade 91 microstructure is also distinguished by a peppering of carbides and nitrides. Firstly, $M_{23}C_6$ precipitates, with M denoting an alloying species, tend to cluster along PAG and packet boundaries [6, 137]. These

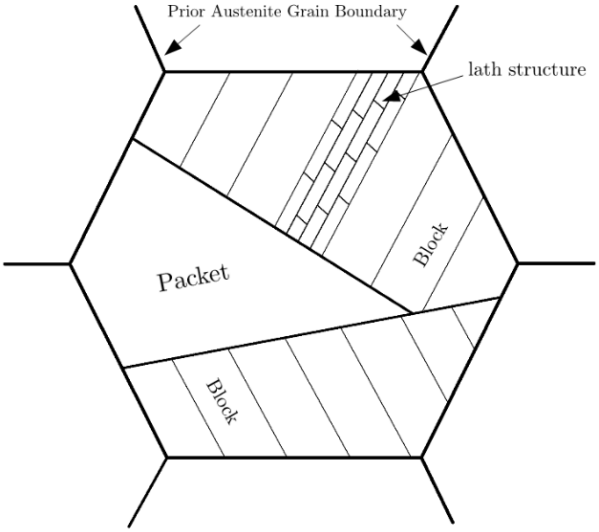

Figure 4-1. Schematic of hierarchical features in Grade 19 microstructure

precipitates with diameters around 100 nm [104] provide increased creep strength to Grade 91 due to their relative stability at high temperatures and their action to pin the dislocation networks. Secondly, finer MC and MN precipitates with sizes about 20 nm are more uniformly distributed across packet and block interiors. Other Laves and Z phases tend to form by coarsening under sustained stress and temperature during service conditions [152-154].

These outlined metallurgical features of Grade 91, differing from other common high-temperature materials such as austenitic alloys, have implications on its macroscopic creep response. For example, within the service temperature range 550-650 °C, these 9-12 Cr steels undergo extended periods of primary creep, with a creep rate that diminishes logarithmically down to a minimum creep rate [29, 104, 130]. This material does not exhibit a prolonged period of "steady state," or secondary, creep at the minimum. Rather, the creep rate begins to progressively accelerate into the tertiary regime, with the time to fracture often scaling with the time to reach the minimum creep rate.

The principle deformation mechanisms in Grade 91 during primary and secondary creep are dislocation motion and point defect motion. The early-time response is characterized by reduction in mobile dislocations [116], which are thermally and mechanically activated, that move across the lath interiors and are entangled in the lath boundaries [80]. Subsequently as the minimum creep rate is approached, the kinetics of the high density of immobilized dislocations are governed by climb over precipitates and other recovery mechanisms [104], manifesting as a power-law dependence of stress versus creep rate. In parallel, point defects such as vacancies can use both subgrain, block, and packet boundaries along with dislocation cores as diffusional highways, since the reduced lattice coherence in these regions increases their effective diffusivity. As a reasonable upscaling of these hierarchical features, the defect network may be assumed to be uniformly geometrically distributed, resulting in effective isotropic diffusion at the PAG scale, with an apparent linear relation of stress and creep rate.

The competition of these mechanisms appears when comparing test data from minimum state creep rates obtained from several experiments and load levels. Figure 3-6 compiles measured minimum creep rates (of Grade 91) under uniaxial tension at 600 °C obtained on P-91 heat resistant steel by Kloc [98] and ASME SA-213 T91 by Kimura [29]. A distinct shift appears in the power-law dependence of strain-rate with stress near the 100 MPa load level. Hence, extrapolating creep lifetime from tests at higher load levels likely underestimates the strain rate and overestimates of the creep lifetime. However, creep tests at loads below 100 MPa are only rarely run to specimen failure since the lifetime exceeds 50,000 hours (6 years). These interacting mechanisms in the PAG bulk are concurrent with the evolving state of the grain boundaries under progressive deformation. A prominent mode of creep damage experimentally observed in metals, including low and high chromium alloy steels, is the formation and growth of cavities along grain boundaries [155, 156]. Creep damage evolves by a combination of nucleation of new cavities and

growth of existing cavities. Cavity expansion and coalescence reduces the intact material interfacial area, causing higher local stresses in their vicinity and also surrounding redistribution of stress to other grains. In Grade 91, post-mortem investigations of creep specimens at 600 °C [81] and 625 °C [128] reveal correlations between coarsening of $M_{23}C_6$ precipitates and emergent Laves phase at PAGB and the location of cavities. Greater numbers of cavities appeared along high-angle boundaries such as grains and packets compared to the low-angle lath boundaries. Three-dimensional images captured by synchrotron X-ray microtomography [129, 157] at various loading stages during creep in Grade 91 and high-Cr alloys also indicate congregation of cavities on PAGB, although number densities on the order of $1{\times}10^{-6}$ μm^{-3} as well as location do vary with load level. Grain boundary sliding has also been observed in Grade 91 [128, 140], which can add to the overall creep straining and also produce stress concentrations around particles and triple junctions of grains that drive cavity nucleation. While the nature of cavity growth and nucleation is not fully understood, several experimental and theoretical efforts [11, 127, 142, 158] present clear effects from the creep strain and triaxial stress state within neighboring grains and the normal traction on grain boundaries onto the growth and nucleation of cavities, leading to void coalesce and creep damage that eventually causes rupture. Thus, a physically-informed grain boundary model for creep damage must take account of the intrinsically linked processes and state in the neighboring grains.

4.3 Modeling

The review of experimental observations of Grade 91 reveals two principal mechanisms: (a) bulk motion of grains mediated by dislocation motion as well as point defect diffusion; and (b) void nucleation, growth, and coalesce on grain boundaries. These two mechanisms motivate a micromechanical finite element modeling approach allowing for both grain

boundary and grain bulk deformation, using the concept of a three-dimensional (3D) cell model. A typical microstructure realization is presented in Figure 4-3 composed of (a) prior austenite grains (PAG) represented as solid elements and (b) prior austenite grain boundaries (PAGB) represented as interface elements. Resolving both features distinctly in the model enables the determination of how the modes interact. Though our simulation cells only capture the coarsest level of the hierarchical microstructure of Grade 91, models of this sort still capture all the key microstructural deformation mechanisms causing creep and creep-rupture in the material. The constitutive relations for the grain boundary and grain bulk are discussed here, while key aspects of their numerical implementation and behavior are addressed in Section 4.

4.3.1 PAGB constitutive model

Each of the approximately planar PAGBs in Grade 91 can add to the overall creep deformation both through its in-plane (tangential) sliding and out-of-plane (normal) opening mechanisms. According to Section 2, we ascribe their opening deformation to cavity formation, growth, and coalescence. The modeling approach employs initially zero-thickness two dimensional (2D) interface elements on the boundaries of 3D PAG, as shown in Figure 4-3 (b), with an associated traction-separation (cohesive) model. The cohesive model for cavity nucleation, growth, coalescence and viscous grain boundary sliding derives from multiple decades of effort starting with Ashby and co-workers [11, 28, 139], and more recently by Sham and co-workers [12, 159]. Our efforts are the first to extend the model to three dimensions that enables far more realistic (geometrical) representations of the surfaces connecting grains. Modifications are also proposed in the near coalescence phase of deformation, the degradation of sliding viscosity under large-scale cavitation, and in the nucleation of cavities.

4.3.1.1 Cavity nucleation and growth

The interface-cohesive model approach herein adopts a smeared representation of the cavities along PAGB as opposed to tracking individual cavities. Hence, the primary state variables at integration points in the interface elements are average cavity radius a, center-to-center spacing $2b$ between adjacent cavities, and number density N per surface area. Nucleation increases the cavity density, growth increases the cavity size, and both contribute to increasing normal separation and decreasing normal traction along PAGB. Note that a uniformly spaced rectangular array of cavities is assumed, such that the number density and cavity spacing are related by $N = 1/\left(\pi b^2\right)$, and that the ratio $\left(a/b\right)^2 \leq 1$ represents the porosity of the grain boundary.

While grain boundary cavities are believed to form at high temperatures due to e.g. cracking/debonding of $M_{23}C_6$ precipitates, stress concentrations, and dislocation slip band pileup [11], the challenges of directly observing nucleation have hindered the quantification of its mechanisms and rates. Existing studies [127, 156, 160] indicated that the continual cavity nucleation process is moderated by local creep strain rates in neighboring grains, with an initialization threshold related to the accumulated creep strain. A cavity nucleation model reflecting these observations was developed by [142] and posits that the initial number density N_I (e.g. cavities/mm^2) evolves according to traction and creep rate as follows:

$$\dot{N} = F_N \left(\langle T_n \rangle / \Sigma_0 \right)^{\beta} \dot{\varepsilon}_{eq}^{C} \tag{4.1}$$

where F_N is a rate constant, ε_{eq}^{C} is the von Mises equivalent creep strain from the neighboring PAG as defined in Section 3.2 (4.17), T_n is the normal traction, $\langle \bullet \rangle$ denotes the Macaulay bracket returning the positive part of its argument, Σ_0 is a normalization parameter, β is a traction exponent typically taken as 0 or 2, and a superimposed dot

denotes material time derivative. Nucleation occurs when the threshold relation (4.2) is satisfied:

$$S \geq S_{thr}, \qquad S = \left(\langle T_n \rangle / \Sigma_0 \right)^{\beta} \varepsilon_{eq}^{C}, \qquad S_{thr} = N_I / F_N \tag{4.2}$$

Lastly, both experimental observation and [142] suggest that the cavity number density reaches a saturation $N_{\max}$ beyond which creep straining does not form new cavities.

Once nucleated, cavities grow by two interacting mechanisms: (a) diffusion of atoms along the cavity periphery and (b) creep deformation of the locally surrounding material. Figure 4-2 depicts the geometry of the cavity and this material flow.

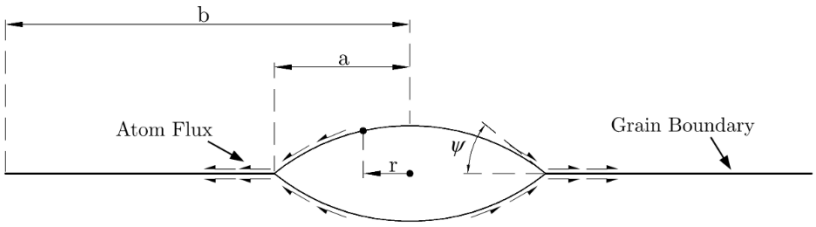

Figure 4-2. Idealized grain boundary cavity, showing atom flow from cavity surface towards its tip into the grain boundary

Detailed finite element models of individual cavities embedded in viscoplastic background material [11, 28] have produced relations for the cavity volumetric growth rate $\dot{V}$. While the diffusional flow is driven solely by the interface normal traction T_n, the creep contribution is also affected by the grain creep strain rate $\dot{\varepsilon}_{eq}^{C}$ and the stress triaxiality according to the ratio of mean stress σ_m and von Mises equivalent stress σ_{eq} (see Section 3.2). Other researchers [6, 28, 104, 135-140] have enhanced these models to fit responses of discrete voids over a wide range of triaxialities and porosities $(a/b)^2$. Our model adopted for Grade 91 cavity growth, stemming closely from [28], is expressed in (4.3) – (4.13) and relates $\dot{V}$ to the evolving cavity radius $\dot{a}$ and normal grain boundary separation rate

$[\![\dot{u}_n^{(i)}]\!]$, with the superscript (i) denoting the irrecoverable portion. The superscripts (d) and (c) indicate respectively the contributions from diffusion and creep, and the subscripts L and H indicate respectively the fitting relations for lower and higher levels of triaxiality.

$$[\![\dot{u}_n^{(i)}]\!] = \dot{V}_{VVNT} \Big/ \left(\pi b^2\right) \tag{4.3}$$

$$\dot{a} = \dot{V}_{VVNT} \Big/ \left[4\pi h(\psi) a^2\right] \tag{4.4}$$

$$\dot{V}_{VVNT} = \begin{cases} \dot{V}_L, \text{ if } \left|\dot{V}_L\right| \geq \left|\dot{V}_H\right| \\ \dot{V}_H, \text{ if } \left|\dot{V}_L\right| < \left|\dot{V}_H\right| \end{cases}, \qquad \dot{V}_L = \dot{V}^{(d)}\left(f_L\right) + \dot{V}_L^{(c)}, \quad \dot{V}_H = \dot{V}^{(d)}\left(f_H\right) + \dot{V}_H^{(c)} \tag{4.5}$$

$$\dot{V}^{(d)}\left(f\right) = 8\pi D \frac{\left\langle T_n \right\rangle}{q(f)} \tag{4.6}$$

$$f_L = \max\left(\frac{a^2}{(a+1.5L)^2}, \frac{a^2}{b^2}\right), \quad f_H = \frac{a^2}{b^2} \tag{4.7}$$

$$\dot{V}_L^{(c)} = \begin{cases} \dot{\varepsilon}_{eq}^C a^3 2\pi h(\psi) m \left\{\alpha_n \left|\dfrac{\sigma_m}{\sigma_{eq}}\right| + \beta_n(m)\right\}^n & \text{if } \left|\dfrac{\sigma_m}{\sigma_{eq}}\right| \geq 1 \\ \dot{\varepsilon}_{eq}^C a^3 2\pi h(\psi) \left\{\alpha_n + \beta_n(m)\right\}^n \dfrac{\sigma_m}{\sigma_{eq}} & \text{if } \left|\dfrac{\sigma_m}{\sigma_{eq}}\right| < 1 \end{cases} \tag{4.8}$$

$$\dot{V}_H^{(c)} = \begin{cases} \dot{\varepsilon}_{eq}^C a^3 2\pi h(\psi) m \left\{\dfrac{1}{1-(0.87a/b)^{3/n}} \left[\alpha_n \left|\dfrac{\sigma_m}{\sigma_{eq}}\right| + \dfrac{m}{n}\right]\right\}^n & \text{if } \left|\dfrac{\sigma_m}{\sigma_{eq}}\right| \geq 1 \\ \dot{\varepsilon}_{eq}^C a^3 2\pi h(\psi) \left\{\dfrac{1}{1-(0.87a/b)^{3/n}} \left[\alpha_n + \dfrac{m}{n}\right]\right\}^n \dfrac{\sigma_m}{\sigma_{eq}} & \text{if } \left|\dfrac{\sigma_m}{\sigma_{eq}}\right| < 1 \end{cases} \tag{4.9}$$

$$m = \operatorname{sgn}\left(\sigma_m\right), \quad \alpha_n = \frac{3}{2n}, \quad \beta_n(m) = \frac{(n-1)[n+g(m)]}{n^2} \tag{4.10}$$

$$g(1) = \ln 3 - \frac{2}{3} \approx 0.4319, \quad g(-1) = \frac{2\pi}{9\sqrt{3}} \approx 0.4031 \tag{4.11}$$

$$h\left(\psi\right) = \left(\frac{1}{1+\cos\psi} - \frac{\cos\psi}{2}\right) \frac{1}{\sin\psi} \tag{4.12}$$

$$q(f) \equiv \left(2\ln\left(\frac{1}{f}\right) - (1-f)(3-f)\right) \tag{4.13}$$

The subscripts VVNT stand for van der Giessen-van der Burg-Needleman-Tvergaard. Note that expression (4.3) for opening rate does not include a term involving $\dot{b}$ which appears erroneously in [161] and subsequent works [142, 143]. The authors intend on providing a consistent derivation of (3) for a spherical cavity accounting for mass conservation in an upcoming publication.

The additional material parameters are the grain boundary diffusion coefficient D and the equilibrium cavity tip half-angle (see Figure 4-2, typically 70°). Also, the Rice creep-diffusion interaction length $L = \left(D\sigma_{eq} / \dot{\varepsilon}_{eq}^{C}\right)^{1/3}$ is a characteristic length scale for which creep flow dominates $(a/L \gg 1)$ over diffusional flow $(a/L \ll 1)$. In the present model, we make the simplification that new cavities that are nucleated have the same radius a as current cavities.

A few notable enhancements have been applied to [11, 28] to make the model suitable for micromechanical modeling combined with crystal plasticity behavior in the grains. Firstly, the creep-drive cavity growth rate terms were derived assuming a power-law viscoplastic relation, namely $\dot{\varepsilon}_{eq}^{C} = B\sigma_{eq}^{n}$ with a constant exponent n, which explicitly appears in (4.8) – (4.10). However, the constitutive response in the neighboring grains discussed in Section 3.2 does not follow a strict power-law relation. Therefore, an effective exponent n_{eff} is computed by the solid elements as described in Appendix A.3 in accord with the evolving dominant deformation mechanism in the grains. Secondly, typical formulations of interface cohesive elements depend only on the traction vector rather than the entire state of stress as in (4.8) – (4.9). Hence, a nonlocal implementation is needed to communicate the material state from the solid elements and is discussed in Section 4. Thirdly, we modify the q function (4.13) to accelerate the growth rate for values of areal porosity f exceeding 0.25 to represent the coalescence of adjacent cavities; see Appendix A.1. Note that the original model can produce non-vanishing tractions along grain boundaries for moderately

large porosity while experimental measurements indicate the traction should vanish at lower levels.

4.3.1.2 Viscous sliding

A simple viscous sliding model is adopted at the PAGB to relate the shear traction $\boldsymbol{T}_s$ to the relative tangential slip rate $[\![\dot{\boldsymbol{u}}_s]\!]$:

$$\boldsymbol{T}_s = \eta_0 f_{sd}(a/b)[\![\dot{\boldsymbol{u}}_s]\!] \tag{4.14}$$

where η_0 is the initial grain boundary viscosity. This model extends to 3D the work of Ashby and co-workers [139, 158, 162] on grain boundary sliding in metals at high temperatures by introducing a decay function f_{sd} that degrades the effective viscosity as cavities nucleate and grow. A simple form is adopted where $f_{sd}=1$ while $a/b \le 0.5$ and degrades linearly to zero as a/b approaches 1. Note that grain boundary sliding does not explicitly contribute to the cavity growth and nucleation model. Instead, sliding displacements indirectly impact cavity growth by leading to geometric effects, such as impingement at triple points, that elevate nearby grain stresses, creep rates and normal tractions acting on grain boundaries.

4.3.2 PAG constitutive model

As shown in Figure 4-3, our cell model for the microstructural evolution of Grade 91 contains many solid finite elements grouped into regions to explicitly represent the PAG. The crystal lattice of the martensite phase is a body-centered tetragonal (BCT) crystal, which is approximated herein as a body-centered cubic (BCC) structure. A crystal plasticity model is developed to account for the effects of dislocation substructure evolution and the transition of dominant deformation mechanisms that are vital to

characterizing the evolution of the creep resistance of Grade 91 during service life [108]. The plastic anisotropy of the crystalline response gives rise to preferential directions of plastic strain that can affect the local stresses and concentrations that promote the actual evolution of defects such as cavities along grain boundaries. Additionally, experimentally obtained creep strain rates at lower stresses [98] suggest a deformation mechanism transition occurs below 100 MPa uniaxial stress at 600 °C. These trends motivated the incorporation of terms reflecting diffusional flow within the grains.

The rate-dependent crystal plasticity kinematics developed previously [87, 163] utilize the Green-Naghdi objective stress rate [17, 70, 71] as well as the elastic-plastic multiplicative split of the deformation gradient to relate the stress and strain evolution. These derivations arrive at an expression relating the unrotated Cauchy stress $\boldsymbol{t} = \boldsymbol{R}^T \boldsymbol{\sigma} \boldsymbol{R}$ to an additive decomposition of the unrotated rate of deformation $\boldsymbol{d} = \frac{1}{2}\left[\dot{\boldsymbol{U}}\boldsymbol{U}^{-1} + \boldsymbol{U}^{-1}\dot{\boldsymbol{U}}\right]$ and total inelastic strain rate $\boldsymbol{d}^{(i)}$. Note that $\boldsymbol{R}$ and $\boldsymbol{U}$ are the rotation and right stretch tensors, respectively, from the polar decomposition $\boldsymbol{F} = \boldsymbol{R}\boldsymbol{U}$. To further understand the deformation mechanism transition in Grade 91 observed in Figure 3-6, a multi-mechanism inelastic rate model (4.15) is proposed that combines dislocation creep and diffusional creep. These two mechanisms, described in subsequent sections, are assumed to occur simultaneously through motion of different types of defects (dislocations and atoms/vacancies), and thus the strain rates from each are summed together.

$$\dot{\boldsymbol{t}} = \boldsymbol{C}_o : \left(\boldsymbol{d} - \boldsymbol{d}^{(i)}\right) + \boldsymbol{R}\bar{\boldsymbol{w}}^{(p)}\boldsymbol{R}^T\boldsymbol{t} - \boldsymbol{t}\boldsymbol{R}\bar{\boldsymbol{w}}^{(p)}\boldsymbol{R}^T \tag{4.15}$$

$$\boldsymbol{d}^{(i)} = \bar{\boldsymbol{d}}^{(p)} + \boldsymbol{d}^{(d)} \tag{4.16}$$

where $\bar{\boldsymbol{d}}^{(p)}$ is the crystal plasticity strain rate, $\bar{\boldsymbol{w}}^{(p)}$ is the crystal plasticity vorticity, $\boldsymbol{d}^{(d)}$ is the diffusional strain rate, and $\boldsymbol{C}_o$ is the elastic moduli tensor in the unrotated frame.

The terms involving plastic vorticity are correction terms that consistently account for the lattice rotation [87].

In the vicinity of the grain boundaries, von Mises equivalent stresses and strains are computed from the tensorial stress and strain values in order to drive the cavity growth and nucleation:

$$\sigma_{eq} = \sqrt{\tfrac{3}{2}\boldsymbol{\sigma}' : \boldsymbol{\sigma}'}, \qquad \boldsymbol{\sigma}' = \boldsymbol{\sigma} - \tfrac{1}{3}\operatorname{tr}(\boldsymbol{\sigma})\boldsymbol{I} \qquad \dot{\varepsilon}^{C}_{eq} = \sqrt{\tfrac{2}{3}\boldsymbol{d}^{(i)} : \boldsymbol{d}^{(i)}}, \qquad \varepsilon^{C}_{eq} = \int_0^T \dot{\varepsilon}^{C}_{eq}\, dt \quad (4.17)$$

4.3.2.1 Dislocation creep

At moderate stresses and high temperature, the primary dislocation mechanism exhibited by Grade 91 [81] is alternating glide and climb over various barriers within the blocks and laths. This manifests as a power-law dependence of the steady state stress during creep tests with a larger exponent indicating the prevalence of precipitates [128]. However, several researchers also observe experimentally a prolonged period of primary creep [164], which is likely associated with the immobilization of free dislocation density remaining after the normalizing process [116] as well as viscous sliding along grain boundaries as mentioned in Section 3.1.2. As revealed in the microstructural simulations in Sections 5.3 and 5.4, both grain and grain boundary deformation terms play a role in representing the transient creep response. Therefore, we include a hardening term in the crystal plasticity constitutive equations that follow.

$$\bar{\boldsymbol{d}}^{(p)} = \sum_{s=1}^{n_{slip}} \dot{\gamma}^{(s)} \boldsymbol{R}^{pT} \left(\tilde{\boldsymbol{m}}^{(s)} \otimes \tilde{\boldsymbol{n}}^{(s)}\right)_S \boldsymbol{R}^{p}, \qquad \bar{\boldsymbol{w}}^{(p)} = \sum_{s=1}^{n_{slip}} \dot{\gamma}^{(s)} \boldsymbol{R}^{pT} \left(\tilde{\boldsymbol{m}}^{(s)} \otimes \tilde{\boldsymbol{n}}^{(s)}\right)_A \boldsymbol{R}^{p} \quad (4.18)$$

$$\left(\tilde{\boldsymbol{m}}^{(s)} \otimes \tilde{\boldsymbol{n}}^{(s)}\right)_S = \tfrac{1}{2}\left[\tilde{\boldsymbol{m}}^{(s)} \otimes \tilde{\boldsymbol{n}}^{(s)} + \tilde{\boldsymbol{n}}^{(s)} \otimes \tilde{\boldsymbol{m}}^{(s)}\right] \quad (4.19)$$

$$\left(\tilde{\boldsymbol{m}}^{(s)} \otimes \tilde{\boldsymbol{n}}^{(s)}\right)_A = \tfrac{1}{2}\left[\tilde{\boldsymbol{m}}^{(s)} \otimes \tilde{\boldsymbol{n}}^{(s)} - \tilde{\boldsymbol{n}}^{(s)} \otimes \tilde{\boldsymbol{m}}^{(s)}\right] \quad (4.20)$$

$$\dot{\gamma}^{(s)}\left(\tau^{(s)}; \tilde{\tau}\right) = \frac{\dot{\bar{\gamma}}}{\tilde{\tau}} \left|\frac{\tau^{(s)}}{\tilde{\tau}}\right|^{n-1} \tau^{(s)} \quad (4.21)$$

$$\tilde{\tau} = \tau_{y} + \tau_{w} \quad (4.22)$$

$$\dot{\tau}_w = \theta_0 \left(1 - \frac{\tau_w}{\tau_v} \right) \sum_{s=1}^{n_{slip}} \left| \dot{\gamma}^{(s)} \right| \tag{4.23}$$

Here, $\tau^{(s)} = \boldsymbol{t} : \left(\boldsymbol{R}^{pT} \tilde{\boldsymbol{m}}^{(s)} \boldsymbol{R}^{p} \right)$ is the resolved shear stress, $\boldsymbol{R}^{p}$ is the plastic rotation tensor, and $\tilde{\boldsymbol{m}}^{(s)}$ and $\tilde{\boldsymbol{n}}^{(s)}$ are the slip direction and slip plane normal unit vectors in the lattice frame for system (s) within the set of 12 primary $\{110\}\langle \bar{1}11 \rangle$ BCC slip systems. A Voce hardening model (4.23) is adopted for the strengthening resistance τ_w within the drag stress $\tilde{\tau}$ of the power-law relation for slip rate $\dot{\gamma}^{(s)}$. The remaining parameters are reference strain rate $\dot{\bar{\gamma}}$, saturation stress τ_v, and flow modulus θ_0. We remark that we also considered dislocation density-based models with unequal hardening across the expanded 48 BCC slip systems. However, we found that such sophisticated models were not needed to capture the relevant microstructural deformation mechanisms. Thus, the simplified model given by (4.21) – (4.23) was adopted to reduce the computational cost of subsequent simulations.

4.3.2.2 Diffusion

The apparently linear relation between the steady state creep rate and applied stress at lower loads [98, 165] is assumed to derive from motion of point defects along various highways, e.g. dislocation cores and grain boundaries, in the complicated microstructure of Grade 91. A continuum strain rate model for these diffusional effects is conceptualized from the flux of atoms or vacancies being driven by differences in chemical potential along the boundaries surrounding an individual grain. Atoms flow from lower-normal-stress boundaries to higher-stressed boundaries since the plating out on the latter leads to effectively lower system energy. The deviator stress provides a first-order measure of the differing normal stresses along a given grain's boundaries, such that a proper accounting

of the geometrical effects of diffusion is achieved. Thus, an effective strain rate $\boldsymbol{d}^{(d)}$ for atomic/vacancy diffusion emerges as being proportional to the deviator stress $\mathrm{dev}(\boldsymbol{t})$, both expressed in the unrotated frame:

$$\boldsymbol{d}^{(d)} = D_\eta \, \mathrm{dev}(\boldsymbol{t}) \tag{4.24}$$

where D_η is a generic diffusion coefficient to be obtained by scaling arguments and fits to experimental data. Diffusion of atoms or vacancies in pure metals is commonly differentiated into one of three classes of mechanisms according to grain-size dependence or activation energy: Nabarro-Herring creep within grains [166], Coble creep along grain boundaries [167], and Harper-Dorn creep [168, 169]. While the complicated microstructure of Grade 91 prevents a clean delineation [98], its high dislocation density and small subgrain sizes suggest that atomic diffusivity is nontrivial in these quenched and tempered alloys even at lower homologous temperatures. Note that the model (4.24) certainly does not capture the local effects of atomic diffusion along and near the grain boundaries (beyond those associated with cavity nucleation and growth) and coupled mechanical deformation and chemical diffusion modeling will be considered in future work.

4.4 Constitutive Model Implementation

The constitutive models for PAG and boundaries from Section 3 are implemented within the finite element code WARP3D [71] due to its features for interface finite elements and its extensibility to enable to nonlocal material state transfer from the solid to interface elements. Quadratic 10-node tetrahedral elements are employed with B-bar formulation of the strain field. The crystal plasticity model implementation uses an implicit backward Euler time integration scheme and solves the resulting local nonlinear equations using the Newton-Raphson method. The details of its implementation are given elsewhere [87, 163, 170]. The key equations are summarized in the Appendix A.2, with the inclusion of the

diffusional creep contribution. Another new calculation required by the interface cavity growth model is the effective power-law exponent n_{eff}. That derivation is given in Appendix A.3.

The PAGB constitutive model for cavity nucleation and growth is implemented into WARP3D using an explicit time integration strategy, which is adopted primarily to simplify the cavity growth formulas that depend on the stress state of the neighboring grains. The time-discrete evolution equations for the interface state variables from Section 3.1 are expressed in detail in Appendix A.1. Gauss quadrature with a 7-point rule is used to evaluate the internal virtual work of the quadratic interface elements, and the state variables are tracked at each Gauss point.

Several noteworthy numerical method enhancements were developed to overcome the challenges of coupling anisotropic nonlinear constitutive models in the grain and grain boundaries. Further details of the implementation and parametric studies of the PAG and boundary models for Grade 91 are contained in prior work [12, 159]. First, the $q(f)$ function in the cavity growth model was modified as described in Appendix A.1 to increase the overall numerical stability. Second, a basic adaptive time step scheme was added to WARP3D to improve convergence and efficiency in the tertiary creep regime. As shown in Section 5, the cell model is loaded by a stress that ramps up quickly and is held constant so that the cell creeps slowly for several 1,000 hours, such that a time step $\Delta t = 500$ hours is reasonable. However, the creep strain rate increases by several orders of magnitude once cavity growth progresses, and the global Newton algorithm requires a time step size less than 1 hour to avoid diverging nonlinearities. Third, the virgin response of the grain boundaries prior to cavity nucleation was approximated by adding a stiff elastic term into the traction-separation relation (4.3), essentially as a penalty contribution and also to prevent interpenetration along boundaries under compression. The linear stiffness must be carefully chosen in a narrow range for this nonlinear problem class to avoid excessive

elastic opening as well as oscillatory tractions along the PAGB. This range was determined through a sensitivity study in Section 5.1, providing new insights into interface element behavior in polycrystalline microstructural models that are gaining popularity [171, 172].

4.5 Microstructure model and algorithmic aspects

This investigation focuses on the creep response of bulk (non-weldment) Grade 91 using a 3D microstructural cell model containing 100 regions representing prior austenite grains. The polycrystalline mesh generator Neper [173] can generate both cuboid and fully periodic collections of grains by Voronoi tessellation and space-fill with quadratic tetrahedral elements, as in Figure 4-3 (a) and (c). Subsequently, interface elements are inserted into the conforming mesh using the fully automated and open source script DEIP [174-176] developed by the authors. The behavior of the two geometrical versions of the cell model are compared for creep loading in [159]. Both cells are $0.2 \times 0.2 \times 0.2$ mm^3 such that the average grain size is about 50 μm with a log-normal distribution instantiated from a random texture. The standard cuboid model (used for all simulations unless specified otherwise) has 25,229 nodes, 10,402 solid elements, 3,921 interface elements, and 467 essentially planar grain boundaries. The interested reader will find details within [12, 159] regarding these software programs and generated mesh geometries.

Each uniaxial creep simulation in this section follows a common load-hold strategy. For the cuboid cell model, symmetry boundary conditions are assigned on the three faces $x = 0$, $y = 0$, $z = 0$, and the nodes along transverse faces $x = 0.2$ and $z = 0.2$ are constrained to move together in the normal direction as a pseudo-periodic boundary condition; the driving uniaxial traction is imposed along $y = 0.2$ via multi-point constraints. The applied traction is ramped from 0 to 100 MPa during 0.1 hours in 10 equal time steps to correspond with the load-ramp period in [29]. The load is then held

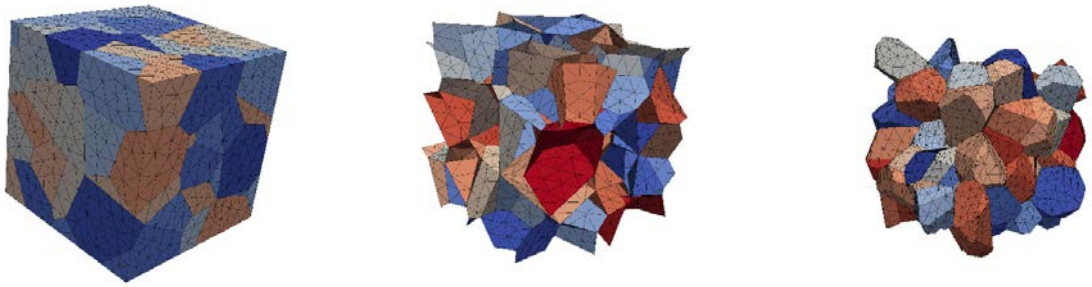

(a) (b) (c)

Figure 4-3. 100 grain cell model finite element mesh: (a) cuboid solid elements; (b) cuboid interface elements; (c) fully periodic solid elements

constant while the simulation is advanced using adaptive time stepping to track the evolution of the PAG and boundary deformation.

The cuboid cell model in Figure 4-3 (a) is employed for all of the calibration tests and creep simulations in this section, which is sufficient for uniaxial tension. The fully-periodic cell model in Figure 4-3 (c) is employed for the triaxial loading conditions in Part 2 of this manuscript. Our previous studies [159] have demonstrated that cuboid and periodic meshes with identical Voronoi grain structure and similar number of finite elements produce nearly identical cell-average creep strain response. These observations agree with the study of cuboid and periodic representative volume elements of matrix-inclusion composites in [177].

4.5.1 Oscillating tractions study

As mentioned in Section 4, several numerical challenges emerged from the coupled nonlinear grain and boundary models that caused divergence of the Newton-Raphson equation solver at the domain level or material integration level. One worrisome observation during the parameter calibration and sensitivity studies of Section 5.2 and

[159] was that the normal traction component T_n along PAGB often exhibited oscillations with an amplitude larger than the applied stress level. These artificially large tractions, believed to be numerical artifacts of the elastic stiffness K_n defined in Appendix A.1, had a detrimental effect on the time to onset of cavity nucleation and growth. Therefore, a study of this penalty parameter was performed to determine a reasonable range of its value to suppress the oscillations.

Relatively few numerical studies have been performed using finite element modeling of representative volume elements containing crystal plasticity within the grains and interface elements along grain boundaries. Most such studies have focused on brittle fracture or crack propagation rather than on ductile void growth [172, 178, 179]. Earlier studies on two-dimensional microstructures considering elasticity [180] and power-law creep [181] revealed that heightened stresses can occur at triple junctions between grains when low sliding resistance is assumed within the models. Also, a wide body of literature from finite element contact mechanics modeling identifies the large stress concentrations that emerge when resolving normal and tangential contact tractions [182], particularly for frictionless contact where the tangential stiffness vanishes.

Thus, a series of numerical tests were conducted with varying normal and tangential interface stiffness and element types to understand the source of the oscillatory traction fields. The initial geometry is shown in Figure 4-3 (a), and all grains are treated as linear isotropic elastic with $E = 150$ GPa and $\nu = 0.285$. Symmetry boundary conditions were applied on the $x = 0$, $y = 0$, $z = 0$ planes, the transverse faces are traction free, and a uniform displacement $u_x = 0.001$ mm was applied on the $x = 0.2$ face to yield an average uniaxial stress of about 750 MPa. For simplicity, the interface element formulation uses a linear relationship between the (normal and tangential) traction components T_n and T_t and the displacement gaps $[\![u_n]\!]$ and $[\![u_t]\!]$ with individual stiffness coefficients K_n and K_t

, respectively. The tangential stiffness replaces the role of viscous grain boundary sliding in order to allow static, linear simulations. Preliminary estimates of the normal stiffness suggested a range of $K_n = 1.0 \times 10^6$ to $K_n = 1.0 \times 10^8$ MPa/mm. The tangential stiffness was varied between $K_t = 1.0$ MPa/mm (approximately free sliding) and $K_t = K_n$.

Three different element types are compared: quadratic tetrahedral, linear tetrahedral, and linear hexahedral. The linear tetrahedral mesh is obtained by subdividing each quadratic element into 8 linear ones, retaining the same number of nodes. A similar subdivision strategy yields 4 hexahedral elements from each quadratic element, with a new node in the center of each face of the tetrahedral element. Mesh refinement was conducted on the linear tetrahedral mesh by uniform subdivision, and these meshes are labeled as coarse, medium, and fine in later discussions.

Fringe plots from the element-averaged stress field σ_{xx} for varying levels of K_t are presented in Figure 4-4. The extreme values on the legend are set to two standard deviations above and below the average stress. The deformed configuration is magnified 50 times to better visualize the grain boundary sliding; hence the grains appear to separate and overlap. The free sliding case $K_t = 1.0$ has the largest variations of stress about the mean. Essentially, much of the concentrations are at triple junctions, where the load transfers between grains by contact at these junctures. As the stiffness increases to $K_t = K_n = 1 \times 10^8$, the amplitude of the stress variation decreases to about 20 MPa with significantly smaller gaps between grains. Overall, while stress gradients emerge within grains, the fields are typically monotonic and do not exhibit values greatly above and below the mean next to each other within the same grain.

We next examine the interface normal traction components for the case of free sliding case $K_t = 1.0$; this represents a worst case since at 600 °C the interface viscosity provides moderate to large sliding resistance. Figure 4-5 (a) and (b) compare the traction field T_n

on the coarse quadratic mesh with low and high normal stiffness. For $K_n = 1.0 \times 10^6$, the traction field is smooth and generally indicates tension on grain boundaries oriented perpendicularly to the load axis and compression along parallel facets, with a magnitude on the same order as the stresses in Figure 4-4. In contrast, the simulation in Figure 4-5 (b) with $K_n = 1 \times 10^8$ exhibits many grain boundaries with neighboring elements having positive or negative traction with values possibly exceeding 1000 MPa. These oscillations are obviously non-physical and likely emerge from the attempts of the model to weakly enforce zero penetration along the interfaces, leading to small positive and negative displacement jumps $[\![u_n]\!]$ that are amplified through the linear traction relation $T_n = K_n [\![u_n]\!]$. To verify that this behavior is not caused by the quadratic polynomial shape functions in the interface elements, the parameters and loading are applied to the linear tetrahedral mesh in Figure 4-5 (c) and hexahedral mesh in Figure 4-5 (d). Oscillations of similar amplitude and finer frequency also appear in these results. Therefore, the coarse mesh appears incapable of accurately resolving the traction field for the free sliding and high normal stiffness case. However, we also remark that the normal displacement jumps $[\![u_n]\!]$ for the model in Figure 4-5 (a) with $K_n = 1.0 \times 10^6$ are excessively large, reaching up to 5 to 10% of the total elongation of the cell. Therefore, this lower stiffness does not accurately represent the contact or bond between the grains and thus can provide too compliant of a solution for use in the creep analyses.

Note that frictionless contact of deformable bodies, such as individual spheres under Hertzian contact as reviewed for example in [183], is known to produce sharp gradients in contact pressures that are only resolved on very fine grids and lead to oscillations on coarse grids without special numerical treatments. The present finite element mesh with only 20 interface elements per grain boundary is not sufficiently refined to capture the concentrated pressure from pinching at triple points. The normal jump field $[\![u_n]\!]$ on a

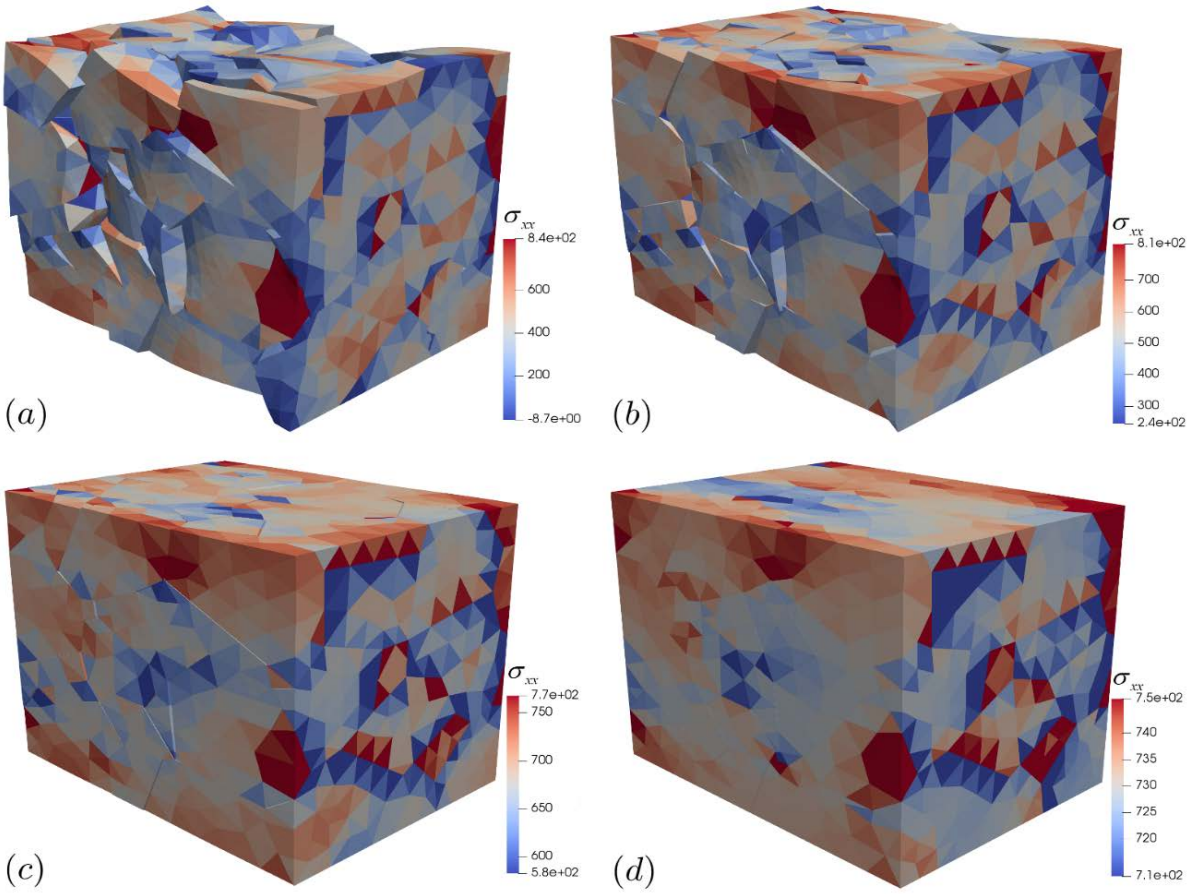

Figure 4-4. Stress field σ_{xx} for exaggerated deformed coarse mesh of quadratic tetrahedral elements with $K_n = 1\times10^8$ and (a) $K_t = 1\times10^0$; (b) $K_t = 1\times10^6$; (c) $K_t = 1\times10^7$; (d) $K_t = 1\times10^8$

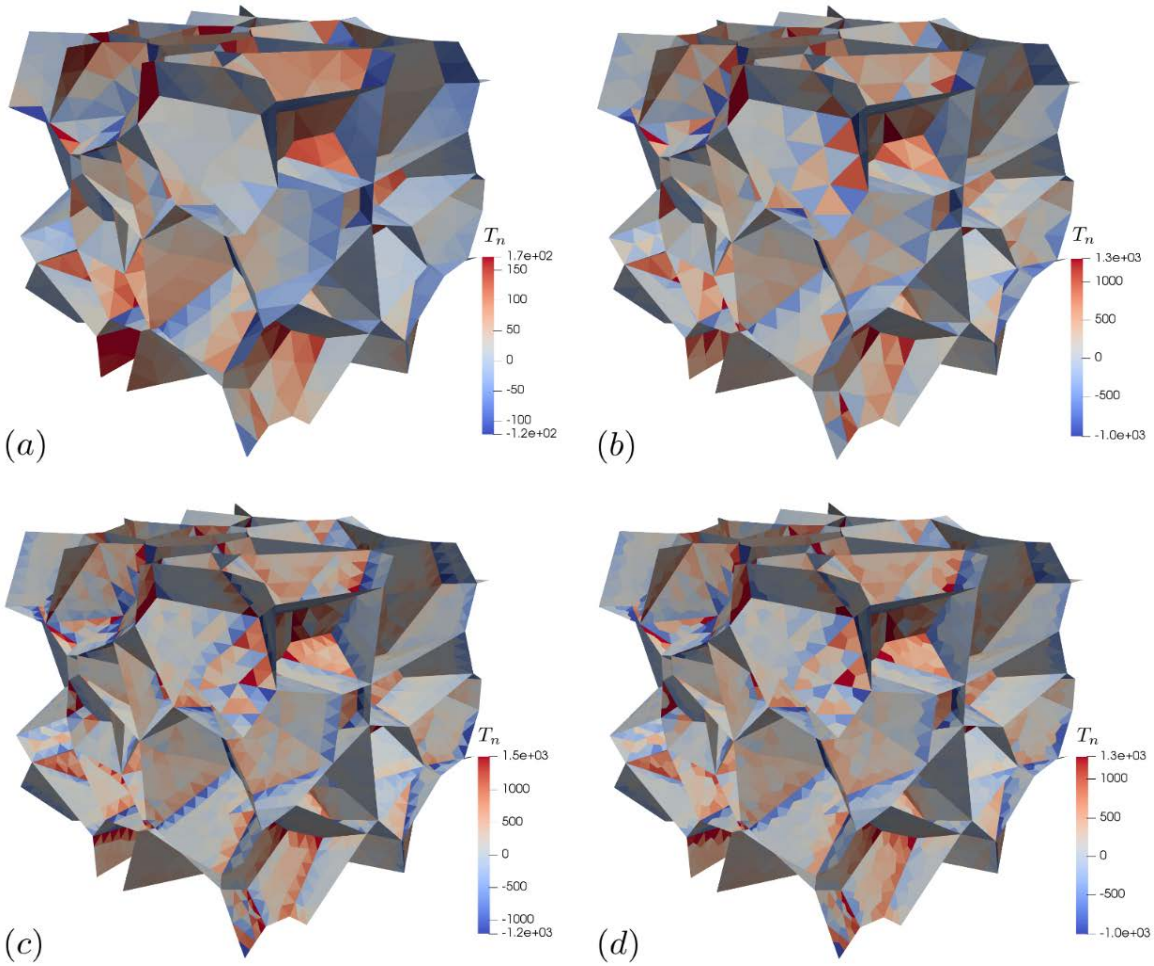

Figure 4-5. Normal traction component field $T_n = K_n [\![u_n]\!]$ on coarse mesh with $K_t = 1\times10^0$ and (a) $K_n = 1\times10^6$, quadratic tetrahedral elements; (b) $K_n = 1\times10^8$, quadratic tetrahedral elements; (c) $K_n = 1\times10^8$, linear tetrahedral elements; (d) $K_n = 1\times10^8$, linear hexahedral elements

series of uniformly bisected meshes of linear tetrahedral elements is shown in Figure 4-6. The oscillations along grain boundaries diminish as the element size decreases. Indeed, the center of PAGB facets typically have a uniform stress state with a sharp gradient approaching the juncture of multiple grains. These features emerge on the medium mesh such that this resolution could be recommended for creep analyses.

However, the medium mesh contains 153,030 nodes and 98,900, which requires about 24 hours of wall time for simulating 2000 time steps of a nonlinear creep analysis. Therefore, we return to Figure 4-4 (a) showing the overlapping grains and reconsider the interfacial material properties. Therein, the discontinuities for $K_t = 1\times10^0$ appear to more closely represent a closely-packed granular material with particles in contact along interfaces. While a certain amount of grain boundary sliding occurs at high temperatures in Grade 91, a larger value of interface tangential stiffness (and viscosity) are likely needed to more closely represent the polycrystalline material. Therefore, Figure 4-7 investigates the effect of increasing the tangential stiffness K_t upon the normal traction field, all with $K_n = 1.0\times10^8$. Notice that as the tangential stiffness is increased from part (a) to part (c), the normal traction oscillations decrease. The smoothness of the grain boundary fields is acceptable for both Figure 4-7 (b) and (c) with the larger values of K_t.

In conclusion, a reasonable range for the tangential stiffness K_t is within a factor of 10 to 100 of the normal stiffness K_n so that artificial oscillations do not appear on the coarse mesh; similar behavior was confirmed for hexahedral and quadratic tetrahedral elements. Returning to the nonlinear cavity growth models in Section 3.1, physically observed ranges for the grain boundary diffusivity of Grade 91 at the temperature of 600 C are on the order of 10^{-16} to 10^{-14} $\mathrm{MPa}^{-1}\cdot\mathrm{hr}^{-1}\cdot\mathrm{mm}^3$; see [12, 184] and references therein. By assuming the viscosity is inversely proportional to the diffusivity provides a corresponding viscosity range of 10^5 to 10^7 $\mathrm{MPa}\cdot\mathrm{hr}\cdot\mathrm{mm}^{-1}$. Thus in Section 5.2, we select an intermediate value of

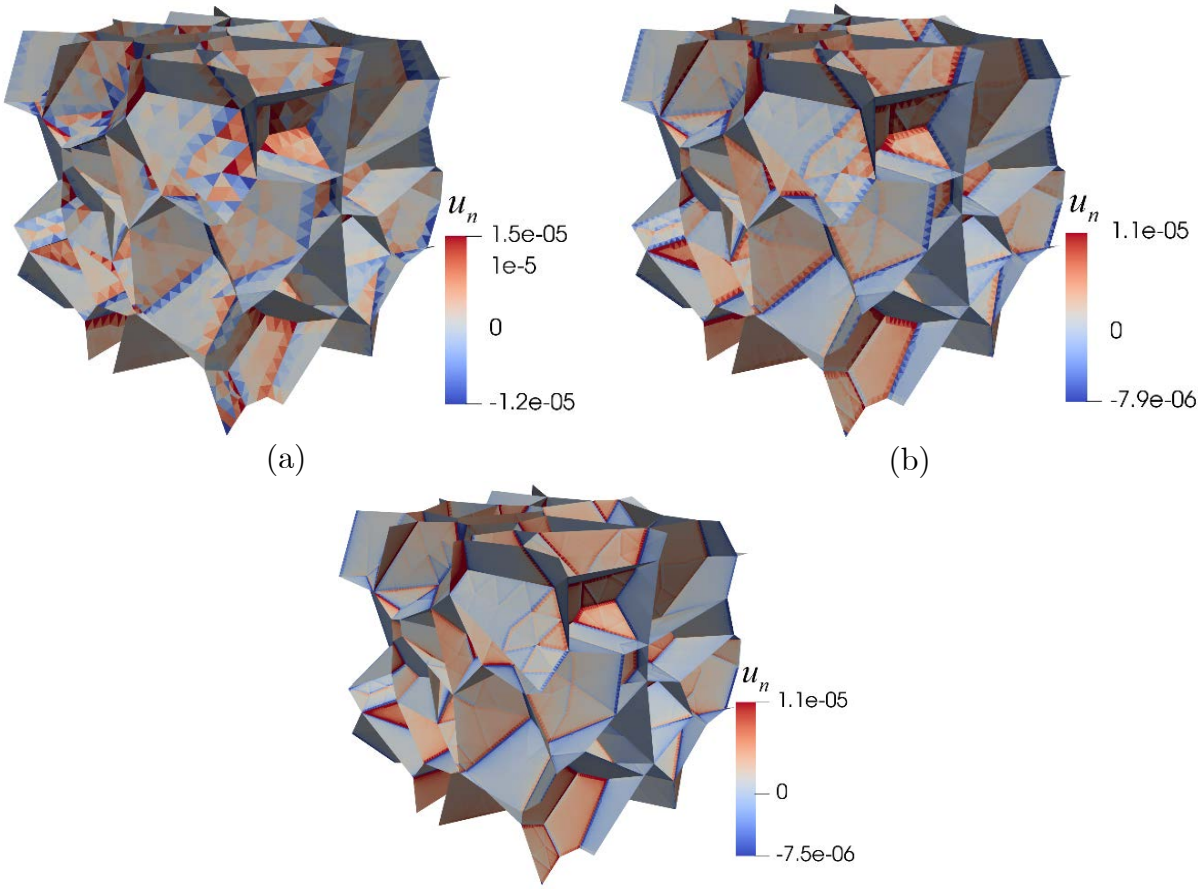

Figure 4-6. Normal displacement jump field $[\![u_n]\!]$ of linear tetrahedral elements with $K_t = 1\times10^0$ and $K_n = 1\times10^8$ on: (a) coarse mesh; (b) medium mesh; (c) fine mesh

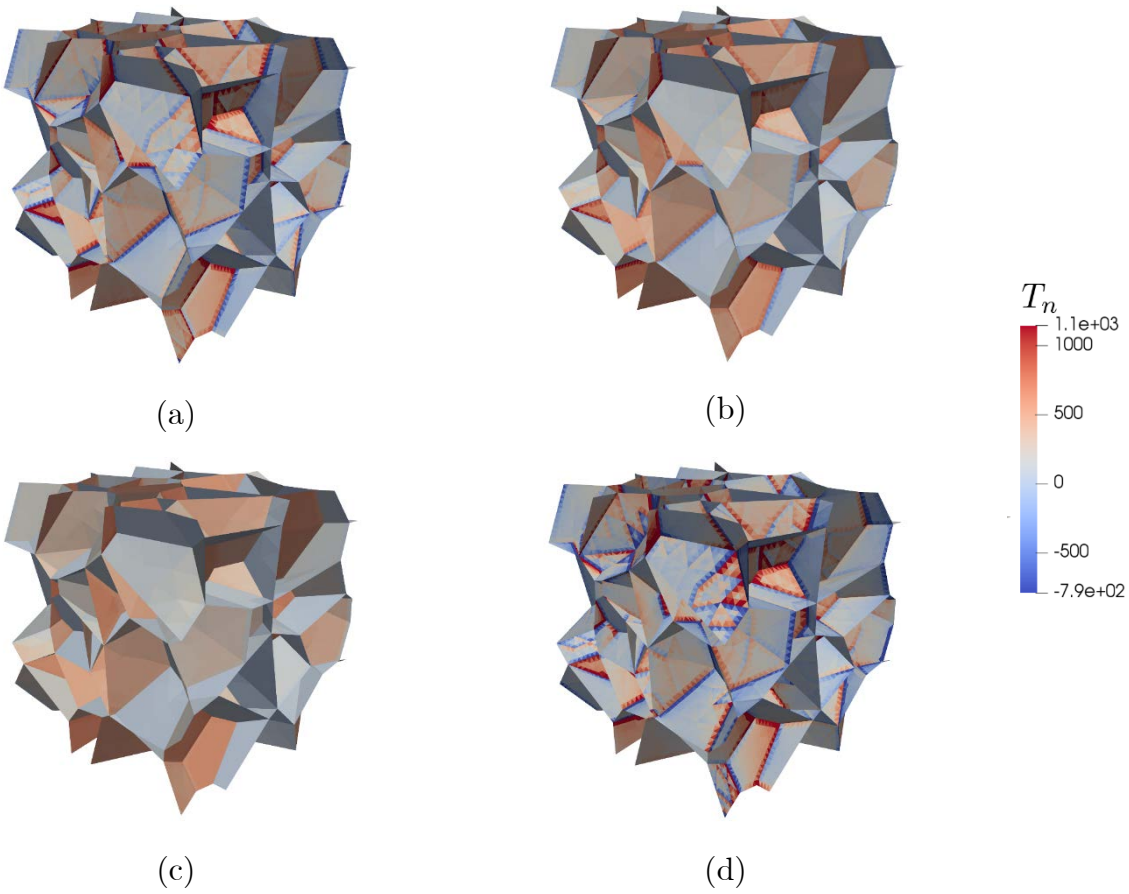

Figure 4-7. Normal traction component field $T_n = K_n [\![u_n]\!]$ with $K_n = 1\times10^8$, linear tetrahedral elements: (a) $K_t = 1\times10^6$; (b) $K_t = 1\times10^7$; (c) $K_t = 1\times10^8$; (d) $K_t = 1\times10^0$

$\eta_b = 10^6$ to capture grain boundary sliding during primary creep along with the normal stiffness $K_n = 1.0 \times 10^8$, and this combination of parameters provided stable results for the normal traction.

4.5.2 Calibration of material parameters

The combined grain and boundary constitutive models have 18 parameters to specify, summarized in Table 4-1. However, certain deformation mechanisms are most influential at particular stages of creep or particular load regimes, enabling small groups of the parameters to be fitted independently. Further details on the calibration are discussed in [159]. The elastic constants E and ν were chosen based on Grade 91 tensile tests at 600 °C, and the grain boundary normal stiffness K_n and viscosity η_b were assigned from the numerical test conclusions in Section 5.1. Next, the grain viscoplastic parameters were estimated using the experimental data for steady state creep strain rates. For applied stress exceeding 100 MPa at 600 °C, uniaxial tests reported by [29] indicate a power-law relation between minimum strain rate and applied stress with a slope of 11.78, suggesting $n = 12$ for our model. The Voce model parameters $\dot{\bar{\gamma}}$ and $\tilde{\tau} = \tau_y + \tau_v$ were also estimated from these results; the initial slip resistance was set to $\tau_y = 40$ MPa similar to other Grade 91 CP models [113, 114]. Next, the CP parameters for saturation τ_v and hardening θ_0 were determined from a series of full-field cell model simulations with cavity growth suppressed and sliding permitted, adjusted to fit the primary creep regime of cases above 100 MPa [29]. The remaining PAG model parameter D_η was established from simulations below 60 MPa to fit the steady state strain rates reported by [98] in the apparently diffusion-dominated regime. This diffusion coefficient arises from reasonable values for the diffusion and activation energy of high-chromium steels [128, 184].

Table 4-1. Grade 91 constitutive model parameters

Property	Value	Units	Property	Value	Units
E	150,000	MPa	η_b	1.0×10^{6}	$\mathrm{MPa\cdot hr\cdot mm^{-1}}$
ν	0.285	dimensionless	K_n	1.0×10^{8}	MPa/mm
τ_y	40.0	MPa	a_0	5.0×10^{-5}	mm
τ_v	12.0	MPa	b_0	0.06	mm
n	12	dimensionless	D	1.0×10^{-15}	$\mathrm{MPa^{-1}\cdot hr^{-1}\cdot mm^{3}}$
$\dot{\bar{\gamma}}$	9.55×10^{-8}	$\mathrm{hr^{-1}}$	ψ	75°	degrees
θ_0	800.0	MPa	Σ_0	200	MPa
D_η	1.2×10^{-9}	$\mathrm{MPa^{-1}\cdot s^{-1}}$	F_N/N_I	2.0×10^{4}	dimensionless
β	2	dimensionless	$N_{\max}/N_I$	1.0×10^{3}	dimensionless

Lastly, the PAGB cavitation parameters were adjusted to fit the cell-averaged strain rate to the measured tertiary creep regime at stresses above 100 MPa [29]. Estimates for some of the physically-based parameters can be established from experimental measurement, such as grain boundary diffusivity D [12, 184] and initial cavity spacing b_0 and size a_0 by assuming that precipitates and cavity nucleation sites are highly correlated. Regarding cavity nucleation, the maximum areal density of cavities N_{max} and traction dependency exponent β can be estimated from post-failure microstructural characterization. The remaining parameters F_N and Σ_0 were adjusted as mentioned in [159]. We remark that identical PAGB parameters were assigned to all interface elements in the cell model. Meanwhile, some experimental evidence supports a misorientation or grain boundary energy dependence for the viscosity and diffusivity [185-187]. We intend to study the effect of non-spatially-uniform PAGB parameters in future work.

4.5.3 3D cell model creep response for various deformation mechanisms

To better understand the effects of each mechanism within the total cell response, we performed a series of creep simulations at 100 MPa loading with certain modes suppressed. Figure 4-8 reports the evolution of the cell volume average strain rate and total strain in the loading direction. In the legend, the mechanisms are denoted by CP=crystal plasticity, D=diffusion, S=sliding, C=cavity growth, and N=nucleation; the listed symbols for a given curve imply the mechanism was included in that simulation. The interface mechanisms of sliding, growth, and nucleation were suppressed by setting $\eta_b = 1.0\times10^{12}\ \mathrm{MPa\cdot hr\cdot mm^{-1}}$, setting radius evolution $\dot{a}=0$, and setting number density $\dot{N}=0$, respectively. These results clearly present sequentially enhanced physics in the cell model. The CP-only case exhibits the slowest strain rate that continually decreases during the entire lifetime and does not reach a steady state.

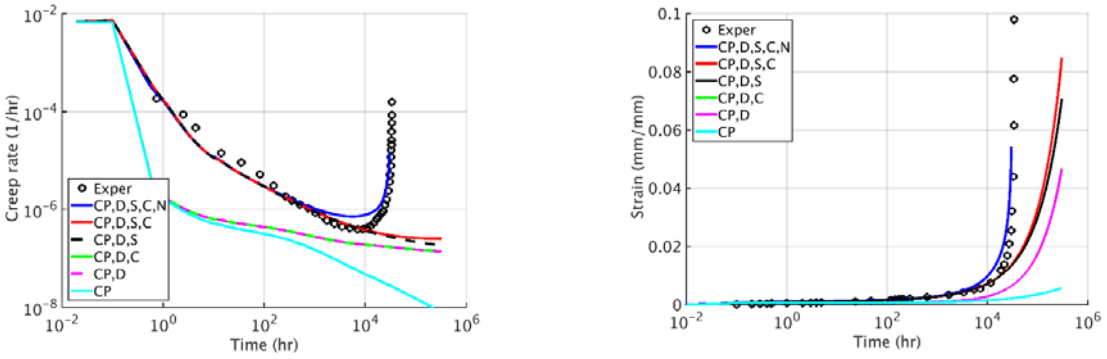

(a) (b)

Figure 4-8. Cell-averaged quantities from uniaxial creep simulation at 100 MPa applied stress versus test results from [29]: (a) creep strain rate; (b) accumulated strain

Recall that only one hardening variable is included in the Voce model (4.23) to represent the immobilization of dislocations [116]. The combination of the CP parameters and large

stress exponent $n=12$ leads to continued hardening that does not saturate by 100,000 hours. Adding the grain diffusion mechanism (CP,D) does produce a minimum strain rate in the model of about 3×10^{-7} 1/hr. The linear stress exponent for diffusion (4.24) implies a lower strain rate sensitivity and also prohibits the average strain rate from dropping unphysically low. Neither of these curves exhibit accelerating strain rates since the grain boundary modes are suppressed. Also, the case with cavity growth included (CP,D,C) does not show acceleration either and appears identical to the (CP,D) result, suggesting that sufficient peak stresses are not reached in the neighborhood of grain boundaries to drive cavity growth.

Next, the (CP,D,S) case in Figure 4-8 (a) including sliding exhibits a larger increase in strain rate during the early time regime. The gradual reduction in strain rate during 1000 hours aligns with the experimental data from [29]. In light of the studies in Section 5.1, grain boundary sliding is shown to create stress concentrations at triple points, where grains impinge on each other. These higher local stresses lead to more dislocation creep in the grains and an overall higher strain rate. The extended period of continually decreasing strain rate does indicate that certain grain boundaries relax their shearing traction by sliding and after a period of time can no longer deform once a grain becomes constrained by its neighbors in contact. Once all boundaries have locked up, the average strain rate approaches to the (CP,D) case without sliding by about 100,000 hours. Next, when cavity growth is included in (CP,D,S,C), the response curve remains similar to (CP,D,S) up to 10,000 hours, after which cavity growth adds a slight acceleration to the strain rate. This occurs only after 2% total accumulated strain in Figure 4-8 (b) and upwards of 10% strain at peak locations in the cell model, which is much later than when the experiments show acceleration.

Lastly, the simulation response (CP,D,S,C,N) possesses all the mechanisms including nucleation. The minimum strain rate in the simulation is actually greater than the rate

from the experimental data. Note that the material parameters in Section 5.2 are specified so that the computed strain rate response curves across several load levels have a balanced error compared to [29]; see Part 2 and [159] for other load levels. Nonetheless, the time (6,000 hours) to minimum creep strain rate is well captured. Note the (CP,D,S,C,N) curve exhibits tertiary creep effects while (CP,D,S,C) does not. We explain this large jump in strain rate by exploring the other output quantities of the cell model, such as the evolved cavity number density. As reported in [159] as well as in Section 5.4, the maximum number density across all interface elements in the cell model at 100 hours is 100 times larger than the initial number density. This greater number of cavities can also grow, leading to reduced traction on some boundaries and shifting of the stress paths within the microstructure to induce overall larger average creep strain rate.

4.5.4 Complete model response and decomposed creep strain rates

The cell volume-average creep strain rate for the complete model in Figure 4-8 is an aggregate response of several mechanisms across the 100 grains and many elements in the domain. Therefore, domain-average strain rate values are computed for the individual mechanisms within this simulation to extract the contributions. The dislocation creep rate $\boldsymbol{d}^{(p)}$ and the diffusional creep rate $\boldsymbol{d}^{(d)}$ are directly outputted for each solid element and integrated over the cell domain. The total strain rate $\boldsymbol{d}$ is obtained as the finite difference in time of the elemental strain field; the difference between the total and the plastic strain rates represents the elastic strain rate. The effective strain from the interfacial deformations (opening and sliding) are obtained according to [12] by integrating the tensor product of the displacement jump vector and interface unit normal, and the effective strain rate is also evaluated as a temporal finite difference. From these tensorial strain

rate averages, the axial component $\dot{\varepsilon}_{yy}$ is extracted and reported in Figure 4-9 and Figure 4-10.

The log-log plot of time versus strain rate in Figure 4-9 highlights the response of the cell model during primary and secondary creep. Clearly, the dominant mechanism changes during the creep simulation. Initially while the load is ramped in 0.1 hours, the elastic strain rate in the grains is most significant. During the next 10 hours, the grain boundaries that were mostly locked together and deforming with the grains during the load ramp begin to slide and shed some of their tangential traction. This process relaxes some of the stress concentrations at triple points between grains, producing a creep strain rate that diminishes by two orders of magnitude during the 10-hour period. In contrast, simulation (CP,D) in Figure 4-8 (a) with grain boundary sliding suppressed has an immediate strain rate reduction and remains near the minimum strain rate value for the remaining duration. Returning to Figure 4-9, the dislocation creep within grains takes over after 10 hours as the dominant mechanism, with grain boundary sliding persisting at about 33% of the total cell strain rate. Another magnitude of strain rate is lost during the next 1,000 hours since the hardening term τ_v in the Voce crystal plasticity leads to increased plastic flow resistance. The minimum total strain rate is reached at 6,000 hours, similar to the time for the experimental measurement in Figure 4-8 (a) from [29].

The average strain rate from the normal direction opening along the grain boundaries, shown as the dashed blue curve in Figure 4-9, decreases steadily for the first 300 hours. As discussed in Section 5.1 and Appendix A.1, the interface opening contains a superposition of the elastic separation/overlap from the K_n term along with the cavity growth term (4.3). After 300 hours, the cell average opening rate begins to accelerate. Additionally, the microstructural cell model provides more details of the cavities along the grain boundaries through the interface element states; such local cavity information is compared at several applied load levels in [159]. Recall from Table 4-1 that the initial

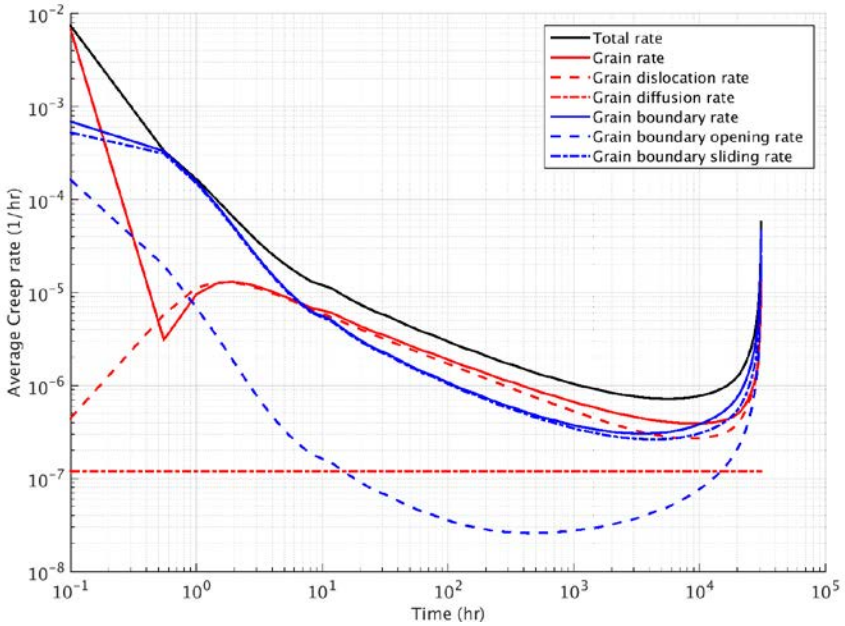

Figure 4-9. Cell-averaged creep strain rate at 100 MPa loading, decomposed mechanisms within grains and along grain boundaries, logarithmic scale

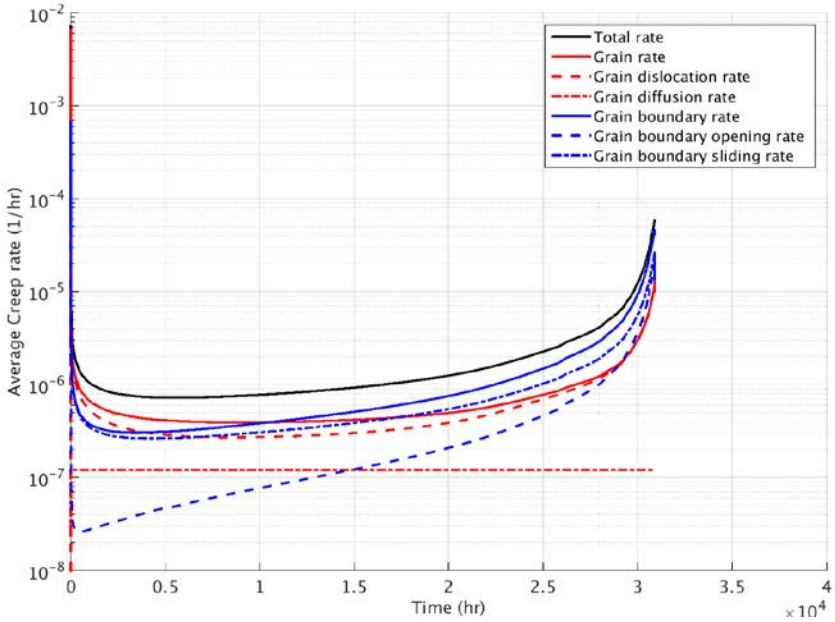

Figure 4-10. Cell-averaged creep strain rate at 100 MPa loading, decomposed mechanisms within grains and along grain boundaries, linear scale

state of all PAGB is $a_0 = 50$ nm, $b_0 = 60$ μm, and $N_0 = 88\ \text{mm}^{-2}$. At 300 hours, the average values across all interface elements are $a_{avg} = 2.5a_0$ and $N_{avg} = 50N_0$, while the maximum values on particular elements are $a_{\max} = 10a_0$ and $N_{\max} = 500N_0$. This maximum areal density $N_{\max} = 500N_0 = 44{,}000\ \text{mm}^{-2}$ is never exceeded by any interface elements during the remaining simulation duration. Part 2 of this manuscript presents grain boundary statistics showing that these maximum values occur along facets having their unit normal vector aligned with the loading axis, as expected.

Next, presenting the same decomposed strain rates on a linear time scale in Figure 4-10 highlights the evolving responses in the tertiary creep regime. Recall that the nucleation threshold (4.2) is based on both traction as well as accumulated plastic strain in the vicinity of a grain boundary. Hence, this threshold has been exceeded at enough grain boundary points by 300 hours so as to produce an accelerating grain boundary opening rate in Figure 4-10, well before the total strain rate achieves a minimum. The grain boundary sliding rate begins increasing at about 3,000 hours, signifying that the interfaces have relaxed and are more flexible due to the opening displacement. The last mechanism to accelerate is the grain dislocation creep rate after 10,000 hours. This minor increase may derive from stress redistribution between grains caused by diminished traction transmission at failed grain boundary facets, which have substantially nucleated and grown populations of cavities. Note that the cell-average diffusional creep rate is found to be constant during the simulation since the volume average stress is constant, even though local stresses may fluctuate during the time history. At the minimum total strain rate of $\dot{\varepsilon}_{yy} = 7\times10^{-7}\ \text{hr}^{-1}$, its rate is about 20% or $\dot{\varepsilon}_{yy}^{(d)} = 1.5\times10^{-7}\ \text{hr}^{-1}$. Thus, diffusion is still a significant fraction of the total cell response, and 100 MPa is near the transition point in [98] between the apparent power law exponents at high and low stress; see Figure 3-6. The simulation progresses up to 20,000 hours, and subsequently the Newton method fails

to converge even with very small time steps of 0.5 hour. We attribute this divergence to the coupled nonlinearities in the model, the stiff crystal plasticity equations, and the explicit time integration of the cavity growth model. At 20,000 hours, the average state values among all interface elements are $a_{avg} = 1$ μm and $N_{avg} = 2500\ \text{mm}^{-2}$, while the maximum values are $a_{\max} = 5$ μm and $N_{\max} = 44{,}000\ \text{mm}^{-2}$. These are physically reasonable values, since the $M_{23}C_6$ precipitates along PAGB are known to coarsen up to a diameter of several microns [108].

We clearly see in Figure 4-9 that the individual mechanism contributions to the overall cell response are different from their isolated response in Figure 4-8 (a), indicating that superposition is obviously invalid for this nonlinear problem. Also, the sequence of dominant mechanisms from the simulation results matches with intuition of the material response and thus provides insight into the primary, secondary, and tertiary creep response of Grade 91.

4.6 Conclusions

A microstructural model has been developed for analyzing creep in Grade 91 ferritic-martensitic steel. The model includes deformation mechanisms from dislocation and diffusional motion within the prior austenite grains (PAG) and viscous sliding and cavity growth and nucleation along grain boundaries, considered to be the material's primary deformations modes. The physically-based cavity growth model extends from the smeared cavity population model of [11, 27, 28] by including the effect of creep strain and stress triaxiality from material points in the grains adjacent to the grain boundary. These models are implemented into a nonlinear finite element code and used for simulations that explicitly capture these features in the geometry of the microstructural cell domain. Several numerical enhancements were required, such as the communication of nonlocal

state variables and the use of adaptive time stepping to solve the stiff nonlinear equations during tertiary creep.

Several simulations were conducted to understand the features of each deformation mode. First, a study on a polycrystalline microstructure with compliant elastic grain boundaries revealed a sensitivity of the finite element method to stress concentrations at triple points. Either a refined mesh or a proper matching of normal and tangential stiffness is required to avoid nonphysical oscillations in the interface traction fields. This study influenced the calibration process of the material parameters for each component mechanism, targeted at 600 °C response against Grade 91 creep data from [29]. Then, a series of creep simulations were performed at 100 MPa with different mechanisms suppressed, and the effect on the cell average creep rate showed that (1) nucleation was crucial to tertiary creep and (2) sliding provides a sizable contribution during primary creep. Lastly, a post-process decomposition approach provided an analysis of the complete cell model response. Each mechanism plays a role at different stages of the creep response, including the effect of grain diffusional creep on the minimum strain rate.

The second part of this work uses the model developed here to examine the effective of stress level, stress triaxiality, and temperature on the engineering and microscale response of Grade 91 under elevated temperature service. A key result is a transition from a high stress, low triaxiality region of notch strengthening behavior to a low stress, high triaxiality region of notch weakening. The paper elucidates this mechanism shift with a simple micromechanical model that reproduces and explains the results of the full CPFEM simulations described here.

Chapter 5

MICROSTRUCTURAL MODELING OF CREEP DEFORMATION IN GRADE 91 AT HIGH AND LOW STRESS

5.1 Introduction

A major focus of this dissertation is on the interactions of two major microstructural mechanisms governing the response of Grade 91 under creep conditions: growth and coalesce of cavities along grain boundaries (modeled by interface elements also including grain boundary sliding) and evolution of dislocations and other defects within grains (modeled by the crystal plasticity finite element method). This chapter presents the combination of the two physics-based models to capture the primary, secondary, and tertiary phases of Grade 91 creep response at 600 C at a range of stresses. Emphasis is placed on the agreement of the model with experimental creep curves during all three phases at higher load levels, the prediction of creep life accounting for grain diffusional creep at lower load levels, and the resulting trends of grain boundary cavity growth that align with experimental observations.

In Section 5.2, the microstructural cell model and problem setup are briefly reviewed. A series of finite element simulations are performed in Section 5.2.1 using the calibrated grain and grain boundary model parameters at loads ranging between 100 MPa to 160 MPa. In Section 5.2.2, the cell average strain rate is decomposed into contributions from each mechanism at loads 100 and 140 MPa to determine the dominant mechanisms during primary, secondary, and tertiary creep. Differences in the trade-off of mechanisms occurring at lower loads 60 to 80 MPa are studied in Section 5.2.3, followed by comparison of minimum creep strain rates at lower stresses with data from Kloc et al. [97] as well as

trends for cavity sizes and density reported by Wu and Sandsttrom [188]. Conclusions about the modeling framework are drawn in Section 5.3.

5.2 Cell model creep response across a range of stresses

The primary benchmark case for evaluating the performance of the crystal plasticity model for creep response is the 100 grain cell model discussed in Chapters 3 and 4. The 3D cell model is a $(0.2\ \text{mm})^2$ cube-shaped domain containing 100 grains that is meshed with 10,402 quadratic tetrahedral finite elements, and 467 internal grain boundaries made from 3,921 interface elements. The crystal orientations in the 100 grains are sampled from a uniform texture. The boundary conditions on the cell consist of symmetry conditions on the faces $x = 0$, $y = 0$, and $z = 0$. The effectively incomplete periodic boundary conditions obtained through multi-point constraints (MPC) are applied on the other 3 faces of the cube. For the simulations herein, a uniform pressure is applied on the $z = 0.2$ mm face to represent the tensile creep loading. The stress is increased linearly during 10 steps at 0.01 hours per step to reach maximum load at 0.1 hours. This stress increase period is subsequently referred to as the "load ramp period". The values of stress are set to 100, 110, 120, 140, and 160 MPa to correspond to the load levels investigated experimentally by Kimura et al. [20]. The temperature is set to 600°C. The series of time steps following the load ramp period vary based on the approximate creep lifetime of the specimen and are listed in Table 3-10.

5.2.1 Calibration of material parameters against higher stress data

The multi-mechanism crystal plasticity model was calibrated in Chapter 4 to capture the primary creep response evident in the experimentally measured creep curves of Kimura et al. [20]. The material parameters for the crystal plasticity model are listed in Table 5-1, and the simulated creep curves for applied stress 100 to 160 MPa are provided in Figure 3-9.

Table 5-1. Material parameters for multi-mechanism (CP) model

Property	**Value**	**Units**
E	$150,000$	MPa
ν	0.285	dimensionless
τ_y	40.0	MPa
τ_v	12.0	dimensionless
n	12	dimensionless
θ_0	800.0	MPa
m	1	dimensionless
D_η	1.2×10^{-9}	$\mathrm{MPa}^{-1}\cdot\mathrm{s}^{-1}$

The strain rate for each load level overlays very closely onto the experimental data during the primary creep regime. The grain boundary parameters for growth and coalescence of cavities were then adjusted along the lines of Section 2.3.1.7 and Section 5.4 to produce a close fit for the tertiary regime, and Table 5-2 contains these parameters. In particular, the grain boundary viscosity η_b and penalty stiffness K_{lin}^{user} have been chosen for moderate degree of sliding and stable interface normal traction fields. The initial cavity size, number density, and growth parameters are within ranges of physical characterizations of Grade 91 from the literature summarized in Chapter 4.

Figure 5-1 examines the evolution of creep strain rate of the cell model as a function of time for various load levels. For the load level 140 MPa, the simulated strain rate

Table 5-2. Material parameters for traction-separation rate equations and units

Property	Value	Units
η_b	1.0×10^{6}	$\mathrm{MPa}\cdot\mathrm{hr}\cdot\mathrm{mm}^{-1}$
K_{lin}^{user}	1.0×10^{8}	MPa/mm
a_0	5.0×10^{-5}	mm
b_0	0.06	mm
D	1.0×10^{-15}	$\mathrm{MPa}^{-1}\cdot\mathrm{hr}^{-1}\cdot\mathrm{mm}^{3}$
ψ	$15\pi/36\ \ (=75°)$	radians
Σ_0	200	MPa
F_N/N_I	2.0×10^{4}	dimensionless
$N_{\max}/N_I$	1.0×10^{3}	dimensionless
β	2	dimensionless

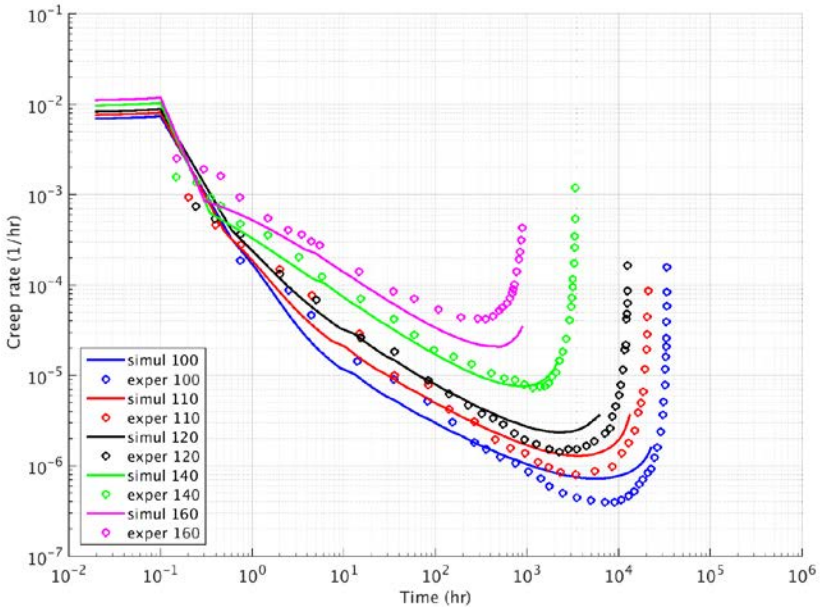

Figure 5-1. Macroscopic cell strain rate (/h) versus model time (h) for cell model using calibrated material parameters including dislocation creep and diffusional creep within the grains and sliding and cavity nucleation along grain boundaries, compared to experimental data from Kimura et al.

history appears almost identical to the experimental curve from Kimura et al. [20] during the entire test duration. At the lower load levels, the minimum strain rate is over-predicted by a factor of two or less, and the experimental curve for 160 MPa has a faster acceleration than the simulated curve. The time elapsed to minimum creep rate is more closely captured by the model. The stress dependence of the cavity nucleation rate, controlled by the parameters β and Σ_0, help to improve the closeness of the fit.

Figure 5-2 presents the history of accumulated strain of the cell model for each load level. Note that the measurements of "strain" for the test specimens are typically measures of the change in length of a gauge section. Thus, the very low strain values during the first hour of test can include other effects such as slip in the grips and local stress redistribution within the specimen that are not accounted for in the cell model. After these trends settle out in 1 to 10 hours, the simulated strain evolution agrees very well with the experimental evolution. The maximum strain level before divergence of the numerical simulations are about 1-2 % strain, while the tests typically reach 20% strain accommodated by necking. Detailed investigations of the cell model solution fields in [159] reveal that significant cavity growth has taken place by the time 1% overall strain is reached, so that the model is capturing the onset and early stages of damage during tertiary creep. Overall, the microstructural model with combined grain and grain boundary deformation mechanisms fits the experimental creep curves quite well considering the typical level of scatter in such experiments.

5.2.2 Decomposition of strain rate into deformation mechanisms

The overall deformation of the microstructural cell model recorded in Figure 5-1 is a combination of several active mechanisms in the grains and grain boundaries, and each of

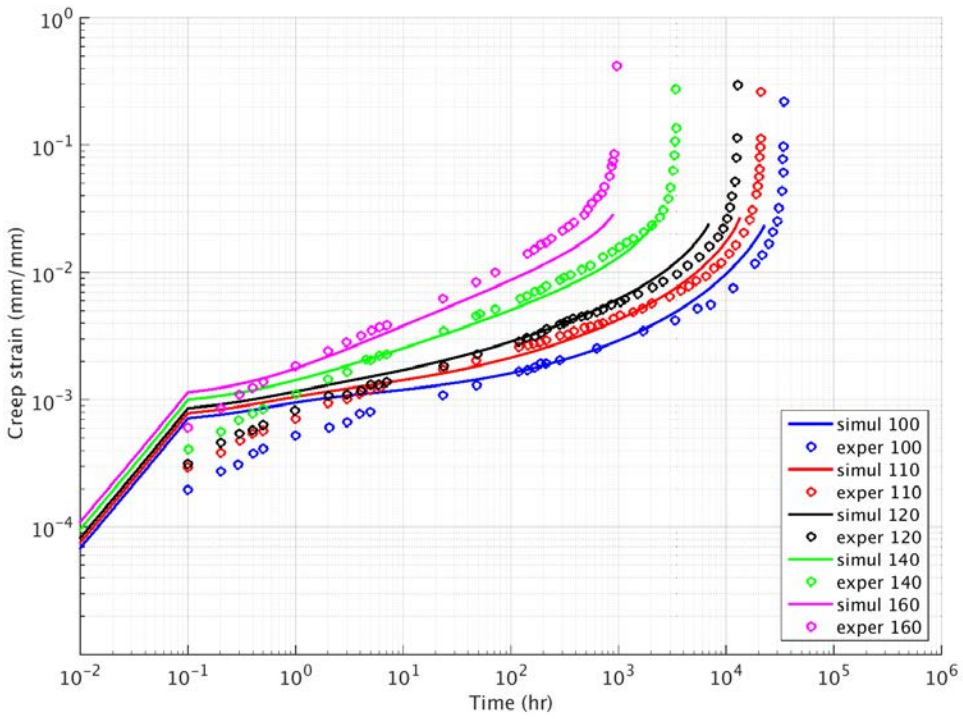

Figure 5-2. Macroscopic accumulated strain (mm/mm) versus model time (h) for cell model using calibrated material parameters

these features are represented by many finite elements that are each in a separate kinematic and kinetic state. To more deeply probe the contributions to the total observed strain rate, domain-average values of strain rate are computed for the solid finite elements and interface finite elements, separated by mechanism. All of the strain-like quantities are evaluated as tensors, and the axial component of strain rate $\dot{\varepsilon}_{xx}$ is reported in the figures that follow.

The dislocation creep rate $\bar{\boldsymbol{d}}^{p}$ from (3.57) and the diffusional creep rate $\boldsymbol{d}^{d}$ from (3.58) are provided directly by WARP3D for each solid element in the model as a state output at each time step. These values are integrated over the domain to compute the volume average. The total strain rate for grains is computed from the finite difference of the elemental strain field, and the elastic strain rate is found by subtracting the dislocation and diffusion tensors from the total rate tensor.

Details for the derivation of interfacial strain rates due to grain boundary opening are given in the literature in [90]. The resulting expression for strain, valid at small deformations, is:

$$\varepsilon_{ij} = \frac{1}{2V} \sum_{k}^{g.b.e.} \left[\int_{S_f^k} \left[\!\left[u_i \right]\!\right] n_j + \left[\!\left[u_j \right]\!\right] n_i \, ds \right] \tag{5.1}$$

where the summation is over all grain boundary elements (g.b.e.), and V is the total volume of the cell. For each interface element, this tensor is decomposed into a component aligned with the unit normal vector of the element (representing opening) and a component lying in the plane of the element (representing sliding). These decomposed tensors, which have a spatial orientation, are then integrated over the domain and the uniaxial component is recorded. While these formulas are approximations, they provide

adequate and useful insight into the dominant deformation mechanism at different times during the cell model creep response.

The decomposition of the cell average strain rate was investigated for specific load levels: 140, 100, 80, and 60 MPa. Figure 5-3 examines the decomposition at the 140 MPa load level. Several distinct phases are evident at the higher applied load levels. During the load ramp period and shortly after, the elastic strain rate in the grains and the sliding along grain boundaries dominates the total cell deformation, up to about 1 hour. Then, the strain rate from sliding continues to decrease by several orders of magnitude over a long period of time, with the transition at 2 hours of grain dislocation creep labeled as "Gra. – plast" becoming the largest component of the total strain rate. Grain boundary sliding continues along a curve that is parallel to the grain strain rate, with a strain rate about one third of that in the grains. During this period, the strain rate due to grain boundary opening labeled "GBs – opening" continually decreases and is several magnitudes below the other components, indicating that only the penalty or elastic part of the grain boundary opening is occurring. At 100 hours, the opening rate begins to increase, most likely corresponding to the onset of cavity nucleation and growth at faster rates. This is the first component to show accelerating strain rate, and it occurs about 700 hours before the observed overall minimum strain rate of the cell model. The second component to accelerate is the grain boundary sliding, signifying that boundaries are likely relaxing from the additional opening displacement and allowing more sliding to take place. Lastly, the grain creep strain rate accelerates after 1000 hours is reached; this may be attributed to redistribution of stress between grains due to failed grain boundary facets with large cavity populations that no longer transmit much traction across the microstructure. Note that because of the large applied load, the strain rate due to diffusional creep in the grains is $2\times10^{-7}\ \mathrm{hr}^{-1}$, which is the lowest mechanism contribution to the total cell strain rate.

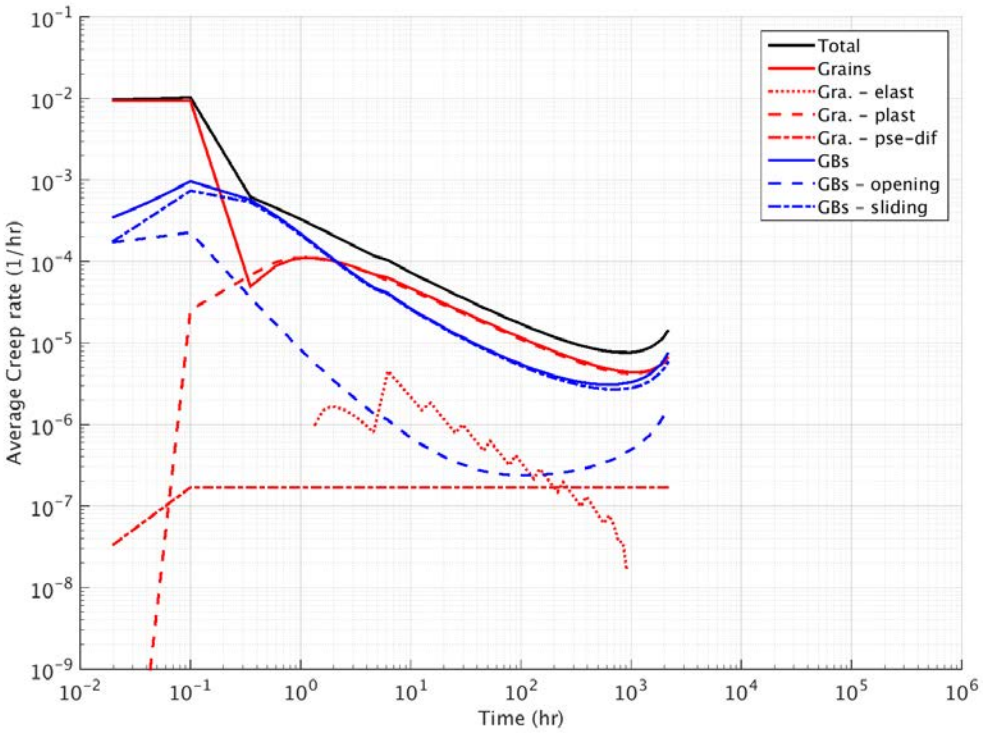

Figure 5-3. Macroscopic cell strain rate decomposition into mechanisms within the grains and along grain boundaries at superimposed load level 140 MPa

Figure 5-4 presents the strain rate decomposition at the superimposed load of 100 MPA. Similar trends appear as for the 140 MPa case; the fraction of total deformation due to grain boundary sliding remains as one third of the grain strain rate during the later portion of primary creep. The transition from sliding to dislocation creep as the dominant mechanism occurs near 10 hours. The sequence of accelerating strain rates, with opening followed by sliding followed by dislocation creep, is again present. The explanation due to unlocking of boundary deformation followed by stress shifting to grains along alternative load paths is a logical explanation of the sequence of mechanisms apparent in the strain rates. Lastly, diffusional creep is a much larger fraction of the total rate at the 100 MPa load level, about one tenth of the total at the time of minimum creep strain rate.

5.2.3 Prediction of creep response at lower stresses

The creep response of Grade 91 at operating stress levels is of interest for design of reactors. The duration of tests at these lower stress levels is often prohibitive, and therefore modeling of material response is desired. The calibrated model is thus employed for a series of creep deformation simulations of the cell model with applied stress below 100 MPa. The load levels of 80, 70, 60, 30, 10, and 1 MPa are chosen because limited experimental data for minimum strain rate during creep tests exist for each of these loads [189-193]. The sequence of time steps for the 60 to 80 MPa simulations are listed in Table 5-3.

First, the decomposition of strain rate during the time history of the cell model is studied for the 80 MPa load level, and the result is given in Figure 5-5. Several distinguishing features emerge compared to the behavior of the 100 MPa case in Figure 5-4. First, the

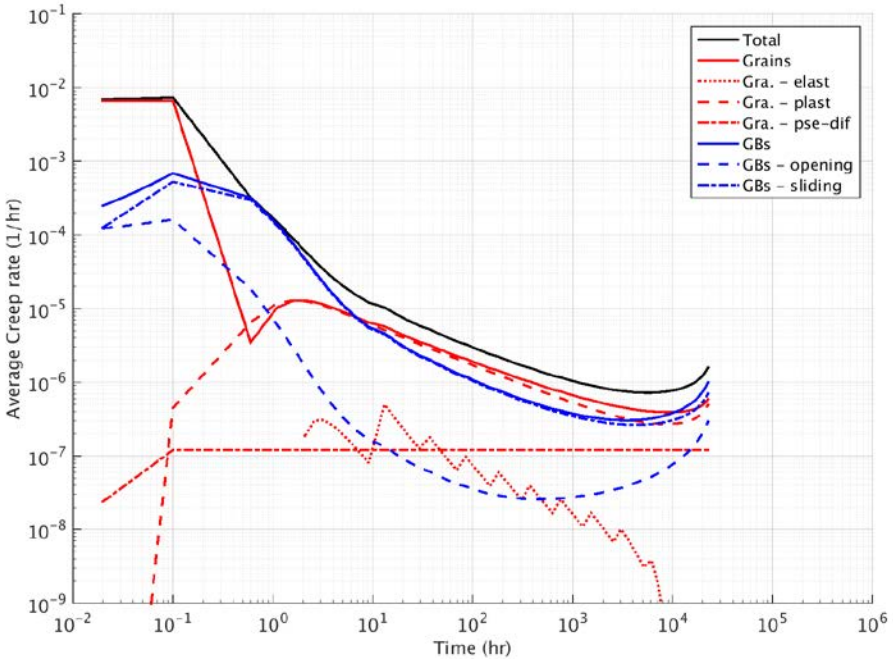

Figure 5-4. Macroscopic cell strain rate decomposition into mechanisms within the grains and along grain boundaries at superimposed load level 100 MPa

Table 5-3: Time step size for sequence of steps for various load levels; step size in hours, uniform during steps between the numbers in first column; last row is total simulation duration in hours

First series step	**80 MPa**	**70 MPa**	**60 MPa**
1	0.01	0.01	0.01
11	0.11	0.11	0.11
101	0.242	0.242	0.242
201	0.5324	0.5324	0.5324
301	1.17128	1.17128	1.17128
401	2.576816	2.576816	2.576816
501	5.668995	5.668995	5.668995
601	12.47179	12.47179	12.47179
701	27.43794	27.43794	27.43794
801	60.36346	60.36346	60.36346
901	132.7996	132.7996	132.7996
1,001	292.1592	292.1592	292.1592
2,000	316,496	316,496	316,496

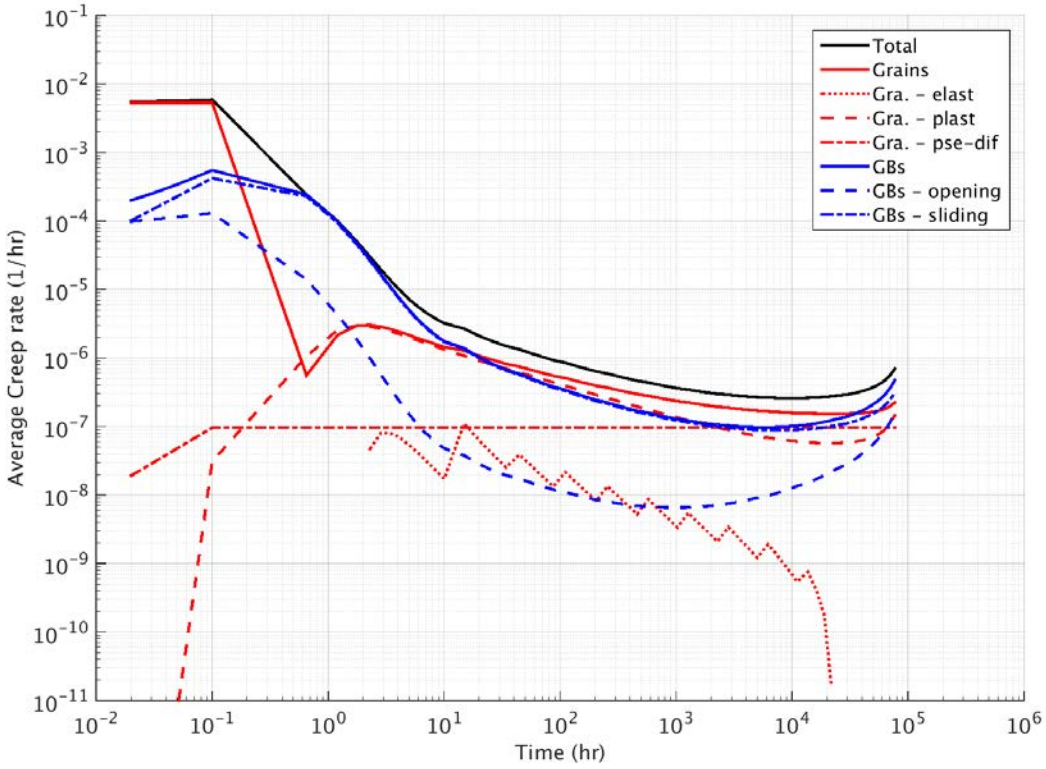

Figure 5-5. Macroscopic cell strain rate decomposition into mechanisms within the grains and along grain boundaries at superimposed load level 80 MPa

transition of dominant mechanism from sliding to grain creep is later for the 80 MPa case, at 30 hours. Also, the dislocation creep rate is comparable to the sliding strain rate during much of the primary creep regime; both of the curve have a similar slope of strain rate versus time. Most importantly, the diffusional creep within the grains exceeds the strain rate for dislocation creep after 2,000 hours, similar to the time at which the opening strain rate reaches its minimum value at 1,000 hours.

The larger contribution from diffusional creep manifests in the total strain rate of the cell model by extending the period of secondary creep, the duration of which the strain rate is nearly constant. Note that the diffusional creep curve is constant after 0.1 hours, the ending of the load ramp period. This behavior agrees with the fact that the volume average stress on the cell model is constant over time because the total load does not change and small deformations are considered. The linear relation between diffusional creep strain rate and deviatoric stress implies that if the volume average of the deviatoric stress is constant, then the volume average of the diffusional creep rate is also constant.

Figure 5-6 presents the decomposed strain rates for the 60 MPA load case. More differences appear compared to the 80 MPa response. The strain rate contribution from dislocation creep is now lower than grain boundary sliding throughout the simulation, and it only exceeds the diffusional creep rate during a short period between 1 and 100 hours. The duration of the simulation lasts until nearly 300,000 hours, when the Newton-Raphson algorithm diverges. As with all cases before, the opening strain rate accelerates first at 2,000 hours, followed by grain boundary sliding at 10,000 hours, and lastly by dislocation creep at 80,000 hours. The dislocation creep strain rate increases relatively rapidly near the end of life, faster than any of the other mechanisms, although the logarithmic scale disguises the fact that the ten-fold increase occurs during 200,000 hours. The dominance of the diffusional creep as the largest strain rate contribution leads to a long period of

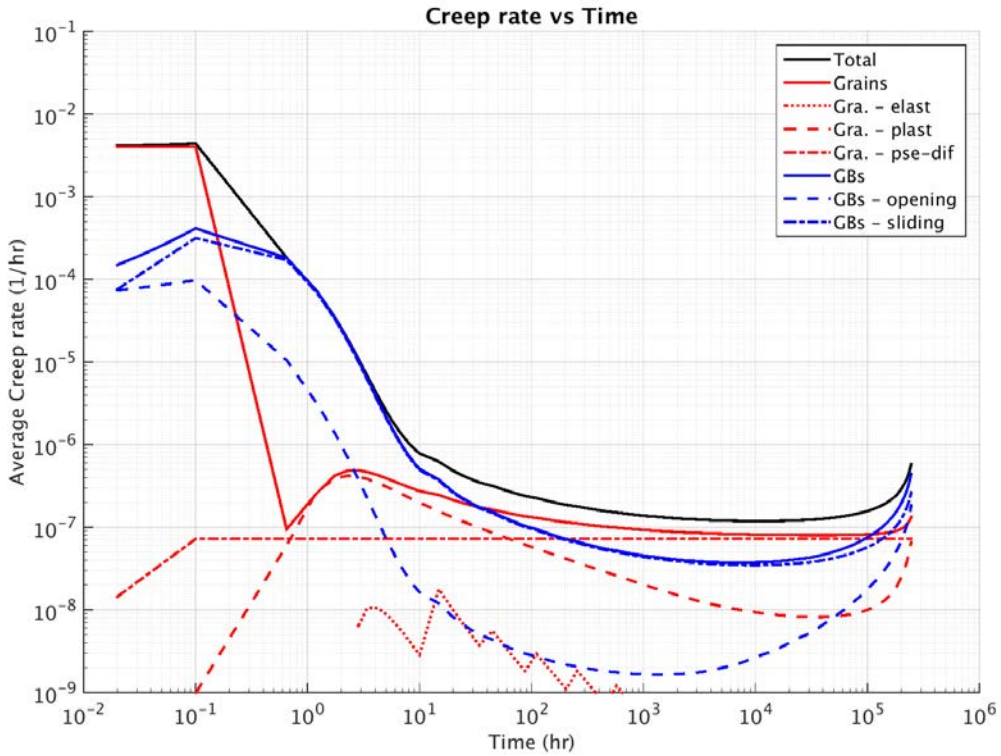

Figure 5-6. Macroscopic cell strain rate decomposition into mechanisms within the grains and along grain boundaries at superimposed load level 60 MPa

secondary creep with a minimum strain rate of 1×10^{-7} hr^{-1} between about 200 to 100,000 hours.

The creep response of the cell model is reported for several lower stress levels in Figure 5-7 for the creep strain rate and Figure 5-8 for the accumulated strain. Note that the equation solver diverges at a similar total strain level of 1% to 3% strain for all of the load levels.

As mentioned above, the creep rate curves become "flatter" at the lower stress levels due to the increased contribution from diffusional creep in the grains, which is assumed to have a time and strain history independent diffusion coefficient. Therefore, grain boundary sliding is the most significant contributor to the transient nature of the total strain rate, and the boundaries appear to relax the majority of the strain rate by the end of 10 hours, when the creep strain rate has decreased by 4 orders of magnitude from the initial strain rate at 0.1 hours (which includes the contribution from grain elasticity due to the applied stress increase during the load ramp period.

Figure 5-9 compares the predicted minimum creep strain rate as computed by the cell model to two experimental datasets [20, 189]. As mentioned in Section 3.3.2, the variation of minimum strain rate reported by Kloc et al. [189] demonstrates a clear shift in dominant mechanism near the load level 100 MPa. This trend is also captured in the simulated response from the cell model. Although the predicted creep rates are about half of those of [189], the slopes of the curves are parallel. This result is very important, considering that this dataset was not the target set for the calibration at higher stress levels. In particular, the simulation results for lower applied stresses of 1, 10, and 30 MPa are also included in Figure 5-9. The simulation results are also in the neighborhood of the data from Kimura et al. [20], with faster rates in some cases and slower in others. Due to the change in slope on the logarithmic plot, which occurs between the stresses of 60 and 100

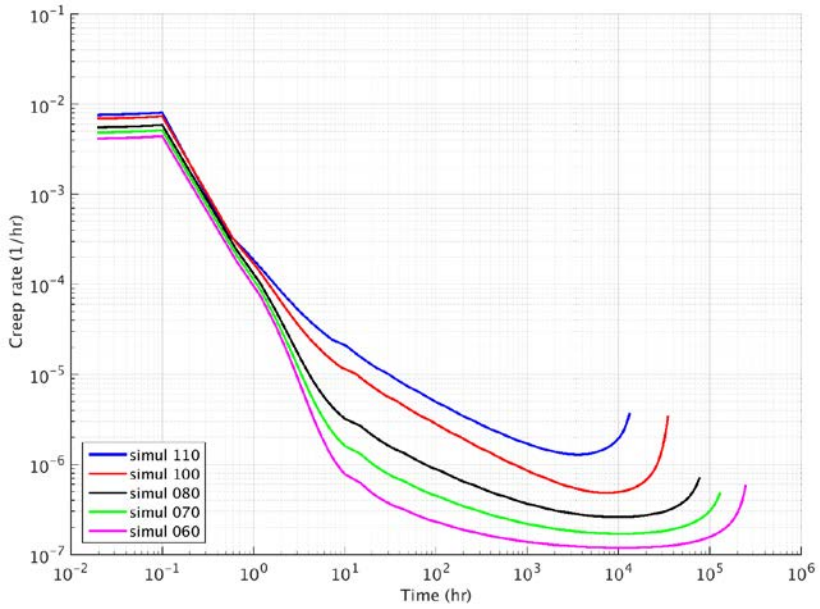

Figure 5-7. Macroscopic cell strain rate (/h) versus model time (h), model predictions for creep response at reduced load levels below 100 MPa

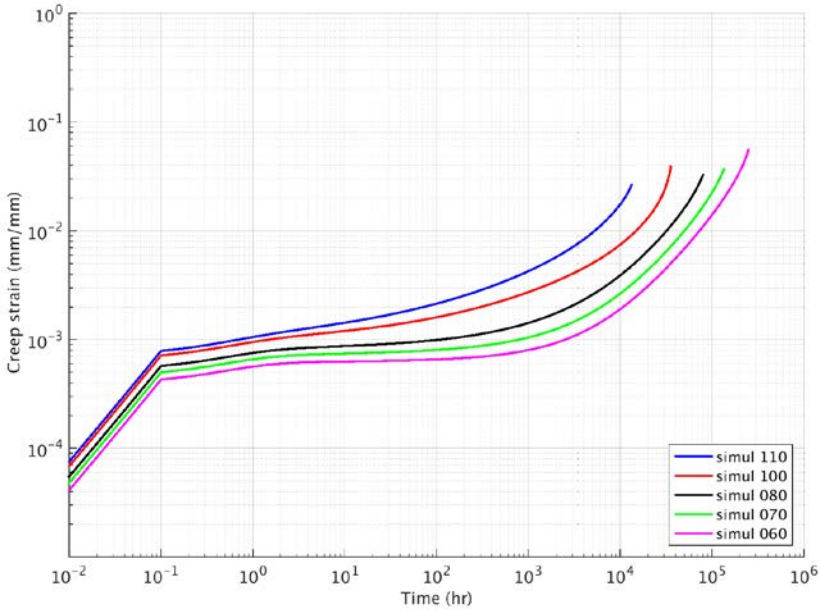

Figure 5-8. Macroscopic accumulated strain (mm/mm) versus model time (h), model predictions for creep response at reduced load levels below 100 MPa

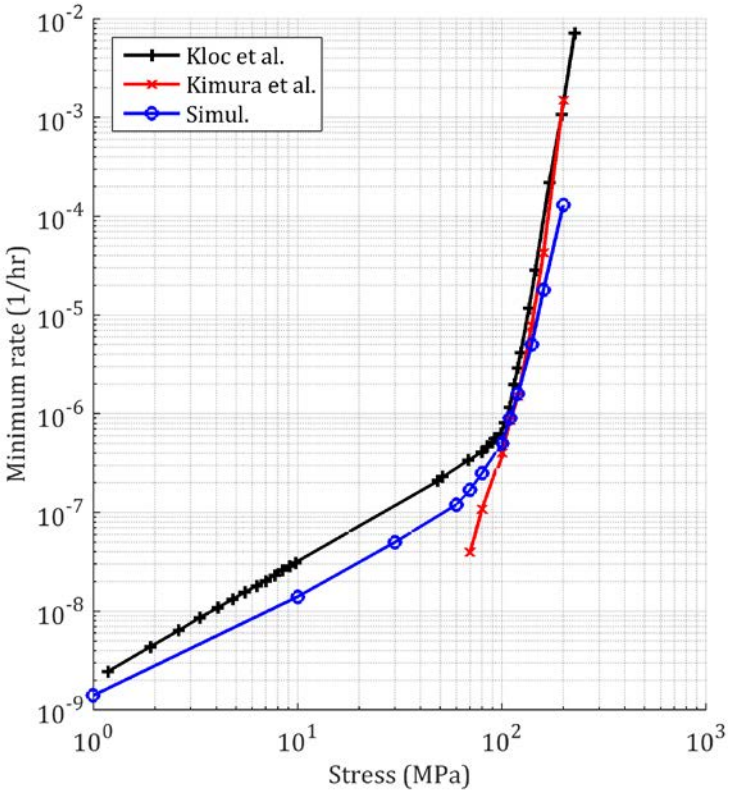

Figure 5-9. Variation of minimum creep strain rate with respect to applied stress from cell model compared to experimentally obtained rates for Grade 91 tests at 600 C from Kimura et al. and Kloc et al.

MPa, the behavior of the cell model is classified into two regimes: "dislocation dominated" for response above 80 MPa and "diffusion dominated" for response below 80 MPa.

Figure 5-10 presents the time to minimum creep rate as a function of applied stress. The time values for the simulations of the cell model are slightly longer than those from the experimental dataset [20]. Also, the variation of the simulation results appear to have a nonlinear relation of time to minimum versus applied stress for loads below 80 MPa.

5.3 Conclusions

This section presents the combination of the two physics-based models to capture the primary, secondary, and tertiary phases of Grade 91 creep response at 600 C: growth and coalesce of cavities along grain boundaries (modeled by interface elements also including grain boundary sliding) and evolution of dislocations and other defects within grains (modeled by the crystal plasticity finite element method). Simulations of the cell model are conducted at several applied loads, and the resulting cell strain rates are decomposed to understand the fraction associated with each mechanism in the modeling framework.

The response of the 3D cell during the early period of the loading history is characterized by sliding of grain boundaries to cause local grain motion, rotation, and elevated stresses near surfaces of certain geometrically preferred strains. At the same time and over a longer period, reduction in mobile dislocation density and other dislocation processes within grains lead to decreasing creep strain rates over time. Both of these phenomena contribute to the accumulated creep strain of the cell. After an extended period, the heightened stresses along grain boundaries drive the growth of cavities which induce an acceleration of the cell creep strain rate. Individual grain boundaries begin to experience failure with the geometrical linking up of sufficient grain boundaries to create

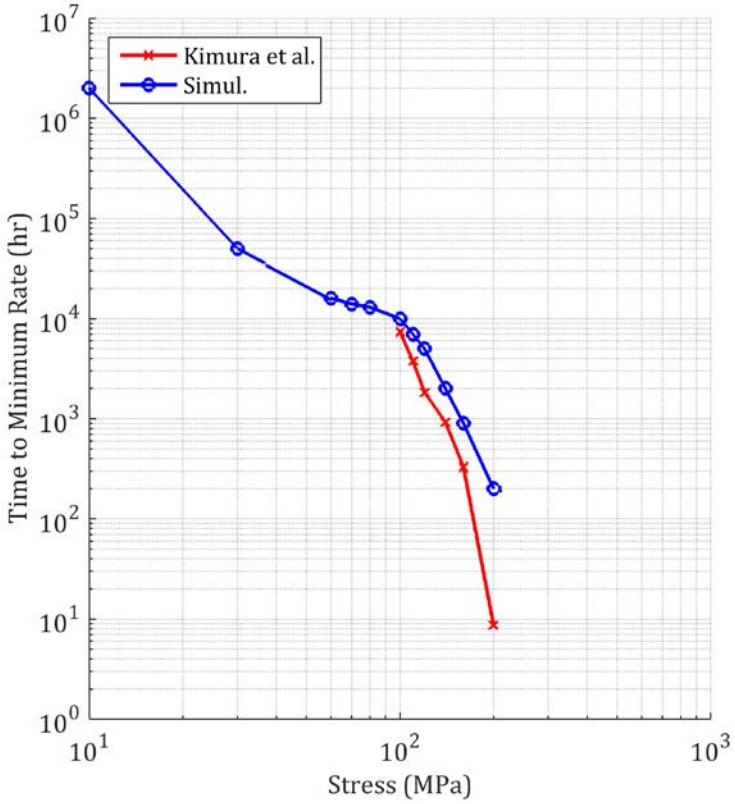

Figure 5-10. Variation of time elapsed to minimum creep strain rate with respect to applied stress from cell model compared to experimentally obtained rates for Grade 91 tests at 600 C from Kimura et al.

a rupture surface over the cell roughly transverse to the applied loading. The elapsed time and total accumulated strain prior to strain rate acceleration are dependent on the applied stress as well as whether dislocation creep or diffusional creep is the dominant deformation mechanism within the grains.

The following points summarize the key findings from these series of simulations.

- The calibrated material models for the grain and grain boundary models are first employed in simulations for remote applied tractions of 100, 110, 120, 140, and 160 MPa at 600^{o}C. For the load level 140 MPa, the simulated strain rate history appears almost identical to the experimental curve from Kimura et al. [20] during the entire test duration. At the lower load levels, the minimum strain rate is over-predicted by a factor of two or less, and the experimental curve for 160 MPa has a faster acceleration than the simulated curve. The time elapsed to minimum creep rate is more closely captured by the model for all load levels. The maximum strain level before divergence of the numerical simulations are about 1-2 % strain, while the tests typically reach 20% strain accommodated by necking. Detailed investigations of the cell model solution fields reveal that significant cavity growth has taken place by the time 1% overall strain is reached, so that the model is capturing the onset and early stages of damage during tertiary creep.

- The total cell average strain rate tensor was decomposed into component mechanisms from grains and grain boundaries by numerically integrating the strain tensors associated with solid and interface finite elements across the cell model. The decomposition of the cell average strain rate was investigated for specific load levels: 140, 100, 80, and 60 MPa. Several distinct phases are evident at the higher applied load levels. During the load ramp period and shortly after, the elastic strain rate in the grains and the sliding along grain boundaries dominates the total

cell deformation, up to about 1 hour. Then, the strain rate from sliding continues to decrease by several orders of magnitude up to 2 to 5 hours when the grain dislocation creep becomes the largest component of the total strain rate. At the 140 MPa load level, the opening rate begins to increase at 100 hours due to the onset of cavity nucleation and growth. The second component to accelerate is the grain boundary sliding, signifying that boundaries are likely relaxing from the additional opening displacement and allowing more sliding to take place. Lastly, the grain creep strain rate accelerates after 1000 hours is reached; this may be attributed to redistribution of stress between grains due to failed grain boundary facets with large cavity populations that no longer transmit much traction across the microstructure. The explanation due to unlocking of boundary deformation followed by stress shifting to grains along alternative load paths is a logical explanation of the sequence of mechanisms apparent in the strain rates.

- The decomposed strain rates at lower applied stresses exhibit distinguishing features compared to the 100 MPa case, the lowest load level reported in [20]. At 80 MPa applied load, the transition of dominant mechanism from sliding to grain creep occurs at 30 hours, while the transition is at 10 hours for the 100 MPa case. Also, the dislocation creep rate is comparable to the sliding strain rate during much of the primary creep regime; both of the curve have a similar slope of strain rate versus time. Most importantly, the diffusional creep within the grains exceeds the strain rate for dislocation creep after 2,000 hours, similar to the time at which the opening strain rate reaches its minimum value at 1,000 hours. The larger contribution from diffusional creep manifests in the total strain rate of the cell model by extending the period of secondary creep, the duration of which the strain rate is nearly constant. Under a 60 MPa applied load, the strain rate contribution from dislocation creep is lower than grain boundary sliding throughout the

simulation, and it only exceeds the diffusional creep rate during a short period between 1 and 100 hours. The duration of the simulated creep response lasts until nearly 300,000 hours. As with all cases before, the opening strain rate accelerates first at 2,000 hours, followed by grain boundary sliding at 10,000 hours, and lastly by dislocation creep at 80,000 hours.

- The predicted minimum creep strain rate computed by the cell model is compared with two experimental datasets [20, 189]. The simulated response of the cell model captures the clear shift in dominant mechanism near the load level 100 MPa reported by Kloc et al. [189]. Although the predicted creep rates are about half of those of [189], the slopes of the curves are parallel. This result is very important, considering that this dataset was not the target set for the calibration at higher stress levels.

Chapter 6

A PRIMAL CONSISTENTLY-EVOLVING STABILIZED DISCONTINOUS GALERKIN INTERFACE FORMULATION FOR FINITE-DISPLACEMENT CRYSTAL PLASTICITY

6.1 Introduction

During the course of the microstructure simulations for Gr91, several numerical stability issues were encountered that complicated the nonlinear solution process. Chief among these was oscillating normal traction field along grain boundaries when the viscous sliding resistance was assumed to be small. A detailed study of this behavior was performed in the Argonne National Laboratory report for linear elastic response in the grains to prescribe a suitable range for the interface viscosity to avoid the oscillations. Another contributing factor to these oscillations was the value of penalty parameter representing the elastic stiffness of the interface. An optimal value of the parameter is required: not to small to allow gaps or penetration along the grain boundary, and not too large to induce instabilities and oscillations.

An alternative formulation for interfacial mechanics including debonding and large deformations has been developed by Truster and coworkers during the last five years utilizing the Discontinuous Galerkin method with stability parameters derived using Variational Multiscale concepts. The majority of developments and analysis of discontinuous variational formulations, such as the interior penalty DG method, hybridized DG, and weak Galerkin, have focused on linear partial differential equations. Fewer methods exist for finite strain hyperelasticity, and even fewer for plasticity. A

notable nonsymmetric formulation for elastoplasticity has been advanced by Liu et al., with improved accuracy of stresses on interfaces but suboptimal L_2 convergence.

The novel contribution proposed to complete this dissertation research is the development and analysis of a finite strain viscoplastic symmetric Discontinuous Galerkin method for crystal plasticity. This derivation will combine the contributions from small strain plasticity [194], large strain hyperelasticity [195], and hypoelastic crystal plasticity with Green-Naghdi rate [87] into a single stabilized interfacial formulation. The first objective is to complete the derivation for the interface formulation without separation or sliding of the interface (full stick model) since the possible instabilities from crystal plasticity will require a detailed analysis first. Time permitting, the second objective would be to incorporate viscous sliding in the tangential direction and model primary creep within the 3D cell models presented in prior sections.

The additional benefit of the Discontinuous Galerkin representation of the interface is that the grain constitutive model and stress tensor are required to be evaluated at the interface (grain boundary). This is beneficial for the cavity growth model which requires this stress and strain rate state information from the neighboring grain. Currently this information is provided through a special algorithmic implementation in WARP3D that only allows an explicit implementation of the cavity growth model using the stress state from the previous converged time step. Using the terms from the Discontinuous Galerkin formulation, this stress would be evaluated at the current time step and would enable a fully coupled and implicit grain boundary model implementation.

The following sections are excerpted from published work of Truster and coworkers on the elastoplastic and hyperelastic formulations of the Variational Multiscale Discontinuous Galerkin (VMDG) method. This information highlights the derivation of the stabilizing

terms using localized fine-scale models at the interface. The new proposed contribution will investigate the validity of the fine-scale modeling assumptions, e.g. for elastic or plastic representation of the fine scales, to provide a robust treatment of discontinuities at grain boundaries with crystal plasticity deformations in the grains.

6.2 Governing equations and interfacial weak form

We begin our developments by treating the case of an interface Γ_I embedded within a plastically deforming body $\Omega \subset \mathbb{R}^{n_{sd}}$, dividing it into two disjoint regions $\Omega^{(1)}$ and $\Omega^{(2)}$ as illustrated in Figure 6-1(a) and (b). The interface of interest Γ_I could arise due to a jump in material properties or a nonconforming finite element discretization.

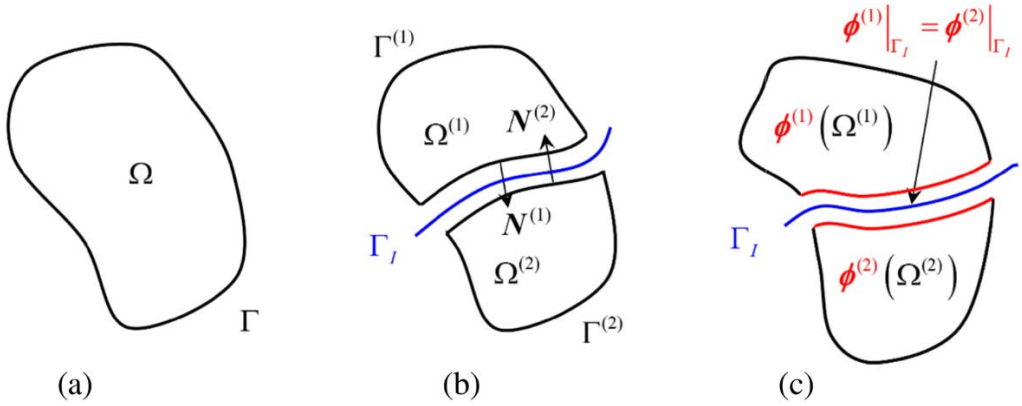

Figure 6-1. (a) reference domain Ω; (b) insertion of interface Γ_I; (c) spatial (current) configuration induced by $\boldsymbol{\phi}^{(1)}$ and $\boldsymbol{\phi}^{(2)}$ [195]

The separate regions on either side of Γ_I are denoted $\Omega^{(\alpha)}$, the superscript α takes the values 1 and 2. Moreover, expressions that applicable to both regions have their superscripts suppressed. Similar to the description in Section 1.2.1, we symbolize points

in the material configuration $\boldsymbol{X} \in \Omega^{(\alpha)}$ and their corresponding images in the spatial configuration by $\boldsymbol{x}(\boldsymbol{X},t) = \boldsymbol{\phi}^{(\alpha)}(\boldsymbol{X},t)$ as shown in Figure 6-1(c). The displacement field $\boldsymbol{u}$ associated with the mapping $\boldsymbol{\phi}^{(\alpha)}$ could then be defined as $\boldsymbol{u}^{(\alpha)}(\boldsymbol{X},t) = \boldsymbol{x}(\boldsymbol{X},t) - \boldsymbol{X}$. Similar to [195], we impose a requirement that $\boldsymbol{\phi}(\Omega) = \boldsymbol{\phi}^{(1)}\left(\Omega^{(1)}\right) \cup \boldsymbol{\phi}^{(2)}\left(\Omega^{(2)}\right)$, meaning that compatibility and equilibrium between regions $\Omega^{(1)}$ and $\Omega^{(2)}$ remains with respect to each other for all time. A similar requirement on the interface, $\boldsymbol{\phi}^{(1)}\big|_{\Gamma_I} = \boldsymbol{\phi}^{(2)}\big|_{\Gamma_I}$, is illustrated in Figure 6-1(c).

Combining the boundary conditions and equilibrium equation for each individual region $\Omega^{(\alpha)}$ with the balance of tractions and deformation continuity along Γ_I yields the system of equations for the composite domain Ω:

$$\mathrm{DIV}\dot{\boldsymbol{P}}^{(\alpha)} + \dot{\boldsymbol{b}}_0^{(\alpha)} = \boldsymbol{0} \qquad \text{in } \Omega^{(\alpha)} \tag{6.1}$$

$$\boldsymbol{u}^{(\alpha)} = \boldsymbol{g}^{(\alpha)} \qquad \text{on } \Gamma_g^{(\alpha)} \tag{6.2}$$

$$\dot{\boldsymbol{P}}^{(\alpha)} \cdot \boldsymbol{N}^{(\alpha)} = \dot{\boldsymbol{h}}^{(\alpha)} \qquad \text{on } \Gamma_h^{(\alpha)} \tag{6.3}$$

$$\dot{\boldsymbol{P}}^{(1)} \cdot \boldsymbol{N}^{(1)} = \dot{\boldsymbol{\lambda}}_0 \qquad \text{on } \Gamma_I \tag{6.4}$$

$$\dot{\boldsymbol{P}}^{(2)} \cdot \boldsymbol{N}^{(2)} = -\dot{\boldsymbol{\lambda}}_0 \qquad \text{on } \Gamma_I \tag{6.5}$$

$$[\![\boldsymbol{u}]\!] := \boldsymbol{u}^{(1)} - \boldsymbol{u}^{(2)} = \boldsymbol{0} \qquad \text{on } \Gamma_I \tag{6.6}$$

where the dot over-script denotes the rate form of a quantity $\dot{(\bullet)} = \dfrac{\partial(\bullet)}{\partial t}$, $\boldsymbol{b}_0^{(\alpha)}$ is the force, $\boldsymbol{g}^{(\alpha)}$ is the prescribed displacement, $\mathrm{DIV}(\bullet) = \mathrm{tr}\left[\mathrm{GRAD}(\bullet)\right]$ is the reference divergence operator, and $\boldsymbol{N}^{(\alpha)}$ is the unit outward normal on the boundary $\Gamma^{(\alpha)}$ of region $\Omega^{(\alpha)}$. The first Piola–Kirchhoff stress tensor is denoted by $\boldsymbol{P}^{(\alpha)}$. In this work, the Lagrange multiplier method was used to weakly impose interface equations (6.4) - (6.6) for its consistent enforcement of the traction equations (6.4) - (6.5) through the incorporating an auxiliary

unknown field $\boldsymbol{\lambda}_0$ at the interface [194, 196]. The weak form of the governing equations (6.1) – (6.6) at a nonspecific instant in time $t \in \mathcal{I}$ becomes: Find $\left\{\boldsymbol{u}^{(1)}, \boldsymbol{u}^{(2)}, \boldsymbol{\lambda}_0\right\} \in \mathcal{S}^{(1)} \times \mathcal{S}^{(2)} \times \mathcal{Q}$ such that for all $\left\{\boldsymbol{\eta}^{(1)}, \boldsymbol{\eta}^{(2)}, \boldsymbol{\mu}\right\} \in \mathcal{V}^{(1)} \times \mathcal{V}^{(2)} \times \mathcal{Q}$:

$$\begin{aligned}\sum_{\alpha=1}^{2} \int_{\Omega^\alpha} \boldsymbol{\eta}^{(\alpha)} \cdot \left(\mathrm{DIV}\, \dot{\boldsymbol{P}}^{(\alpha)}\right) \mathrm{d}V_0 + \sum_{\alpha=1}^{2} \int_{\Omega^\alpha} \boldsymbol{\eta}^{(\alpha)} \cdot \dot{\boldsymbol{b}}_0^{(\alpha)}\, dV_0 + \int_{\Gamma_I} [\![\boldsymbol{\eta}]\!] \cdot \dot{\boldsymbol{\lambda}}\, \mathrm{d}A_0 \\ = \int_{\Gamma_h^\alpha} \boldsymbol{\eta}^{(\alpha)} \cdot \dot{\boldsymbol{h}}^{(\alpha)}\, \mathrm{d}A_0\end{aligned} \tag{6.7}$$

$$-\int_{\Gamma_I} \boldsymbol{\mu} \cdot [\![\boldsymbol{u}]\!]\, \mathrm{d}A = 0 \tag{6.8}$$

The expression (6.7) correspond to the weak statement of equilibrium (6.1) while the second equation (6.8) corresponds to interface continuity conditions (6.4) - (6.6) expressed in terms of the vector-valued jump operator $[\![\bullet]\!] = (\bullet)^{(1)} - (\bullet)^{(2)}$; see [194, 197] for further details. The definitions for composite functional spaces contained in (6.7) – (6.8), for example $\mathcal{S} = \left\{\mathcal{S}^{(1)}, \mathcal{S}^{(2)}\right\}$, are well-defined for the regions $\Omega^{(\alpha)} \subset \Omega$ as follows:

$$\mathcal{S}^{(\alpha)} = \left\{ \boldsymbol{u}^{(\alpha)} \,\middle|\, \boldsymbol{u}^{(\alpha)} \in \left[H^1\left(\Omega^{(\alpha)}\right)\right]^{n_{\mathrm{sd}}},\ \boldsymbol{u}^{(\alpha)}\big|_{\Gamma_g^{(\alpha)}} = \boldsymbol{g}^{(\alpha)} \right\} \tag{6.9}$$

$$\mathcal{V}^{(\alpha)} = \left\{ \boldsymbol{\eta}^{(\alpha)} \,\middle|\, \boldsymbol{\eta}^{(\alpha)} \in \left[H_o^1\left(\Omega^{(\alpha)}\right)\right]^{n_{\mathrm{sd}}},\ \boldsymbol{\eta}^{(\alpha)}\big|_{\Gamma_g^{(\alpha)}} = \boldsymbol{0} \right\} \tag{6.10}$$

$$\mathcal{Q} = \left\{ \boldsymbol{\lambda} \,\middle|\, \boldsymbol{\lambda} \in \left[H^{-\frac{1}{2}}\left(\Gamma_I\right)\right]^{n_{\mathrm{sd}}} \right\} \tag{6.11}$$

Likewise, the displacement field $\boldsymbol{u}$ is regarded as the unification of the restricted displacement fields $\boldsymbol{u}^{(\alpha)}$ defined over $\Omega^{(\alpha)}$. Integrating the first term of equation (6.7) by parts and applying the divergence theorem gives:

$$\begin{aligned}\int_{\Omega^\alpha} \boldsymbol{\eta}^{(\alpha)} \cdot \left(\mathrm{DIV}\, \dot{\boldsymbol{P}}^{(\alpha)}\right) \mathrm{d}V_0 = -\int_{\Omega^\alpha} \mathrm{GRAD}\, \boldsymbol{\eta}^{(\alpha)} : \dot{\boldsymbol{P}}^{(\alpha)}\, \mathrm{d}V_0 + \int_{\Gamma_h^\alpha} \boldsymbol{\eta}^{(\alpha)} \cdot \dot{\boldsymbol{h}}^{(\alpha)}\, \mathrm{d}A_0 \\ + \int_{\Gamma_g^\alpha} \boldsymbol{\eta}^{(\alpha)} \cdot \dot{\boldsymbol{h}}^{(\alpha)}\, \mathrm{d}A_0\end{aligned} \tag{6.12}$$

Note that the term $\int_{\Gamma_g^\alpha} \boldsymbol{\eta}^{(\alpha)} \cdot \dot{\boldsymbol{h}}^{(\alpha)}\, \mathrm{d}A_0$ in equation (6.12) vanishes due to (6.10). Inserting (6.12) back into (6.7) gives:

$$\sum_{\alpha=1}^{2}\int_{\Omega^{\alpha}} \mathrm{GRAD}\,\boldsymbol{\eta}^{(\alpha)} : \dot{\boldsymbol{P}}^{(\alpha)}\,\mathrm{d}V_0 - \sum_{\alpha=1}^{2}\int_{\Omega^{\alpha}} \boldsymbol{\eta}^{(\alpha)}\cdot\dot{\boldsymbol{b}}_0^{(\alpha)}\,\mathrm{d}V_0 - \int_{\Gamma_I}[\![\boldsymbol{\eta}]\!]\cdot\dot{\boldsymbol{\lambda}}_0\,\mathrm{d}A_0 = \boldsymbol{0} \tag{6.13}$$

Applying the chain rule to the time derivative of $\dot{\boldsymbol{P}}$ and using the definition of the velocity gradient $\boldsymbol{L} = \dot{\boldsymbol{F}}\boldsymbol{F}^{-1}$:

$$\dot{\boldsymbol{P}} = \dot{\boldsymbol{F}}\boldsymbol{S} + \boldsymbol{F}\dot{\boldsymbol{S}} = \left(\boldsymbol{L}\boldsymbol{F}\boldsymbol{S}\boldsymbol{F}^{T} + \boldsymbol{F}\dot{\boldsymbol{S}}\boldsymbol{F}^{T}\right)\boldsymbol{F}^{-T} = J\left(\dot{\boldsymbol{F}}\boldsymbol{U}^{-1}\boldsymbol{t}\boldsymbol{R}^{T} + \boldsymbol{R}\dot{\boldsymbol{t}}\boldsymbol{R}^{T}\right)\boldsymbol{F}^{-T} \tag{6.14}$$

Where $\dot{\boldsymbol{t}} = \boldsymbol{R}^{T}\left(\frac{1}{J}\boldsymbol{F}\dot{\boldsymbol{S}}\boldsymbol{F}^{T}\right)\boldsymbol{R} = \boldsymbol{R}^{T}\dot{\boldsymbol{\sigma}}\boldsymbol{R}$ is the unrotated Cauchy stress tensor described in Section 1.2.1. The history-dependent nonlinear plasticity problem is best described in an increment form such that the first Piola–Kirchhoff stress tensor can be described as: $\boldsymbol{P}_{n+1} = \boldsymbol{P}_n + \Delta\boldsymbol{P}_{n+1}$, where the n subscript denotes the previous time step and the $n+1$ subscript denotes the time step we are solving for, throughout this chapter we shall suppress the $n+1$ subscript $(\bullet)_{n+1} = (\bullet)$ as:

$$\boldsymbol{P} = \boldsymbol{P}_n + \Delta\boldsymbol{P} \tag{6.15}$$

The stress increment $\Delta\boldsymbol{P}$ can then be defines using (6.14) and (1.16) as:

$$\begin{aligned}\Delta\boldsymbol{P} &= J\left(\Delta\boldsymbol{F}\boldsymbol{U}^{-1}\boldsymbol{t}\boldsymbol{R}^{T} + \boldsymbol{R}\Delta\boldsymbol{t}\boldsymbol{R}^{T}\right)\boldsymbol{F}^{-T} \\ &= J\left\{\Delta\boldsymbol{F}\boldsymbol{U}^{-1}\boldsymbol{t}\boldsymbol{R}^{T} + \boldsymbol{R}\left[\mathbf{C}_0 : \left(\Delta\boldsymbol{d} - \Delta\boldsymbol{d}^{p}\right) - \boldsymbol{t}\Delta\boldsymbol{W}^{p} + \Delta\boldsymbol{W}^{p}\boldsymbol{t}\right]\boldsymbol{R}^{T}\right\}\boldsymbol{F}^{-T}\end{aligned} \tag{6.16}$$

Equation (6.16) shall be solved for implicitly since the unknown appears in both sides of the equation. For ease of implementation, we solve for the $\Delta\boldsymbol{P}$ using the algorithmic tangent $\mathbf{A}$ developed in Mark's work [15], reducing equation (6.16) to:

$$\Delta\boldsymbol{P} \approx J\left[\mathbf{A} : \mathrm{grad}\left(\Delta\boldsymbol{u}\right)\right]\boldsymbol{F}^{-T} \tag{6.17}$$

The expression (6.17) is essential serves an essential role in the derivations of the following section.

6.3 Multiscale decomposition

The objective at this point is converting the mixed interface weak form (6.7) - (6.8) into a stabilized displacement formulation by extending the derivations for elastic domains in [194, 196]. This framework is underlain by concepts from the Variational Multiscale (VMS) method [198]; in particular, a modeling procedure is applied to the fine-scale displacement field localized to the interface. The result of the derivation is a stabilized primal formulation in which the interface Lagrange multipliers are condensed from the method. The main advantages are that fewer unknowns appear in the final system of equations and the complications of selecting discrete multiplier interpolations that satisfy the BB stability condition [199] are avoided. In what follows, we summarize the major steps from the framework of [194, 196] and highlight the distinguishing features arising due to inelasticity. For other examples of stabilized methods for solid mechanics developed using the VMS method, see the works of [61, 197, 200-202] and references therein.

To begin the derivation, an overlapping disintegration of the displacement field $\boldsymbol{u}^{(\alpha)}$ into coarse and fine scales is applied in each region:

$$\boldsymbol{u}^{(\alpha)} = \underbrace{\hat{\boldsymbol{u}}^{(\alpha)}}_{\text{coarse scale}} + \underbrace{\tilde{\boldsymbol{u}}^{(\alpha)}}_{\text{fine scale}} \tag{6.18}$$

$$\boldsymbol{\eta}^{(\alpha)} = \underbrace{\hat{\boldsymbol{\eta}}^{(\alpha)}}_{\text{coarse scale}} + \underbrace{\tilde{\boldsymbol{\eta}}^{(\alpha)}}_{\text{fine scale}} \tag{6.19}$$

Next, we apply consistent linearization to the localized problems according to [196]. Motivated by the simplified approaches followed in [200, 202] and similar to [203] the history effects of the fine scales are treated as negligible, implying that the stress field $\boldsymbol{P}^{(\alpha)}$ is a function of the coarse-scale fields alone. Instead, the fine scales $\tilde{\boldsymbol{u}}^{(\alpha)}$ are viewed as an incremental perturbation $\Delta\tilde{\boldsymbol{u}}^{(\alpha)}$ about the current course-scale deformation state. the stress field can then be described as:

$$\boldsymbol{P}\left(\hat{\boldsymbol{u}}+\tilde{\boldsymbol{u}}\right)^{(\alpha)} \approx \boldsymbol{P}\left(\hat{\boldsymbol{u}}\right)^{(\alpha)} + \Delta\boldsymbol{P}\left(\tilde{\boldsymbol{u}}\right)^{(\alpha)} = \boldsymbol{P}\left(\hat{\boldsymbol{u}}\right)^{(\alpha)} + J\left[\mathbf{A}^{(\alpha)} : \operatorname{grad}\left(\Delta\tilde{\boldsymbol{u}}\right)^{(\alpha)}\right]\boldsymbol{F}^{-T} \tag{6.20}$$

We directly adopt the notations of [194, 196] for the finite element partitions. While conforming discretizations of each region $\Omega^{(\alpha)}$ into finite elements $\Omega_e^{(\alpha)}$ is employed, the discrete spaces are not required to match up along interface Γ_I and are allowed to be both nonconforming and of different polynomial order. Also, the fine scales are not assumed to vanish along the interface Γ_I, in contrast to earlier VMS modeling approaches [197].

Substituting the scale decompositions (6.18) – (6.20) into the time-discrete weak form of (6.13), we employ the linearity of the weighting function slot to separate the system into a coarse-scale problem $\mathcal{C}$ and a fine-scale problem $\mathcal{F}$:

Coarse-Scale Problem $\mathcal{C}$

$$\begin{aligned}&\sum_{\alpha=1}^{2}\int_{\Omega^{\alpha}} \operatorname{grad}\hat{\boldsymbol{\eta}}^{(\alpha)} : \mathbf{A}^{(\alpha)} : \operatorname{grad}\left(\Delta\tilde{\boldsymbol{u}}\right)^{(\alpha)}\,\mathrm{d}V \\ &+\sum_{\alpha=1}^{2}\int_{\Omega^{\alpha}}\left(\operatorname{grad}\hat{\boldsymbol{\eta}}^{(\alpha)} : \mathbf{A}^{(\alpha)} : \operatorname{grad}\hat{\boldsymbol{u}}^{(\alpha)} - \hat{\boldsymbol{\eta}}^{(\alpha)}\cdot\boldsymbol{b}^{(\alpha)}\right)\mathrm{d}V - \int_{\Gamma_I}[\![\hat{\boldsymbol{\eta}}]\!]\cdot\boldsymbol{\lambda}\,\mathrm{d}A = \boldsymbol{0}\end{aligned} \tag{6.21}$$

$$-\int_{\Gamma_I}\boldsymbol{\mu}\cdot[\![\hat{\boldsymbol{u}}+\tilde{\boldsymbol{u}}]\!]\,\mathrm{d}A = 0 \tag{6.22}$$

Fine-Scale Problem $\mathcal{F}$

$$\begin{aligned}\sum_{\alpha=1}^{2}\int_{\Omega^{\alpha}} \operatorname{grad}\tilde{\boldsymbol{\eta}}^{(\alpha)} : \mathbf{A}^{(\alpha)} : \operatorname{grad}\left(\Delta\tilde{\boldsymbol{u}}\right)^{(\alpha)}\,\mathrm{d}V &= -\sum_{\alpha=1}^{2}\int_{\Omega^{\alpha}} \operatorname{grad}\tilde{\boldsymbol{\eta}}^{(\alpha)} : \boldsymbol{\sigma}\left(\hat{\boldsymbol{u}}\right)^{(\alpha)}\,\mathrm{d}V \\ &\quad+\sum_{\alpha=1}^{2}\int_{\Omega^{\alpha}}\tilde{\boldsymbol{\eta}}^{(\alpha)}\cdot\boldsymbol{b}^{(\alpha)}\,\mathrm{d}V + \int_{\Gamma_I}[\![\tilde{\boldsymbol{\eta}}]\!]\cdot\boldsymbol{\lambda}\,\mathrm{d}A\end{aligned} \tag{6.23}$$

We now aim to convert the multiscale system (6.21) – (6.23) into a stabilized reduced system expressed only in terms of the coarse-scale displacement field $\hat{\boldsymbol{u}}_{n+1}^{(\alpha)}$ by extending the framework of [194, 196]. The two major steps are, first, to apply modeling assumptions to (6.23) to derive an analytical expression for $\tilde{\boldsymbol{u}}_{n+1}^{(\alpha)}$ at the interface, and second, to embed

this expression into (6.22), enabling the condensation of the multiplier field $\boldsymbol{\lambda}$ from the coarse-scale problem.

6.3.1 Modeling of fine scales

Beginning from (6.23), we assume that the fine scales are localized to a boundary layer surrounding the interface Γ_I, which is reasonable since the destabilizing effects of Γ_I tend to be localized due to the Saint-Venant principle. In particular, we represent $\tilde{\boldsymbol{u}}^{(\alpha)}$ in the vicinity of the interface using a conforming sub-partition, the details of which are contained in [194, 196]. The main idea is that the layer of elements on the sides of the interface are partitioned into sectors $\omega_s^{(\alpha)}$ so that a conforming discretization of the interface into segments γ_s outcomes. An illustration is shown in Figure 6-2.

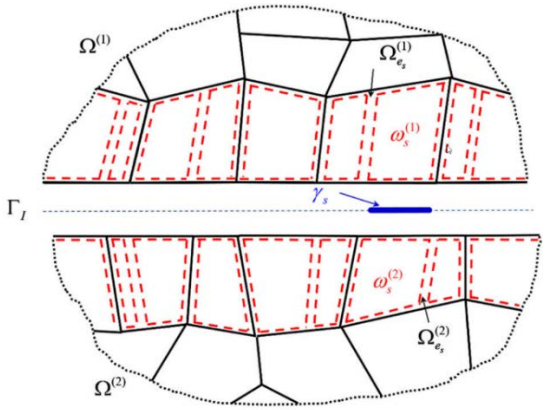

Figure 6-2. partitioning the interface into sectors $\omega_s^{(\alpha)}$ and segments γ_s [195]

This partition facilitates the representation of $\tilde{\boldsymbol{u}}^{(\alpha)}$ using edge bubble functions $b_s^{(\alpha)}$ supported over the sectors:

$$\tilde{\boldsymbol{u}}^{(\alpha)}\Big|_{\omega_s^{(\alpha)}} = \boldsymbol{\beta}_s^{(\alpha)} \boldsymbol{b}_s^{(\alpha)}, \qquad \tilde{\boldsymbol{\eta}}^{(\alpha)}\Big|_{\omega_s^{(\alpha)}} = \boldsymbol{\xi}_s^{(\alpha)} \boldsymbol{b}_s^{(\alpha)} \tag{6.24}$$

where the bubble function $b_s^{(\alpha)}$ vanishes on the boundary of the sector $\partial\omega_s^{(\alpha)}$ except along the adjoining interface segment γ_s. The primary result of this localized representation is that the fine-scale problem (6.23) can be decoupled into a series of local ones posed over pairs of adjacent sectors $\omega_s^{(\alpha)}$ sharing segments γ_s.

The specific procedure for the definition of the segments and sectors based on the interface topology is discussed in greater detail within [194, 196].

The resulting localized counterpart of (6.23) is expressed as follows for each segment $s = 1, ..., n_{seg}$:

$$\sum_{\alpha=1}^{2} \int_{\omega_s^{(\alpha)}} \operatorname{grad} \tilde{\boldsymbol{\eta}}^{(\alpha)} : \mathbf{A}^{(\alpha)} : \operatorname{grad} \left(\Delta \tilde{\boldsymbol{u}} \right)^{(\alpha)} \mathrm{d}V = -\sum_{\alpha=1}^{2} \int_{\omega_s^{(\alpha)}} \operatorname{grad} \tilde{\boldsymbol{\eta}}^{(\alpha)} : \boldsymbol{\sigma} \left(\hat{\boldsymbol{u}} \right)^{(\alpha)} \mathrm{d}V + \sum_{\alpha=1}^{2} \int_{\omega_s^{(\alpha)}} \tilde{\boldsymbol{\eta}}^{(\alpha)} \cdot \boldsymbol{b}^{(\alpha)} \, dV + \int_{\gamma_s} [\![\tilde{\boldsymbol{\eta}}]\!] \cdot \boldsymbol{\lambda} \, \mathrm{d}A \tag{6.25}$$

The next major step toward deriving an analytical model for the fine scales according to the framework of [194, 196] is to perform integration by parts on the coarse-scale volume term in (6.25) to obtain an interface traction term on γ_s:

$$\sum_{\alpha=1}^{2} \int_{\omega_s^{(\alpha)}} \operatorname{grad} \tilde{\boldsymbol{\eta}}^{(\alpha)} : \mathbf{A}^{(\alpha)} : \operatorname{grad} \left(\Delta \tilde{\boldsymbol{u}} \right)^{(\alpha)} \mathrm{d}V = \sum_{\alpha=1}^{2} \int_{\omega_s^{(\alpha)}} \tilde{\boldsymbol{\eta}}^{(\alpha)} \cdot \left(\operatorname{div} \boldsymbol{\sigma} \left(\hat{\boldsymbol{u}} \right)^{(\alpha)} + \boldsymbol{b}^{(\alpha)} \right) \mathrm{d}V + \sum_{\alpha=1}^{2} \int_{\gamma_s} \tilde{\boldsymbol{\eta}}^{(\alpha)} \cdot \left[(-1)^{\alpha-1} \boldsymbol{\lambda} - \boldsymbol{\sigma} \left(\hat{\boldsymbol{u}} \right)^{(\alpha)} \cdot \boldsymbol{n}^{(\alpha)} \right] \mathrm{d}A \tag{6.26}$$

By substituting the representation of the fine scales through bubble functions (6.24) and the integration by parts formula (6.26) into the localized fine-scale problems (6.25) we obtain the expression:

$$\sum_{\alpha=1}^{2} \left(\int_{\omega_s^{(\alpha)}} \operatorname{grad} \boldsymbol{b}_s^{(\alpha)} : \mathbf{A}^{(\alpha)} : \operatorname{grad} \boldsymbol{b}_s^{(\alpha)} \, \mathrm{d}V \right) \cdot \Delta \boldsymbol{\beta}_s^{(\alpha)} = \sum_{\alpha=1}^{2} \int_{\omega_s^{(\alpha)}} \boldsymbol{b}_s^{(\alpha)} \cdot \left(\operatorname{div} \boldsymbol{\sigma} \left(\hat{\boldsymbol{u}} \right)^{(\alpha)} + \boldsymbol{b}^{(\alpha)} \right) \mathrm{d}V + \sum_{\alpha=1}^{2} \int_{\gamma_s} \boldsymbol{b}_s^{(\alpha)} \cdot \left[(-1)^{\alpha-1} \boldsymbol{\lambda} - \boldsymbol{\sigma}^{(\alpha)} \cdot \boldsymbol{n}^{(\alpha)} \right] \mathrm{d}A \tag{6.27}$$

where $\boldsymbol{b}_s^{(\alpha)} = \sum_{j=1}^{n_{sd}} b_s^{(\alpha)} \boldsymbol{e}_j$ is a valued as vector bubble function, $\boldsymbol{e}_j$ are the basis-vectors. To further simplify (6.28), additional assumptions are employed like the ones in [194]. First, we ignore the interior residual term. By doing so, we assume orthogonality between the coarse-scale residual and the fine-scale bubble function, which is a common assumption used by residual-free bubble methods [204, 205]. Second, we extract the traction boundary residual outside the integral by applying the mean-value theorem (MVT), converting (6.27) from a nonlocal expression to a local one in terms of $\hat{\boldsymbol{u}}$ and $\boldsymbol{\lambda}$. This technique is common among stabilized methods [206, 207]. Finally, we use the average value of the bubble function in expression (6.24) for $\hat{\boldsymbol{u}}$. Applying those three assumptions to (6.27), leads to an expression for $\Delta\hat{\boldsymbol{u}}$ along each indivial interface segment γ_s, analogous to stabilized methods:

$$\Delta\tilde{\boldsymbol{u}}^{(1)} = \boldsymbol{\tau}_s^{(1)} \left[\boldsymbol{\lambda} - \boldsymbol{\sigma}\left(\hat{\boldsymbol{u}}\right)^{(1)} \cdot \boldsymbol{n}^{(1)} \right] \tag{6.28}$$

$$\Delta\tilde{\boldsymbol{u}}^{(2)} = \boldsymbol{\tau}_s^{(2)} \left[-\boldsymbol{\lambda} - \boldsymbol{\sigma}\left(\hat{\boldsymbol{u}}\right)^{(2)} \cdot \boldsymbol{n}^{(2)} \right] \tag{6.29}$$

where the stability tensor $\boldsymbol{\tau}_s^{(\alpha)}$ can be expressed as:

$$\boldsymbol{\tau}_s^{(\alpha)} = \frac{\left(\int_{\gamma_s} \boldsymbol{b}_s^{(\alpha)} \mathrm{d}A \right)^2}{\int_{\gamma_s} \mathrm{d}A} \cdot \left(\int_{\omega_s^{(\alpha)}} \operatorname{grad} \boldsymbol{b}_s^{(\alpha)} : \mathbf{A}^{(\alpha)} : \operatorname{grad} \boldsymbol{b}_s^{(\alpha)} \, \mathrm{d}V \right)^{-1} \tag{6.30}$$

Similar to other stabilized methods [194, 197, 198, 202], the fine-scale model is residual-driven. Presently, the residual corresponds to the interface traction equilibrium conditions (6.4) - (6.5) accounting for the Lagrange multiplier field $\boldsymbol{\lambda}$.

6.3.2 Embedding in the coarse-scale problem variationally

With the interfacial representation of the fine-scale field in hand, we return to the coarse-scale continuity equation (6.22) to perform condensation of the Lagrange multipliers $\boldsymbol{\lambda}$

in order to derive a definition for the numerical flux at the interface. Employing the linearity of the jump operator $[\![\hat{\boldsymbol{u}}+\tilde{\boldsymbol{u}}]\!]=[\![\hat{\boldsymbol{u}}]\!]+[\![\Delta\tilde{\boldsymbol{u}}]\!]$ and making the substitutions (6.28) - (6.29) within (6.22) leads to the following:

$$-\int_{\Gamma_I}\boldsymbol{\mu}\cdot\left[[\![\hat{\boldsymbol{u}}]\!]+\boldsymbol{\tau}_s^{(1)}\cdot\left(\boldsymbol{\lambda}-\boldsymbol{\sigma}\left(\hat{\boldsymbol{u}}\right)^{(1)}\cdot\boldsymbol{n}^{(1)}\right)-\boldsymbol{\tau}_s^{(2)}\cdot\left(-\boldsymbol{\lambda}-\boldsymbol{\sigma}\left(\hat{\boldsymbol{u}}\right)^{(2)}\cdot\boldsymbol{n}^{(2)}\right)\right]\mathrm{d}A=0 \tag{6.31}$$

By adopting a piece-wise L^2 representation of the multipliers over the interface segments γ_s as in [194, 196], we directly solve for $\boldsymbol{\lambda}$ in terms of the coarse-scale displacements and tractions. Since the intervening steps are exactly similar to the linear context in [194], the resulting expression is simply recorded as follows:

$$\boldsymbol{\lambda}=\boldsymbol{\delta}_s^{(1)}\cdot\boldsymbol{\sigma}^{(1)}\cdot\boldsymbol{n}^{(1)}-\boldsymbol{\delta}_s^{(2)}\cdot\boldsymbol{\sigma}^{(2)}\cdot\boldsymbol{n}^{(2)}-\boldsymbol{\tau}_s\cdot[\![\hat{\boldsymbol{u}}]\!] \tag{6.32}$$

Where $\boldsymbol{\tau}_s=\left(\boldsymbol{\tau}_s^{(1)}+\boldsymbol{\tau}_s^{(2)}\right)^{-1}$. The representation of the multiplier field (6.32) could be interpreted as the numerical flux for the stabilized Nitsche formulation, where the tensor $\boldsymbol{\delta}_s^{(\alpha)}$ is expressed as follows:

$$\boldsymbol{\delta}_s^{(\alpha)}=\boldsymbol{\tau}_s\cdot\boldsymbol{\tau}_s^{(\alpha)} \tag{6.33}$$

Observe that, as in [194, 196], (6.33) naturally implies that $\boldsymbol{\delta}_s^{(1)}+\boldsymbol{\delta}_s^{(2)}=\boldsymbol{1}$. However, only in restricted circumstances does $\boldsymbol{\delta}_s^{(1)}=\boldsymbol{\delta}_s^{(2)}=\frac{1}{2}\boldsymbol{1}$ as is typically assumed in DG methods [208].

Equations (6.28) - (6.29) can then be simplified as:

$$\Delta\tilde{\boldsymbol{u}}^{(1)}=\boldsymbol{\delta}_s\left(\boldsymbol{\sigma}\left(\hat{\boldsymbol{u}}\right)^{(1)}\cdot\boldsymbol{n}^{(1)}+\boldsymbol{\sigma}\left(\hat{\boldsymbol{u}}\right)^{(2)}\cdot\boldsymbol{n}^{(2)}\right)-\boldsymbol{\delta}_s^{(1)T}\cdot[\![\hat{\boldsymbol{u}}]\!] \tag{6.34}$$

$$\Delta\tilde{\boldsymbol{u}}^{(2)}=\boldsymbol{\delta}_s\left(\boldsymbol{\sigma}\left(\hat{\boldsymbol{u}}\right)^{(1)}\cdot\boldsymbol{n}^{(1)}+\boldsymbol{\sigma}\left(\hat{\boldsymbol{u}}\right)^{(2)}\cdot\boldsymbol{n}^{(2)}\right)+\boldsymbol{\delta}_s^{(2)T}\cdot[\![\hat{\boldsymbol{u}}]\!] \tag{6.35}$$

where the additional stability tensor $\boldsymbol{\delta}_s$ arises from substitution as:

$$\begin{aligned}\boldsymbol{\delta}_s=-\boldsymbol{\tau}_s^{(1)}\cdot\left(\boldsymbol{\tau}_s^{(1)}+\boldsymbol{\tau}_s^{(2)}\right)^{-1}\cdot\boldsymbol{\tau}_s^{(2)}&=-\boldsymbol{\tau}_s^{(2)}\cdot\left(\boldsymbol{\tau}_s^{(1)}+\boldsymbol{\tau}_s^{(2)}\right)^{-1}\cdot\boldsymbol{\tau}_s^{(1)}\\&=-\left[\left(\boldsymbol{\tau}_s^{(1)}\right)^{-1}+\left(\boldsymbol{\tau}_s^{(2)}\right)^{-1}\right]^{-1}\end{aligned} \tag{6.36}$$

Integrating the left-hand side of equation (6.21) by parts would give the equation:

$$\int_{\omega_s^{(\alpha)}} \operatorname{grad}\hat{\boldsymbol{\eta}}^{(\alpha)} : \mathbf{A}^{(\alpha)} : \operatorname{grad}\left(\Delta\tilde{\boldsymbol{u}}\right)^{(\alpha)} \mathrm{d}V = -\int_{\omega_s^{(\alpha)}} \operatorname{div}\left(\operatorname{grad}\hat{\boldsymbol{\eta}}^{(\alpha)} : \mathbf{A}^{(\alpha)}\right) \cdot \Delta\tilde{\boldsymbol{u}} \, \mathrm{d}V + \int_{\gamma_s} \left(\operatorname{grad}\hat{\boldsymbol{\eta}}^{(\alpha)} : \mathbf{A}^{(\alpha)}\right) \cdot \boldsymbol{n}^{(\alpha)} \cdot \Delta\tilde{\boldsymbol{u}}^{(\alpha)} \, \mathrm{d}A \tag{6.37}$$

As implemented in [194], we ignore the contribution of the domain interior term from the right-hand side of (6.37):

$$\int_{\omega_s^{(\alpha)}} \operatorname{grad}\hat{\boldsymbol{\eta}}^{(\alpha)} : \mathbf{A}^{(\alpha)} : \operatorname{grad}\left(\Delta\tilde{\boldsymbol{u}}\right)^{(\alpha)} \mathrm{d}V = \int_{\gamma_s} \left(\operatorname{grad}\hat{\boldsymbol{\eta}}^{(\alpha)} : \mathbf{A}^{(\alpha)}\right) \cdot \boldsymbol{n}^{(\alpha)} \cdot \Delta\tilde{\boldsymbol{u}}^{(\alpha)} \, \mathrm{d}A \tag{6.38}$$

this is in alignment with our assumption that the fine-scales will become vanishingly small as we get distant from the interface. Additionally, this assumption serves as to simplify the final form of this method and it also enables the direct substitution of the interface fine-scale model.

Finally, embedding the fine-scale models (6.34) - (6.35) and numerical flux (6.31) into the coarse-scale equilibrium equation would give rise to the weak form of the Crystal Plasticity DG:

$$\begin{aligned}
&\sum_{\alpha=1}^{2} \int_{\omega_s^{(\alpha)}} \left(\operatorname{grad}\hat{\boldsymbol{\eta}}^{(\alpha)} : \mathbf{A}^{(\alpha)} : \operatorname{grad}\hat{\boldsymbol{u}}^{(\alpha)} - \hat{\boldsymbol{\eta}}^{(\alpha)} \cdot \boldsymbol{b}^{(\alpha)}\right) \mathrm{d}V \\
&- \int_{\gamma_s} [\![\hat{\boldsymbol{\eta}}]\!] \cdot \left[\boldsymbol{\delta}_s^{(1)} \cdot \boldsymbol{\sigma}\left(\hat{\boldsymbol{u}}\right)^{(1)} \cdot \boldsymbol{n}^{(1)} - \boldsymbol{\delta}_s^{(2)} \cdot \boldsymbol{\sigma}\left(\hat{\boldsymbol{u}}\right)^{(2)} \cdot \boldsymbol{n}^{(2)}\right] \mathrm{d}A \\
&- \int_{\gamma_s} \left[\left(\operatorname{grad}\hat{\boldsymbol{\eta}}^{(1)} : \mathbf{A}^{(1)}\right) \cdot \boldsymbol{n}^{(1)} \cdot \boldsymbol{\delta}_s^{(1)T} - \left(\operatorname{grad}\hat{\boldsymbol{\eta}}^{(2)} : \mathbf{A}^{(2)}\right) \cdot \boldsymbol{n}^{(2)} \cdot \boldsymbol{\delta}_s^{(2)T}\right] \cdot [\![\hat{\boldsymbol{u}}]\!] \mathrm{d}A \\
&+ \int_{\gamma_s} [\![\hat{\boldsymbol{\eta}}]\!] \cdot \boldsymbol{\tau}_s \cdot [\![\hat{\boldsymbol{u}}]\!] \mathrm{d}A \\
&+ \sum_{\alpha=1}^{2} \int_{\gamma_s} \left(\operatorname{grad}\hat{\boldsymbol{\eta}}^{(\alpha)} : \mathbf{A}^{(\alpha)}\right) \cdot \boldsymbol{n}^{(\alpha)} \cdot \boldsymbol{\delta}_s \cdot \left(\boldsymbol{\sigma}\left(\hat{\boldsymbol{u}}\right)^{(1)} \cdot \boldsymbol{n}^{(1)} + \boldsymbol{\sigma}\left(\hat{\boldsymbol{u}}\right)^{(2)} \cdot \boldsymbol{n}^{(2)}\right) \mathrm{d}A = \boldsymbol{0}
\end{aligned} \tag{6.39}$$

Equation (6.39) can be cast in a more compact form by defining the weighted average flux operators:

$$\{\boldsymbol{\sigma} \cdot \boldsymbol{n}\} = \boldsymbol{\delta}_s^{(1)} \cdot \boldsymbol{\sigma}\left(\hat{\boldsymbol{u}}\right)^{(1)} \cdot \boldsymbol{n}^{(1)} - \boldsymbol{\delta}_s^{(2)} \cdot \boldsymbol{\sigma}\left(\hat{\boldsymbol{u}}\right)^{(2)} \cdot \boldsymbol{n}^{(2)} \tag{6.40}$$

$$\left\{\left(\operatorname{grad}\hat{\boldsymbol{\eta}} : \mathbf{A}\right) \cdot \boldsymbol{n}\right\} = \left(\operatorname{grad}\hat{\boldsymbol{\eta}}^{(1)} : \mathbf{A}^{(1)}\right) \cdot \boldsymbol{n}^{(1)} \cdot \boldsymbol{\delta}_s^{(1)T} - \left(\operatorname{grad}\hat{\boldsymbol{\eta}}^{(2)} : \mathbf{A}^{(2)}\right) \cdot \boldsymbol{n}^{(2)} \cdot \boldsymbol{\delta}_s^{(2)T} \tag{6.41}$$

Additionally, we ignore the stress jump term contribution, which is the final term in (6.39), improving the computational feasibility of the method, since the number of terms that would normally be needed to be calculated for the stiffness matrix and residual force

vector are reduced. This term is not usually applied in interface methods [208-212] . However, this term may provide additional stability in the occurrence of vastly nonlinear material response. Implementing those conventions in (6.39) and removing the superimposed signs for clarity, we reach to the stabilized finite-strain CP interface formulation in its final form:

$$\begin{aligned}&\sum_{\alpha=1}^{2}\int_{\omega_s^{(\alpha)}}\left(\operatorname{grad}\boldsymbol{\eta}^{(\alpha)}:\mathbf{A}^{(\alpha)}:\operatorname{grad}\boldsymbol{u}^{(\alpha)}-\boldsymbol{\eta}^{(\alpha)}\cdot\boldsymbol{b}^{(\alpha)}\right)\mathrm{d}V\\&-\int_{\gamma_s}[\![\boldsymbol{\eta}]\!]\cdot\{\boldsymbol{\sigma}\cdot\boldsymbol{n}\}\,\mathrm{d}A-\int_{\gamma_s}\left\{\left(\operatorname{grad}\boldsymbol{\eta}:\mathbf{A}\right)\cdot\boldsymbol{n}\right\}\cdot[\![\boldsymbol{u}]\!]\,\mathrm{d}A+\int_{\gamma_s}[\![\boldsymbol{\eta}]\!]\cdot\boldsymbol{\tau}_s\cdot[\![\boldsymbol{u}]\!]\,\mathrm{d}A=\boldsymbol{0}\end{aligned}\tag{6.42}$$

Note that a similarity is apparent between (6.42) and both linear [208, 212, 213] and nonlinear [210, 214-217] Nitsche and DG methods. Nevertheless, a key difference here is the definitions for the numerical flux (6.40) - (6.41) and the penalty parameter (6.33), where they are derived through the modeling of fine scales to stabilize a Lagrange multiplier interface formulation. Specifically, (6.42) is independent from user-defined parameters hence no calibrations are needed.

6.4 Numerical Results

We investigate the accuracy, robustness and stability performance of the proposed interface method across a range of numerical problems. Only three-dimensional problems are presented, but two-dimensional problems were verified for some problems to give similar results. A crystal-plasticity material model is employed for each of the problems with a number of different hardening models. Sufficient degrees are used when evaluating integral expressions over surfaces and volumes using Gauss quadrature rules. Two test cases are considered, to investigate different features of the method. The first problem is a patch test with a non-conforming mesh, testing the robustness of the method. Robustness in a non-conforming mesh would by default imply that the method is also

robust for conforming meshes. The second problem comprises of a 100-grains cell model described similar to the one described in section 4.5. This problem was designed to test stability under finite displacements as well as benchmarking it to problem where cohesive elements were used on the interface. Numerical simulations were conducted using a Matlab finite element code which was sped up by converting part of it to the mex format.

6.4.1 Non-conforming mesh patch test

For this problem, the monotonic uniaxial loading of a single crystal block is investigated. A schematic of the domain is shown in Figure 6-3. Presently, our objective is to verify that displacement continuity is weakly enforced through the interface. Having the problem verified for a non-confirming mesh insures that all surface integrals in equation (6.42) are adequately integrated. Additionally, since the stabilizing parameters are dependant of elements' geometry, the problem also serves to test their robustness.

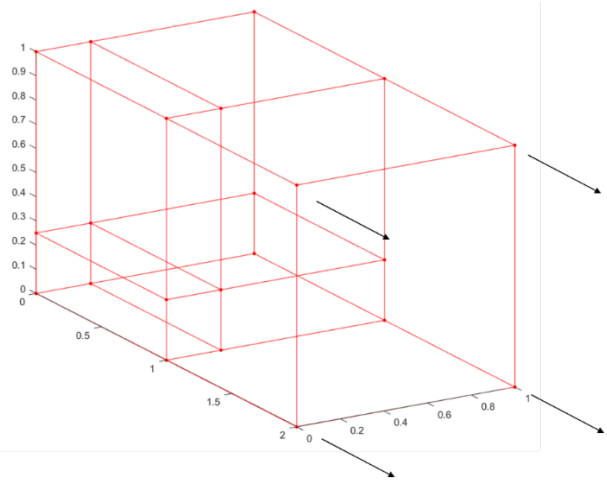

Figure 6-3. Single-crystal uniaxial tension problem

The domain dimensions are $2\times1\times1\,\mathrm{mm}$. The left part of the domain is divided into four blocks while one cube element is on the right side of the interface. Periodic boundary

conditions are applied to surfaces $x = 0, y = 0$ and $z = 0$ while loading is applied to nodes at $x = 2$ mm, the other surfaces are treated as traction-free. The MTS model is used to for the problem to utilize the FCC slip system. The twelve FCC slip systems $\{111\}\langle 110\rangle$ are assigned to the elements of the single crystal, and the orientation of the lattice is specified through the Kock's Euler angles as $\Psi = 45.0^{\circ}$, $\Theta = 90.0^{\circ}$ and $\phi = 0.0^{\circ}$. This results in only four activated slip systems and no stresses in the transverce direction. This was done to have stress response only in the x-direction. The material properties for the problem are the same as the one listed in Table 2-1 which corresponds to the Aluminum alloy AL5182. In this simulation, the prescribed displacements are incremented during 2000 load steps at a strain rate of $\dot{\varepsilon} = 1\times10^{-5}$ s^{-1} up to a maximum value $\varepsilon = 0.3$ as shown in Figure 6-4. The large deformations generated by this applied displacements ensure that the block's plastic response is significant.

The temperature effect on the model is deactivated (T = 0 K), Figure 6-5 shows the contour plot of the first principle stress σ_1. It's clear that the stress field is constant across the entire domain. The deformed body also behaves as a single block. The constant stress field is due to the same material properties shared by the two sides of the interface, this would be different if there was a difference in material properties between the two sides or if the slip systems activated aloowed for transverse stress response., That case is explored in the next section. It is also worth noting that adapting a different hardening model is fairly easy as Equation (6.42) is general for different types of hardenings as will be shown in the next section.

6.4.2 3D cell model response

The objective of this problem is to investigate the stability and accuracy of the stabilized

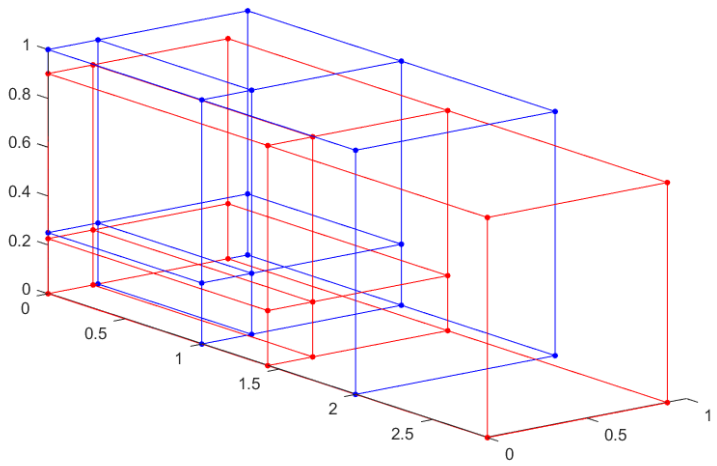

Figure 6-4. Initial (blue) vs deformed (red) configuration of the model

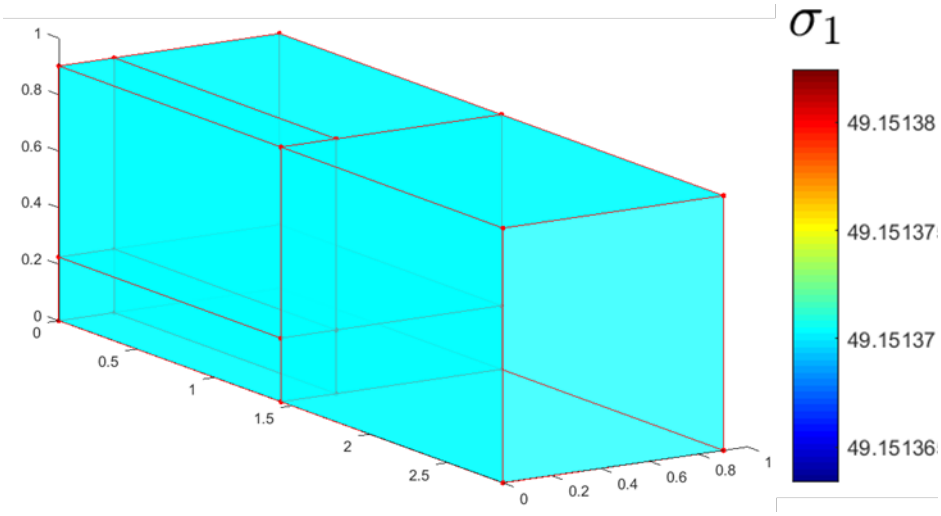

Figure 6-5. Contour plot of the first principle stress.

DG for Crystal Plasticity. The model used is the cell model described in Section 4.5.3. Similar boundary conditions are applied with loading on the top surface reaching a total true strain of $\varepsilon = 10\%$ over 400 steps. The strain rate used was $\dot{\varepsilon} = 1\times10^{-6}\ \mathrm{s}^{-1}$. Similar to Section 4.5.3, The 100 grains had randomly distributed orientations and Figure 6-6(a) shows pole figures of the initial configuration of the grains' elements. Due to the large displacements the model is subjected to, the final orientations of the elements become more distributed as shown in Figure 6-6(b) and the misorientations between grains become larger.

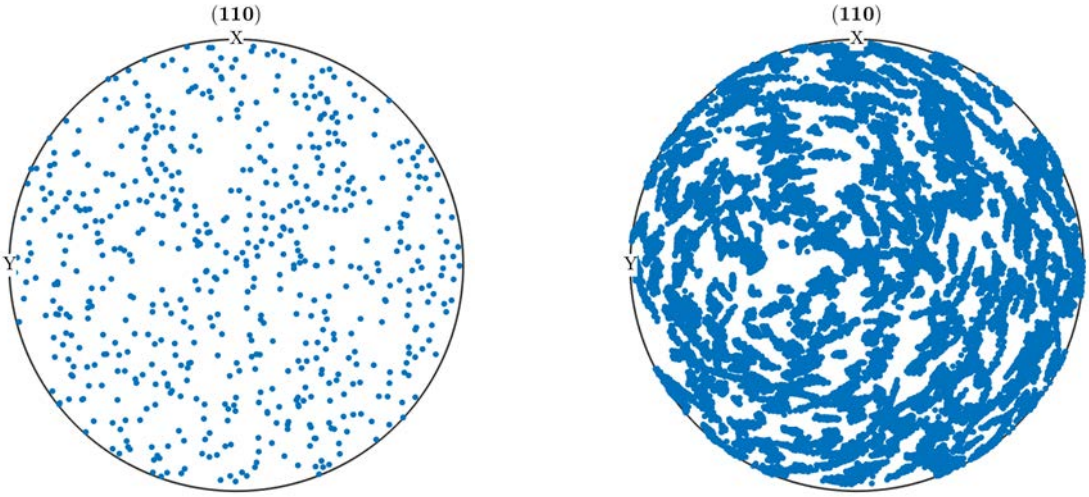

(a) (b)

Figure 6-6. Pole figures for the elements' orientations in (a) initial configurations and (b) final configurations.

The model itself was run with two scenarios for the interface elements: once modeled as cohesive zone elements where sliding was not allowed, this is done by assigning a large enough η_0 value in Equation (4.14). The convergence rate for the DG scenario was similar to that of the CZM with the average number of iterations per loading step close to 3. As mentioned previously, the finite strains result in larger misorientations between grains.

This could cause instabilities at the interfaces as the contrast on both sides of the interface increases. Figure 6-7(a) shows the total interface elements with a highlighted selected grain boundary for comparison. The normal traction field $\boldsymbol{T}_n = \boldsymbol{\sigma} \cdot \boldsymbol{n}$ is selected as contour. This specific GB was selected for the large angle of misorientation ($\Phi = 33.87^{\circ}$) between the grains on both of its sides. Figure 6-7(b) shows the aforementioned contour plot for cohesive zone elements, oscillations are very apparent as the traction field switch signs along the edges. However, Figure 6-7(c), which shows DG-modeled interface elements, shows a smoother gradient of tractions with no oscillations at the edge. This result can be seen throughout the model and is due to the stabilizing nature of the DG model. While the simulation was not done for a creep test, it should not be a factor as no creep term is present in the interface model.

6.5 Conclusion

In this chapter, a formulation fo DG interface for finite-strain Crystal Plasticity is derived by further extending the for finite-strain developments for hyper-elasticity [195] and small-strain J2 plasticity [203]. A starting point for the derivation is to treat interface continuity constraints using Lagrange multipliers concept, which is then stabilized by the usage of concepts from the VMS method. A unique feature of this type of formulation is the linearization at the interface of the localized fine-scale problems. By doing so, we analytically develop models for the fine-scale $\boldsymbol{u}$ field. Through inserting the fine-scale models into the coarse-scale problem, we enhance stability obtained and subsequently derive a primal weak form analogous to the classical DG method by enabling the Lagrange multipliers to be condensed from the formulation.

Similar to the hyper-elastic nonlinear context [195], the fine-scale models progress with geometric nonlinearity and the local material of the domain. The numerical flux is

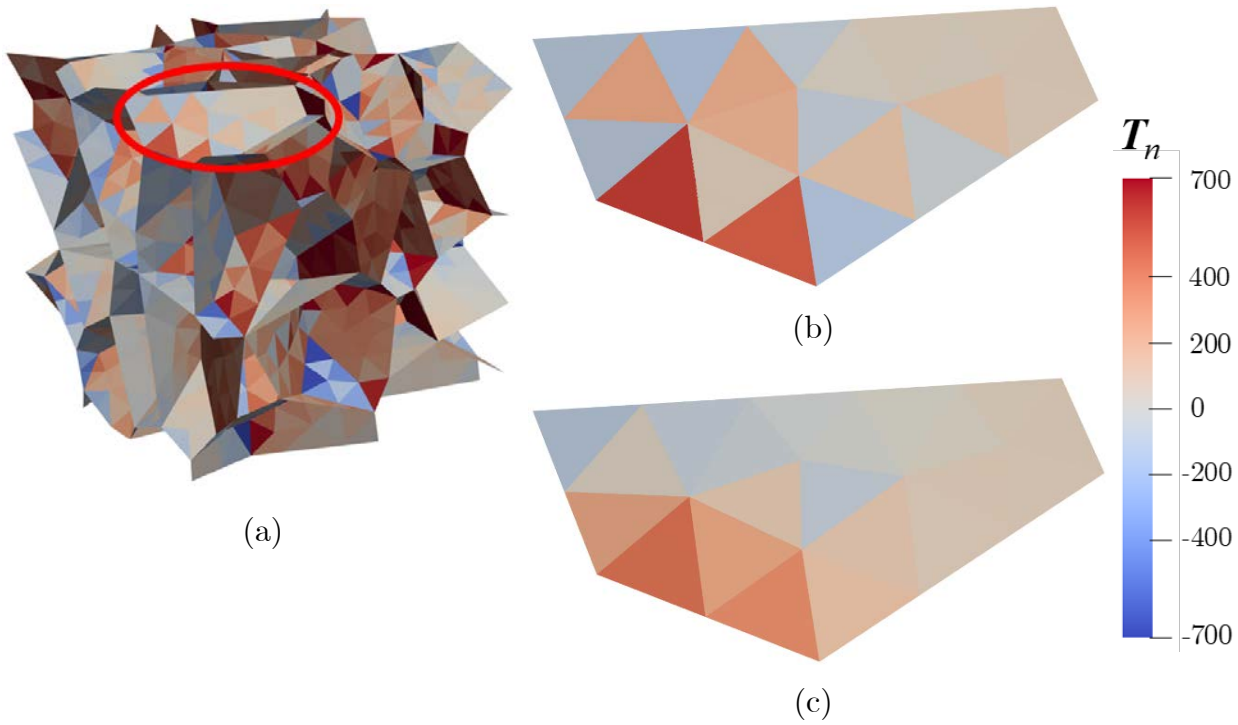

Figure 6-7. Normal traction field for cell model's interface elements: (a) highlighted investigated grain boundary, (b) interface modeled as cohesive zone elements and (c) interface modeled as DG elements.

defined by accounting the length scale and element geometry, constitutive material model, and nonlinear effects, the definitions for the numerical flux and penalty parameter in this work accomodate instabilities due to increasing deformations and grains misorientations adaptively.

To simplify the execution of the method, the fine-scale fields were presented through polynomial bubble-functions. A similar technique was investigated in previous works. Although the method was developed to weakly impose continuity over non-conforming meshes within the domain, a trivial extension of the ideas could be done over the discretized domain for fully-discontinuous approximations. A non-conforming mesh was investigated for robustness and convergence under finite-displacements, as well as the 100-grain cell model for stability and accuracy. Emphasizing problems with significant deformations to verify that the fine-scale models provide stability and retain objectivity under large-strains. In the tests, results were accurately attained without additional calibration, only using the stability parameters derived. Acceptable performance is shown by both quadrilateral and triangular elements for problems with significant mesh nonconformity and material mismatch.

Chapter 7

CONCLUDING REMARKS AND FUTURE WORK

This dissertation develops a physically-based microstructural model for creep behavior in Grade 91 steel combining crystal plasticity and interface finite element methods. The modeling studies performed provided insights into the trade-offs in active mechanisms for Grade 91 loaded under low and high stresses. A new numerical method is also developed for including the effects of geometrically necessary dislocation on the creep resistance of the microstructure by studying a gradient formulation. Also, an interface formulation was developed for capturing more accurately the interface traction fields along grain boundaries within polycrystalline materials that would be suited towards extension to include grain boundary sliding and cavity growth. The original overall goal of the microstructural model was to achieve a unified model that could be calibrated at moderate strain rates using tension tests and then extended to low and lower strain rates relevant for creep. While the dislocation density-based material model of Chapter 3 was not able to successfully complete this transition, the multi-mechanism model of Chapter 4 was able to capture experimentally observed trends as well as provide insights into the response of the material under different triaxiality ratios as well as other insights.

The present work had the following significant contributions and conclusions:

- Chapter 2 focused on a gradient method for crystal plasticity that captured the effect of the geometrically necessary dislocation effects without using a separate gradient field. A projection method was proposed based on Lie group and algebra relations to preserve the tensorial properties of the internal variable fields. The proposed nodal method was found to be economical compared to the existing element-based method while capable of being extended to higher order gradients.

- Chapter 3 developed the dislocation density-based model for Grade 91. The model was based on thermal and athermal dislocation motion by climb and glide. The model did not completely satisfy material response at both moderate and low string rates.
- Therefore, in Chapter 4 we developed a multi mechanism-based model. That model should better fit to data at both high and low stresses in the creep regime. It's distinguishing feature is that the model had terms accounting for both cavities as well as dislocation evolutions in the material. We observed from strain rate decomposition figures the effects of each mechanism during primary, secondary, and tertiary creep.
- Chapter 5 extended results for that method across the other stress levels. Particularly it extrapolated to lower stresses beyond which creep tests are not practical.
- The last section worked on developing a Discontinuous Galerkin method to help deal with the instabilities that were found in Chapter 4 at interfaces during the modeling. A couple of numerical results for shown. We were testing to see that the method is indeed more robust for interfaces and can treat problems with crystals having different levels of misorientation between grains.

In terms of future work in modeling Grade 91 as well as augmenting the microstructural modeling framework, a few areas of extension are proposed for emphasis.

These topics include extending the Lie Group/Algebra method of Chapter 2 to GND model of Bailey and Geers. Also, comparing uniform and preferential texture effects in RVE of Grade 91 crystal plasticity creep model, as well as extending the stabilized DG crystal plasticity method in Chapter 6 to include grain boundary sliding effects, and applying machine learning method (e.g. Neural networks) to improve the fit of model parameters to experimental data and quantify sensitivities.

LIST OF REFERENCES

[1] V.K. Sikka, C.T. Ward, K.C. Thomas, "Modified 9Cr-1Mo steel - an improved alloy for steam generator applications", in *Proceedings for the ASM International Conference on Production, Fabrication, Properties, and Applications of Ferritic Steels for High Temperature Applications*, Warren, 1982.
[2] R.W. Swindeman, M.L. Santella, P.J. Marziasz, B.W. Roberts, K. Colman, "Issues in replacing Cr-Mo steels and stainless steels with 9Cr-1Mo-V steel", *International Journal of Pressure Vessels and Piping*, 81 (2004) 507-512.
[3] E. Cerri, E. Evangelista, S. Spigarelli, P. Bianchi, "Evolution of microstructure in a modified 9Cr-1Mo steel during short term creep", *Materials Science and Engineering: A*, 245 (1998) 285-292.
[4] I. Chant, K.L. Murty, "Structural materials issues for the next generation fission reactors", *The Member Journal of The Minerals, Metals, & Materials Society*, 62 (2010) 67-74.
[5] G. Eggeler, W. Tato, P. Jemmely, B. deMestral, "Creep rupture of circular notched P91-specimens: Influence of heat treatment and notch geometry", *Scripta Metallurgica et Materilia*, 27 (1992) 1091-1096.
[6] B.G. Gieseke, C.R. Brinkman, P.J. Maziasz, "The influence of thermal aging on the microstructure and fatigue properties of modified 9Cr-1Mo steel", in, Oak Ridge National Lab., TN (United States), 1993.
[7] S. Goyal, K. Laha, C.R. Das, S. Panneerselvi, M.D. Mathew, "Finite element analysis of effect of triaxial state of stress on creep cavitation and rupture behavior of 2.25Cr-1Mo steel", *International Journal of Mechanical Sciences*, 75 (2013) 233-243.
[8] B. Fournier, M. Sauzay, F. Barcelo, E. Rauch, A. Renault, T. Cozzika, L. Dupuy, A. Pineau, "Creep-fatigue interactions in a 9 Pct Cr-1 Pct Mo martensitic steel: Part II. Microstructural evolutions", *Metallurgical and Materials Transactions A: Physical Metallurgy and Materials Science*, 40 (2009) 330-341.
[9] T. Shrestha, M. Basirat, I. Charit, G.P. Potirniche, K.K. Rink, U. Sahaym, "Creep deformation mechanisms in modified 9Cr-1Mo steel", *Journal of Nuclear Materials*, 423 (2012) 110-119.
[10] B.K. Choudhary, E. Isaac Samuel, "Creep behaviour of modified 9Cr-1Mo ferritic steel", *Journal of Nuclear Materials*, 412 (2011) 82-89.
[11] E. Van Der Giessen, V. Tvergaard, "Micromechanics of intergranular creep failure under cyclic loading", *Acta Materialia*, 44 (1996) 2697-2710.
[12] R.H. Dodds, T.T. Truster, K.B. Cochran, D.M. Parks, T.-L. Sham, "Unpublished information", in, Argonne National Laboratory, 2016.
[13] M. Ashby, "Boundary defects, and atomistic aspects of boundary sliding and diffusional creep", *Surface Science*, 31 (1972) 498-542.
[14] B. Dyson, "Continuous cavity nucleation and creep fracture", *Scripta Metallurgica*, 17 (1983) 31-37.

[15] M. Messner, "Micromechanical models of delamination in aluminum-lithium alloys". University of Illinois at Urbana-Champaign, 2014.
[16] J.R. Rice, "Inelastic constitutive relations for solids: An internal-variable theory and its application to metal plasticity", *Journal of the Mechanics and Physics of Solids*, 19 (1971) 433-455.
[17] A.E. Green, P.M. Naghdi, "A general theory of an elastic-plastic continuum", *Archive for Rational Mechanics and Analysis*, 18 (1965) 251-281.
[18] M. Messner, B. Armand, D. Robert, "Consistent crystal plasticity kinematics and linearization for the implicit finite element method", *Engineering Computations*, 32 (2015) 1526-1548.
[19] J. Fish, K. Shek, "Finite deformation plasticity based on the additive split of the rate of deformation and hyperelasticity", *Computer Methods in Applied Mechanics and Engineering*, 190 (2000) 75-93.
[20] K. Kimura, H. Kushima, K. Sawada, "Long-term creep deformation property of modified 9Cr-1Mo steel", *Materials Science and Engineering, A*, (2009) 58-63.
[21] O.C. Zienkiewicz, J.Z. Zhu, "A simple error estimator and adaptive procedure for practical engineerng analysis", *International Journal for Numerical Methods in Engineering*, 24 (1987) 337-357.
[22] C.-S. Han, A. Ma, F. Roters, D. Raabe, "A Finite Element approach with patch projection for strain gradient plasticity formulations", *International Journal of Plasticity*, 23 (2007) 690-710.
[23] R.A. Barrett, P.E. O-Donoghue, S.B. Leen, "A dislocation-based model for high temperature cyclic viscoplasticity of 9-12Cr steels", *Computational Materials Science*, 92 (2014) 286-297.
[24] E.P. Busso, F.A. McClintock, "A dislocation mechanics-based crystallographic model of a B2-type intermetallic alloy", *International Journal of Plasticity*, 12 (1996) 1-28.
[25] R.W. Swindeman, "Cyclic Stress-Strain-Time Response of a 9Cr-1Mo-V-Nb Pressure Vessel Steel at High Temperature", in: H. D. Solomon, G. R. Halford, L. R. Kaisand, and B. N. Leis, ASTM, Philadelphia, PA, USA, 1987, pp. 107-122.
[26] S. Barakat, O. Nassif, "Optimization of Truss Structures Using Genetic Algorithms with Domain Trimming (GADT)", *IJCSE*, 2 (2015) 144-148.
[27] T.L. Sham, A. Needleman, "Effects of triaxial stressing on creep cavitation of grain boundaries", *Acta Metallurgica*, 31 (1983) 919-926.
[28] E. Van Der Giessen, M.W.D. Van Der Burg, A. Needleman, V. Tvergaard, "Void growth due to creep and grain boundary diffusion at high triaxialities", *Journal of the Mechanics and Physics of Solids*, 43 (1995) 123-165.
[29] K. Kimura, H. Kushima, K. Sawada, "Long-term creep deformation property of modified 9Cr–1Mo steel", *Materials Science and Engineering: A*, 510–511 (2009) 58-63.

[30] E.O. Hall, "The Deformation and Ageing of Mild Steel: III Discussion of Results", *Proc. Phys. Soc. B*, 64 (1951) 747.
[31] N.J. Petch, "The cleavage strength of polycrystals", *Journal of the Iron and Steel Institute*, 174 (1953) 25-28.
[32] N.A. Fleck, G.M. Muller, M.F. Ashby, J.W. Hutchinson, "Strain gradient plasticity: Theory and experiment", *Acta Metallurgica et Materialia*, 42 (1994) 475-487.
[33] S. Kok, A.J. Beaudoin, D.A. Tortorelli, "On the development of stage IV hardening using a model based on the mechanical threshold", *Acta Materialia*, 50 (2002) 1653-1667.
[34] L. Scardia, R.H.J. Peerlings, M.A. Peletier, M.G.D. Geers, "Mechanics of dislocation pile-ups: A unification of scaling regimes", *Journal of the Mechanics and Physics of Solids*, 70 (2014) 42-61.
[35] S. Wulfinghoff, T. Böhlke, "Gradient crystal plasticity including dislocation-based work-hardening and dislocation transport", *International Journal of Plasticity*, 69 (2015) 152-169.
[36] F.T. Meissonnier, E.P. Busso, N.P. O'Dowd, "Finite element implementation of a generalised non-local rate-dependent crystallographic formulation for finite strains", *International Journal of Plasticity*, 17 (2001) 601-640.
[37] G.Z. Voyiadjis, R.K.A. Al-Rub, "Gradient plasticity theory with a variable length scale parameter", *International Journal of Solids and Structures*, 42 (2005) 3998-4029.
[38] J.F. Nye, "Some geometrical relations in dislocated crystals", *Acta Metallurgica*, 1 (1953) 153-162.
[39] N.A. Fleck, J.W. Hutchinson, "Strain gradient plasticity", *Advances in applied mechanics*, 33 (1997) 295-361.
[40] S.D. Mesarovic, "Energy, configurational forces and characteristic lengths associated with the continuum description of geometrically necessary dislocations", *International Journal of Plasticity*, 21 (2005) 1855-1889.
[41] S. Forest, "Micromorphic Approach for Gradient Elasticity, Viscoplasticity, and Damage", *J. Eng. Mech.*, 135 (2009) 117-131.
[42] J.R. Mayeur, D.L. McDowell, D.J. Bammann, "Dislocation-based micropolar single crystal plasticity: Comparison of multi- and single criterion theories", *Journal of the Mechanics and Physics of Solids*, 59 (2011) 398-422.
[43] C.J. Bayley, W.A.M. Brekelmans, M.G.D. Geers, "A comparison of dislocation induced back stress formulations in strain gradient crystal plasticity", *International Journal of Solids and Structures*, 43 (2006) 7268-7286.
[44] J.K. Djoko, F. Ebobisse, A.T. McBride, B.D. Reddy, "A discontinuous Galerkin formulation for classical and gradient plasticity – Part 1: Formulation and analysis", *Computer Methods in Applied Mechanics and Engineering*, 196 (2007) 3881-3897.

[45] J.K. Djoko, F. Ebobisse, A.T. McBride, B.D. Reddy, "A discontinuous Galerkin formulation for classical and gradient plasticity. Part 2: Algorithms and numerical analysis", *Computer Methods in Applied Mechanics and Engineering*, 197 (2007) 1-21.
[46] D.E. Hurtado, M. Ortiz, "Finite element analysis of geometrically necessary dislocations in crystal plasticity", *International Journal for Numerical Methods in Engineering*, 93 (2013) 66-79.
[47] H. Dai, "Geometrically-necessary dislocation density in continuum plasticity theory, FEM implementation and applications". Thesis, Massachusetts Institute of Technology, 1997.
[48] K.S. Cheong, E.P. Busso, A. Arsenlis, "A study of microstructural length scale effects on the behaviour of FCC polycrystals using strain gradient concepts", *International Journal of Plasticity*, 21 (2005) 1797-1814.
[49] R.K. Abu Al-Rub, G.Z. Voyiadjis, "A direct finite element implementation of the gradient-dependent theory", *International Journal for Numerical Methods in Engineering*, 63 (2005) 603-629.
[50] X. Gan, J.E. Akin, "Superconvergent second derivative recovery technique and its application in a nonlocal damage mechanics model", *Finite Elements in Analysis and Design*, 70–71 (2013) 27-35.
[51] X. Gan, J.E. Akin, "Super-convergent second derivative recovery for lower-order strain gradient plasticity", *Computers & Structures*, 135 (2014) 118-127.
[52] A. Mota, W. Sun, J.T. Ostien, J.W.F. Iii, K.N. Long, "Lie-group interpolation and variational recovery for internal variables", *Computational Mechanics*, 52 (2013) 1281-1299.
[53] M. Ortiz, J.J. Quigley Iv, "Adaptive mesh refinement in strain localization problems", *Computer Methods in Applied Mechanics and Engineering*, 90 (1991) 781-804.
[54] S. Kok, A.J. Beaudoin, D.A. Tortorelli, "A polycrystal plasticity model based on the mechanical threshold", *International Journal of Plasticity*, 18 (2002) 715-741.
[55] A. Acharya, J.L. Bassani, A. Beaudoin, "Geometrically necessary dislocations, hardening, and a simple gradient theory of crystal plasticity", *Scripta Materialia*, 48 (2003) 167-172.
[56] T.J. Truster, T.L. Sham, "Preliminary Report on Creep Deformation Simulation Using Dislocation-Based Crystal Plasticity Model", in, Oak Ridge National Laboratory, Oak Ridge, TN, 2014, pp. 1-43.
[57] A.J. Beaudoin, A. Acharya, S.R. Chen, D.A. Korzekwa, M.G. Stout, "Consideration of grain-size effect and kinetics in the plastic deformation of metal polycrystals", *Acta Materialia*, 48 (2000) 3409-3423.

[58] A.J. Beaudoin, M. Obstalecki, R. Storer, W. Tayon, J. Mach, P. Kenesei, U. Lienert, "Validation of a crystal plasticity model using high energy diffraction microscopy", *Modelling Simul. Mater. Sci. Eng.*, 20 (2012) 024006.
[59] J.C. Simo, T.J.R. Hughes, "Computational Inelasticity", 7 ed., Springer New York, New York, NY, USA, 1998.
[60] L.P. Evers, D.M. Parks, W.A.M. Brekelmans, M.G.D. Geers, "Crystal plasticity model with enhanced hardening by geometrically necessary dislocation accumulation", *Journal of the Mechanics and Physics of Solids*, 50 (2002) 2403-2424.
[61] A. Masud, T.J. Truster, "A framework for residual-based stabilization of incompressible finite elasticity: Stabilized formulations and methods for linear triangles and tetrahedra", *Computer Methods in Applied Mechanics and Engineering*, 267 (2013) 359-399.
[62] E.A.d.S. Neto, F.M.A. Pires, D.R.J. Owen, "F-bar-based linear triangles and tetrahedra for finite strain analysis of nearly incompressible solids. Part I: formulation and benchmarking", *International Journal for Numerical Methods in Engineering*, 62 (2005) 353-383.
[63] Z. Zhao, S. Kuchnicki, R. Radovitzky, A. Cuitiño, "Influence of in-grain mesh resolution on the prediction of deformation textures in fcc polycrystals by crystal plasticity FEM", *Acta Materialia*, 55 (2007) 2361-2373.
[64] A. Ma, F. Roters, D. Raabe, "A dislocation density based constitutive model for crystal plasticity FEM including geometrically necessary dislocations", *Acta Materialia*, 54 (2006) 2169-2179.
[65] E. Hinton, T. Rock, O.C. Zienkiewicz, "A note on mass lumping and related processes in the finite element method", *Earthquake Engng. Struct. Dyn.*, 4 (1976) 245-249.
[66] E.A. de Souza Neto, "The exact derivative of the exponential of an unsymmetric tensor", *Computer Methods in Applied Mechanics and Engineering*, 190 (2001) 2377-2383.
[67] M.-G. Lee, C.-S. Han, "An explicit finite element approach with patch projection technique for strain gradient plasticity formulations", *Comput Mech*, 49 (2011) 171-183.
[68] E. Bittencourt, "Dynamic explicit solution for higher-order crystal plasticity theories", *International Journal of Plasticity*, 53 (2014) 1-16.
[69] R. Dodds, "WARP3D User-Theory Manual", in.
[70] P.M. Pinsky, M. Ortiz, K.S. Pister, "Numerical integration of rate constitutive equations in finite deformation analysis", *Computer Methods in Applied Mechanics and Engineering*, 40 (1983) 137-158.
[71] R. Dodds, "WARP3D User-Theory Manual", in, 2016.
[72] J.S. Stölken, A.G. Evans, "A microbend test method for measuring the plasticity length scale", *Acta Materialia*, 46 (1998) 5109-5115.

[73] H.H.M. Cleveringa, E. Van der Giessen, A. Needleman, "A discrete dislocation analysis of bending", *International Journal of Plasticity*, 15 (1999) 837-868.
[74] S. Yefimov, E.V.d. Giessen, I. Groma, "Bending of a single crystal: discrete dislocation and nonlocal crystal plasticity simulations", *Modelling Simul. Mater. Sci. Eng.*, 12 (2004) 1069.
[75] M. Knezevic, B. Drach, M. Ardeljan, I.J. Beyerlein, "Three dimensional predictions of grain scale plasticity and grain boundaries using crystal plasticity finite element models", *Computer Methods in Applied Mechanics and Engineering*, 277 (2014) 239-259.
[76] F. Abe, "Progress in Creep-Resistant Steels for High Efficiency Coal-Fired Power Plants", *Journal of Pressure Vessel Technology*, 138 (2016) 40804-40804.
[77] G. Kurdjumow, G. Sachs, "Über den Mechanismus der Stahlhärtung", *Z. Physik*, 64 325-343.
[78] K.B. Cochran, R.H. Dodds, T.L. Sham, "Progress Report on the Modeling of Deformation Behavior in the Packets and Cavitation of Prior Austenite Grain Boundaries and Packet Boundaries", in, Oak Ridge National Laboratory, Oak Ridge, TN, 2015, pp. 1-110.
[79] H. Kraus, "Creep Analysis", John Wiley & Sons Inc, Etobicoke, On, Canada, 1980.
[80] F. Abe, "Coarsening behavior of lath and its effect on creep rates in tempered martensitic 9Cr–W steels", *Materials Science and Engineering: A*, 387–389 (2004) 565-569.
[81] C.G. Panait, A. Zielińska-Lipiec, T. Koziel, A. Czyrska-Filemonowicz, A.-F. Gourgues-Lorenzon, W. Bendick, "Evolution of dislocation density, size of subgrains and MX-type precipitates in a P91 steel during creep and during thermal ageing at 600 C for more than 100,000 h", *Materials Science and Engineering: A*, 527 (2010) 4062-4069.
[82] H. Magnusson, R. Sandstrom, "Creep Strain Modeling of 9 to 12 Pct Cr Steels Based on Microstructure Evolution", *Metallurgical and Materials Transactions A*, 38 (2007) 2033-2039.
[83] B. Fournier, M. Sauzay, A. Pineau, "Micromechanical model of the high temperature cyclic behavior of 9-12%Cr martensitic steels", *International Journal of Plasticity*, 27 (2011) 1803-1816.
[84] R. Pohja, A. Nurmela, P. Moilanen, S. Holmström, "CREEP-FATIGUE PROPERTIES OF GRADE 91 STEEL", *Advances in Materials Technology for Fossil Power Plants*, (2014) 679-689.
[85] M. Sauzay, B. Fournier, M. Mottot, A. Pineau, I. Monnet, "Cyclic softening of martensitic steels at high temperature—Experiments and physically based modelling", *Materials Science and Engineering: A*, 483-484 (2008) 410-414.
[86] A. Arsenlis, D.M. Parks, "Crystallographic aspects of geometrically-necessary and statistically-stored dislocation density", *Acta Materialia*, 47 (1999) 1597-1611.

[87] M.C. Messner, A.J. Beaudoin, R.H. Dodds, "Consistent crystal plasticity kinematics and linearization for the implicit finite element method", *Engineering Computations*, 32 (2015) 1526-1548.
[88] L.P. Evers, W.A.M. Brekelmans, M.G.D. Geers, "Non-local crystal plasticity model with intrinsic SSD and GND effects", *Journal of the Mechanics and Physics of Solids*, 52 (2004) 2379-2401.
[89] M.G.D. Geers, W.a.M. Brekelmans, C.J. Bayley, "Second-order crystal plasticity: internal stress effects and cyclic loading", *Modelling Simul. Mater. Sci. Eng.*, 15 (2007) S133.
[90] R.H. Dodds, T.J. Truster, K.B. Cochran, D.M. Parks, T.L. Sham, "Modeling of Creep Deformation and Fracture of Grade 91 Steel through Crystal Plasticity and Grain Boundary Cavitation", in, Argonne National Laboratory, Chicago, IL, 2016, pp. 1-207.
[91] A. Ma, F. Roters, "A constitutive model for fcc single crystals based on dislocation densities and its application to uniaxial compression of aluminium single crystals", *Acta Materialia*, 52 (2004) 3603-3612.
[92] S. Nemat-Nasser, T. Okinaka, L. Ni, "A physically-based constitutive model for bcc crystals with application to polycrystalline tantalum", *Journal of the Mechanics and Physics of Solids*, 46 (1998) 1009-1038.
[93] B.F. Dyson, "Microstructure based creep constitutive model for precipitation strengthened alloys: theory and application", *Materials Science and Technology*, 25 (2009) 213-220.
[94] J.C. Moosbrugger, "Nonisothermal Constitutive Model for the Small Strain Behavior of 9Cr-1 Mo-V-Nb Pressure Vessel Steel", *Journal of Engineering Materials and Technology*, 114 (1992) 354-361.
[95] S. Barakat, O. Nassif, "Optimization of Truss Structures Using Genetic Algorithms with Domain Trimming (GADT)", in *2015 International Conference on Applied Mathematics and Computational Methods in Engineering*, 2015, --.
[96] K. Kimura, H. Kushima, K. Sawada, "Long-term creep deformation property of modified 9Cr-1Mo steel", 510â€“511 (2009) 58-63.
[97] L. Kloc, V. Sklenicka, "Transition from power-law to viscous creep behaviour of p-91 type heat-resistant steel", *Materials Science and Engineering: A*, 234 (1997) 962-965.
[98] L. Kloc, V. Sklenička, "Transition from power-law to viscous creep behaviour of p-91 type heat-resistant steel", *Materials Science and Engineering: A*, 234 (1997) 962-965.
[99] V.K. Sikka, C.T. Ward, K.C. Thomas, "Modified 9Cr-1Mo steel - an improved alloy for steam generator applications", Warren, 1982.
[100] R.W. Swindeman, M.L. Santella, P.J. Maziasz, B.W. Roberts, K. Coleman, "Issues in replacing Cr–Mo steels and stainless steels with 9Cr–1Mo–V steel", *International Journal of Pressure Vessels and Piping*, 81 (2004) 507-512.

[101] I. Charit, K.L. Murty, "Structural materials issues for the next generation fission reactors", *JOM*, 62 (2010) 67-74.
[102] B. Wilshire, P.J. Scharning, "A new methodology for analysis of creep and creep fracture data for 9–12% chromium steels", *International Materials Reviews*, 53 (2008) 91-104.
[103] C.G. Panait, W. Bendick, A. Fuchsmann, A.F. Gourgues-Lorenzon, J. Besson, "Study of the microstructure of the Grade 91 steel after more than 100,000 h of creep exposure at 600 °C", *International Journal of Pressure Vessels and Piping*, 87 (2010) 326-335.
[104] T. Shrestha, M. Basirat, I. Charit, G.P. Potirniche, K.K. Rink, U. Sahaym, "Creep deformation mechanisms in modified 9Cr–1Mo steel", *Journal of Nuclear Materials*, 423 (2012) 110-119.
[105] J.L. Chaboche, "Continuum Damage Mechanics: Part II—Damage Growth, Crack Initiation, and Crack Growth", *J. Appl. Mech*, 55 (1988) 65-72.
[106] J.L. Chaboche, "Constitutive equations for cyclic plasticity and cyclic viscoplasticity", *International Journal of Plasticity*, 5 (1989) 247-302.
[107] K. Sawada, H. Kushima, T. Hara, M. Tabuchi, K. Kimura, "Heat-to-heat variation of creep strength and long-term stability of microstructure in Grade 91 steels", *Materials Science and Engineering: A*, 597 (2014) 164-170.
[108] F. Abe, "Progress in creep-resistant steels for high efficiency coal-fired power plants", *Journal of Pressure Vessel Technology*, (2015).
[109] M. Basirat, T. Shrestha, G.P. Potirniche, I. Charit, K. Rink, "A study of the creep behavior of modified 9Cr–1Mo steel using continuum-damage modeling", *International Journal of Plasticity*, 37 (2012) 95-107.
[110] R. Oruganti, M. Karadge, S. Swaminathan, "A Comprehensive Creep Model for Advanced 9-10% Cr Ferritic Steels", *Procedia Engineering*, 55 (2013) 727-734.
[111] J. Christopher, B.K. Choudhary, "Dislocation-density-based constitutive modelling of tensile flow and work-hardening behaviour of P92 steel", *Philosophical Magazine*, 94 (2014) 2992-3016.
[112] J. Christopher, B. Choudhary, "Prediction of long-term creep behaviour of Grade 91 steel at 873 K in the framework of microstructure-based creep damage mechanics approach", *International Journal of Damage Mechanics*, (2018) 105678951879611.
[113] B. Fournier, M. Sauzay, A. Pineau, "Micromechanical model of the high temperature cyclic behavior of 9–12%Cr martensitic steels", *International Journal of Plasticity*, 27 (2011) 1803-1816.
[114] R.A. Barrett, P.E. O'Donoghue, S.B. Leen, "A dislocation-based model for high temperature cyclic viscoplasticity of 9–12Cr steels", *Computational Materials Science*, 92 (2014) 286-297.

[115] B. Chen, J.N. Hu, P.E.J. Flewitt, D.J. Smith, A.C.F. Cocks, S.Y. Zhang, "Quantifying internal stress and internal resistance associated with thermal ageing and creep in a polycrystalline material", *Acta Materialia*, 67 (2014) 207-219.
[116] F. Laliberte, M. Li, J. Almer, L. Liu, "In-situ synchrotron X-ray study of microstructural evolution during creep deformation in Grade 91 steel", *Materials Science and Engineering: A*, 737 (2018) 115-123.
[117] E.D. Meade, F. Sun, P. Tiernan, N.P. O'Dowd, "Experimental study and multiscale modelling of the high temperature deformation of tempered martensite under multiaxial loading", *Materials Science and Engineering: A*, (2018).
[118] B.J. Golden, D.F. Li, N.P. O'Dowd, P. Tiernan, "Microstructural Modeling of P91 Martensitic Steel Under Uniaxial Loading Conditions", *Journal of Pressure Vessel Technology*, 136 (2014) 021404.
[119] D.-F. Li, B.J. Golden, N.P. O'Dowd, "Multiscale modelling of mechanical response in a martensitic steel: A micromechanical and length-scale-dependent framework for precipitate hardening", *Acta Materialia*, 80 (2014) 445-456.
[120] D.-F. Li, B.J. Golden, S.-Y. Zhang, V. Davydov, P. Tiernan, N.P. O'Dowd, "The Role of Plasticity in the Transverse Lattice Strain Evolution of a Martensitic Steel", *Metall and Mat Trans A*, 45 (2014) 5829-5833.
[121] B.J. Golden, D.-F. Li, Y. Guo, P. Tiernan, S.B. Leen, N.P. O'Dowd, "Microscale deformation of a tempered martensite ferritic steel: Modelling and experimental study of grain and sub-grain interactions", *Journal of the Mechanics and Physics of Solids*, 86 (2016) 42-52.
[122] D.-F. Li, R.A. Barrett, P.E. O'Donoghue, C.J. Hyde, N.P. O'Dowd, S.B. Leen, "Micromechanical finite element modelling of thermo-mechanical fatigue for P91 steels", *International Journal of Fatigue*, (2016).
[123] P.E. McHugh, R. Mohrmann, "Modelling of creep in a Ni base superalloy using a single crystal plasticity model", *Computational Materials Science*, 9 (1997) 134-140.
[124] A. Ma, D. Dye, R.C. Reed, "A model for the creep deformation behaviour of single-crystal superalloy CMSX-4", *Acta Materialia*, 56 (2008) 1657-1670.
[125] M. Li, M.-S. Pham, Z. Peng, G. Tian, B.A. Shollock, "Creep deformation mechanisms and CPFE modelling of a nickel-base superalloy", *Materials Science and Engineering: A*, 718 (2018) 147-156.
[126] J. Zhao, J. Gong, A. Saboo, D.C. Dunand, G.B. Olson, "Dislocation-based modeling of long-term creep behaviors of Grade 91 steels", *Acta Materialia*, 149 (2018) 19-28.
[127] R. Wu, R. Sandsttröm, "Strain dependence of creep cavity nucleation in low alloy and 12%Cr steels", *Materials Science and Technology*, 12 (1996) 405-415.
[128] V. Gaffard, "Experimental study and modelling of high temperature creep flow and damage behaviour of 9Cr1Mo-NbV". Ecole Des Mines De Paris, Paris, 2004.

[129] C. Gupta, H. Toda, C. Schlacher, Y. Adachi, P. Mayr, C. Sommitsch, K. Uesugi, Y. Suzuki, A. Takeuchi, M. Kobayashi, "Study of creep cavitation behavior in tempered martensitic steel using synchrotron micro-tomography and serial sectioning techniques", *Materials Science and Engineering: A*, 564 (2013) 525-538.
[130] T. Shrestha, M. Basirat, I. Charit, G.P. Potirniche, K.K. Rink, "Creep rupture behavior of Grade 91 steel", *Materials Science and Engineering: A*, 565 (2013) 382-391.
[131] X. Wang, X. Wang, B. Luo, J. Guo, "Analysis of cavity evolution in 9%Cr heat-resistant steel welded joint during creep", *Engineering Fracture Mechanics*, (2018).
[132] F.A. McClintock, "A Criterion for Ductile Fracture by the Growth of Holes", *J. Appl. Mech*, 35 (1968) 363-371.
[133] J.R. Rice, D.M. Tracey, "On the ductile enlargement of voids in triaxial stress fields", *Journal of the Mechanics and Physics of Solids*, 17 (1969) 201-217.
[134] A.L. Gurson, "Continuum Theory of Ductile Rupture by Void Nucleation and Growth: Part I—Yield Criteria and Flow Rules for Porous Ductile Media", *J. Eng. Mater. Technol*, 99 (1977) 2-15.
[135] S. Goyal, K. Laha, C.R. Das, S. Panneerselvi, M.D. Mathew, "Finite element analysis of effect of triaxial state of stress on creep cavitation and rupture behaviour of 2.25Cr–1Mo steel", *International Journal of Mechanical Sciences*, 75 (2013) 233-243.
[136] G. Eggeler, W. Tato, P. Jemmely, B. deMestral, "Creep rupture of circular notched P91-specimens: Influence of heat treatment and notch geometry", *Scripta Metallurgica et Materialia*, 27 (1992) 1091-1096.
[137] E. Cerri, E. Evangelista, S. Spigarelli, P. Bianchi, "Evolution of microstructure in a modified 9Cr–1Mo steel during short term creep", *Materials Science and Engineering: A*, 245 (1998) 285-292.
[138] B. Fournier, M. Sauzay, F. Barcelo, E. Rauch, A. Renault, T. Cozzika, L. Dupuy, A. Pineau, "Creep-Fatigue Interactions in a 9 Pct Cr-1 Pct Mo Martensitic Steel: Part II. Microstructural Evolutions", *Metall and Mat Trans A*, 40 (2009) 330-341.
[139] F.W. Crossman, M.F. Ashby, "The non-uniform flow of polycrystals by grain-boundary sliding accommodated by power-law creep", *Acta Metallurgica*, 23 (1975) 425-440.
[140] B.K. Choudhary, E. Isaac Samuel, "Creep behaviour of modified 9Cr–1Mo ferritic steel", *Journal of Nuclear Materials*, 412 (2011) 82-89.
[141] C. Westwood, J. Pan, A.D. Crocombe, "Nucleation, growth and coalescence of multiple cavities at a grain-boundary", *European Journal of Mechanics - A/Solids*, 23 (2004) 579-597.
[142] P. Onck, E.v.d. Giessen, "Growth of an initially sharp crack by grain boundary cavitation", *Journal of the Mechanics and Physics of Solids*, 47 (1998) 99-139.

[143] J.-F. Wen, A. Srivastava, A. Benzerga, S.-T. Tu, A. Needleman, "Creep crack growth by grain boundary cavitation under monotonic and cyclic loading", *Journal of the Mechanics and Physics of Solids*, 108 (2017) 68-84.
[144] M.E. Kassner, T.A. Hayes, "Creep cavitation in metals", *International Journal of Plasticity*, 19 (2003) 1715-1748.
[145] A.A. Benzerga, J.-B. Leblond, "Ductile Fracture by Void Growth to Coalescence", in: H. Aref, E.v.d. Giessen (Eds.) Advances in Applied Mechanics, Elsevier, 2010, pp. 169-305.
[146] F. Scheyvaerts, P.R. Onck, C. Tekog˘lu, T. Pardoen, "The growth and coalescence of ellipsoidal voids in plane strain under combined shear and tension", *Journal of the Mechanics and Physics of Solids*, 59 (2011) 373-397.
[147] C.-H. Yu, C.-W. Huang, C.-S. Chen, Y. Gao, C.-H. Hsueh, "Effects of grain boundary heterogeneities on creep fracture studied by rate-dependent cohesive model", *Engineering Fracture Mechanics*, 93 (2012) 48-64.
[148] C.-H. Yu, C.-W. Huang, C.-S. Chen, Y. Gao, C.-H. Hsueh, "A micromechanics study of competing mechanisms for creep fracture of zirconium diboride polycrystals", *Journal of the European Ceramic Society*, 33 (2013) 1625-1637.
[149] C. Pu, Y. Gao, Y. Wang, T.L. Sham, "Diffusion-coupled cohesive interface simulations of stress corrosion intergranular cracking in polycrystalline materials", *Acta Materialia*, 136 (2017) 21-31.
[150] P.M. Anderson, J.R. Rice, "Constrained creep cavitation of grain boundary facets", *Acta Metallurgica*, 33 (1985) 409-422.
[151] S. Mahesh, K.C. Alur, M.D. Mathew, "A creep model for austenitic stainless steels incorporating cavitation and wedge cracking", *Modelling Simul. Mater. Sci. Eng.*, 19 (2011) 015005.
[152] G. Dimmler, P. Weinert, E. Kozeschnik, H. Cerjak, "Quantification of the Laves phase in advanced 9–12% Cr steels using a standard SEM", *Materials Characterization*, 51 (2003) 341-352.
[153] O. Prat, J. Garcia, D. Rojas, C. Carrasco, G. Inden, "Investigations on the growth kinetics of Laves phase precipitates in 12% Cr creep-resistant steels: Experimental and DICTRA calculations", *Acta Materialia*, 58 (2010) 6142-6153.
[154] D. Rojas, J. Garcia, O. Prat, G. Sauthoff, A.R. Kaysser-Pyzalla, "9%Cr heat resistant steels: Alloy design, microstructure evolution and creep response at 650 °C", *Materials Science and Engineering: A*, 528 (2011) 5164-5176.
[155] A.S. Argon, "Mechanisms and mechanics of fracture in creeping alloys, Recent Advances in Creep and Fracture of Engineering Materials and Structures, pp", *Mechanisms and Mechanics of Fracture in Creeping Alloys, Recent Advances in Creep and Fracture of Engineering Materials and Structures*, (1982) 1-52.

[156] B.F. Dyson, "Continuous cavity nucleation and creep fracture", *Scripta Metallurgica*, 17 (1983) 31-37.
[157] F. Sket, K. Dzieciol, A. Borbély, A.R. Kaysser-Pyzalla, K. Maile, R. Scheck, "Microtomographic investigation of damage in E911 steel after long term creep", *Materials Science and Engineering: A*, 528 (2010) 103-111.
[158] R. Raj, M.F. Ashby, "On grain boundary sliding and diffusional creep", *MT*, 2 (1971) 1113-1127.
[159] M.C. Messner, T.J. Truster, K.B. Cochran, D.M. Parks, T.L. Sham, "Fy17 Status Report on the Micromechanical Finite Element Modeling of Creep Fracture of Grade 91 Steel", in, Argonne National Lab. (ANL), Argonne, IL (United States), 2017.
[160] L.C. Lim, "Cavity nucleation at high temperatures involving pile-ups of grain boundary dislocations", *Acta Metallurgica*, 35 (1987) 1663-1673.
[161] V. Tvergaard, "On the creep constrained diffusive cavitation of grain boundary facets", *Journal of the Mechanics and Physics of Solids*, 32 (1984) 373-393.
[162] M.F. Ashby, "Boundary defects, and atomistic aspects of boundary sliding and diffusional creep", *Surface Science*, 31 (1972) 498-542.
[163] R. Ma, A.L. Pilchak, S.L. Semiatin, T.J. Truster, "Modeling the evolution of microtextured regions during α / β processing using the crystal plasticity finite element method", *International Journal of Plasticity*, (2018).
[164] K. Kimura, K. Sawada, H. Kushima, "Creep Rupture Ductility of Creep Strength Enhanced Ferritic Steels", *Journal of Pressure Vessel Technology*, 134 (2012) 031403.
[165] E.M. Haney, F. Dalle, M. Sauzay, L. Vincent, I. Tournié, L. Allais, B. Fournier, "Macroscopic results of long-term creep on a modified 9Cr–1Mo steel (T91)", *Materials Science and Engineering: A*, 510–511 (2009) 99-103.
[166] C. Herring, "Diffusional Viscosity of a Polycrystalline Solid", *Journal of Applied Physics*, 21 (1950) 437-445.
[167] R.L. Coble, "A Model for Boundary Diffusion Controlled Creep in Polycrystalline Materials", *Journal of Applied Physics*, 34 (1963) 1679-1682.
[168] M.E. Kassner, P. Kumar, W. Blum, "Harper–Dorn creep", *International Journal of Plasticity*, 23 (2007) 980-1000.
[169] J. Harper, J.E. Dorn, "Viscous creep of aluminum near its melting temperature", *Acta Metallurgica*, 5 (1957) 654-665.
[170] T.J. Truster, O. Nassif, "Variational projection methods for gradient crystal plasticity using Lie algebras", *International Journal for Numerical Methods in Engineering*, 110 (2017) 303-332.
[171] L. Benabou, Z. Sun, "Analytical homogenization modeling and computational simulation of intergranular fracture in polycrystals", *Int J Fract*, 193 (2015) 59-75.
[172] I. Benedetti, M.H. Aliabadi, "A three-dimensional cohesive-frictional grain-boundary micromechanical model for intergranular degradation and failure in

polycrystalline materials", *Computer Methods in Applied Mechanics and Engineering*, 265 (2013) 36-62.
[173] R. Quey, P.R. Dawson, F. Barbe, "Large-scale 3D random polycrystals for the finite element method: Generation, meshing and remeshing", *Computer Methods in Applied Mechanics and Engineering*, 200 (2011) 1729-1745.
[174] S.C. Aduloju, T.J. Truster, "On topology-based cohesive interface element insertion along periodic boundary surfaces", *Engineering Fracture Mechanics*, 205 (2019) 10-13.
[175] T.J. Truster, "On interface element insertion into three-dimensional meshes", *Engineering Fracture Mechanics*, 153 (2016) 171-174.
[176] T.J. Truster, "DEIP, discontinuous element insertion Program — Mesh generation for interfacial finite element modeling", *SoftwareX*, 7 (2018) 162-170.
[177] K. Schneider, B. Klusemann, S. Bargmann, "Fully periodic RVEs for technological relevant composites: not worth the effort!", *Journal of Mechanics of Materials and Structures*, 12 (2017) 471-484.
[178] J.D. Clayton, R.H. Kraft, R.B. Leavy, "Mesoscale modeling of nonlinear elasticity and fracture in ceramic polycrystals under dynamic shear and compression", *International Journal of Solids and Structures*, 49 (2012) 2686-2702.
[179] A. Musienko, G. Cailletaud, "Simulation of inter- and transgranular crack propagation in polycrystalline aggregates due to stress corrosion cracking", *Acta Materialia*, 57 (2009) 3840-3855.
[180] C.R. Picu, V. Gupta, "Stress singularities at triple junctions with freely sliding grains", *International Journal of Solids and Structures*, 33 (1996) 1535-1541.
[181] C.W. Lau, A.S. Argon, F.A. McClintock, "Application of the finite method in micromechanical analyses of creep fracture problems", *Computers & Structures*, 17 (1983) 923-931.
[182] J. Dundurs, M.S. Lee, "Stress concentration at a sharp edge in contact problems", *J Elasticity*, 2 (1972) 109-112.
[183] J.P. Dempsey, G.B. Sinclair, "On the stress singularities in the plane elasticity of the composite wedge", *J Elasticity*, 9 (1979) 373-391.
[184] R. Lim, "Numerical and experimental study of creep of Grade 91 steel at high temperature". MINES ParisTech, Cedex, France, 2011.
[185] H.B. Aaron, G.F. Bolling, "Free volume as a criterion for grain boundary models", *Surface Science*, 31 (1972) 27-49.
[186] H.B. Aaron, G.F. Bolling, "Free volume as a guide to grain boundary phenomena", *Scripta Metallurgica*, 6 (1972) 553-562.
[187] D.L. Olmsted, E.A. Holm, S.M. Foiles, "Survey of computed grain boundary properties in face-centered cubic metals—II: Grain boundary mobility", *Acta Materialia*, 57 (2009) 3704-3713.

[188] R. Wu, R. Sandsttrom, "Strain dependence of creep cavity nucleation in low alloy and 12%Cr steels", *Materials Science and Technology*, 12 (1996) 405-415.
[189] L. Kloc, V.c. SkleniÄka, "Transition from power-law to viscous creep behaviour of p-91 type heat-resistant steel", *Materials Science and Engineering: A*, 234 (1997) 962-965.
[190] G.P. Potirniche, "Prediction and Monitoring Systems of Creep-Fracture Behavior of 9Cr-1Mo Steels for Reactor Pressure Vessels", in, University of Idaho, 2013, pp. --.
[191] V. Gaffard, "Experimental study and modelling of high temperature creep ow and damage behaviour of 9Cr1Mo-NbV", in, 2007, pp. --.
[192] A.H. Chokshi, "Analysis of constrained cavity growth during high temperature creep deformation", *Materials Science and Technology*, 3 (1987) 656-664.
[193] P.J. Ennis, A. Zielinska-Lipiec, O. Wachter, A. Czyrska-Filemonowicz, "Microstructural stability and creep rupture strength of the martensitic steel P92 for advanced power plant", *Acta Materialia*, 45 (1997) 4901-4907.
[194] T.J. Truster, A. Masud, "Primal interface formulation for coupling multiple PDEs: A consistent derivation via the Variational Multiscale method", *Computer Methods in Applied Mechanics and Engineering*, 268 (2014) 194-224.
[195] T.J. Truster, P. Chen, A. Masud, "Finite strain primal interface formulation with consistently evolving stabilization", *International Journal for Numerical Methods in Engineering*, 102 (2015) 278-315.
[196] T.J. Truster, P. Chen, A. Masud, "Finite strain primal interface formulation with consistently evolving stabilization", *Int. J. Numer. Meth. Engng*, (2014).
[197] A. Masud, T.J. Truster, L.A. Bergman, "A variational multiscale a posteriori error estimation method for mixed form of nearly incompressible elasticity", *Computer Methods in Applied Mechanics and Engineering*, 200 (2011) 3453-3481.
[198] T.J.R. Hughes, "Multiscale phenomena: Green's functions, the Dirichlet-to-Neumann formulation, subgrid scale models, bubbles and the origins of stabilized methods", *Computer Methods in Applied Mechanics and Engineering*, 127 (1995) 387-401.
[199] F. Brezzi, M. Fortin, "Mixed and Hybrid Finite Elelement Methods", Springer-Verlag, New York, NY, USA, 1991.
[200] A. Masud, K. Xia, "A variational multiscale method for inelasticity: Application to superelasticity in shape memory alloys", *Computer Methods in Applied Mechanics and Engineering*, 195 (2006) 4512-4531.
[201] R. Calderer, A. Masud, "Residual-based variational multiscale turbulence models for unstructured tetrahedral meshes", *Computer Methods in Applied Mechanics and Engineering*, 254 (2012) 238–253.

[202] M. Cervera, M. Chiumenti, Q. Valverde, C. Agelet de Saracibar, "Mixed linear/linear simplicial elements for incompressible elasticity and plasticity", *Computer Methods in Applied Mechanics and Engineering*, 192 (2003) 5249-5263.
[203] T.J. Truster, "A stabilized, symmetric Nitsche method for spatially localized plasticity", *Computational Mechanics*, 57 (2015) 75-103.
[204] F. Brezzi, M.-O. Bristeau, L.P. Franca, M. Mallet, G. Rogé, "A relationship between stabilized finite element methods and the Galerkin method with bubble functions", *Computer Methods in Applied Mechanics and Engineering*, 96 (1992) 117-129.
[205] J.E. Dolbow, L.P. Franca, "Residual-free bubbles for embedded Dirichlet problems", *Computer Methods in Applied Mechanics and Engineering*, 197 (2008) 3751-3759.
[206] A. Masud, R.A. Khurram, "A multiscale/stabilized finite element method for the advection–diffusion equation", *Computer Methods in Applied Mechanics and Engineering*, 193 (2004) 1997-2018.
[207] A. Masud, K. Xia, "A Stabilized Mixed Finite Element Method for Nearly Incompressible Elasticity", *J. Appl. Mech.*, 72 (2005) 711-720.
[208] D.N. Arnold, F. Brezzi, B. Cockburn, L.D. Marini, "Unified analysis of discontinuous Galerkin methods for elliptic problems", *SIAM Journal on Numerical Analysis*, 39 (2002) 1749-1779.
[209] C. Annavarapu, M. Hautefeuille, J.E. Dolbow, "A robust Nitsche's formulation for interface problems", *Computer Methods in Applied Mechanics and Engineering*, 225-228 (2012) 44-54.
[210] A.T. Eyck, F. Celiker, A. Lew, "Adaptive stabilization of discontinuous Galerkin methods for nonlinear elasticity: Analytical estimates", *Computer Methods in Applied Mechanics and Engineering*, 197 (2008) 2989-3000.
[211] J. Sanders, M.A. Puso, "An embedded mesh method for treating overlapping finite element meshes", *International Journal for Numerical Methods in Engineering*, 91 (2012) 289-305.
[212] J.D. Sanders, T.A. Laursen, M.A. Puso, "A Nitsche embedded mesh method", *Computational Mechanics*, 49 (2012) 243-257.
[213] A. Masud, T.J. Truster, L.A. Bergman, "A unified formulation for interface coupling and frictional contact modeling with embedded error estimation", *International Journal for Numerical Methods in Engineering*, 92 (2012) 141-177.
[214] A. Ten Eyck, A. Lew, "Discontinuous Galerkin methods for non-linear elasticity", *International Journal for Numerical Methods in Engineering*, 67 (2006) 1204-1243.
[215] J. Mergheim, P. Steinmann, "A geometrically nonlinear FE approach for the simulation of strong and weak discontinuities", *Computer Methods in Applied Mechanics and Engineering*, 195 (2006) 5037-5052.

[216] L. Noels, R. Radovitzky, "A general discontinuous Galerkin method for finite hyperelasticity. Formulation and numerical applications", *International Journal for Numerical Methods in Engineering*, 68 (2006) 64-97.
[217] J.P. Whiteley, "Discontinuous Galerkin finite element methods for incompressible non-linear elasticity", *Computer Methods in Applied Mechanics and Engineering*, 198 (2009) 3464-3478.
[218] E. Lorentz, "A mixed interface finite element for cohesive zone models", *Computer Methods in Applied Mechanics and Engineering*, 198 (2008) 302-317.
[219] T.J. Truster, A. Masud, "A Discontinuous/continuous Galerkin method for modeling of interphase damage in fibrous composite systems", *Computational Mechanics*, 52 (2013) 499-514.
[220] V.P. Nguyen, "Discontinuous Galerkin/extrinsic cohesive zone modeling: Implementation caveats and applications in computational fracture mechanics", *Engineering Fracture Mechanics*, 128 (2014) 37-68.
[221] S.C. Aduloju, T.J. Truster, "A variational multiscale discontinuous Galerkin formulation for both implicit and explicit dynamic modeling of interfacial fracture", *Computer Methods in Applied Mechanics and Engineering*, 343 (2019) 602-630.
[222] M.G.A. Tijssens, B.L.J. Sluys, E. van der Giessen, "Numerical simulation of quasi-brittle fracture using damaging cohesive surfaces", *European Journal of Mechanics - A/Solids*, 19 (2000) 761-779.
[223] H.D. Espinosa, P.D. Zavattieri, "A grain level model for the study of failure initiation and evolution in polycrystalline brittle materials. Part II: Numerical examples", *Mechanics of Materials*, 35 (2003) 365-394.
[224] S. Jimenez, R. Duddu, "On the parametric sensitivity of cohesive zone models for high-cycle fatigue delamination of composites", *International Journal of Solids and Structures*, 82 (2016) 111-124.

APPENDICIES

A.1 GB model implementation

The grain boundary constitutive model in Chapter 4 is treated using an explicit forward Euler time integration scheme within so-called interface finite elements. The most common approach for realizing interface traction-separation models is the intrinsic cohesive zone method, although recently other approaches have been proposed such as mixed formulations using Lagrange multipliers [218] and primal formulations using numerical fluxes [219-221]. In the cohesive zone method, the traction at the interface is an explicit function of the displacement jump at the interface, implying that traction vanishes if and only if the jump vanishes. Therefore, an artificial stiffness is required to express the traction-separation relation prior to cavity nucleation to suppress separation as well as for compression to suppress interpenetration:

$$T_n = K_n \left[\!\left[u_n^{(e)} \right]\!\right], \qquad \dot{T}_n = K_n \left[\!\left[\dot{u}_n^{(e)} \right]\!\right] \tag{43}$$

Here, $\left[\!\left[u_n^{(e)} \right]\!\right]$ is the elastic or recoverable normal separation and K_n is the normal direction stiffness. Ideally, this stiffness will be large enough that grain boundary opening prior to cavity growth is a small fraction of the deformations from grain boundary sliding and grain creep. However, an overly large normal stiffness is known to cause numerical inaccuracies and convergence problems; see studies within [159, 222-224]. A stiffness of $10K_n$ is applied when the traction state is compressive to both ensure numerical stability and minimize grain boundary penetration.

The time-discrete counterparts of the normal traction-separation relation are developed as follows. For simplicity, all of the state variables at an interface quadrature point are grouped into a state vector $\chi_n = \chi(t_n) = \{a_n, b_n, V_n, N_n\}$ for a series of time steps 0 to T with time step Δt and time at step n as t_n. All evolution equations (4.3) – (4.9) are then determined from the state at step n depending on whether the facet is opening or closing

(determined by the sign of $\left[\!\left[\left(u_{n,n+1}-u_{n,n}\right)/\Delta t\right]\!\right]$). When the point is not opening, the sole contribution to traction is from (43). For the opening case, the evolved interface state is computed from the boundary diffusion $\dot{V}^{(d)}$ plus the local creep $\dot{V}^{(c)}$ contributions evaluated at state $\boldsymbol{\chi}_n$ from step n. In particular, $\dot{V}^{(c)}\left(\boldsymbol{\chi}_n\right)$ is evaluated according to (4.8) or (4.9) using the neighboring solid element stresses and state that are stored from the previous converged time step, as discussed in Appendix A.3. The cavity size and number density are then expressed using forward Euler expressions as follows:

$$a_{n+1} = a_n + \Delta t\left[\dot{V}^{(c)}\left(\boldsymbol{\chi}_n\right)+\dot{V}^{(d)}\left(\boldsymbol{\chi}_n\right)\right]/\left[4\pi h(\psi)a_n^2\right] \tag{44}$$

$$N_{n+1} = N_n + \Delta t F_N\left(\left\langle T_{n,n}\right\rangle/\Sigma_0\right)^{\beta}\dot{\varepsilon}^{C}_{eq,n} \tag{45}$$

$$b_{n+1} = 1/\sqrt{\pi N_{n+1}} \tag{46}$$

Note that the diffusion-based component $\dot{V}^{(d)}$ of the cavity volume growth rate depends on the cavity size and spacing through the geometric function $q(f)$ according to (4.13). A modified version $\tilde{q}(f)$ has been developed in order to simulate cavity coalescence at lower porosity $f = a^2/b^2$ as well as to avoid numerical difficulties from the unbounded nature of (4.13). The modified function is specified such that $\tilde{q}(f) = q(f)$ for low porosity $f < f_i$ and $\tilde{q}(f) = q_{\min}$ for high porosity $f > f_j$. The modification employs a cubic Hermitian polynomial for the transitional range $f_i < f < f_j$, ensuring continuity of magnitude and slope at the endpoints of this range. Our numerical sensitivity studies have identified these parameters as $f_i = 0.25$, $f_j = 0.49$, and $q_{\min} = 10^{-9}$.

Now combining the separation from the linear stiffness (43) in series with the cavity growth equations (4.3), (4.5), and (4.6), we obtain:

$$\left[\!\left[\dot{u}_n\right]\!\right] = \left[\!\left[\dot{u}_n^{(i)}\right]\!\right] + \left[\!\left[\dot{u}_n^{(e)}\right]\!\right] = \left[\dot{V}^{(c)}+\dot{V}^{(d)}\right]/\left(\pi b^2\right) + \dot{T}_n/K_n \tag{47}$$

Discretization in time yields:

$$\left[\!\left[\left(u_{n,n+1}-u_{n,n}\right)/\Delta t\right]\!\right]=\left[\dot{V}^{(c)}\left(\boldsymbol{\chi}_n\right)+8\pi D\left\langle T_{n,n+1}\right\rangle/q(f_n)\right]/\left(\pi b_n^2\right)+\left(T_{n,n+1}-T_{n,n}\right)/K_n\Delta t \quad (48)$$

In the nonlinear finite element method at an iteration of the Newton method, the current displacement jump estimate will be given and the traction is required for evaluating the internal force vector. Therefore, (48) is solved for the traction at time t_{n+1} to obtain:

$$T_{n,n+1}=\frac{\left[\!\left[\left(u_{n,n+1}-u_{n,n}\right)/\Delta t\right]\!\right]-\dot{V}^{(c)}\left(\boldsymbol{\chi}_n\right)/\left(\pi b_n^2\right)+T_{n,n}/K_n\Delta t}{8D/b_n^2 q(f_n)+1/K_n\Delta t} \quad (49)$$

Note that the normal traction T_n can experience oscillations when evaluated directly from (49), leading to premature cavity nucleation in (45). Therefore, our code provides an option to compute a pseudo traction $\tilde{T}_n=\boldsymbol{n}\cdot\boldsymbol{\sigma}\cdot\boldsymbol{n}$ using the stress state in the neighboring solid elements from step n. This modification increases the stability and does not degrade the physical accuracy when small time step sizes are employed.

Lastly, the tangential traction is computed from a straightforward expression of (4.14):

$$\boldsymbol{T}_{s,n+1}=\eta_0 f_{sd}\left(a_n/b_n\right)\left[\!\left[\left(\boldsymbol{u}_{s,n+1}-\boldsymbol{u}_{s,n}\right)/\Delta t\right]\!\right] \quad (50)$$

While explicit treatment is applied to the interface model, the global equilibrium equation remains as a coupled nonlinear system of equations due to the solid elements. To solve this system with the Newton-Raphson method, linearized interface expressions are required. These expressions for the algorithmic stiffness are obtained from the two traction components as:

$$\frac{\partial T_{n,n+1}}{\partial\left[\!\left[u_{n,n+1}\right]\!\right]}=\frac{K_n b_n^2 q(f_n)}{8D\Delta t K_n+b_n^2 q(f_n)}=\frac{K_n}{K_n\left[8D\Delta t/b_n^2 q(f_n)\right]+1} \quad (51)$$

$$\frac{\partial \boldsymbol{T}_{s,n+1}}{\partial\left[\!\left[\boldsymbol{u}_{s,n+1}\right]\!\right]}=\eta_0 f_{sd}\left(a_n/b_n\right)/\Delta t\left(\boldsymbol{I}-\boldsymbol{n}\otimes\boldsymbol{n}\right) \quad (52)$$

Note that employing the calibrated material parameters of $a_0=50\ \text{nm}$, $b_0=60\ \mu\text{m}$, and $D=1\times10^{-15}\ \text{MPa}^{-1}\cdot\text{h}^{-1}\cdot\text{mm}^3$ produces values for the stiffness $\left[8D\Delta t/b_n^2 q(f_n)\right]^{-1}$ ranging from 10^{14} MPa/mm when $\Delta t=0.01\ \text{h}$ to 10^{11} MPa/mm when $\Delta t=10\ \text{h}$.

A.2 PAG model implementation

The solid finite element material model for the PAG utilizes backward Euler integration of the evolution equations in Chapter 4 along the lines of [163]. The discrete equations extended to include the diffusive contribution are presented as follows for a generic time step $t_{n+1} = t_n + \Delta t$:

$$\mathbf{0} = \boldsymbol{R}_1 = \boldsymbol{t}_{n+1} - \left[\boldsymbol{t}_n + \boldsymbol{C}_o : \left(\Delta \boldsymbol{d}_{n+1} - \Delta \bar{\boldsymbol{d}}^{(p)}_{n+1} - \Delta \bar{\boldsymbol{d}}^{(d)}_{n+1} \right) + \Delta \bar{\boldsymbol{W}}^{(p)}_{n+1} \boldsymbol{t}_{n+1} - \boldsymbol{t}_{n+1} \Delta \bar{\boldsymbol{W}}^{(p)}_{n+1} \right] \tag{53}$$

$$0 = R_2 = \tau_{w,n+1} - \theta_0 \left(1 - \tau_{w,n+1} / \tau_v \right) \sum_{s=1}^{n_{slip}} \left| \Delta \gamma^{(s)}_{n+1} \right| \tag{54}$$

$$\Delta \gamma^{(s)}_{n+1} \left(\tau^{(s)}; \tilde{\tau} \right) = \frac{\dot{\bar{\gamma}}}{\tilde{\tau}_{n+1}} \left| \frac{\tau^{(s)}_{n+1}}{\tilde{\tau}_{n+1}} \right|^{n-1} \tau^{(s)}_{n+1}, \qquad \tau^{(s)}_{n+1} = \boldsymbol{t}_{n+1} : \left(\boldsymbol{R}^{pT}_n \tilde{\boldsymbol{m}}^{(s)} \boldsymbol{R}^p_n \right) \tag{55}$$

$$\Delta \boldsymbol{d}^{(d)}_{n+1} = D_\eta \Delta t \, \mathrm{dev} \left(\boldsymbol{t}_{n+1} \right) \tag{56}$$

$$\Delta \bar{\boldsymbol{d}}^{(p)}_{n+1} = \sum_{s=1}^{n_{slip}} \Delta \gamma^{(s)}_{n+1} \boldsymbol{R}^{pT}_n \tilde{\boldsymbol{m}}^{(s)} \boldsymbol{R}^p_n \tag{57}$$

$$\Delta \bar{\boldsymbol{W}}^{(p)}_{n+1} = \boldsymbol{R}_{n+1} \left[\sum_{s=1}^{n_{slip}} \Delta \gamma^{(s)}_{n+1} \boldsymbol{R}^{pT}_n \tilde{\boldsymbol{q}}^{(s)} \boldsymbol{R}^p_n \right] \boldsymbol{R}^T_{n+1} \tag{58}$$

Herein, $\Delta \boldsymbol{d}_{n+1} = \boldsymbol{d}_{n+1} \Delta t$ is the current strain increment, and notice that an explicit treatment of the plastic rotation tensor is utilized. The two residual equations (53) and (54) are solved using the Newton-Raphson method expressed via a linearized system:

$$\begin{bmatrix} \boldsymbol{J}_{11} & \boldsymbol{J}_{12} \\ \boldsymbol{J}_{21} & J_{22} \end{bmatrix} \begin{bmatrix} \delta \boldsymbol{t} \\ \delta \tau_w \end{bmatrix} = \begin{bmatrix} \boldsymbol{R}_1 \\ R_2 \end{bmatrix} \tag{59}$$

$$\begin{aligned} J_{11,ijkl} = {} & \tfrac{1}{2} \left(\delta_{ik} \delta_{jl} + \delta_{il} \delta_{jk} \right) + \tfrac{1}{2} \left(\delta_{ik} \Delta \bar{W}^{(p)}_{lj} + \delta_{il} \Delta \bar{W}^{(p)}_{kj} \right) - \tfrac{1}{2} \left(\Delta \bar{W}^{(p)}_{ik} \delta_{jl} + \Delta \bar{W}^{(p)}_{il} \delta_{jk} \right) \\ & + D_\eta \Delta t C_{0,ijmn} \left[\tfrac{1}{2} \left(\delta_{mk} \delta_{nl} + \delta_{ml} \delta_{nk} \right) - \tfrac{1}{3} \delta_{mn} \delta_{kl} \right] + \sum_{s=1}^{n_{slip}} \bar{C}^{(s)}_{ij} \frac{\partial \Delta \gamma^{(s)}_{n+1}}{\partial \tau^{(s)}} R^p_{mk} \tilde{m}^{(s)}_{mn} R^p_{nl} \end{aligned} \tag{60}$$

$$J_{12,ij} = \sum_{s=1}^{n_{slip}} \bar{C}^{(s)}_{ij} \frac{\partial \Delta \gamma^{(s)}_{n+1}}{\partial \tau_w} \tag{61}$$

$$J_{21,ij\alpha} = -\theta_0 \left(1 - \tau_{w,n+1}/\tau_v\right) \frac{\partial \Delta\gamma_{n+1}^{(s)}}{\partial \tau^{(s)}} R_{mi}^p \tilde{m}_{mn}^{(s)} R_{nj}^p \tag{62}$$

$$J_{22} = 1 + \theta_0/\tau_v \sum_{s=1}^{n_{slip}} \left|\Delta\gamma_{n+1}^{(s)}\right| - \theta_0 \left(1 - \tau_{w,n+1}/\tau_v\right) \sum_{s=1}^{n_{slip}} \frac{\partial \Delta\gamma_{n+1}^{(s)}}{\partial \tau_w} \tag{63}$$

$$\bar{C}_{ij}^{(s)} = C_{0,ijmn} R_{km}^p \tilde{m}_{kl}^{(s)} R_{ln}^p + t_{im} R_{mo} R_{ko}^p \tilde{q}_{kl}^{(s)} R_{lp}^p R_{jp} - t_{mj} R_{io} R_{ko}^p \tilde{q}_{kl}^{(s)} R_{lp}^p R_{mp} \tag{64}$$

$$\frac{\partial \Delta\gamma_{n+1}^{(s)}}{\partial \tau^{(s)}} = \frac{n \dot{\bar{\gamma}} \Delta t}{\tilde{\tau}_{n+1}^n} \left|\tau_{n+1}^{(s)}\right|^{n-1} \tag{65}$$

$$\frac{\partial \Delta\gamma_{n+1}^{(s)}}{\partial \tau_w} = -\frac{n}{\tilde{\tau}_{n+1}} \Delta\gamma_{n+1}^{(s)} \tag{66}$$

Notice that the chain rule and product rule of differentiation have been applied several times, so that the model-dependent terms are (54) and (55) along with (62), (63), (65), and (66). These tensorial component expressions are implemented using Voigt notation in [71]. Line search techniques can be included into the updates of increments $\delta \boldsymbol{t}$ and $\delta \tau_w$ to improve the numerical robustness. Further comments on these and other details of implementation are contained in [71, 159, 163].

A.3 Nonlocal variables and effective power law exponent for PAGB model

As mentioned in Chapter 4, the grain boundary cavity growth models of [28, 150, 161] includes terms for creep-driven growth that are mediated by an assumed isotropic power-law viscous representation of matrix flow. In particular, expressions (4.8) – (4.10) have a dependence on the exponent n as well as the effective creep strain and stress. Since the mechanical model for the grains in Chapter 4 combines anisotropic crystal plasticity and linear viscous diffusive flow, an effective definition for this exponent is needed to account for the dominant mechanism shift between high and low stresses both remotely and in the neighborhood of certain boundaries, as opposed to simply specifying a constant. This

allows a different value for each volumetric finite element incident on a grain boundary finite element.

Recall that Grade 91 has a BCT lattice which we approximate as body-centered cubic. Such cubic crystals exhibit only mild viscoplastic anisotropy at elevated temperatures compared to lower-symmetry hexagonal crystals. Therefore, it is reasonable to adopt equivalent "effective" stress σ_{eq} and strain rate $\dot{\varepsilon}^C_{eq}$ states according to (4.17) from the local material state as the driving forces in the cavity model. These quantities are simply evaluated from the dislocation creep (4.18) and diffusional creep (4.24) strain rates. However, the more challenging interpretation is the (instantaneous) effective isotropic power-law creep exponent, to be extracted from an effective power-law model of the form:

$$\ln \dot{\varepsilon}^C_{eq} = \ln B + n \ln \sigma_{eq} \tag{67}$$

Assuming a constant rate coefficient B, taking the derivative with respect to σ_{eq} and rearranging, we obtain an effective strain-rate sensitivity exponent:

$$n_{\text{eff}} = \frac{\sigma_{eq}}{\dot{\varepsilon}^C_{eq}} \frac{d(\dot{\varepsilon}^C_{eq})}{d\sigma_{eq}} \tag{68}$$

In the isotropic case, with $\boldsymbol{\sigma}'$ coaxial with $\dot{\boldsymbol{\varepsilon}}^C$, the creep exponent relates changes in the magnitude of the creep rate to corresponding changes in the magnitude of the stress deviator; see relations (4.17). This interpretation of 'magnitude sensitivity' will be retained in the interpretation of an effective creep exponent for crystal plasticity. Thus, a small proportional change in the stress deviator is considered in terms of a dimensionless number z (ultimately set to zero), leading to a set of 'starred' state variables in the perturbed state:

$$\boldsymbol{\sigma}^\star(z) \equiv (1+z)\,\boldsymbol{\sigma}', \tag{69}$$

$$\sigma^\star_{eq}(z) = \sqrt{\frac{3}{2}\boldsymbol{\sigma}^\star(z) : \boldsymbol{\sigma}^\star(z)} = |1+z|\,\sigma_{eq}, \tag{70}$$

$$\dot{\gamma}^{(s);\star} = f(\tau^{(s);\star};\tilde{\tau}), \qquad \tau^{(s);\star} = (1+z)\tau^{(s)} \tag{71}$$

$$\dot{\boldsymbol{\varepsilon}}^{\star} = \boldsymbol{d}^{(d);\star}\left(\boldsymbol{\sigma}^{\star}(z)\right) + \sum_{s=1}^{n_{\text{slip}}} \dot{\gamma}^{(s);\star}\left(\boldsymbol{m}^{(s)} \otimes \boldsymbol{n}^{(s)}\right)_S, \tag{72}$$

$$\dot{\varepsilon}^{\star}_{eq} = \sqrt{\frac{2}{3}\dot{\boldsymbol{\varepsilon}}^{\star} : \dot{\boldsymbol{\varepsilon}}^{\star}} \ . \tag{73}$$

The derivative of the effective creep strain rate with respect to stress can be interpreted as:

$$\frac{d\dot{\varepsilon}^{C}_{eq}}{d\sigma_{eq}} = \left.\frac{d\dot{\varepsilon}^{\star}_{eq}}{d\sigma^{\star}_{eq}}\right|_{z=0} = \left.\frac{d\dot{\varepsilon}^{\star}_{eq}}{dz}\right|_{z=0} \Big/ \left.\frac{d\sigma^{\star}_{eq}}{dz}\right|_{z=0} = \frac{1}{\sigma_{eq}} \left.\frac{d\dot{\varepsilon}^{\star}_{eq}}{dz}\right|_{z=0} . \tag{74}$$

where according to (70) the denominator simplifies to $d\sigma^{\star}_{eq}/dz = \sigma_{eq}$. Evaluating the numerator requires accounting for the crystallographic slip rate relation (4.21):

$$\begin{aligned}
\frac{d\dot{\varepsilon}^{\star}_{eq}(z)}{dz} &= \frac{1}{2}\frac{1}{\dot{\varepsilon}^{\star}_{eq}} 2\frac{2}{3}\dot{\boldsymbol{\varepsilon}}^{\star} : \frac{d\dot{\boldsymbol{\varepsilon}}^{\star}}{dz} \\
&= \frac{2}{3\dot{\varepsilon}^{\star}_{eq}}\dot{\boldsymbol{\varepsilon}}^{\star} : \left[\frac{d\boldsymbol{d}^{(d);\star}}{d\sigma^{\star}_{eq}}\frac{d\sigma^{\star}_{eq}}{dz} + \sum_{s=1}^{n_{\text{slip}}} \frac{\partial f(\tau^{(s);\star};\tilde{\tau})}{\partial \tau^{(s);\star}}\frac{d\tau^{(s);\star}}{dz}\left(\boldsymbol{m}^{(s)} \otimes \boldsymbol{n}^{(s)}\right)_S\right] \\
&= \frac{2}{3}\frac{\dot{\boldsymbol{\varepsilon}}^{\star}}{\dot{\varepsilon}^{\star}_{eq}} : \left[\frac{d\boldsymbol{d}^{(d);\star}}{d\sigma^{\star}_{eq}}\frac{d\sigma^{\star}_{eq}}{dz} + \sum_{s=1}^{n_{\text{slip}}} \tau^{(s)}\frac{\partial f(\tau^{(s);\star};\tilde{\tau})}{\partial \tau^{(s);\star}}\left(\boldsymbol{m}^{(s)} \otimes \boldsymbol{n}^{(s)}\right)_S\right].
\end{aligned} \tag{75}$$

Evaluating at $z = 0$ leads to the result

$$\left.\frac{d\dot{\varepsilon}^{C}_{eq}(z)}{dz}\right|_{z=0} = \frac{2}{3}\frac{\dot{\boldsymbol{\varepsilon}}^{C}}{\dot{\varepsilon}^{C}_{eq}} : \left[\frac{d\boldsymbol{d}^{(d)}}{d\sigma_{eq}}\sigma_{eq} + \sum_{s=1}^{n_{\text{slip}}} \tau^{(s)}\frac{\partial f(\tau^{(s)};\tilde{\tau})}{\partial \tau^{(s)}}\left(\boldsymbol{m}^{(s)} \otimes \boldsymbol{n}^{(s)}\right)_S\right]. \tag{76}$$

Finally, combining expressions (68), (74), and (76) yields the suggested form for "equivalent" viscoplastic rate-sensitivity as:

$$n_{\text{eff}} = \frac{2}{3}\frac{\dot{\boldsymbol{\varepsilon}}^{C}}{\dot{\varepsilon}^{C}_{eq}} : \left[\frac{d\boldsymbol{d}^{(d)}}{d\sigma_{eq}}\frac{\sigma_{eq}}{\dot{\varepsilon}^{C}_{eq}} + \sum_{s=1}^{n_{\text{slip}}} \frac{\partial f(\tau^{(s)};\tilde{\tau})}{\partial \tau^{(s)}}\frac{\tau^{(s)}}{\dot{\varepsilon}^{C}_{eq}}\left(\boldsymbol{m}^{(s)} \otimes \boldsymbol{n}^{(s)}\right)_S\right]. \tag{77}$$

Note that the partial derivative $\partial f(\tau^{(s)};\tilde{\tau})/\partial \tau^{(s)}$ is required for the nonlinear solution algorithm for crystal plasticity in Appendix A.3 and thus is readily available.

This effective exponent is computed along with the other variables σ_{eq} and $\dot{\varepsilon}_{eq}^{C}$ from (4.17) as an output after the convergence of the Appendix A.3 Newton algorithm at a solid element quadrature point. For an explicit integration of the PAGB model as in Appendix A.2, the values of these quantities are retained (and those converged) from time step t_n and used for step t_{n+1} of the interface element material update. For simplicity, the values of σ_{eq}, $\dot{\varepsilon}_{eq}^{C}$, σ_m, and n across all quadrature points of the two elements neighboring an interface element are averaged together.

VITA

Omar Nassif was born in Sharjah, UAE on April 29, 1989. He received his B.Sc. degree in Civil Engineering from University of Sharjah, Sharjah in September, 2011. He received his M.Sc. degree in Civil Engineering from University of Sharjah, Sharjah in June, 2014. Omar is currently pursuing doctoral studies in Civil and Environmental Engineering Department at the University of Tennessee, Knoxville.